
Coupled-resonator Optical Waveguides and Multiplexed Solitons

Engineering linear and nonlinear periodic
phenomena for optical communications

Shayan Mookherjea

*In partial fulfillment of the requirements for
the degree of **Doctor of Philosophy** at the
California Institute of Technology, June 2003*

Defended Sept. 6, 2002, Revised Apr. 9, 2003.

Copyright 2003
California Institute of Technology
All rights reserved

Figs 1.1 and 1.2 were generated by the author using data obtained from the software package *Translight* written by Andrew L. Reynolds at the Photonic Band Gap Materials Research Group within the Optoelectronics Research Group of the Department of Electronics and Electrical Engineering, the University of Glasgow. *Translight* is based on the Transfer Matrix Method developed by J. Pendry, P. M. Bell, A. J. Ward, and L. M. Moreno of the Imperial College, London.

Thesis Committee

Amnon Yariv

Martin and Eileen Summerfield Professor of Applied Physics

Thomas A. Tombrello

William R. Kenan, Jr., Professor and Professor of Physics

Donald S. Cohen

Charles Lee Powell Professor of Applied Mathematics

David B. Rutledge

Kiyo and Eiko Tomiyasu Professor of Electrical Engineering

Axel Scherer

*Bernard A. Neches Professor of Electrical Engineering,
Applied Physics and Physics*

Practically, we are not interested in exact transmission when we have a continuous source, but only in transmission to within a certain tolerance.

—C. E. Shannon, *Bell Syst. Tech. J.*, **27**, pp. 379–423, 623–656 (1948).

We observe from Fig. 1.1 that communication system architecture centers or pivots around the communications channel ... Modeling the effects of the physical channel on the propagating electromagnetic field in different frequency bands and under various scenarios is a continuous and ongoing task.

—M. K. Simon, S. M. Hinedi and W. C. Lindsey *Digital Communication Techniques*, Prentice Hall (Englewood Cliffs, NJ, 1995).

Preface

The brevity of life does not allow us the luxury of spending time on problems which will lead to no new results.

—L. D. Landau, as quoted by E. M. Lifshitz in L. D. Landau and E. M. Lifshitz, *Mechanics*, Vol. 1 of *Course of Theoretical Physics*, Pergamon Press (Oxford, 1976).

This thesis addresses two topics in lightwave communication systems—increasing the bit rate of data transmission, and finding a way to temporarily store information-carrying optical pulses in compact semiconductor devices. The former identifies a way to utilize existing (nonlinear) transmission phenomena to advantage in sending information across optical fiber, and the latter is a proposal for a class of devices that are frontline components in packet-switched optical networks.

The fundamental format for carrying information is an optical pulse, a localized packet of electromagnetic energy. The output light from a laser, at a particular carrier optical frequency, is turned on and off at a particular rate (amplitude modulation¹) to create a train of pulses which represents the information in a sequence of bits. The frequency (Fourier) spectrum of an amplitude modulated signal contains a narrow band of frequency components around the carrier frequency; the faster the rate of modulation, the greater the spectral width of this band.

It is necessary that this band of frequencies fits within the “transparency window” of the transmission medium. Fibers made of high-purity silica have a very wide range of frequencies available for carrying information, and therefore, the modulation rate can be quite high. It is, in fact, other practical issues that place a lower limit on the minimum pulse width—a few hundred femtoseconds in long-distance communications. A minimum pulse width means that the maximum spread of the modulation band

¹The overwhelming majority of practical schemes for optical communications use amplitude modulation (on-off keying), although other forms of modulation (frequency or phase) have been investigated.

around the center (carrier) frequency is restricted, and the available spectrum of the optical fiber outside this band is not utilized.

For higher data-rate communications, a number of different lasers with different center frequencies can be modulated simultaneously², so that more of the available transmission channel bandwidth is used efficiently. A simple picture of a digital transmission format is the so-called wavelength-division multiplexing (WDM) over time-division multiplexing (TDM): the presence of a pulse of light at a particular frequency (wavelength) in a particular timeslot signifies a “one” and whose absence then signifies a “zero.” The successful operation of a high-speed multichannel communication system depends on the degree to which the noise of the system can be compensated for, and the principal sources of noise in optical channels include the dispersion of the fiber, effects of nonlinearities in the dielectric material that comprises the fiber, and the noise added by optical amplifiers. Conventional systems try to minimize the effect of dispersion and of the nonlinearities; the recent development of optical solitons makes it possible to design a system that utilizes dispersion and nonlinearity constructively.

■ Prof. Amnon Yariv has always made himself available for counsel, and has generously let me define my own thesis, based on topics I found promising and meaningful. My experiences associated with his research group will be invaluable in the years ahead. Profs. Don Cohen and Bruno Crosignani have been valuable collaborators in aspects of this work, particularly deserving of acknowledgment in an environment where effective scientific collaboration is difficult. Profs. Tom Tombrello, Don Cohen, Dave Rutledge, and Axel Scherer graciously served on my thesis committee and have been a source of continuing help and advice over many years.

At MIT, Prof. Vincent Chan supported my research on optical networks, a collaboration and friendship that extended even when I returned to Caltech. The encouragement of Profs. Hermann Haus and Erich Ippen was a source of inspiration. I’d also like to take this opportunity to thank a few other outstanding teachers I’ve had the privilege of learning from: Profs. Jim Fujimoto, Glen George, Jin Au Kong, Bob McEliece, and Mark Wise.

²Or a number of designated wavelengths can be filtered from a single source of sufficient bandwidth.

■ *Historical outline:* In January 2001, Yi Li, with whom I shared an office at the time, told me of his conversations with Prof. Yariv on the frozen-light experiments performed by the Harvard groups (Hau and Lukin), which led to my interpreting their approach based on electromagnetically induced transparency as phenomenologically very similar to holography (February 1, 2001, and in later conversations with Lene Hau, June 6, 2002). At that time, we weren't quite sure how to translate the slow-light phenomenology to the optical domain. A month later (March 14, 2001), Yong Xu told me about his idea of using defect states pulled outside a CROW band to trap light propagating in the CROW band. Although this wasn't in itself a solution to our problem, it seemed plausible that combining the reduction in the group velocity of light propagating in a CROW band with the photorefractive process would lead to interesting new applications. But there were few studies of pulse propagation in photonic crystal waveguides at that time beyond that of numerical simulations, and none of nonlinear processes such as the photorefractive effect in such waveguides.

We are now able to characterize pulse propagation in CROWs not only in the linear dispersion approximation—as is most practical for applications based on index gratings, e.g., holography—but using the complete (nonlinear) dispersion relationship. This led to our prediction and analyses of a class of super-resonant modes in CROWs comprised of $\chi^{(3)}$ material, which are essentially Schrödinger solitons but with zero group velocity—they remain spatially frozen to a finite section of the waveguide.

My work on solitons in optical fibers began soon after I joined Caltech (July 2000). There are interesting analogies between the diffraction of a Gaussian beam in a rotationally symmetric quadratic index medium and the propagation of a Gaussian pulse in the presence of the Kerr effect. Some of the analogies cannot be explained algebraically, i.e., the ABCD matrix translation rules fail, but topological arguments are very effective (January 2001, following a suggestion by Prof. D. S. Cohen). Inasmuch as conformal mappings have become an important tool in waveguide design, geometric arguments may offer a new way to design nonlinear optical transmission links.

We have analyzed the Hamiltonian approach to designing a nonlinearly multiplexed dispersion-managed soliton transmission communication system (June 2001). Breathing pulse shapes traverse closed orbits in phase space, and therefore, we may identify different trajectories with different codes to achieve higher channel capacity than possible in linear channels.

■ My closest collaborators, George T. Paloczi and Dr. Yanyi Huang, are particularly deserving of thanks for their friendship, and sharing in both the excitement and the difficulties of research in exciting new fields as part of the Yariv Group at Caltech. I'm very grateful for the continued support and enthusiasm of my office mates, Prof. Avishay Eyal, Yi Li, Joyce Poon, and Dr. Koby Scheuer. John Choi, Will Green, Dr. Reginald Lee, George Ouyang, Shervin Taghavi, and Dr. Yong Xu contributed to our research, activities and conversations. Past and present students of Prof. Axel Scherer's group, including Dr. Marco Lončar, Prof. Oskar Painter, Prof. Jelena Vučković, and Tomo Yoshie, have made numerous helpful suggestions. Dr. Zhiwen Liu's expertise on photorefractive holography was useful in designing the experiments on ultrafast photorefractive holography. Dr. Bill Marshall participated in some of our discussions on the effects of noise on the nonlinear propagation of breathers. More than once, Daniel Katz helped as a friendly and informal mathematical consultant. To them and to the many others who have talked to me about their own work, and kept me interested in research problems beyond my own, my sincere thanks.

Andre Tkacenko has been a great guy to hang out with since our days as undergrads at Caltech, and to share a love of mathematics, L^AT_EX, cool computers, and the finer aspects of life, cars, and electrical engineering. Salil Parikh will make his millions in matter of months now, and then we'll hang out in Vegas—or Portland—like we've been promising to. Cheewei Wong and Shashi Murthy have been wonderful friends, and are a perennial excuse to go to Boston anytime, even in winter. Dr. John Cortese's advice on physics, mathematics, and electrical engineering over many years is much appreciated. And, more than these few words say, a special note of thanks to Joyce Poon for her friendship and support. I'd also like to acknowledge the friendly and cheerful assistance of Linda Dosza, Ling Lin, Irene Loera, Connie Rodriguez, and Michelle Vine.

This work is dedicated, with all my love, to my parents, who through their lives have given and taught me far more than I could have ever wished. No words can begin to repay the debt of gratitude I owe them.

Shayan Mookherjea
Pasadena, CA

Abstract

Whether over micron-long or kilometer-long distances, periodic phenomena can strongly affect both the propagation and the confinement of optical pulses. Periodicities can be engineered through the structural design of optical waveguides, or they may manifest self-consistently from induced nonlinear polarizations. In light of recent developments in fabrication technologies for semiconductor waveguides, polymeric materials, and optical fiber, we show that both strongly- and weakly-nonlinear channels are promising for new devices and systems in optical communications. This thesis proposes and discusses applications of guided wave periodicities in the framework of photonic crystals (coupled-resonator optical waveguides as well as transverse Bragg resonance waveguides and amplifiers), nonlinear phenomena in photorefractive semiconductors, and the nonlinear evolution of temporal solitons in dispersion-managed fibers.

Coupled-resonator optical waveguides (CROWs) are composed of a periodic array of electromagnetic resonators, typically on the micron or sub-micron length scales. A photon in such a waveguide sees a periodic potential, and according to the Floquet-Bloch theorems, has a wavefunction that reflects this periodicity. CROWs have a unique dispersion relationship compared to other semiconductor waveguides, and can be used to slow down the speed of propagation, enhance nonlinear interactions such as second-harmonic generation and four-wave mixing, and form frozen soliton-type field distributions that use the optical Kerr nonlinearity to stabilize themselves against decay via adjacent-resonator or waveguide-resonator coupling.

In optical fibers that possess the optical Kerr nonlinearity in addition to group-velocity dispersion, it is possible to propagate pulses with envelopes that “breathe” with distance, typically at kilometer or longer length scales. Such waveforms are characterized by a set of parameters—e.g., amplitude, chirp, etc.—that vary in a periodic manner as the pulse propagates. Borrowing an idea from field theory, e.g., of classical pendulums, or quantum-mechanical elementary particles, the pulse envelope

may be viewed as a particle traversing a trajectory in a phase space defined by its characteristic parameters. Distinct, non-overlapping trajectories are assigned as symbols of a multilevel communication code. Since it is the periodicity, arising from the Kerr nonlinearity, that generates this diversity in phase-space, there is no analog of this multiplexed system in linear optical transmission links. The overall bit-rate can be improved several fold above the current limits.

Contents

1	Fundamentals	15
1.1	Pulse propagation in a linear waveguide	17
1.2	Field evolution in a linear structure	18
1.3	Nonlinear pulse propagation: solitons	19
1.4	Quasi-solitons and breathers	23
1.5	Photonic crystals	24
2	Linear propagation in the tight-binding approximation	33
2.1	Eigenmodes and “coupled mode theory”	33
2.2	The tight-binding approximation	36
2.2.1	Dispersion relationship	37
2.3	Pulse propagation	42
2.4	Frequency, space, and time sampling	46
2.4.1	K -space representation of Eq. (2.24)	48
2.5	Linear pulse propagation: Bloch waves	49
2.6	Using the full dispersion relationship	52
3	Two-pulse nonlinear interactions	61
3.1	Description of a pulse with an envelope in a CROW	62
3.2	Representation in the Bloch form	65
3.3	Second harmonic generation: formulation	67
3.4	Solutions to the SHG equations	71
4	Holography and four-pulse mixing	75
4.1	Applications: Nonlinear Delay Lines	80
4.2	Picosecond dynamics of photorefractive gratings in GaAs	84

5	The Kerr effect and super-resonant modes	89
5.1	Formulation of the nonlinear propagation problem	90
5.2	The stationary super-resonant mode	92
6	Dispersion-managed solitons and breathers	99
6.1	Lagrangian and Hamiltonian formulation	101
6.1.1	Existence of breathing solutions for third-order dispersion . . .	106
6.2	Phase-plane analysis	107
6.3	Dispersion maps including third-order dispersion	113
7	Multilevel communications in nonlinear fibers	119
7.1	Formulation	120
7.2	Analytical framework	121
7.3	Multiple orbits and multiplexing	126
7.3.1	RMS radius of the random walk in the phase plane	132
7.4	Gordon-Haus timing jitter	135
7.5	Comments	139
7.5.1	Optimum amplifier gain for fixed total distance	141
8	Space-time analogies in pulse propagation	145
8.1	Gaussian beam diffraction and pulse propagation	147
8.2	The <i>ABCD</i> formalism for Gaussian pulses	149
8.3	DM soliton transmission experiment	157
8.4	Hermite-Gaussian basis	162
8.5	Geometric analogies	164
A	Superstructure gratings	175
B	Watson's criterion and Gaussian envelopes	177
C	Outline of the proof of the Hermiticity of H	179
D	Nonlinear polarization for SHG	181
E	Period of orbits in the phase plane	185

Chapter 1

Fundamentals

It is my experience that the direct derivation of many simple, well-known formulae from first principles is not easy to find in print. The original papers do not follow the easiest path, the authors of reviews find the necessary exposition too difficult—or beneath their dignity—and the treatises are too self-conscious about completeness and rigour.
—J. M. Ziman, Principles of the Theory of Solids (1998).

The distinction between the propagation of monochromatic CW waves and the propagation of pulses is not a trivial one, particularly in many of the waveguide structures of recent interest. These include geometries that don't satisfy space-translation invariance symmetry, such as certain types of waveguides defined by the coupling of defects in photonic crystals, and nonlinear waveguides, such as optical fibers in the presence of chromatic dispersion and the Kerr effect.

In studies of linear propagation, which are nowadays a standard part of any undergraduate or graduate optics curriculum, most textbooks don't explicitly account for a temporal dependency in the envelope of the eigenmodes of a waveguide¹. For example, we have the *Ansatz* of Eq. (8.2-7) in [154], which forms the basis for the remainder of the chapter, and the assumption of Eqs. (9.9) and (9.10) in [50]. The study of CW waves is certainly more venerable than that of pulses, and there are still a few surprises that one uncovers in the analysis of pulses—superpositions of CW waveguide modes—that aren't a trivial extension of the CW analysis. Further, whereas CW wave propagation in periodic waveguides is becoming part of the common base of knowledge at least at the professional level, evinced by the large number of recent papers that use the terminology of “Bloch functions” and “periodically modulated

¹Beyond that of invariance in the reference frame $t - z/v$, where v is a characteristic velocity of energy transport of the pulse.

plane waves” without apologia, we haven’t seen an application of this discussion at a fundamental level to the study of pulse propagation in such structures.

In descriptions of time-dependent phenomena in electromagnetics and solid-state physics, the focus is often limited to wave packets, in which the eigenfunctions depend on time² but the envelope is a function of only one variable. As an example, we have the wave packets considered by Raimès [112, pp. 320-326],

$$\Psi(x, t) = \int_{-\infty}^{\infty} A(k) e^{i(kx - \omega t)} dk. \quad (1.1)$$

In certain cases, the envelope is taken to be a separable function as in Raimès [112, pp. 334-335],

$$\Psi(\mathbf{r}, t) = \sum_{\mathbf{k}} A_{\mathbf{k}}(t) \psi_{\mathbf{k}}(\mathbf{r}) e^{-i\mathcal{E}(\mathbf{k})t/\hbar} \quad (1.2)$$

for the purposes of calculating transition probabilities in time-dependent perturbation theory. We will use such an approach in Chapter 5. However, one can also come across scenarios of pulse propagation in *linear* waveguides in which an *ab initio* derivation is called for, as in Chapters 2 and 3.

In studies of nonlinear propagation, the need to account for pulses differently than CW waves is self-evident. Solitons are, by definition, envelopes of the electromagnetic field that are invariant in a moving reference frame. They represent a propagating concentration of electromagnetic energy with certain precisely defined properties. We’ve applied a particular type of variational analysis to a class of optical communications system of current interest. The “dispersion-managed soliton,” or “breather,” communication system discussed in Chapter 7 accounts the combined effects of third-order dispersion and nonlinearity in optical fibers (in addition to group-velocity dispersion). Dispersion maps can be constructed analytically, if approximately, to guide the evolution of pulse parameters such as width and quadratic chirp along specified system design parameters. A new scheme of multiplexed communications, in addition to wavelength-division and time-division, is proposed that takes advantage of the unique properties of nonlinear (soliton- or breather-based) communication formats.

A simple way of characterizing via two-by-two matrices the propagation of Gaussian breathers in nonlinear fibers with second-order dispersion is presented. We’ll see that this method offers a quick and accurate way to design simple dispersion maps,

²Usually in a simple way, such as $\exp(i\omega t)$.

without requiring intensive numerical simulations. This is based on the well-known space-time analogies between (linear) beam diffraction and pulse dispersion, extended to the nonlinear domain. In addition to such algebraic space-time translation rules, there exist geometric correspondences, based on the algebraic topology of the spaces of solutions to nonlinear evolution problems. These new rules can help understand either nonlinear beam diffraction phenomena or nonlinear pulse propagation.

We'll set the stage for the remainder of the thesis by briefly describing the state of the art in the standard descriptions of pulse propagation [154, 152, 50, 57, 113, 126] in linear and nonlinear media. Space-time analogies are introduced in Chapter 8.

1.1 Pulse propagation in a linear waveguide

Proceeding as in [152, pp. 642–644], we consider an input pulse

$$\mathcal{E}(z = 0, t) = f(t) e^{i\omega_0 t} = e^{i\omega_0 t} \int_{-\infty}^{\infty} \frac{d\Omega}{2\pi} F(\Omega) e^{i\Omega t}, \quad (1.3)$$

where ω_0 is the carrier optical angular frequency of the laser source modulated to produce \mathcal{E} and $F(\Omega)$ is the Fourier transform of the complex input pulse envelope, $F(\Omega) = \int_{-\infty}^{\infty} dt \exp[-i\Omega t] f(t)$.

In the words of Yariv [152, pp. 643], “the field at a distance z is obtained by multiplying each frequency component ($\omega_0 + \Omega$)” in Eq. (1.3) “by $\exp[-i\beta(\omega_0 + \Omega)z]$,” where $\beta(\omega)$ is the propagation constant at the optical frequency. This presentation uses $k(\omega)$ in place of $\beta(\omega)$. Therefore,

$$\mathcal{E}(z, t) = e^{i\omega_0 t} \int_{-\infty}^{\infty} \frac{d\Omega}{2\pi} F(\Omega) e^{i\Omega t} e^{-ik(\omega_0 + \Omega)z}. \quad (1.4)$$

Expanding $k(\omega)$ in a Taylor series about ω_0 (called a dispersion relationship),

$$k(\omega_0 + \Omega) = k(\omega_0) + \left. \frac{dk}{d\omega} \right|_{\omega=\omega_0} \Omega + \dots \equiv k_0 + \frac{1}{v} \Omega + \dots, \quad (1.5)$$

where v is the group velocity so that Eq. (1.4) becomes

$$\begin{aligned}\mathcal{E}(z, t) &= e^{i(\omega_0 t - k_0 z)} \int_{-\infty}^{\infty} \frac{d\Omega}{2\pi} F(\Omega) e^{i\Omega(t - z/v)} \\ &= e^{i(\omega_0 t - k_0 z)} f(t - z/v).\end{aligned}\quad (1.6)$$

In words, Eq. (1.6) says that a pulse propagates unchanged in shape in a linearly dispersive medium, apart from an overall phase factor. Moreover, the velocity of propagation is given by the group velocity of the pulse³.

1.2 Field evolution in a linear structure

We can get the same result in a complementary way. We'll write down an expression for the field distribution at $t = 0$,

$$\mathcal{E}(z, t = 0) = g(z) e^{-ik_0 z} = e^{-ik_0 z} \int_{-\infty}^{\infty} \frac{dK}{2\pi} G(K) e^{-iKz}, \quad (1.7)$$

where k_0 references the central wavenumber or propagation constant of the pulse, and using the Fourier transform relationships, $G(K) = \int_{-\infty}^{\infty} dK \exp[iKz] g(z)$.

The field at time $t > 0$ is obtained by multiplying each frequency component at $k_0 + K$ by $\exp[i\omega(k_0 + K)t]$,

$$\mathcal{E}(z, t) = e^{-ik_0 z} \int_{-\infty}^{\infty} \frac{dK}{2\pi} G(K) e^{-iKz} e^{i\omega(k_0 + K)t}. \quad (1.8)$$

Writing the dispersion relationship in a Taylor series [57, pp. 323–324],

$$\omega(k_0 + K) = \omega(k_0) + \left. \frac{d\omega}{dk} \right|_{k=k_0} K + \dots \equiv \omega_0 + v K + \dots, \quad (1.9)$$

³The sign convention in the exponents in Sections 1.1 and 1.2 and in Chapters 2 and 3 follows that of Yariv [154, 152] rather than the one found in [57]. Rather curiously, in the same book, Section 15.4 on self-induced transparency [152, pp. 358] uses the opposite sign convention, $E(z, t) \propto \exp[i(k_0 z - \omega_0 t)]$.

where v once again represents the group velocity, we can simplify Eq. (1.8) to

$$\begin{aligned}\mathcal{E}(z, t) &= e^{i(\omega_0 t - k_0 z)} \int_{-\infty}^{\infty} \frac{dK}{2\pi} G(K) e^{-iK(z-vt)} \\ &= e^{i(\omega_0 t - k_0 z)} g(z - vt).\end{aligned}\tag{1.10}$$

It's obvious that Eq. (1.10) has a completely equivalent (analogous) structure as Eq. (1.6)⁴. But there are subtle implications in the two different *approaches* that are important in certain types of waveguide structures.

1.3 Nonlinear pulse propagation: solitons

The theoretical prediction and experimental verifications of optical solitons have revolutionized the field of optics [47]. Whereas in conventional (e.g., non-return to zero, NRZ) communications, fiber nonlinearities are impediments that must be compensated for, solitons explicitly rely on the existence of these nonlinear effects to achieve the very same properties that are desirable in linear communications. In particular, we look for bounded variations in the pulse parameters such as width and chirp, and robustness to perturbations [63, 41]. As the understanding of soliton properties has grown, researchers have developed promising applications in optical communications, leading to the demonstration of new forms of (fiber) lasers [48, 49], of repeaterless transmission [51], ultrashort pulse propagation, and all-optical switching and logic circuitry.

One of the most important features of soliton-based communication is the observation (see, e.g., [44, pp. 102–108]) that a soliton pulse moves with a velocity that is different from that characterizing the propagation of a linear pulse. In short, a soliton can separate itself from linear additive noise, opening a new realm of possibilities for system design in communication theory. It's no longer true that the traditional metric for information transmission, the signal-to-noise ratio (SNR), necessarily worsens when the signal is sent through a dissipative or amplifying media.

More recently, a slightly modified form of the fundamental ‘‘Schrödinger’’ soliton has been shown to demonstrate many advantageous properties as the pulse shape of choice in optical communications. This will be introduced in the next section.

⁴Compare Eq. (1.10) with [57, Eq. (7.84)].

This section, closely following the presentation in [4], presents a derivation of the equation governing the evolution of the Schrödinger soliton envelope in a fiber with second- and third-order dispersion and the Kerr nonlinearity. In keeping with the convention used in the majority of the literature, the sign and notation convention is $E(z, t) \propto \exp[i(\beta z - \omega t)]$, where β is the propagation constant⁵.

From Maxwell's equations,

$$\nabla^2 \mathbf{E} - \frac{1}{c^2} \frac{\partial^2 \mathbf{E}}{\partial t^2} = -\mu_0 \frac{\partial^2 \mathbf{P}}{\partial t^2}, \quad (1.11)$$

where the complex field envelope $\mathbf{E}(\mathbf{r}, t)$ satisfies the following Fourier transform relationships

$$\tilde{\mathbf{E}}(\mathbf{r}, \omega) = \int_{-\infty}^{\infty} dt \mathbf{E}(\mathbf{r}, t) \exp(i\omega t), \quad (1.12)$$

$$\mathbf{E}(\mathbf{r}, t) = \int_{-\infty}^{\infty} \frac{d\omega}{2\pi} \tilde{\mathbf{E}}(\mathbf{r}, \omega) \exp(-i\omega t). \quad (1.13)$$

We'll write $\mathbf{E}(\mathbf{r}, t)$ in terms of a rapidly varying exponent and a slowly varying envelope, so that along a particular (implicit) polarization of the field,

$$E(\mathbf{r}, t) = \frac{1}{2} [\bar{E}(\mathbf{r}, t) e^{-i\omega_0 t} + \text{c.c.}]. \quad (1.14)$$

Using Eq. (1.13), we can formulate the Fourier transform of the envelope $\tilde{E}(\mathbf{r}, \omega - \omega_0)$, which is the solution to

$$\nabla^2 \tilde{E} + \epsilon(\omega) k_0^2 \tilde{E} = 0, \quad (1.15)$$

where $k_0 = \omega/c$ and $\epsilon(\omega)$ is the dielectric constant. To solve this equation, let's assume that \tilde{E} can be written as a product of two functions: one will depend only on the transverse coordinates x and y , and the other on the longitudinal coordinate z ,

$$\tilde{E}(\mathbf{r}, \omega - \omega_0) = f(x, y) \tilde{A}(z, \omega - \omega_0) \exp(i\beta_0 z). \quad (1.16)$$

By substituting Eq. (1.16) into Eq. (1.15), we obtain the following pair of equa-

⁵For a presentation using the convention used in Sections 1.1 and 1.2, see [28].

tions,

$$\nabla^2 f + [\epsilon(\omega)k_0^2 - \bar{\beta}^2] F = 0 \quad (1.17)$$

$$2i\beta_0 \frac{\partial \tilde{A}}{\partial z} + (\bar{\beta}^2 - \beta_0^2) \tilde{A} = 0. \quad (1.18)$$

The standard method of solving Eq. (1.17) uses first-order perturbation theory, writing ϵ in terms of the constant refractive index and a small deviation,

$$\epsilon \simeq n^2 + 2n\Delta n = n^2 + 2n \left[n_2 |E|^2 + i \frac{\alpha}{2k_0} \right], \quad (1.19)$$

so that Δn accounts for the Kerr nonlinearity and fiber loss. At this level of approximation, Δn does not affect $F(x, y)$ but changes the mode constant $\bar{\beta}(\omega) = \beta(\omega) + \Delta\beta$ [4], where $\Delta\beta$ is given by

$$\Delta\beta = k_0 \frac{\iint dx dy \Delta n |F(x, y)|^2}{\iint dx dy |F(x, y)|^2}. \quad (1.20)$$

Then, Eq. (1.18) becomes

$$\frac{\partial \tilde{A}}{\partial z} = i [\beta(\omega) + \Delta\beta - \beta_0] \tilde{A}. \quad (1.21)$$

We can expand the mode propagation constant, which depends on the optical angular frequency ω in a Taylor series around ω_0 ,

$$\beta(\omega) = \beta_0 + (\omega - \omega_0)\beta' + \frac{1}{2}(\omega - \omega_0)^2\beta'' + \frac{1}{6}(\omega - \omega_0)^3\beta''' + \dots, \quad (1.22)$$

where $1/\beta' \equiv d\beta/d\omega|_{\omega=\omega_0}$ defines the group velocity, and higher derivatives of β evaluated at ω_0 give the higher-order dispersion coefficients [4, pp. 8–9].

Consequently, converting Eq. (1.21) to the time domain by taking the inverse Fourier transform,

$$\frac{\partial A}{\partial z} + \beta' \frac{\partial A}{\partial t} + i \frac{\beta''}{2} \frac{\partial^2 A}{\partial t^2} - \frac{\beta'''}{6} \frac{\partial^3 A}{\partial t^3} = i\Delta\beta A = -\frac{\alpha}{2} A + i\kappa |A|^2 A, \quad (1.23)$$

using the definition of δn from Eq (1.19). In this equation, $\kappa = n_2\omega_0/(cA_{\text{eff}})$ is the nonlinearity coefficient defined in terms of an effective core area A_{eff} [4].

Now, we transform to moving coordinates, $t - \beta'z \mapsto T$ and ignore the loss by setting $\alpha = 0$. To normalize the equation, we introduce [4, Chap. 5]

$$U = \frac{A}{\sqrt{P_0}}, \quad \xi = \frac{z}{L_D}, \quad \tau = \frac{T}{T_0}, \quad (1.24)$$

where P_0 is the peak power, T_0 is the width of the input pulse, and L_D is the dispersion length, $L_D = T_0^2/|\beta''|$. Next, using a parameter $N = \sqrt{\gamma P_0 T_0^2/|\beta''|}$, let's introduce $u = NU$ so that

$$i\frac{\partial u}{\partial \xi} + \frac{1}{2} \text{sgn}(\beta'') \frac{\partial^2 u}{\partial \tau^2} + |u|^2 u - i\gamma \frac{\partial^3 u}{\partial \tau^3} = 0, \quad (1.25)$$

where $\gamma = \beta'''/(6|\beta''|t_0)$. We define $\sigma = -\text{sgn}(\beta'')$ and use the original symbols z and t for ξ and τ , respectively,

$$i\frac{\partial u}{\partial z} + \frac{\sigma}{2} \frac{\partial^2 u}{\partial t^2} + |u|^2 u - i\gamma \frac{\partial^3 u}{\partial t^3} = 0. \quad (1.26)$$

The case $\beta'' < 0$, or $\sigma = 1$ is called ‘‘anomalous dispersion,’’ and correspondingly, the case $\beta'' > 0$ or $\sigma = -1$ is known as ‘‘normal dispersion.’’

Soliton solutions to Eq. (1.26) are known for the case of anomalous dispersion. The family of soliton solutions, comprising of the fundamental Schrödinger soliton and higher-order Schrödinger solitons, can be found analytically by the inverse scattering method [160] and by method proposed by Hirota [53]. There's a large literature on the remarkable properties of these pulse shapes.

There are a number of partial differential equations in two or more dimensions that have soliton solutions [55]. An example in optics, other than the propagating Schrödinger soliton, which is a consequence of a third-order (cubic) nonlinearity, is the family of quadratic solitons, which are a consequence of a second-order (quadratic) nonlinearity. A review of optical spatial solitons is presented in [122], and a paper by Snyder *et al.* is noteworthy [130].

1.4 Quasi-solitons and breathers

In recent studies, the term “soliton” has broadened to include self-trapped solutions of non-integrable systems [71]. In particular, we’ll consider the physical implications of allowing σ in Eq. (1.26) to vary with propagation distance z .

$$i\frac{\partial u}{\partial z} + \frac{\sigma(z)}{2}\frac{\partial^2 u}{\partial t^2} + |u|^2 u - i\gamma\frac{\partial^3 u}{\partial t^3} = 0. \quad (1.27)$$

The variations in this group-velocity dispersion (GVD) parameter are chosen according to some prescription (usually piecewise constant) over a length Z_0 , which then defines a dispersion map, and the pulse propagates over several such periods. Eq. (1.27) has been found to support soliton-like solutions, which have come to be known as dispersion-managed solitons, referring to the management (i.e., design) of the dispersion map that the pulse shape traverses with propagation distance [103]. The pulse amplitude, width, and certain other parameters describing the envelope demonstrate periodic oscillations over the map period, and these pulses are consequently also known as “breathers.” It’s useful to note that breathing solutions can exist even without a dispersion map, as have been shown in one context in [68] and will be seen in a different setting in Chapter 6.

Waveform distortion consequent of self-phase modulation and dispersion can be reduced by decreasing the path-averaged dispersion. On the other hand, interchannel crosstalk in a wavelength-division multiplexed (WDM) communication system arising from four-wave mixing or cross-phase modulation becomes smaller as the magnitude of the GVD parameter β'' is increased [4]. To simultaneously achieve both these properties, the dispersion map is designed to use sections of fiber with high local GVD, but low path-averaged GVD [124], e.g., by using nonzero dispersion fibers to achieve large local GVD and inserting dispersion compensators at regular intervals to compensate for accumulated GVD [139], or by using reverse dispersion fiber in conjunction with single-mode fiber [134].

Perhaps the most important analytical tool in the construction of dispersion maps, i.e., in the specification of $\sigma(z)$, is the formulation of equations of motion of the pulse parameters describing the evolution of a dispersion-managed soliton [7, 68]. This is based on a variational approach borrowed from classical mechanics, where the system of interest is described by a Hamiltonian functional [39].

Once the averaged GVD coefficient is made small, the effects of third-order dispersion (TOD) become significant. While one approach is to design dispersion compensators that attempt to cancel both GVD and TOD (also called dispersion slope) [151], another approach is to design the dispersion map to explicitly take into account the effects of TOD [99]. This recent paper is based on numerical simulations, since no analytical theory of TOD comparable to [68] has existed. This is the problem tackled in Chapter 6.

1.5 Photonic crystals

Photonic crystals are periodic arrays of dielectric materials with different dielectric constants. Alternating layers of two materials, e.g., GaAs and $\text{Al}_{0.3}\text{Ga}_{0.7}\text{As}$ of thickness ≈ 200 nm, creates a one-dimensional photonic crystal (1DPC), more commonly known as a dielectric multilayer, or a Bragg stack [159]. When we observe the propagation of waves through such a Bragg stack, we see that for certain ranges of wavelengths ($\lambda = 1.15 \mu\text{m} \pm 200$ nm), the incident light is completely reflected. These bands of frequencies are called “forbidden” bands or gaps. The underlying physics is that of Bragg reflection: at the center of each forbidden gap, the wavelength of light is an integer multiple of the period of the Bragg stack. Successive reflections from neighboring interfaces add up in phase with each other, leading to constructive superposition at the plane of incidence to the stack. A concise derivation of the dispersion relationship for such a 1DPC is given in [117].

A uniform photonic crystal is a periodic dielectric medium usually thought of as the equivalent of a “nearly free electron” metal, in which electronic energy levels can be calculated using the assumption of a weak periodic potential [129]. In a photonic crystal, the potential is a consequence of the lattice of dielectric material rather than a periodic array of atoms. We know that plane waves are solutions to the unperturbed Schrödinger equation, and we assume that in such a medium, the “true” solution can be expanded in this basis. From solid-state theory, a weak periodic potential strongly affects those free electron levels whose wave vectors are close to ones at which Bragg reflections can occur [9, pp. 152–159].

Photonic bands of eigenfrequencies and band gaps between these bands are analogous to their counterparts in solid-state physics: when an external field changes an electron’s wave vector across a Bragg plane, the presence of an energy gap implies

that the electron must be found in same branch of the energy level across the Bragg plane. In terms of experimentally observed quantities, a bandgap refers to a gap in the density of states of the propagating eigenmodes. A measurement of the transmission characteristics of plane waves will reveal intervals of frequencies where the transmission is very small. Photonic bandgaps in the optical regime can be used to inhibit spontaneous emission, localize donor and acceptor modes, etc., and also lead to the formation of stable solitary waves and a nonexponential decay of spontaneous emission, and in the Anderson localization of light.

As an example of a two-dimensional photonic crystal (2DPC), consider a periodic array of air columns drilled into a dielectric volume, or the converse. Assuming that the columns are of infinite length (height), a cross-sectional slice is characterized by a dielectric constant (rather, the dielectric “function” since it isn’t a *constant*) that is periodic in *two* dimensions. The two most common patterns for the columns are at the vertices of an equilateral triangle (or hexagon), and a square.

For a triangular lattice of GaAs cylinders ($\epsilon = 11.56$) in air, the lowest-frequency TE bandgap is widest when the ratio of the cylinder radius to the lattice constant $r/a = 0.376$. This gap extends from $f = 0.2875$ to $f = 0.3193$ in units of c/a . In order to position $\lambda_{\text{vac}} = 1.55 \mu\text{m}$ at midgap, we determine the lattice spacing to be $a = 470 \text{ nm}$. This structure then has a TE bandgap from $1.472 \mu\text{m}$ to $1.635 \mu\text{m}$, and a TM bandgap from $1.087 \mu\text{m}$ to $1.279 \mu\text{m}$.

A 2-D photonic crystal comprising of a square lattice of identical cylindrical rods (of dielectric constant $\epsilon = 8.9$) shows a bandgap in the TM polarization⁶ [58, 115]. A triangular lattice of holes in a dielectric material ($\epsilon = 13$) supports a bandgap for both TM and TE polarizations, with a gap-midgap ratio $\Delta\omega/\omega_0$ of 18.6%, where ω_0 is the frequency at the middle of the gap [58, Fig. 5.10]. In Figs. 1.1 and 1.2, the height of the contour corresponds to transmission, with ‘Frequency’ represented in units of c/a and ‘K-vector’ normalized to the reciprocal lattice vector. (Fabry-Perot resonances from the finite length of the simulated structure are visible in the passband.)

The extension to three-dimensional structures is simple conceptually, but presents formidable difficulties in fabrication. Their most appealing attribute is that 3DPC’s can possess a complete band gap, characterized by no propagating electromagnetic modes of a given range of frequencies for *all* k -vectors over the entire 3-D Brillouin

⁶TM modes have \mathbf{E} as a scalar normal to the $x - y$ plane of the crystal and pointing in the \hat{z} direction, so that $\mathbf{E} = E(\rho)\hat{z}$ and $\mathbf{H}(\rho) \cdot \hat{z} = 0$.

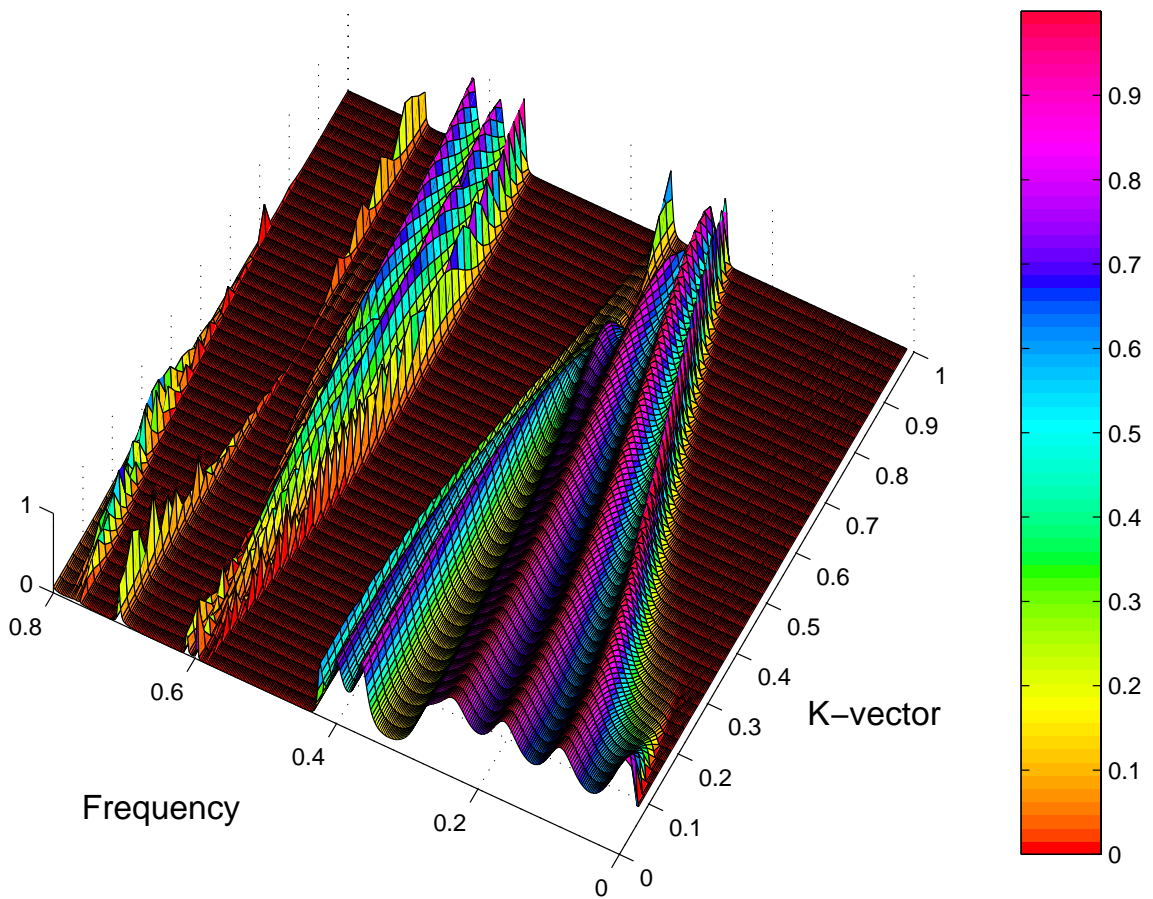


Figure 1.1: Photonic band structure and transmission characteristics for the TM modes in the ΓM direction for a triangular array of air columns in a dielectric material of $\epsilon = 13$. Data generated by the software package *Translight* by Andrew L. Reynolds at the Photonic Band Gap Materials Research Group, University of Glasgow.

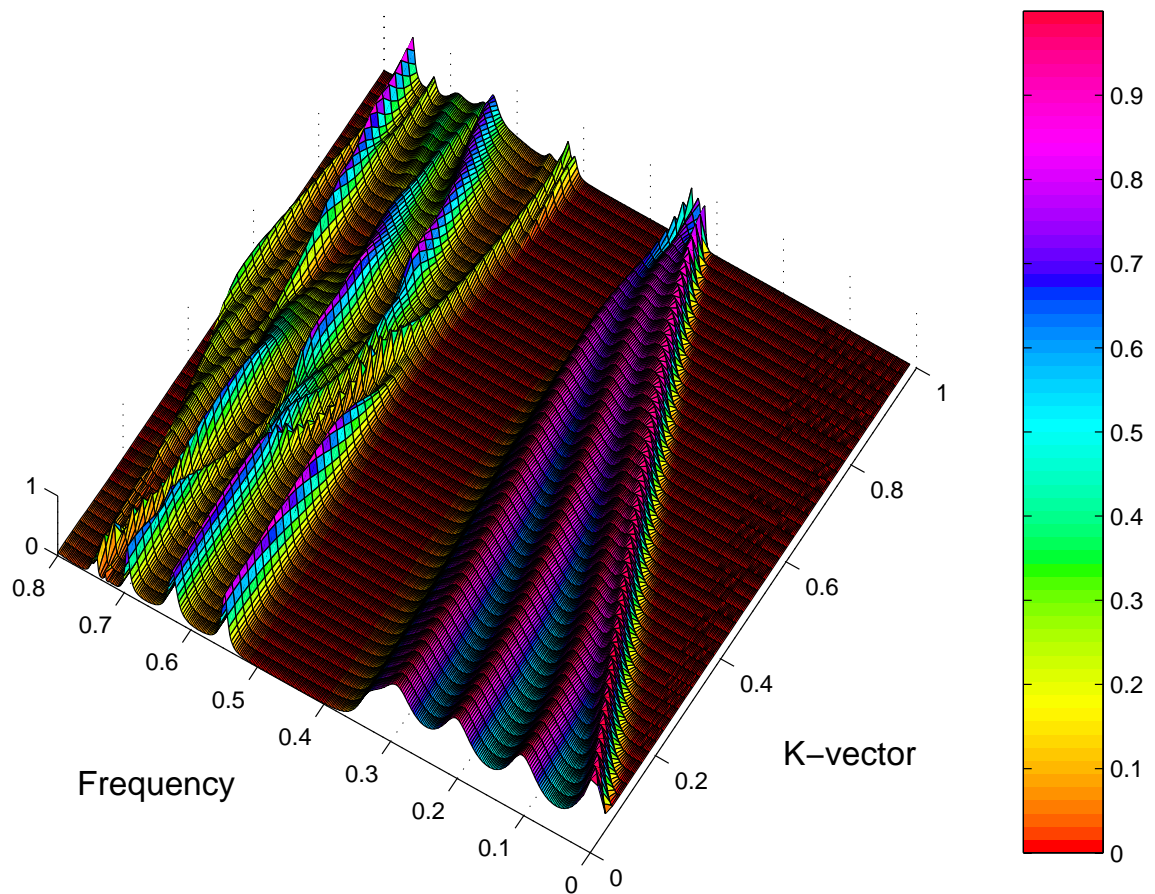


Figure 1.2: Photonic band structure and transmission characteristics for the TE modes in the ΓM direction for a triangular array of air columns in a dielectric material of $\epsilon = 13$. Data generated by the software package *Translight* by Andrew L. Reynolds at the Photonic Band Gap Materials Research Group, University of Glasgow.

zone. A well-studied example is the face-centered cubic (diamond) lattice of air spheres in GaAs ($\epsilon = 13$), where the radius r is related to the lattice constant a by $r/a = 0.325$. (The diameter of the air spheres is larger than the distance between spheres, $a\sqrt{3}/2$.)

Quasi-3-D structures such as photonic crystal slabs are similar to 2DPC's in the transverse profile of the dielectric function, but are of finite extent vertically. They rely on index contrast with the surrounding material (e.g., air surrounding a slab of GaAs) to confine modes to the slab vertically.

Many of the most interesting properties of photonic crystal structures arise when the periodicity is intentionally interrupted, e.g., by filling in one of a periodic array of air columns drilled into a GaAs slab. Borrowing once again from the terminology of crystalline solids, this creates a “point defect” in the crystal. Point defects can support localized high-Q modes [143], and line or surface defects can give rise to propagating waveguide modes [108]. Much of the current understanding of photonic crystal waveguides based on defects relies on numerical simulations, since the mode structure of the individual defect modes is complicated. However, certain qualitative features can be readily understood: as the translational symmetry of the structure is destroyed, we can no longer use an in-plane wave vector to classify waveguide modes, but mirror-reflection symmetry is still intact for in-plane propagation so that TE and TM modes are still decoupled. If the eigenfrequency of the defect mode lies in the photonic band gap, the defect-induced state must be evanescent, i.e., decay exponentially away from the location of the defect in the plane of the structure.

We will examine the defect modes of a triangular lattice of air holes in GaAs ($\epsilon = 11.4$) in some detail, because these modes will be used as the basic constituents of coupled-resonator optical waveguides (CROWs). The transverse variation of the dielectric function over the computational unit cell is shown in Fig. 1.3. The TE band structure of the uninterrupted periodic crystal shows a bandgap from $\omega a/(2\pi c) = 0.307$ to $\omega a/(2\pi c) = 0.495$. Since the uninterrupted crystal exhibits the C_{6v} spatial symmetry, each localized eigenmode of the defect may be attributed to one of its irreducible representations. There are four “one-dimensional” representations (non-degenerate eigenvalues) and two “two-dimensional representations” (doubly degenerate eigenvalues) [117, Ch. 6].

The defect mode field distributions may be calculated using either frequency-domain or time-domain methods; here, we use a freely available software package

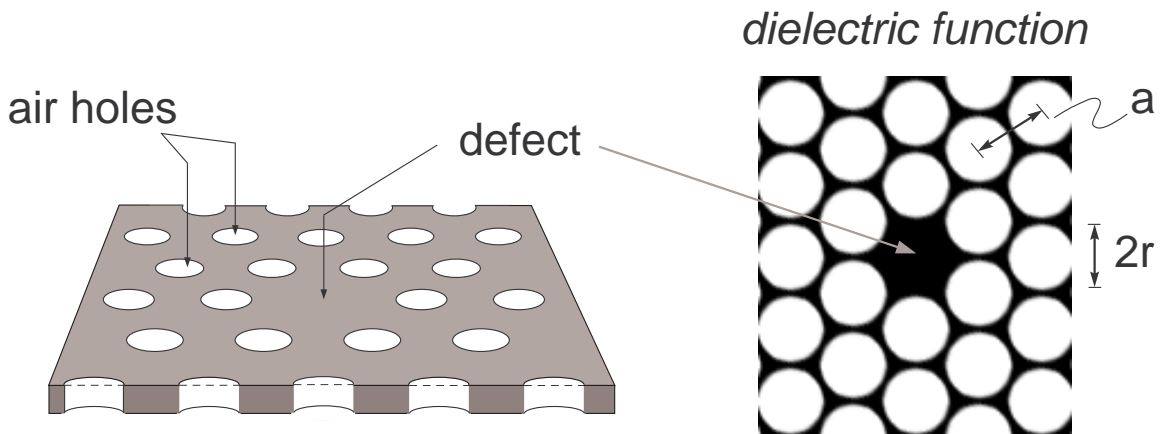


Figure 1.3: Geometrical structure and the assumed variation of the dielectric function, for computational purposes, across a 5×5 unit cell of air holes in GaAs with a defect in the center. The dark regions correspond to GaAs, and $r/a = 0.45$.

based on the former method [60]. The H -field distributions (TE polarization) for two one-dimensional and the two two-dimensional modes are shown in Figs. 1.4 and 1.5. The fields are clearly localized around the defect cavity, and show characteristic spatial symmetries. The A_1 mode is particularly simple, and will be the archetypical resonator field in the study of coupled-resonator waveguides.

A different form of waveguide, not based on point defects, is formed by altering every element along one row of holes, either increasing or decreasing the radius [61]. These are called “line-defect” waveguides; in particular, increasing the radius of air holes creates a reduced-index waveguide, and correspondingly, the other case forms an increased-index waveguide. We will not discuss line-defect waveguides here. Altering the amount of dielectric in the waveguide by changing the hole size may make it more difficult to realize a single mode waveguide, as the number of defect states in the band gap is altered. Calculations for a multilayer slab waveguide structure with external coupling are somewhat complicated [146]: the band structure is solved in each transverse layer to find a set of modes that propagate in the vertical direction as plane waves. These are used as the basis states to construct the fields in each layer, with appropriate continuity conditions at the boundaries. Further, the waveguide modes of a slab waveguide can occur at eigenfrequencies out of the photonic band gap of the photonic crystal [2].

The important phenomenon of the reduction of the group-velocity in 2-D and

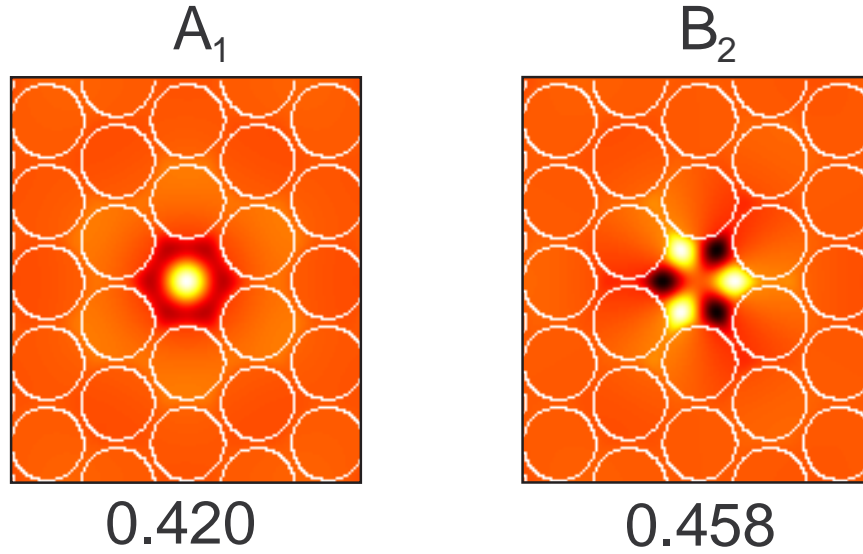


Figure 1.4: Field distributions for two one-dimensional fields: the A_1 mode with $\omega a/(2\pi c) = 0.420$ and the B_2 mode with $\omega a/(2\pi c) = 0.458$. The colorbar is the same as in the next figure.

3-D photonic crystals in discussed by Sakoda [116]. Not only does this lead to the enhancement of nonlinear optical processes as discussed in other parts of this report, the stimulated emission from active defects is also enhanced [34] as a consequence of the long interaction time between the radiation field and the emitting atoms

Photonic crystals have been fabricated in GaAs/AlGaAs structures [23, 105], in silicon [78], in photopolymerizable resins by using laser beam interference [127], as alumina rods in the microwave (gigahertz) regime [84, 13]. Chow *et al.* have reported measurements of transmission at 1550 nm in a (vertically asymmetric) photonic crystal GaAs slab coupled to ridge waveguides [23]. Photonic crystal waveguides fabricated in a silicon slab (with an undercut air region for symmetry) for both triangular and square lattice have demonstrated low scattering-loss transmission around bends at 1550 nm [78].

Recently, Busch and John [19] have proposed a tunable bandgap structure—a microscopic lattice of air spheres in silicon, the “inverse opal” structure, infiltrated with a birefringent nematic liquid crystal that can be made to control the transmission properties via an external electric field.

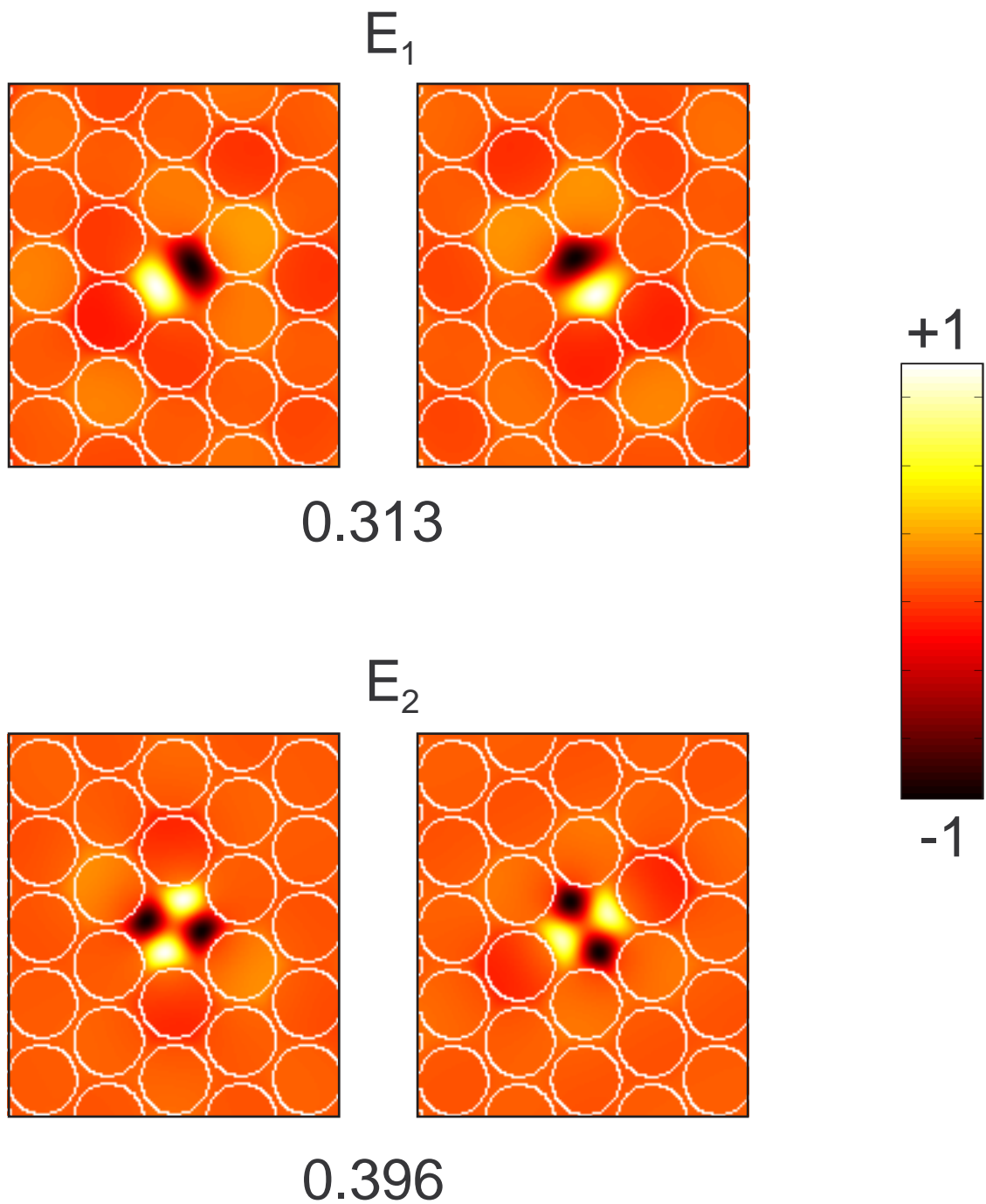


Figure 1.5: Field distributions for the two two-dimensional fields: the E_1 modes with $\omega a / (2\pi c) = 0.313$ and the E_2 modes with $\omega a / (2\pi c) = 0.396$. Both eigenfunctions of the doubly-degenerate modes are shown.

Chapter 2

Linear propagation in the tight-binding approximation

Operator techniques, functional techniques, renormalization group methods, etc., are all available to take on any problem. What is left open and is simply outside the scope of any of these methods is the choice of “Equation (1)”, namely the starting point. No solution technique, no matter how powerful, can derive a result that is not already implicit in the starting equation.
—John R. Klauder, *Beyond Conventional Quantization*, Cambridge (2000).

The development of integrated optoelectronic devices depends, in part, on the understanding of electromagnetic propagation in microstructure waveguides. Since this electromagnetic radiation, for applications in communications, consists of pulses of light, it’s important to explicitly account for temporal variations in the envelopes of the fields. Mathematically, we discuss linear pulse propagation in one-dimensional waveguides which do not exhibit spatial translation invariance symmetry, i.e., the modes are not plane waves. Physical realizations of such structures include modulated gratings in optical fibers or semiconductor materials, a linear array of defects in a two-dimensional photonic crystal slab, and a chain of polystyrene microspheres.

2.1 Eigenmodes and “coupled mode theory”

Coupled-mode theory is a well-known formalism applicable to the problem of propagation in an optical waveguide [154, Ch. 13]. It is a method of analysis of the wave equation [154, 126, 57],

$$\nabla \times [\nabla \times \mathbf{E}] + \frac{\epsilon(\mathbf{r})}{c^2} \frac{\partial^2 \mathbf{E}}{\partial t^2} = -\frac{1}{c^2} \frac{\partial^2}{\partial t^2} \mathbf{P}_{\text{pert}}(\mathbf{r}, t), \quad (2.1)$$

where $\mathbf{P}_{\text{pert}}(\mathbf{r}, t)$ is a perturbation polarization that represents any deviation from the unperturbed waveguide.

In the paraxial approximation, the total field in the waveguide is written as a superposition of confined modes¹; for TE modes propagating in a slab waveguide along the z direction, the electric field,

$$E_y(\mathbf{r}, t) = \frac{1}{2} \sum_m A_m(z) \mathcal{E}_y^{(m)}(x) e^{i(\omega t - k_m z)} + \text{c.c.}, \quad (2.2)$$

is a sum of m discrete confined eigenmodes $\mathcal{E}_y^{(m)}(x)$, with propagation constants k_m arising from an eigenvalue equation, modulated by an envelope $A_m(z)$.

Substituting the Ansatz Eq. (2.2) into Eq. (2.1) and assuming that derivatives of second order of $A_m(z)$ can be ignored, we can obtain an ordinary differential equation for $A_m(z)$ in terms of $\mathbf{P}_{\text{pert}}(\mathbf{r}, t)$ and $\mathcal{E}_y^{(m)}(x)$ [154, Eq. (13.3-9)]. This approximation in neglecting $|d^2 A_m/dz^2|$ compared to $k_m |dA_m/dz|$ is known as the slowly varying envelope approximation (SVEA).

This approach is useful in the description of wave propagation in gratings and other periodic optical systems where the strength of the perturbation (relative to the free-space equations) is weak. Not surprisingly, the same formalism has been applied in solid state physics to the description of electrons in a weak periodic potential [129, 9]. The structure is viewed as a gas of nearly free conduction electrons, each of which obeys the Schrödinger equation with a weak perturbation—the periodic potential of the ions. When the periodic potential is exactly zero, the solutions to the Schrödinger equation are plane waves [25], and these functions form a complete orthonormal basis (over a finite interval) as in the well-known Fourier series expansion of periodic functions². The perturbative solution to the problem of a weak periodic potential is then written as a superposition of these plane waves, with coefficients whose values depend on the expansion of $\mathbf{P}_{\text{pert}}(\mathbf{r}, t)$ in this basis.

Complementary to this weakly perturbative theory of coupled modes (which, confusingly, is itself often called coupled-mode theory) is the tight-binding approximation, also known as the linear combination of atomic orbitals (LCAO) [62]. This approach

¹Any coupling to radiation modes, which do not decay exponentially away from the waveguide, is ignored [154, pp. 492–494].

²Periodic functions can be thought of as the periodic extension of functions defined over a finite interval. For example, $\sin(x)$ over the entire real axis comprises replicas of the function $f(x) = \sin(x)$, $|x| \leq \pi$, and which is identically zero for $|x| > \pi$.

describes electrons in a crystalline solid with a strong periodic potential due to the lattice structure of localized atoms, characterized by a weak overlap between the atomic wave functions [129, 9]. By analogy, the optical structures that can be described using the tight-binding approximation are those that consist of isolated structural elements (e.g., high-Q resonators such as defect modes in photonic crystals) weakly coupled to one another. The propagating eigenmodes of the overall system are then closely related to the eigenmodes of the individual elements, rather than the free-space eigenmodes.

The wave function for a free electron wave is given by $\exp(-i\mathbf{k} \cdot \mathbf{r})$, where \mathbf{k} is the wave vector³. This eigenmode is trivially of the Bloch form [129, pp. 156–160], since free space can be thought of as periodic medium with an arbitrary small (or large) period. In the tight-binding approximation, plane waves are not eigenmodes, but the eigenmodes can still be written in the Bloch form. Lehmann and Ziesche point out the differences between these two approaches quite early in their text [76, pp. 20–28], as “the approximation starting from free electrons” and “the approximation starting from free atoms.” In the words of Raimis [112, pp. 133],

One cannot say that either method is *correct*, but one or the other will give better results in given circumstances and will be the more *convenient* as a basis for more accurate calculations.

The energy of the wavefunction \mathcal{E} is a function of the wave vector \mathbf{k} . In terms of the effective mass $d^2\mathcal{E}/dk^2$ associated with electron levels, as the overlap between the atomic energy levels decreases, the effective mass becomes very large, so that electrons are indeed “tightly bound” to their atoms. For completely isolated atoms, the group velocity $d\mathcal{E}/dk$ is zero, since the energies of all atoms are the same. But once a band of energies is formed, an electron can move through the crystal, although its group velocity may be small and its effective mass large.

Lehmann and Ziesche state in their text [76, pp. 36] that the tight-binding expansion of the wave function of the crystal in terms of atomic orbital wavefunctions $\phi_n^{\text{at}}(\mathbf{r} - \mathbf{R})$ is overcomplete since the latter form a complete system for each single \mathbf{R} . On the other hand, Ziman points out [161, pp. 95] that this set is incomplete as “it lacks all the scattered-wave eigenstates of the Schrödinger equation in the

³In the terminology of solid-state physics, such functions when properly normalized are the eigenfunctions of the Hartree equation describing a free-electron gas, and of the Hartree-Fock equation for a monovalent metal, but with different eigenvalues in the two cases [112].

continuum,” i.e., above the zero-energy level of the individual atomic wavefunction potential (see Figs. 54 and 55 in [161].)

As pointed out, among other, by Jones [62, pp. 228–229], a significant criticism of the tight-binding description, or perhaps of the independent electron approximation that is implicitly assumed in this description of electron levels in metals is that it ignores positional correlations between electrons with antiparallel spins. In the description of photons, this is not relevant as bands formed by different polarizations can be shown to be decoupled [150]. Further, every component of the electromagnetic four-vector potential obeys the massless Klein-Gordon equation (in the Lorentz gauge), without the need for anti-commutation relationships as are necessary to describe spinor (Dirac) fields such as electrons [110]. In this way, we avoid the overcounting of the states of a half-filled band in the case of electrons in a crystal of widely separated monovalent atoms described by Jones.

The formalism is independent of the material in which the CROW geometry is realized. Stefanou and Modinos have used the tight-binding method to analyze impurity photonic bands in photonic insulators which can be described by a real negative dielectric function $\epsilon(\omega)$ [131]. The impurity cells are formed by introducing nonabsorbing dielectric spheres in a chain, and the resonances of the individual spheres widen into a band of frequencies because of nearest-neighbor interactions. In this chapter, we’ll focus on a particular case of the analysis in which the pulse envelope propagates undistorted; these solutions may be thought of as the time-dependent eigensolutions in the tight-binding approximation.

2.2 The tight-binding approximation

Assume that the resonators comprising the waveguide are identical and lie along the z axis separated by a distance R as shown in Fig. 2.1. The total length of the waveguide is taken to be L so that the number of resonators is $N = L/R$. A waveguide mode—an eigenmode of a time-independent Hamiltonian— $\phi_k(z)$ with wavevector \mathbf{k} and propagation constant $k = |\mathbf{k}|$ is written as a linear combination of the individual modes $\psi_l(\mathbf{r})$ of the resonators that comprise the structure [9],

$$\phi_k(\mathbf{r}) = \sum_n \exp(-inR\mathbf{k} \cdot \hat{z}) \sum_l \psi_l(\mathbf{r} - nR\hat{z}) \quad (2.3)$$

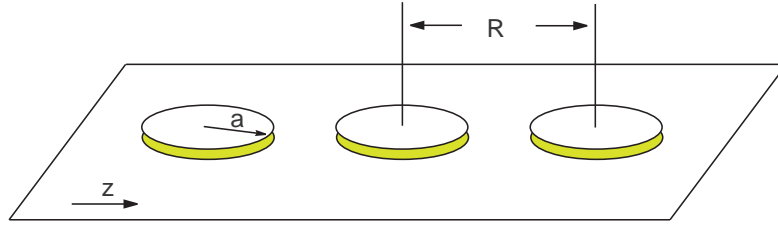


Figure 2.1: Schematic of a 1-D coupled-resonator optical waveguide, formed by coupled microdisk resonators of radius a separated by distance R along the z direction.

where the summation over n runs over the N resonators and the summation over l (with implicit coefficients absorbed into $\psi_l(z)$) refers to the bound states in each individual element. In a CROW, for instance, the individual resonator modes at a particular frequency may be doubly degenerate as discussed in Section 1.5, so that the waveguide modes may require $l = \pm 1$, whereas in an SSG, it's usually sufficient to consider a single l [32].

In the description of a periodic waveguide of finite length, the propagation constant k is restricted according to the Born—von Karman periodic boundary condition [9]

$$k_m = m \left(\frac{2\pi}{L} \right), \quad (2.4)$$

where m is an integer; k_m then ranges over the Brillouin zones and because $\phi_k(z)$ is of the Bloch form [9], we may only consider the first Brillouin zone $m = 0, 1, \dots, N - 1$ to characterize the dispersion relationship in the structure [156]. From Eq. (2.4), $\Delta k \equiv k_{m+1} - k_m = 2\pi/L$ so that in the theoretical limit of an infinitely long structure, the discrete distribution of eigenmodes goes over to a continuous spectrum.

2.2.1 Dispersion relationship

From Maxwell's equations and the definition of the eigenmodes as in Eq. (2.3), the dispersion relationship, sometimes called the characteristic equation, can be derived. In Gaussian units, $\mathbf{E}_k(z, t) \equiv \exp(i\omega_k t) \phi_k(\mathbf{r})$ satisfies

$$\nabla \times (\nabla \times \mathbf{E}_k) = \epsilon(\mathbf{r}) \frac{\omega_k^2}{c^2} \mathbf{E}_k, \quad (2.5)$$

where $\epsilon(\mathbf{r})$ is the location-dependent dielectric coefficient of the waveguide and ω_k is the eigenfrequency of the waveguide mode. Replacing ϕ_k with ψ_l in Eq. (2.5) and ω_k with Ω_l , the eigenfrequency of the l -th mode of a single resonator, we get a similar equation that describes the eigenmode of a single resonator,

$$\nabla \times (\nabla \times \boldsymbol{\psi}_l) = \epsilon_0(\mathbf{r}) \frac{\Omega_l^2}{c^2} \boldsymbol{\psi}_l. \quad (2.6)$$

To derive the dispersion relationship, we substitute Eq. (2.3) into Eq. (2.5), multiply both sides from the left by $\boldsymbol{\psi}_l(\mathbf{r})^*$, and integrate over a unit cell, using the normalization condition⁴

$$\int d\mathbf{r} \epsilon_0(\mathbf{r}) \boldsymbol{\psi}_l(\mathbf{r})^* \cdot \boldsymbol{\psi}_m(\mathbf{r}) = \delta_{lm}, \quad (2.7)$$

where $\epsilon_0(\mathbf{r})$ is the dielectric coefficient of a single resonator in isolation, e.g., as shown in Fig. 1.3.

After some algebra, the coefficient b_l is found to satisfy a transcendental equation [150, Eq. (5)] which can be simplified under the conditions of weak (nearest-neighbor) coupling and from symmetry considerations. Further, based on the symmetry of the individual resonator modes⁵ and considering the lowest-order individual resonator modes, the dispersion relationship can be further simplified. Although the single defect cavity modes are actually doubly degenerate, the two resultant CROW bands have opposite polarity and can't couple to each other; therefore, the dispersion relation of each band has the same form.

The dispersion relationship for a single CROW band (one particular, implicit, value of l) around a central wave number k_0 is

$$\begin{aligned} \omega_{k_0+K} &= \Omega(1 - \Delta\alpha/2) + \Omega \kappa \cos(KR) \\ &\equiv \omega_0 + \Delta\omega \cos(KR), \end{aligned} \quad (2.8)$$

where Ω is the eigenfrequency of the individual resonators, and both $\Delta\alpha$ and κ are overlap integrals involving the individual resonator modes and the spatial variation

⁴A more general normalization condition will be used in Eq. (2.36).

⁵It's assumed that each of the individual planar resonator eigenmodes possesses a mirror reflection symmetry with respect to a transverse plane. This leads to a classification of the single resonator modes according to the even and odd parity of this discrete symmetry.

of the dielectric constant,

$$\begin{aligned}\Delta\alpha &= \int d^3\mathbf{r} [\epsilon_{\text{wg}}(\mathbf{r} - R\mathbf{e}_z) - \epsilon_{\text{res}}(\mathbf{r} - R\mathbf{e}_z)] |\boldsymbol{\psi}_l(\mathbf{r})|^2 \\ \kappa &= \int d^3\mathbf{r} [\epsilon_{\text{res}}(\mathbf{r} - R\mathbf{e}_z) - \epsilon_{\text{wg}}(\mathbf{r} - R\mathbf{e}_z)] \\ &\quad \boldsymbol{\psi}_l(\mathbf{r}) \cdot \boldsymbol{\psi}_l(\mathbf{r} - R\mathbf{e}_z),\end{aligned}\tag{2.9}$$

where ϵ_{res} is the dielectric constant of the individual resonators, and ϵ_{wg} is the dielectric constant of the waveguide. This is similar to an equivalent derivation in the electronic levels of crystalline solids in the tight-binding approximation [129, pp. 200–212].

The formation, when the number of resonators is increased, of a continuous dispersion relationship such as Eq. (2.8) from a discrete spectrum by reduction of the mode energy splitting of the individual resonators has been discussed elsewhere [12, 11]. In the limit of nearest-neighbor coupling, as applicable to waveguides formed by coupling high-Q resonators, the parameter $\Delta\omega$ in Eq. (2.8) is given in terms of the spatial variation of the dielectric constant by $\Delta\omega = \Omega\kappa$. For the 2-D photonic crystal structures we discuss, finite-difference time-domain simulations indicate that $|\Delta\omega/\Omega| \sim 10^{-3} - 10^{-4}$ [150], and similar numbers have been measured for CROWs constructed of polystyrene microspheres and microcavities in lithographically patterned in GaAs.

The k -dependent group velocity [154, p. 37] is given by

$$v_{g,l}(k) = \frac{d\omega_{k,l}}{dk} = -\Omega R \kappa_l \sin(kR),\tag{2.10}$$

which clearly depends on the coupling factor κ , and therefore, on the physical structure of the device that was designed. A low coupling factor implies a substantial reduction of the group velocity of the pulse, leading to pulse compression with respect to free space in the structure. Based on numerical simulations, values of κ as low as 10^{-4} have been predicted [150].

Particular realizations of waveguides that are appropriately described by the tight-binding formalism include superstructure Bragg gratings in semiconductor materials and in fibers, polystyrene microspheres, alumina rods (microwave), resonators in GaAs without a photonic crystal structure, and defects in GaAs 2-D photonic crystal slabs.

1. The optical modes of a linear array of GaAs cavities, with InGaAs quantum wells as the optically active material, were measured by angle-resolved photoluminescence spectroscopy, demonstrating the creation of a continuum of mode energy distributions from a discrete family as the number of resonators increases [11]. Narrowing the width of the GaAs channels connecting the cavities resulted in a larger band gap at the Brillouin zone boundaries, in accordance with the increased modulation of the dielectric function along the waveguide.
2. Coupling between whispering-gallery modes of two polystyrene microspheres was demonstrated to follow the tight-binding theory [98]. An intersphere coupling parameter between microspheres of diameter 2 to 5 μm was measured to be in the range $2.8 - 3.5 \times 10^{-3}$, and decreases as the size of the spheres increases since the field is less confined in smaller structures.
3. Among the early demonstrations of the validity of the tight-binding description of weakly coupled electromagnetic structures were the microwave experiments of Bayindir *et al.* [13]. A multilayer photonic crystal based on square-shaped alumina rods was found to exhibit a three-dimensional band gap from 10.6 to 12.8 GHz; removing rods from this periodic structure corresponds to introducing localized defect modes, and the authors have measured the transmission through the structure with a single, two, and three consecutive defects to show the presence of one, two, and three resonance frequencies, respectively. Further, the authors validate the nearest-neighbor approximation used in the derivation of the dispersion relationship for a weakly coupled CROW since the second-nearest neighbor coupling parameters are found to be an order of magnitude smaller than their first-order counterparts. To demonstrate the formation of a photonic band within the photonic band gap (11.47 to 12.62 GHz), Bayindir *et al.* remove a single rod from ten consecutive unit cells, thereby forming a ten-element CROW and show excellent agreement between the calculated and measured dispersion relationship of the resulting waveguiding band (see Fig. 4 in [13]).
4. Olivier *et al.* [105] have measured the dispersion characteristics of a coupled-resonator optical waveguide in the near infrared (1 μm .) One particular structure consists of a row of nine hexagonal cavities in a GaAs-based two-dimensional

photonic crystal formed as a triangular array of holes perforating a monomode heterostructure waveguide with index confinement along the axis out of the plane (see Fig. 1a in [105]). The cavities consist of seven missing holes and are separated by one row of holes for a total structure length of about $8 \mu\text{m}$. The experiment uses a few layers of InAs quantum dots in the planar waveguide of the heterostructure as an internal source of photoluminescence to measure the transmission characteristics.

Several transmission and stop bands (“minibands separated by minigaps”) are observed within the photonic bandgap for TE modes, with transmission minima about -20 dB of the maxima. Olivier *et al.* calculate the dispersion relations and field patterns of an infinite CROW using a plane-wave expansion method [111] to compare with measurements. Within the photonic bandgap, all the bands observed must necessarily arise from the modes that are laterally localized in the CROW cavities, and these bands can be indexed by the discrete modes of the isolated cavity. The lowest-order (fundamental) CROW mode is calculated to have a single lobe in the transverse direction, which may explain why it is observed to persist as an index-guided mode below the photonic bandgap.

5. Another application of the tight-binding method is in the description of superstructure Bragg gratings (SSGs, see Appendix A), also called optical superlattices, which are fiber or semiconductor gratings with parameters that vary periodically as a function of position [17]. Whereas shallow SSGs can be described by the standard coupled-mode theory, deep SSGs require the complementary approach of the tight-binding approximation [32].

In the context of photonic bandgaps and associated topics, it is useful to recall a discussion by Lang and Yariv [75] about certain implicit assumptions in such theories that may be especially relevant in waveguide and resonant waveguide problems. When one solves for the eigenmodes of an isolated resonator, one usually makes the assumption that all fields outside the resonator are outgoing. Consequently, the eigenmodes lie in the discrete spectrum of the operator corresponding to wave propagation in the resonator. These eigenmodes form a complete basis only for outgoing fields.

In a coupled resonator structure, it must be the case that there exist incoming fields in each cavity—or else the resonators simply cannot couple to one another.

These fields cannot be described by the modes of an individual resonator, to which must be added the modes corresponding to the continuous spectrum, corresponding to fields incident on the cavity from the outside. If we drop this continuous part of the spectrum, we conceptually introduce “black hole” modes, which in rate equations act as sinks for energy from the discrete modes but never as sources to the discrete modes. There is no mechanism for the scattering of energy back from the black hole modes to the modes we do consider. As a result, calculations of threshold gains from such a theory will be overestimated, and the fraction of overestimation depends on the relative fraction of the coupled-cavity modes that is described by the black hole modes.

For weakly coupled resonators, as in a CROW waveguide, this may be small, but when the coupling becomes significant, as in a CROW laser, it may be significant. Although the CROW laser is not discussed here, we point out that Lang and Yariv have formulated local-field rate equations in terms of the amplitudes of traveling waves at fixed points inside the composite cavity, rather than the amplitude of an individual cavity mode [74, 75]. The central approximation made is that the optical field adiabatically follows the characteristics of the resonator.

2.3 Pulse propagation

Based on our earlier analysis of the individual resonator modes, and the waveguide modes, we can now analyze how a pulse propagates in a CROW. At a fixed time, taken for simplicity to be $t = 0$, the field in the waveguide is given by a superposition of eigenmodes,

$$\mathcal{E}(\mathbf{r}, t = 0) = \int \frac{dk}{2\pi} c_k \phi_k(\mathbf{r}), \quad (2.11)$$

where $\phi_k(\mathbf{r})$ are the eigenmodes at wavevector (propagation constant) k as given by Eq. (2.3) and c_k are certain ‘weights’ to be determined from the boundary condition⁶.

For a structure of finite length, not all k ’s are allowed, according to Eq. (2.4), and the integral over k in Eq. (2.11) should be replaced by a sum over the allowed k . Alternatively, we can redefine $\phi_k(z)$ for a 1D structure of finite length along the

⁶The geometry of the problem dictates that we adopt the methodology of Section 1.2 rather than of Section 1.1.

z -axis as

$$\phi_k(\mathbf{r}) = \left[|\Delta k| \sum_{m=-\infty}^{\infty} \delta(k - m\Delta k) \right] \sum_n \exp(-inkR) \sum_l \psi_l(\mathbf{r} - nR\mathbf{e}_z) \quad (2.12)$$

to preserve the form of Eq. (2.11). The factor $|\Delta k|$ inside the square brackets in Eq. (2.12) follows from the usual definition of the Riemann-Stieltjes integral [8]: for a long waveguide, as $L \rightarrow \infty$ and $\Delta k \rightarrow 0$, the field $\mathcal{E}(z, t = 0)$ retains the same form as given directly by Eq. (2.11) with $\phi_k(z)$ defined by Eq. (2.3), i.e., without the impulse train (in square brackets) in Eq. (2.12).

Since the system is linear and time invariant, the field at time t is given by

$$\mathcal{E}(z, t) = \int \frac{dk}{2\pi} e^{i\omega(k)t} c_k \phi_k(z). \quad (2.13)$$

Since the dispersion relationships of the waveguide modes are approximately linear in the middle of the band gap (the group velocity goes to zero at the band edges) [156, 32], we can write the dispersion relationship around the central propagation constant of the pulse k_0 as

$$\omega(k_0 + K) = \omega(k_0) + \left. \frac{d\omega}{dk} \right|_{k=k_0} K + \dots \approx \omega_0 + v_g K, \quad (2.14)$$

where v_g is the group velocity of the pulse. Then,

$$\mathcal{E}(\mathbf{r}, t) = e^{i\omega_0 t} \int \frac{dK}{2\pi} e^{iv_g t K} c_{k_0+K} \phi_{k_0+K}(\mathbf{r}). \quad (2.15)$$

The boundary conditions specify a pulse shape at the $z = 0$ edge of the waveguide and centered at the optical frequency ω_0 ,

$$\mathcal{E}(\mathbf{r} = 0, t) = e^{i\omega_0 t} E(z = 0, t) \hat{\mathbf{u}}, \quad (2.16)$$

where $\hat{\mathbf{u}}$ is a unit-magnitude vector that describes the vectorial nature of the field at $\mathbf{r} = 0$. The vectorial behavior of $\phi_{k_0+K}(0)$ must follow $\hat{\mathbf{u}}$.

We'll work with the scalar functions $\phi_{k_0+K}(z)$ and $\psi_l(z)$ in the remainder of this section, and in the following section. From the equality of Eq. (2.15) evaluated at

$z = 0$ and Eq. (2.16), it follows that

$$c_{k_0+K} = \frac{1}{\phi_{k_0+K}(0)} \int d(|v_g|t') E(z=0, t') e^{-iv_g t' K}. \quad (2.17)$$

Combining Eq. (2.15) and Eq. (2.17),

$$\boxed{\mathcal{E}(z, t) = e^{i\omega_0 t} \int d(|v_g|t') E(z=0, t') \int \frac{dK}{2\pi} \frac{\phi_{k_0+K}(z)}{\phi_{k_0+K}(0)} e^{iv_g(t-t')K}.} \quad (2.18)$$

In free space, which can be thought of as a “linear space-invariant system,” the eigenfunctions are $\phi_k(z) = \exp(-ikz)$, instead of Eq. (2.3). Substituting this into Eq. (2.18), we get

$$\begin{aligned} \mathcal{E}(z, t) &= e^{i\omega_0 t} \int d(|v_g|t') E(z=0, t') \int \frac{dK}{2\pi} e^{-i(k_0+K)z} e^{iv_g(t-t')K} \\ &= e^{i(\omega_0 t - k_0 z)} E\left(z=0, t - \frac{z}{v_g}\right). \end{aligned} \quad (2.19)$$

This is the well-known result (similar to Eq. (1.6) and Jackson [57, pp. 322–326]) that a pulse propagates unchanged in shape in a weakly dispersive medium, apart from an overall phase factor, and that the velocity of propagation is given by the group velocity of the pulse v_g defined from the dispersion relationship as in Eq. (2.14).

In Chapter 3, we’ll extend the above description to account for propagation in waveguides that can amplify or attenuate the pulse, or otherwise transfer power between the various waveguide modes that comprise the pulse. The goal is to identify, if possible, a component of that field description that is analogous to, e.g., the envelope of a conventional waveguide mode, $\exp[i(\omega t - kz)]$. By identifying the envelope component of the full field description, we may obtain equations that describe the change in the envelope alone, and do not involve the variables describing the non-envelope part of the field. It’s usually the case that the envelope usually varies on a longer spatial scale than the remainder of the field.

CROWs and SSGs in the tight-binding approximation do not have plane-wave eigenmodes of the form $\exp[i(\omega t - kz)]$. For a structure whose eigenmodes are given by Eq. (2.3) or Eq. (2.12) with $\psi(z)$ rapidly decaying in magnitude for distances on the order of R , we can carry out further simplifications to the field expression Eq. (2.18).

The individual resonator eigenmodes are normalized as $\psi_l(0) = 1$ and are highly localized around $z = 0$ so that $|\psi_l(nR)| \ll 1$ for all $n \neq 0$. We assume that these eigenmodes are symmetric, so that $\psi_l(-z) = \psi_l(z)$. Then,

$$\begin{aligned}\phi_{k_0+K}(0) &= \sum_n e^{-i(k_0+K)nR} \sum_l \psi(-nR) \\ &= 1 + \sum_l \psi_l(R) 2 \cos[(k_0 + K)R] + \dots\end{aligned}\quad (2.20)$$

ignoring terms on the order of $\sum_l \psi(2R)$ or smaller. Consequently, we can write

$$[\phi_{k_0+K}(0)]^{-1} \approx 1 - \sum_l \psi_l(R) 2 \cos[(k_0 + K)R], \quad (2.21)$$

which can be used in Eq. (2.18).

The leading order contribution to $\mathcal{E}(z, t)$ is given by including the first term of Eq. (2.21),

$$\begin{aligned}\mathcal{E}(z, t) &= e^{i\omega_0 t} \sum_n e^{-ik_0 nR} \sum_l \psi_l(z - nR) \int d(|v_g|t') E(z = 0, t') \\ &\quad \times \int \frac{dK}{2\pi} \left[|\Delta K| \sum_m \delta(K - m\Delta K) \right] e^{iT K},\end{aligned}\quad (2.22)$$

where $T \equiv v_g(t - nR/v_g - t')$, and the index m of the infinite summation can be translated as desired. The expression on the second line of Eq. (2.22) is the inverse Fourier transform (evaluated at T) of an impulse train in the K domain, which evaluates to an impulse train in the T domain [107],

$$|\Delta K| \sum_{m=-\infty}^{\infty} \delta(K - m\Delta K) \Rightarrow \sum_{m=-\infty}^{\infty} \delta(T - m\Delta T), \quad (2.23)$$

where $\Delta T = 2\pi/\Delta K = L$. Carrying out the integrals over t' for each m ,

$$\mathcal{E}(z, t) = e^{i\omega_0 t} \sum_n e^{-ik_0 nR} \sum_l \psi_l(z - nR) \sum_m E\left(z = 0, t - \frac{nR + mL}{v_g}\right). \quad (2.24)$$

This expression is the tight-binding approximation analog of Eq. (2.19). The vectorial extension is written in Eq. (2.32).

It will be shown in Section 2.5 that Eq. (2.24) is of the Bloch form, i.e., $\mathcal{E}(z, t)$ can be written as the product of a plane wave $\exp[i(\omega t - kz)]$ and a function $u(z, t)$ with the periodicity of the “lattice” that defines the CROW. It’s important to note, however, that this does not imply that plane waves of the form $\exp[i(\omega t - kz)]$ are eigenfunctions of the CROW as the function $u(z, t)$ is not necessarily slowly varying (and in fact, varies as “rapidly” as $\exp[-ikz]$ does).

The contribution of the first-order corrections to Eq. (2.24) based on Eq. (2.21) can be evaluated in the same way,

$$\begin{aligned} \Delta\mathcal{E}(z, t) = & - \sum_{l'} \psi_{l'}(R) e^{i\omega_0 t} \left\{ \sum_n e^{-ik_0(n-1)R} \sum_l \psi_l(z - nR) \times \right. \\ & \sum_m E \left(z = 0, t - \frac{(n-1)R + mL}{v_g} \right) + \sum_n e^{-ik_0(n+1)R} \times \\ & \left. \sum_l \psi_l(z - nR) \sum_m E \left(z = 0, t - \frac{(n+1)R + mL}{v_g} \right) \right\}. \quad (2.25) \end{aligned}$$

Fig. 2.2 shows an annotated frame from an MPEG animation of Gaussian pulse propagation in a structure described by the tight-binding approximation to the leading order, using the approximations that the structure is of infinite length and that it’s sufficient to consider a single l in Eq. (2.24).

Although Eq. (2.15) is a good approximation to the dispersion relationship in a CROW [156, 150], it may be necessary for wideband pulses to consider higher-order terms in Eq. (2.15). The resulting Eq. (2.17) is then obtained from the solution of a Fredholm integral equation, and Eqs. (2.18) and (2.24) will in general involve envelope distortion (as for free space propagation [154]).

2.4 Frequency, space, and time sampling

As we’ve already noted, the allowed k vectors are quantized in a structure of finite length, and using Eq. (2.14), the allowed $\omega = \omega_0 + \Omega$ values are quantized. To prevent aliasing [107], the temporal interval between two samples $2\pi/\Delta\Omega$ must be greater than twice the temporal extent of the pulse envelope T , where $\Delta\Omega = v_g\Delta K$

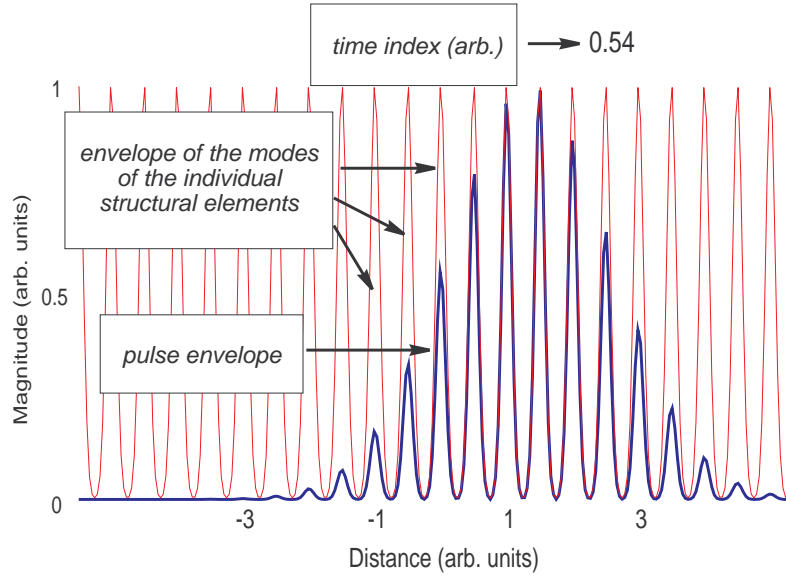


Figure 2.2: Pulse propagation in a structure described by the tight-binding approximation. The envelope of the eigenmode of the structure is shown in red, and the Gaussian pulse envelope in blue, propagating from left to right, indexed by an arbitrary time coordinate at the upper-right corner.

according to Eq. (2.14)⁷. Therefore,

$$\frac{2\pi}{(2\pi/L)v_g} = 2T_{\max}, \quad \text{which implies} \quad T_{\max} = \frac{1}{2} \frac{L}{v_g}. \quad (2.26)$$

In addition to the consequences of the dispersion relationship, the geometrical structure of the waveguide is also important. The eigenmode $\phi_k(z)$ represents a *spatial* sampling function for the propagating pulse envelope, especially in the limit that the individual structural eigenmodes $\psi_l(z)$ are tightly confined (see Fig. 2.2). Again, to prevent aliasing, it's necessary that the spectral content in k -space be no

⁷A physical rationalization of this may be helpful: the spectrum of the field envelope in the waveguide is represented by a discrete set of complex exponentials with frequencies $\omega_0 + m\Delta\Omega$ according to Eq. (2.4) and the dispersion relationship, Eq. (2.14). To successfully characterize the continuous free-space spectral envelope by this discrete set, we require that within the time interval T_{\max} , the frequency change between successive exponentials is “small,” i.e., $T_{\max}\Delta\Omega < \pi$. The pulse envelope in the waveguide then consists of replicas of the free-space envelope, analogous to the spectral replicas formed by reconstruction of time-sampled signals [107].

greater than K_{\max} ,

$$\frac{2\pi}{R} = 2K_{\max} \quad \text{which implies} \quad K_{\max} = \frac{1}{2} \left(\frac{2\pi}{R} \right). \quad (2.27)$$

But the free-space pulse envelope is invariant in the frame $z - v_g t$, and this maximum K -space extent translates into a *minimum* pulse width T_{\min} ,⁸

$$\frac{1}{2} v_g T_{\min} = R \quad \text{which implies} \quad T_{\min} = \frac{2R}{v_g}. \quad (2.28)$$

In a structure of finite length described by the tight-binding approximation, therefore, there exists both a maximum and a minimum allowed pulse duration; the former arises because of the finite length of the structure, and the latter because of the sampling train-like eigenmodes of the waveguide.

Eq. (2.28) limits the bandwidth (where most of the energy of the pulse is concentrated) in the Fourier K -space associated with the propagation distance z , and since the pulse is propagating with group velocity v_g , also in the Fourier Ω -space associated with the temporal coordinate t . The dimension of the space of finite-energy signals (pulse envelopes) that are identically zero outside the time interval $[-T_0/2, T_0/2]$ and have most of their energy concentrated in the bandwidth $[-\Omega_0/2, \Omega_0/2]$ is approximately $D = \Omega_0 T_0 + 1$ [147],

$$D = \left(\frac{1}{R} v_g \right) \left(\frac{1}{2} \frac{L}{v_g} \right) + 1 = \frac{N}{2} + 1, \quad (2.29)$$

where $N = L/R$ is the number of individual structural elements in the waveguide. These pulse envelopes can be represented in the mean-square sense by a superposition of the prolate spheroidal wave functions within the interval $[-T_{\max}/2, T_{\max}/2]$.

2.4.1 K -space representation of Eq. (2.24)

It's often convenient in certain problems (e.g., four-wave mixing processes [91]) to have a description of the spatial Fourier transform of Eq. (2.24) in terms of plane

⁸As a guideline, it's useful to recall that the Fourier transform of a rectangular pulse between $\pm v_g T$ in the $v_g t$ frame is a *sinc* function with first nulls at $\pm\pi/(v_g T)$ in K -space [107].

waves,

$$\begin{aligned}\tilde{\mathcal{E}}(K, t) &\equiv \int \mathcal{E}(z, t) e^{-iKz} dz \\ &= e^{i\omega_0 t} \sum_n e^{-i(k_0 + K)nR} \sum_m E \left[z = 0, t - \frac{nR + mL}{v_g} \right] \sum_l \tilde{\psi}_l(K),\end{aligned}\quad (2.30)$$

where $\tilde{\psi}_l(K) = \int \psi_l(z) \exp(-iKz) dz$ is the spatial Fourier transform of $\psi_l(z)$.

Eqs. (2.24) and (2.30) describe the propagation of a pulse in a medium described by the tight-binding approximation. They can be used, for example, to describe the index grating formed by the interference pattern of two counterpropagating pulses (at the same optical frequency for simplicity),

$$\delta n(z) \propto \int \frac{dK_1}{2\pi} \int \frac{dK_2}{2\pi} \delta \hat{n}(K_1, K_2) e^{i(K_1 - K_2)z} \tilde{\mathcal{E}}(K_1, t) \tilde{\mathcal{E}}(K_2, t)^*, \quad (2.31)$$

where $\delta \hat{n}(K_1, K_2)$ is the coupling coefficient between two plane waves defined by K_1 and K_2 and depends on the material properties, the orientation of the medium and the polarization of the waves [123].

We've formed equations describing the evolution of optical pulses in the tight-binding approximation, which is of increasing importance in the description of a variety of recently developed structures such as coupled resonator optical waveguides in photonic crystals and superstructure Bragg gratings in both semiconductors and in optical fiber. These equations form a useful starting point for the analysis of linear and nonlinear pulsed phenomena in such structures.

2.5 Linear pulse propagation: Bloch waves

In this section, we'll modify Eq. (2.24) in three ways. Firstly, we limit our attention to the limiting case of an infinitely long waveguide and drop the summation over m . Secondly, we'll account for the vectorial nature of the individual resonator modes $\psi(\mathbf{r})$ but we'll continue to look at pulse propagation along the z -axis. For simplicity, we'll also omit the summation over the multiple modes of individual resonators, indexed

by l : their re-introduction is straightforward. The electric field distribution $\mathbf{E}_k(\mathbf{r}, t)$ describing a pulse at the frequency ω and wave vector \mathbf{K} is

$$\mathbf{E}_k(\mathbf{r}, t) = e^{i\omega_0 t} \sum_n e^{-iknR} \boldsymbol{\psi}(\mathbf{r} - nR\mathbf{e}_z) \mathcal{E} \left[z = 0, t - \frac{nR}{v} \right] \quad (2.32)$$

where $\boldsymbol{\psi}(\mathbf{r})$ is the individual resonator eigenmode, $\mathcal{E}(z = 0, t)$ is the input pulse envelope⁹ and v is the group velocity at $K = |\mathbf{K}|$.

For an infinitely long CROW, where the summation over n in Eq. (2.32) can be relabeled to $n \pm 1$, $\mathbf{E}_K(\mathbf{r}, t)$ satisfies the (3+1)D Bloch theorem [154, 9],

$$\mathbf{E}_k(\mathbf{r} + R\mathbf{e}_z, t + R/v) = e^{i\omega R/v} e^{-ikR} \mathbf{E}_k(\mathbf{r}, t). \quad (2.33)$$

Consequently, the waveguide field distribution can be written in the Bloch form,

$$\mathbf{E}_k(\mathbf{r}, t) = e^{i\omega t} e^{-ik(\omega)z} \mathbf{u}_{k(\omega)}(\mathbf{r}, t), \quad (2.34)$$

where $\mathbf{u}_{k(\omega)}(\mathbf{r}, t)$ is a vector-valued function with the periodicity of the CROW “lattice” and can be written out explicitly as

$$\mathbf{u}_{k(\omega)}(\mathbf{r}, t) = \sum_n e^{ik(z-nR)} \boldsymbol{\psi}(\mathbf{r} - nR\mathbf{e}_z) \mathcal{E} \left[z = 0, t - \frac{nR}{v} \right]. \quad (2.35)$$

The notation emphasises that the propagation constant k and the Bloch wave function depend on the frequency ω (we’ll sometimes write k_ω in place of $k(\omega)$ so that the mathematical structure of certain equations is not obscured). Nevertheless, our writing the electromagnetic field distribution in the Bloch form, Eq. (2.34), is mainly for notational convenience in Section 3.3.

The Bloch wave function is normalized according to the following inner product definition between the vector space of the Bloch wave function and its dual space,

$$\int \frac{dt}{T} \int d\mathbf{r} \epsilon(\mathbf{r}) [\mathbf{u}_{k(\omega)}(\mathbf{r}, t)]^* \cdot \mathbf{u}_{k(\omega)}(\mathbf{r}, t) = 1, \quad (2.36)$$

⁹The terminology “input pulse envelope” shouldn’t be taken too literally since the structures we consider are infinitely long: it merely means that we focus on the field evolution along a section of an infinite waveguide, and the “input” refers to the field distribution at one edge of this structure, i.e., a boundary condition, as discussed in Chapter 2. The precise mathematical meaning of this assumption is rather technical and is discussed at the end of Appendix C.

where the spatial integration extends over a unit cell and the temporal integration over the extent of the pulse envelope, with a characteristic time constant T . This ensures that Eq. (2.36) still represents an electromagnetic energy conservation relationship [57], and can be interpreted as yielding a time-averaged energy stored in a unit cell volume [113, pp. 404–405]. We'll abbreviate the notation in Eq. (2.36) to an integration over the 4-vector r .

Based on Maxwell's equation, the waveguide field distribution satisfies the following equation: [154, 57]

$$\nabla \times [\nabla \times \mathbf{E}] + \frac{\epsilon(\mathbf{r})}{c^2} \frac{\partial^2 \mathbf{E}}{\partial t^2} = 0. \quad (2.37)$$

Substituting Eq. (2.34) for $\mathbf{E}(\mathbf{r}, t)$, we can write Eq. (2.37) as an eigenvalue problem [96] for the Bloch wavefunction $\mathbf{u}_{k(\omega)}(\mathbf{r}, t)$,

$$\begin{aligned} H_k \mathbf{u}_{k(\omega)} &\equiv -k_\omega^2 \mathbf{e}_z \times [\mathbf{e}_z \times \mathbf{u}_{k(\omega)}] + \nabla \times [\nabla \times \mathbf{u}_{k(\omega)}] \\ &\quad - ik_\omega \left[\mathbf{e}_z \times [\nabla \times \mathbf{u}_{k(\omega)}] + \nabla \times [\mathbf{e}_z \times \mathbf{u}_{k(\omega)}] \right] \\ &\quad + \frac{\epsilon(\mathbf{r})}{c^2} \left[\frac{\partial^2 \mathbf{u}_{k(\omega)}}{\partial t^2} + i 2\omega \frac{\partial \mathbf{u}_{k(\omega)}}{\partial t} \right] \\ &= \frac{\omega^2}{c^2} \epsilon(\mathbf{r}) \mathbf{u}_{k(\omega)}. \end{aligned} \quad (2.38)$$

It can be shown that the operator H is Hermitian (see Appendix C for an outline of the proof.) As a consequence of the dispersion relationship in the waveguide [57], the eigenvalue ω^2/c^2 is parametrized by K and we can use the Hellman-Feynman¹⁰ theorem [52, 37, 25, 119],

$$\begin{aligned} \frac{d(w/c)^2}{dk} &= \int d^4 r [\mathbf{u}_{k(\omega)}]^* \cdot \left[-2k_\omega \mathbf{e}_z \times [\mathbf{e}_z \mathbf{u}_{k(\omega)}] \right. \\ &\quad \left. - i \mathbf{e}_z \times [\nabla \times \mathbf{u}_{k(\omega)}] - i \nabla \times [\mathbf{e}_z \times \mathbf{u}_{k(\omega)}] \right] \\ &\quad + i \frac{2}{c^2} \frac{d\omega}{dk} \int d^4 r \epsilon(\mathbf{r}) [\mathbf{u}_{k(\omega)}]^* \cdot \frac{\partial \mathbf{u}_{k(\omega)}}{\partial t}. \end{aligned} \quad (2.39)$$

Recognizing that $d\omega/dk$ defines the group velocity v [154], Eq. (2.39) can be re-

¹⁰R. P. Feynman was an undergraduate at MIT at the time of writing this paper (1939).

written as

$$v \left[\frac{2\omega}{c^2} - i \frac{2}{c^2} \int d^4r \epsilon(\mathbf{r}) [\mathbf{u}_{k(\omega)}]^* \cdot \frac{\partial \mathbf{u}_{k(\omega)}}{\partial t} \right] = \int d^4r [\mathbf{u}_{k(\omega)}]^* \cdot \left[-2k_\omega \mathbf{e}_z \times [\mathbf{e}_z \mathbf{u}_{k(\omega)}] - i \mathbf{e}_z \times [\nabla \times \mathbf{u}_{k(\omega)}] - i \nabla \times [\mathbf{e}_z \times \mathbf{u}_{k(\omega)}] \right]. \quad (2.40)$$

This equation will be of considerable use in Chapter 3, where we discuss nonlinear optical phenomena in CROWs.

2.6 Using the full dispersion relationship

From Eq. (2.16), the coefficients c_{k_0+K} are derived from

$$E(z=0, t) = \int_{-\pi/R}^{\pi/R} \frac{dK}{2\pi} e^{i\Delta\omega t \cos(KR)} c_{k_0+K} \phi_{k_0+K}(0). \quad (2.41)$$

This is easily inverted in the limit of a linear dispersion relationship in place of Eq. (2.8)—the integral operator reduces to the well-known Fourier transform, and this is the analysis we have discussed earlier. In considering higher-order dispersion terms in the Taylor series expansion of the dispersion relationship, the integral equation, Eq. (2.41), can't in general be inverted to obtain the c 's in closed form. This is clearly evident when, for example, the exponent involves terms of quadratic or higher polynomial powers of K . Therefore, rather than work with the successive terms in a Taylor-series expansion of the dispersion relationship, we'll work with the full form of Eq. (2.8).

Note that the dispersion relationship is symmetric about $K = 0$. We'll assume that $E(z=0, t)$ is a symmetric envelope. Consequently, $c_{k_0+K} \phi_{k_0+K}(0) = c_{k_0-K} \phi_{k_0-K}(0)$ for all K within the first Brillouin zone. This is not a critical assumption, and relates to the choice of cosines rather than sines a subsequent step [Eq. (2.44)].

We introduce changes of variables to highlight the mathematical structure of

Eq. (2.41),

$$\begin{aligned}
 \varphi &\equiv KR, \\
 x &\equiv \Delta\omega t, \\
 h(\phi) &\equiv c_{k_0+K} \phi_{k_0+K}(0), \\
 f(x) &\equiv 2R E(z = 0, x/\Delta\omega),
 \end{aligned}
 \tag{2.42}$$

so that Eq. (2.41) becomes

$$\pi f(x) = \int_{-\pi}^{\pi} d\varphi e^{ix \cos \varphi} h(\varphi),
 \tag{2.43}$$

where $f(x)$ is a known function, in terms of which we want to find $h(\varphi)$. For the majority of cases of practical interest, we can instead find the coefficients in the expansion of $h(\varphi)$ as a Fourier cosine series,

$$h(\varphi) = \sum_{n=0}^{\infty} c_n \cos(n\varphi).
 \tag{2.44}$$

Using the identity [154, Eq. (9.4-5)],

$$\begin{aligned}
 e^{ix \cos \varphi} &= \sum_{m=0}^{\infty} b_m J_m(x) \cos(m\varphi), \\
 \text{where } b_m &= \begin{cases} 1, & m = 0 \\ 2i^m, & m \geq 1 \end{cases}
 \end{aligned}
 \tag{2.45}$$

and the orthogonality of the cosines over the interval $(-\pi, \pi)$, we can simplify Eq. (2.43) to

$$f(x) = \sum_{n=0}^{\infty} (b_n c_n) J_n(x) \equiv \sum_{n=0}^{\infty} a_n J_n(x).
 \tag{2.46}$$

Therefore, if we can expand $f(x)$ [which describes the envelope at the $z = 0$ cross section—see Eq. (2.42)] in a Neumann series [145, Chap. IX], we can find the coefficients c_n , and by subsequently using Eq. (2.44) and Eq. (2.42), the coefficients $c_{k_0 \pm K}$.

The envelopes of practical interest are usually analytic (more specifically, the complex signal description of the envelope—e.g., the Fourier transform—has no sin-

gularities) in some circle (of radius c) around the origin (if it's not entire), and a general way of obtaining the a_n 's is

$$a_n = \frac{1}{2\pi i} \int_{|z|=c'} dz f(z) O_n(z), \quad \text{for } 0 < c' < c, \quad (2.47)$$

where

$$\begin{aligned} O_{2n}(z) &= \frac{n}{2} \sum_{m=0}^n \frac{(n+m-1)!}{(n-m)!} \left(\frac{z}{2}\right)^{-2m-1}, \\ O_{2n+1}(z) &= \frac{n+1/2}{2} \sum_{m=0}^n \frac{(n+m)!}{(n-m)!} \left(\frac{z}{2}\right)^{-2m-2}, \end{aligned} \quad (2.48)$$

are the Neumann polynomials [145, Chap. IX]

Since the temporal envelope is a real function, we can use a simpler representation that does not require integration in the complex plane, and is readily implementable numerically. The following identity [36, pp. 64–65]

$$\int_0^\infty \frac{dt}{t} J_{\nu+2n+1}(t) J_{\nu+2m+1}(t) = (4n+2\nu+2)^{-1} \delta_{mn} \quad (2.49)$$

holds for $\nu > -1$ and implies that a real function $g(x)$ of a real variable x defined on the interval $(0, \infty)$ can be written as

$$\begin{aligned} g(x) &= \sum_{n=0}^\infty J_{\nu+2n+1}(x) \left[(2\nu+2+4n) \right. \\ &\quad \left. \int_0^\infty \frac{dt}{t} g(t) J_{\nu+2n+1}(t) \right], \quad \nu > -1. \end{aligned} \quad (2.50)$$

The derivation of this representation (for the special case $\nu = 0$) is known as the Webb-Kapteyn theory of the Neumann series.

Adding the series that results from Eq. (2.50) using $\nu = 0$ and $\nu = 1$, and assuming that the terms can be rearranged, we can write the coefficients a_n that appear in Eq. (2.46) as

$$a_n = \begin{cases} 0, & n = 0, \\ n \int_0^\infty \frac{dt}{t} g(t) J_n(t), & n \geq 1. \end{cases} \quad (2.51)$$

It's obvious that the function $g(t)$ should have no "d.c. value" since $J_n(z) \sim z^n$ near the origin. Referring back to Eq. (2.42), the function that we expand in the Neumann series is $g(t) \equiv f(t) - f(0)$.

An important, but technical, point relevant to the validity of this simpler representation of the Neumann coefficients is discussed in Appendix B for the particular case of Gaussian envelopes,

$$E(z = 0, t) = \exp\left(-\frac{t^2}{T^2}\right), \quad (2.52)$$

with a pulse width indicated by T . In this case, the coefficients evaluate to [1, 11.4.28]

$$a_n = 2R \left\{ \left[\frac{\Delta\omega T}{2} \right]^n \frac{\Gamma(n/2)}{2\Gamma(n)} {}_1F_1 \left[\frac{n}{2}; n+1; -\left(\frac{\Delta\omega T}{2} \right)^2 \right] - 1 \right\}, \quad (2.53)$$

in terms of the confluent hypergeometric function.

Returning to the original notation, we've shown that as a consequence of the dispersion relationship Eq. (2.8), the field describing the propagation of a pulse in a CROW can be written as

$$\begin{aligned} \mathcal{E}(z, t) = e^{i\omega_0 t} \int_{-\pi/R}^{\pi/R} \frac{dK}{2\pi} e^{i\Delta\omega t \cos(KR)} \frac{\phi_{k_0+K}(z)}{\phi_{k_0+K}(0)} \left\{ \sum_{n=1}^{\infty} \frac{2nR}{b_n} \left(\int_0^{\infty} \frac{dt'}{t'} \left[E(z=0, t'/\Delta\omega) \right. \right. \right. \\ \left. \left. \left. - E(0, 0) \right] J_n(t') \right) \cos(nKR) + c_{k_0} \phi_{k_0}(0) \right\}, \end{aligned} \quad (2.54)$$

where the b_n 's are given by Eq. (2.45), and the integral can be evaluated for a specific case as in Eqs. (2.52)–(2.53). It's assumed in this analysis that the waveguide modes are known, i.e., $\phi_{k_0+K}(z)$ is given by Eq. (2.3) and $\phi_{k_0+K}(0)$ evaluates to a known number.

There's one extraneous degree of freedom in Eq. (2.54), physically representing an overall scale factor and represented by c_{k_0} , which can be accounted for by Parseval's relationship,

$$\int_{-\infty}^{\infty} dt |\mathcal{E}(z=0, t)|^2 = \int_{-\pi/R}^{\pi/R} \frac{dK}{2\pi} \left(\frac{2}{R} \right) |c_{k_0+K}|^2 |\phi_{k_0+K}(0)|^2. \quad (2.55)$$

The integral over K in Eq. (2.54) can be carried out by writing the exponential in the form of Eq. (2.45), and using Eq. (2.21). We define the coefficients

$$\beta_n = \begin{cases} \frac{1}{2R} c_{k_0}, & n = 0 \\ \frac{n}{i^n} \int_0^\infty \frac{dt'}{t'} [E(0, t') - E(0, 0)] J_n(\Delta\omega t'), & n \geq 1 \end{cases} \quad (2.56)$$

A few pages of straightforward algebra based on the orthogonality of the cosines leads to the expression,

$$\mathcal{E}(z, t) = e^{i\omega_0 t} \sum_{m=0}^{\infty} b_m J_m(\Delta\omega t) \sum_{n=0}^{\infty} \beta_n \left\{ \frac{1}{4} e^{-i(\pm m \pm n)_+ k_0 R} \sum_l \psi_l [z - (\pm m \pm n)_+ R] \right\} \quad (2.57)$$

where the coefficients b_m are defined as

$$b_m = \begin{cases} 1, & m = 0 \\ 2i^m, & m \geq 1 \end{cases} . \quad (2.58)$$

We've used the symbol ' $()_+$ ' in Eq. (2.57) as a compact notation for the sum over both choices of sign of ' \pm ' that yield a non-negative number for the expression inside the brackets.

Fig. 2.3 shows the temporal profiles of an input Gaussian envelope as would be detected along such a waveguide. The crest of the envelope travels with a group velocity $\Delta z/\Delta t \lesssim \Delta\omega R$. The dispersion relationship is nonlinear, and there's no single number for the group velocity valid to all propagation distances, but the error in assuming an equality is less than 0.5% for much of the regime shown in Fig. 2. Higher-order dispersion develops an oscillatory structure at the trailing edge of the pulse (see, e.g., Agrawal [4, Fig. 3.7]).

We ask what temporal waveform would be measured by an observer sitting at one of the resonators, i.e., $\mathcal{E}(z, t)$ as a function of t with the spatial coordinate z set to the location of one of the resonators (so that z/R is an integer). In the practically important limit of high-Q resonators, $\psi_l(z)$ is narrowly peaked around $z = 0$, $|\psi_l(z = \pm R)| \ll |\psi_l(z = 0)|$ and we can simplify the double summations over

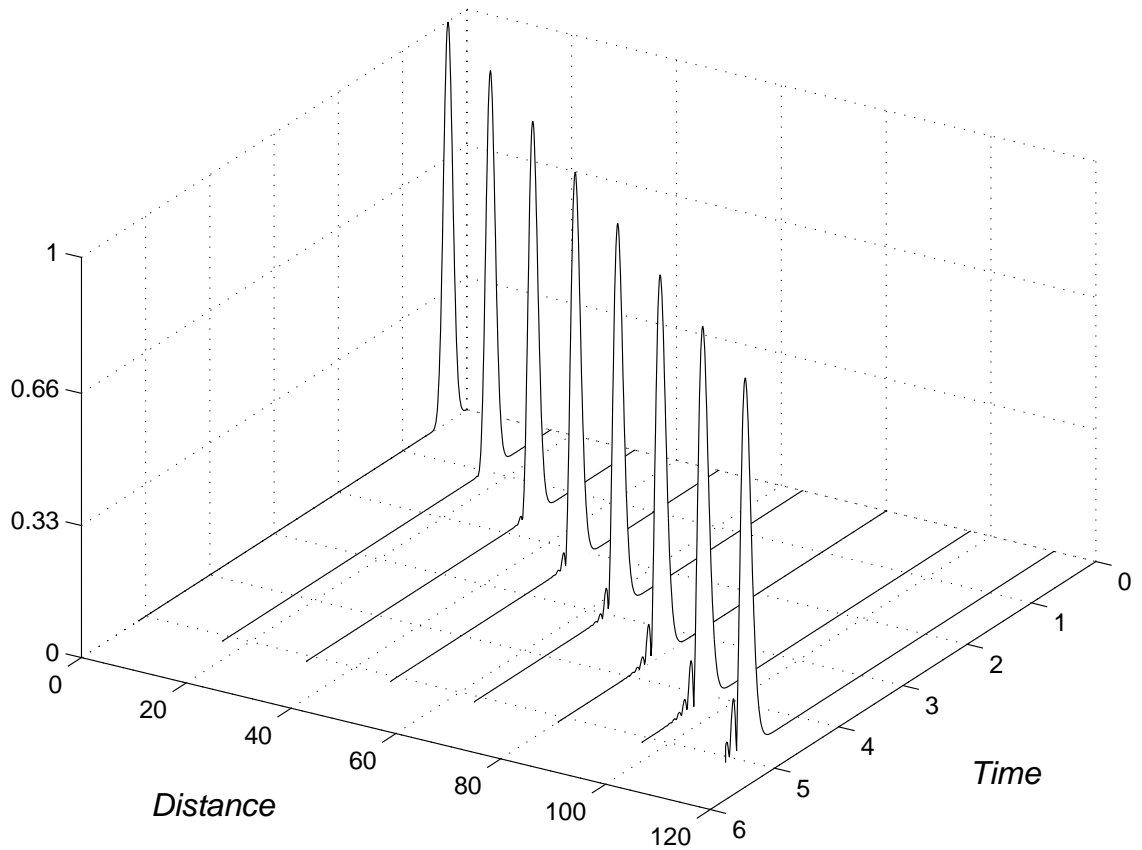


Figure 2.3: Temporal evolution of a Gaussian envelope at specific distances inside a CROW, showing the effects of dispersive propagation. ‘Distance’ is normalized to R , the inter-resonator spacing, ‘Time’ is normalized to $1/\Delta\omega$. The vertical axis represents $|\mathcal{E}(z, t = 0)|$ normalized to its maximum value. At greater depths, the peak of the envelope arrives at a later time, and ripples in the trailing edge indicate higher-order distortion.

m and n in Eq. (2.57) by representing this condition as a Kronecker delta function. After some algebra, we may write an expression for the envelope $E(z, t)$ defined by the usual relationship, $|\mathbf{E}(\mathbf{r}, t)| \equiv \exp[i(\omega_0 t - k_0 z)]E(z, t)$, as the sum of two terms,

$$E(z, t) = \frac{1}{4} \sum_{n=-\infty}^{z/R} \tilde{b}_n J_n(\Delta\omega t) \beta_{z/R-n} \sum_l \psi_l(z=0) + \frac{1}{4} \sum_{n=z/R}^{\infty} b_n J_n(\Delta\omega t) \beta_{n-z/R} \sum_l \psi_l(z=0), \quad (2.59)$$

where

$$\tilde{b}_n = \begin{cases} 2b_0, & n = 0 \\ b_n, & n \neq 0. \end{cases} \quad (2.60)$$

Note that this equates the magnitudes of the \tilde{b} 's, as a consequence of the original definition, Eq. (2.58).

As functions of t , the first term on the right-hand side of Eq. (2.59) represents a backward propagating pulse and the second term gives the forward-propagating pulse. One way to see this is by using the fact that for small t , $J_n(t) \sim t^n$, so that as we increase n , $J_n(t)$ “rises from zero” at larger t . As z increases (and consequently so does the integer, z/R), a larger n is required to maintain the same argument of β in the second term of Eq. (2.59). Through its corresponding Bessel function, this term will contribute significantly at larger t than a term involving a smaller n . Physically, this describes a point on the envelope reaching greater values of z at later t , i.e., a forward-propagating pulse. A similar argument shows that the first term in Eq. (2.59), with the modified coefficients \tilde{b}_n , describes a backward-propagating pulse.

A pulse envelope, as a function of t , is therefore described by a contiguous set of Bessel functions: the field at z is written as a superposition of an appropriately translated set of these functions $\{J_{z/R}(t), J_{z/R+1}(t), \dots\}$, multiplied by the coefficients $\{\beta_0, \beta_1, \dots\}$. Distortion accumulates with distance as a consequence of the changing inter-relations between neighboring Bessel functions, e.g., the difference between the set $\{J_0(t), J_1(t), \dots, J_p(t)\}$ and the set $\{J_5(t), J_6(t), \dots, J_{5+p}(t)\}$ for a given $\{\beta_0, \beta_1, \dots\}$. Note that the Bessel functions are replaced by sinusoids in the limit of a linear dispersion relationship in place of Eq. (2.8): these basis functions maintain the same relationships between neighbors irrespective of the origin of the set, which is why distortionless propagation may be achieved in this limit.

One additional simplification is illuminatory and may also considerably speed up numerical computations. The normalizations in the identity [145]

$$n \int_0^\infty \frac{dx}{x} J_n(bx) = 1, \quad (2.61)$$

may be used in the definition of β_n in Eq. (2.56). For slowly varying envelopes $E(z = 0, t')$, the asymptotic limit of the Bessel function is a cosine that, when multiplied by a slowly varying function and integrated over several periods, averages out to zero. We replace $n/t' J_n(\Delta\omega t')$ with $\delta(t' - n/\Delta\omega)$ so that

$$\beta_n = i^{-n} E(z = 0, n/\Delta\omega), \quad n \geq 1, \quad (2.62)$$

i.e., the β 's represent temporal samples of the input pulse envelope along the $\Delta\omega t$ axis. The infinite summations in Eq. (2.59) may thereby be restricted to a finite number, based on the temporal extent of the pulse, without significant loss of accuracy.

Further details may be found in [95, 87].

This analytical formulation allows waveguides to be designed to achieve desired propagation characteristics. In a waveguide of a given length, the inter-resonator spacing, which determines the parameters in Eq. (2.8), may be chosen to limit the distortion, and achieve a certain (effective) group velocity of propagation. Even though the dispersion relationship is non-polynomial and nonlinear, this analysis yields a closed-form result for arbitrary input pulse shapes, and to all orders of dispersion.

Waveguides constructed in electro-optically tunable material will allow the waveguide modes to be altered in realtime, through $\psi(\mathbf{r})$ in Eq. (2.3), and consequently, the eigenmode overlap integrals that appear in Eq. (2.8). Similar effects may be achieved in MEMS waveguides constructed out of a patterned membrane with piezoelectric actuators that cause a mechanical deformation; in this case, the physical geometry of the resonators is altered rather than the refractive index difference between the resonators and their surroundings. This leads to the development of microscale tunable all-optical delay lines and signal processing devices, such as interleavers and multiplexers.

Chapter 3

Two-pulse nonlinear interactions

...the powerful unified approach of coupled mode theory makes the earlier analyses almost obsolete, and ... provides a straightforward logical approach to the understanding of the phenomena and to the design of structures. In exchange for the fascination and adventure of the historical approach to a new art, it provides the beauty and unity of a natural logical mathematical approach.

—C.C. Cutler, preface to W.H. Louisell, *Coupled Mode and Parametric Electronics*, John Wiley & Sons (1960).

Among the most interesting applications of the framework of linear propagation of pulses in the tight-binding method is a description of the basic nonlinear phenomena in CROWs, such as second harmonic generation. Once we have a successful description of the “free” propagation of a CW field (a waveguide mode) or of a pulse (a superposition of waveguide modes), it’s appropriate to attempt a description of the effects of a nonlinear polarization generated in the waveguide, e.g., describing the generation of a second harmonic field in a nonlinear CROW in the CW regime [150] or using pulses [93]. The formalism presented here, based on [93], is central to the description of more complicated nonlinear phenomena, and is most generally described as a coupled mode formalism of the time-dependent waveguide field distributions as derived in Chapter 2. As in the previous chapter, we’ll consider the uniaxial propagation of pulses—along the z axis, to be specific. We do not discuss here any particular features in the transverse geometry of the waveguide. As in the previous chapter, we’ll restrict our discussion to modes of a particular parity.

There are certain general aspects of this investigation [93] that are important in the discussion of *any* pulsed nonlinear phenomenon in the tight-binding analysis of CROWs. A nonlinear polarization generated in the waveguide drives the evolution of

the amplitude (envelope) of the waveguide mode, typically under the slowly-varying envelope approximation (SVEA, which we maintain) [152]. The CW waveguide modes which comprise a pulse [92] may each be assumed to be multiplied by an envelope function, which complicates the analysis somewhat compared to the CW case. Furthermore, an analysis of CW second harmonic generation in CROWs [150] that is not prohibitively complicated relies on isolating the envelope of the waveguide mode from the remainder of the field; the latter can be shown to follow the Bloch theorem [156]. Can such an approach be applied to the analysis of pulse propagation in the presence of a nonlinear polarization? We'll show that it can, although it requires a Bloch function that depends both on spatial and temporal coordinates, in contrast with the usual approach of a spatial Bloch function [94].

The efficiency of (unsaturated) second harmonic generation in a CROW with CW waves is enhanced relative to that in bulk crystals by the inverse ratio of the group velocities at the second harmonic frequency in the two waveguides [150], which can approach 10^3 or 10^4 for weakly coupled CROWs [156]. It's known that the efficiency of second harmonic generation is enhanced at the band-edge of photonic crystals, for exactly similar reasons of a reduction in the group velocity. Second harmonic generation in a CROW combines this advantage with the enhancement of the optical field found, e.g., in defect cavities in photonic crystals [143, 108]. A numerical simulation of second harmonic generation with pulses in related structures is presented in [120] and shows many features that are predicted by our analytical formulation for this general class of structures.

The equations describing second harmonic generation in a CROW using pulses rather than CW waves are formulated, allowing for a spatial and temporal variation in the description of the rapidly varying part of the waveguide field distributions and their envelopes.

3.1 Description of a pulse with an envelope in a CROW

A pulse is written as a superposition of waveguide modes, Eq. (2.32), with their respective time evolution propagators,

$$\mathcal{E}(z, t) = \sum_{\text{allowed } k\text{'s}} [\text{coefficients}]_k e^{i\omega(k)t} \phi_k(z), \quad (3.1)$$

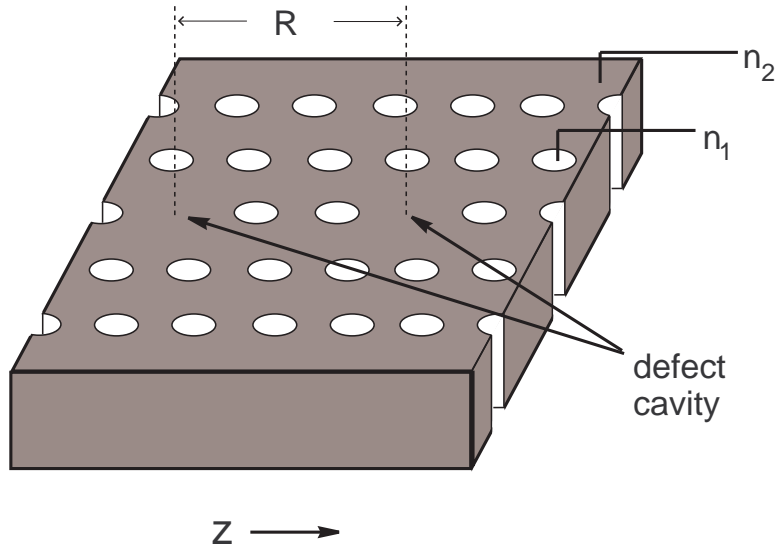


Figure 3.1: Schematic of an infinitely long 1-D CROW with periodicity R consisting of defect cavities embedded in a 2-D photonic crystal.

where the summation reflects the Born—von Karman boundary conditions in a structure of finite length L , so that $\Delta k = 2\pi/L$ as discussed in [92]. Since we take $L \gg R$, we may replace the summation by an integral, either by accounting for the “density of states”, i.e., of allowed k -vectors, or by the impulse train arguments employed in Chapter 2. Then, we may write

$$\mathcal{E}(z, t) = \int \frac{dk}{2\pi} b_k e^{i\omega(k)t} \phi_k(z), \quad (3.2)$$

where the b_k 's are appropriately normalized.

We'll account for the change in power carried by the modes due to a driving polarization by including a z -dependency in the coefficients b_{k_0+K} . These coefficients will account for not only the effect of the driving polarization, but also the initial superposition of k 's that comprise the pulse at the $z = 0$ edge of the waveguide. It's convenient to separate these two components of $b_{k_0+K}(z)$, and we write $b_{k_0+K}(z) \rightarrow c_{k_0+K} \tilde{A}_k(z)$, where c_{k_0+K} is independent of z and $\tilde{A}_k(z=0) = 1$. The field thus described may be written as

$$\hat{\mathcal{E}}(z, t) = e^{i\omega_0 t} \int \frac{dK}{2\pi} c_{k_0+K} \tilde{A}_{k_0+K}(z) e^{iv_g t K} \phi_{k_0+K}(z). \quad (3.3)$$

As in Eq. (2.17), the coefficients c_{k_0+K} arise from a specified pulse shape at the $z = 0$ edge of the waveguide and centered at the optical frequency ω_0 ,

$$\hat{\mathcal{E}}(z = 0, t) = e^{i\omega_0 t} E(z = 0, t), \quad (3.4)$$

so that from the equality of Eq. (3.3) evaluated at $z = 0$ and Eq. (3.4), it follows that

$$c_{k_0+K} = \frac{1}{\phi_{k_0+K}(0)} \int d(|v_g|t') E(z = 0, t') e^{-iv_g t' K}. \quad (3.5)$$

Combining Eq. (3.5) with Eq. (3.3), we may write

$$\hat{\mathcal{E}}(z, t) = e^{i\omega_0 t} \int d(|v_g|t') E(z = 0, t') \int \frac{dK}{2\pi} \frac{\phi_{k_0+K}(z)}{\phi_{k_0+K}(0)} \tilde{A}_{k_0+K}(z) e^{iv_g(t-t')K}. \quad (3.6)$$

Eq. (3.6) may be simplified, based on the properties of a CROW. As represented by Eq. (2.21), to leading order, $1/\phi(0) \approx 1$, and using the explicit form for $\phi_k(z)$ in Eq. (2.3),

$$\begin{aligned} \hat{\mathcal{E}}(z, t) = & e^{i\omega_0 t} \sum_n e^{-ik_0 n R} \sum_l \psi_l(z - nR) \int d(|v_g|t') E(z = 0, t') \\ & \times \int \frac{dK}{2\pi} \tilde{A}_{k_0+K}(z) e^{iTK}, \end{aligned} \quad (3.7)$$

where $T \equiv v_g(t - nR/v_g - t')$. Using the following notation for the Fourier transform relationship,

$$\int \frac{dK}{2\pi} \tilde{A}_{k_0+K}(z) e^{iTK} = A_T(z) \equiv A(z; T), \quad (3.8)$$

we can rewrite Eq. (3.7) as

$$\begin{aligned} \hat{\mathcal{E}}(z, t) = & e^{i\omega_0 t} \sum_n e^{-ik_0 n R} \sum_l \psi_l(z - nR) \left[\right. \\ & \left. \int d(|v_g|t') E(z = 0, t') A\left(z; v_g \left[t - \frac{nR}{v_g} \right] - v_g t'\right) \right]. \end{aligned} \quad (3.9)$$

3.2 Representation in the Bloch form

We see that the dispersion relationship, Eq. (2.14), dictates a temporal dependency of the envelope A ; however, if A were independent of K , then such would not be the case. (As an aside, this shows that an assumption in Eq. (3.3) of an envelope of the form $\tilde{A}_k(z, t)$ would lead to overspecification.) The CROW dispersion relationship, Eq. (2.14), doesn't include group-velocity dispersion or higher-order dispersion terms, and in many problems, the polarization term driving the evolution of the field may be assumed to be constant over the relatively narrow range of propagation constants $k_0 \pm K$ that comprise the pulse in the center of the waveguide band. In such cases, we would not expect a change in the temporal description of the envelope of the pulse, since pulse envelopes of any shape (within certain parametric ranges related to the sampling theorems (see Section 2.4) can propagate undistorted. It would seem reasonable, therefore, to assume that the envelope A is indeed independent of the propagation constant.

We can state these arguments and their consequences in the mathematical framework of the previous section, assuming that the envelope is separable, $A(z, t) = \alpha(z)\zeta(t)$. Then, we may write

$$\begin{aligned} \hat{\mathcal{E}}(z, t) &= \alpha(z) e^{i\omega_0 t} \sum_n e^{-ik_0 nR} \sum_l \psi_l(z - nR) \left\{ \int d\tau E(z = 0, \tau/v_g) \right. \\ &\quad \left. \times \zeta \left[v_g \left(t - \frac{nR}{v_g} \right) - \tau \right] \right\}, \end{aligned} \quad (3.10)$$

or, in a more convenient form,

$$\hat{\mathcal{E}}(z, t) = \alpha(z) e^{i(\omega_0 t - k_0 z)} u_{k_0}(z, t), \quad (3.11)$$

where we define

$$u_{k_0}(z, t) \equiv \sum_n e^{ik_0(z - nR)} \sum_l \psi_l(z - nR) \int d\tau E(z = 0, \tau/v_g) \zeta \left[v_g \left(t - \frac{nR}{v_g} \right) - \tau \right]. \quad (3.12)$$

Since the structure is infinitely long, the summation over n in Eq. (3.12) may be translated as desired. We see that $u_{k_0}(z + R, t + R/v) = u_{k_0}(z, t)$, and therefore $\exp[i(\omega_0 t - k_0 z)]u_{k_0}(z, t)$ is of the Bloch form (in spatial and temporal coordinates),

i.e., a plane wave multiplying a function with an inherent periodicity reflecting that of a lattice structure [9]. Consequently, $\hat{\mathcal{E}}(z, t)$ may be viewed as an amplitude $\alpha(z)$ modulating a Bloch wavefunction, $u_{k_0}(z, t)$. This observation leads to a powerful and general way to analyze nonlinear phenomena with pulses in CROWs [93], similar to the analysis of cw phenomena [150].

Note that the spatial periodicity of the Bloch wavefunction is exactly that of the CROW structure. The temporal periodicity is the time taken by the pulse envelope to travel the distance defining the spatial periodicity. This is similar to the invariance in the reference frame $t - z/v_g$ of the field envelope in weakly dispersive fibers and semiconductor waveguides.

Further, since we've assumed $\tilde{A}_k(0) = 1$, we may use Eq. (3.8) and the consequent observation $\alpha(z = 0) = 1$ to write

$$\zeta(T) = \int \frac{dK}{2\pi} e^{iTK} = \delta(T), \quad (3.13)$$

using the Dirac delta function. Therefore, the convolution integral in Eq. (3.12) can be evaluated, and

$$u_{k_0}(z, t) = \sum_n e^{ik_0(z-nR)} \sum_l \psi_l(z - nR) E \left(z = 0, t - \frac{nR}{v_g} \right). \quad (3.14)$$

An extension of Eq. (3.14) to three spatial dimensions (with pulse propagation along the z axis) is straightforward, since the only vectorial functions are the modes of the individual resonators, $\boldsymbol{\psi}_l(\mathbf{r})$. We'll also generalize the notation from ω_0 to ω , since the description is equally valid at any carrier optical frequency, and from k_0 to $k(\omega)$, as the dispersion relationship dictates the propagation constant corresponding to ω . (We'll sometimes write k_ω in place of $k(\omega)$ so that the mathematical structure of certain equations is not obscured.) In place of Eq. (3.14), we write

$$\mathbf{u}_{k(\omega)}(\mathbf{r}, t) = \sum_n e^{ik_\omega(z-nR)} \sum_l \boldsymbol{\psi}_l(\mathbf{r} - nR\mathbf{e}_z) E \left(z = 0, t - \frac{nR}{v_g} \right). \quad (3.15)$$

We can write the polarization in terms of this representation of the field describing a pulse—an envelope modulating a spatio-temporal Bloch wavefunction—and thereby obtain an evolution equation for the envelope.

In characterizing the effects on pulse propagation of a polarization in a coupled resonator optical waveguide (CROW), we've introduced a slowly varying envelope for each of the waveguide modes comprising the pulse. We've shown that the *Ansatz* of the envelope is strongly dictated by the geometry of the waveguide. Under relatively mild assumptions, the field distribution describing the pulse can be written as the product of a spatial envelope function (which may in subsequent analyses be assumed to be slowly varying if desired) and a wavefunction of the Bloch form, i.e., a plane wave multiplying a periodic function. The periodicity of the Bloch function depends both on spatial and temporal coordinates.

3.3 Second harmonic generation: formulation

The standard approach to second harmonic generation (SHG) in bulk crystals accounts for the generation of the envelope of the second harmonic field as a consequence of the nonlinear polarization in the medium using a formalism commonly known as coupled-wave theory [126, 154]. The definition of the eigenmodes is from the linear tight-binding equations, i.e., we don't consider second harmonic generation of intrinsically nonlinear pulse shapes such as solitons in this analysis. In bulk crystals, the eigenmodes are usually of a simple form— $\exp[i(\omega t - kz)]$ —and the resultant equations for both CW waves and slowly varying envelope pulses are derived in [126, Chap. 6–7]. In a CROW, the eigenmodes are more complicated as in Eq. (2.32), but we've seen that the analysis may be carried out on similar lines.

Based on the discussion in Section 3.2, we assume the following ansatz for the second harmonic field distribution

$$\mathbf{E}_2(\mathbf{r}, t) = E_2(z) e^{i2\omega t} e^{-ik_2\omega z} \mathbf{u}_{k(2\omega)}(\mathbf{r}, t), \quad (3.16)$$

so that the equation analogous to Eq. (2.40) is

$$\begin{aligned}
v_2 \left[\frac{4\omega}{c^2} - i \frac{2}{c^2} \int d^4r \epsilon(\mathbf{r}) [\mathbf{u}_{k(2\omega)}]^* \cdot \frac{\partial \mathbf{u}_{k(2\omega)}}{\partial t} \right] \\
= \int d^4r [\mathbf{u}_{k(2\omega)}]^* \cdot \left[-2k_{2\omega} \mathbf{e}_z \times [\mathbf{e}_z \mathbf{u}_{k(2\omega)}] \right. \\
\left. - i \mathbf{e}_z \times [\nabla \times \mathbf{u}_{k(2\omega)}] - i \nabla \times [\mathbf{e}_z \times \mathbf{u}_{k(2\omega)}] \right], \quad (3.17)
\end{aligned}$$

where $v_2 \equiv d(2\omega)/dk$.

The nonlinear polarization $\mathbf{P}_{\text{NL}}(\mathbf{r}, t)$ generates the second harmonic field $\mathbf{E}_2(\mathbf{r}, t)$ according to [154, 126, 57]

$$\nabla \times [\nabla \times \mathbf{E}_2] + \frac{\epsilon(\mathbf{r})}{c^2} \frac{\partial^2 \mathbf{E}_2}{\partial t^2} = -\frac{1}{c^2} \frac{\partial^2}{\partial t^2} \mathbf{P}_{\text{NL}}(\mathbf{r}, t). \quad (3.18)$$

In Eq. (3.16), the exponential evolution factors and the Bloch wave function are all explicitly dependent on spatial and temporal coordinates. Consequently, the algebra is somewhat complicated and a table of vector identities is useful in simplifying the component terms on the left-hand side of Eq. (3.18). We use the slowly varying approximation [154, 126] to neglect the second-order derivatives of the envelope,

$$\left| \frac{d^2 E_2}{dz^2} \right| \ll k_{2\omega} \left| \frac{dE_2}{dz} \right|, \quad k_{2\omega}^2 |E_2|. \quad (3.19)$$

The spatial derivatives can be written as

$$\begin{aligned}
\nabla \times [\nabla \times \mathbf{E}_2] = e^{i2\omega t} e^{-ik(2\omega)z} \left[i \frac{\partial E_2}{\partial z} \left\{ -2k_{2\omega} \mathbf{e}_z \times [\mathbf{e}_z \times \mathbf{u}_{k(2\omega)}] \right. \right. \\
\left. \left. - i \mathbf{e}_z \times [\nabla \times \mathbf{u}_{k(2\omega)}] - i \nabla \times [\mathbf{e}_z \times \mathbf{u}_{k(2\omega)}] \right\} \right. \\
+ E_2 \left\{ -k_{2\omega}^2 \mathbf{e}_z \times [\mathbf{e}_z \times \mathbf{u}_{k(2\omega)}] + \nabla \times [\nabla \times \mathbf{u}_{k(2\omega)}] \right. \\
\left. \left. - ik_{2\omega} [\mathbf{e}_z \times [\nabla \times \mathbf{u}_{k(2\omega)}] - i \nabla \times [\mathbf{e}_z \times \mathbf{u}_{k(2\omega)}]] \right\} \right], \quad (3.20)
\end{aligned}$$

and the temporal derivatives can be written as

$$\frac{\partial^2 \mathbf{E}_2}{\partial t^2} = e^{i2\omega t} e^{-iK(2\omega)z} \left\{ E_2 \left[\frac{\partial^2 \mathbf{u}_{k(2\omega)}}{\partial t^2} + i2(2\omega) \frac{\partial \mathbf{u}_{k(2\omega)}}{\partial t} - (2\omega)^2 \mathbf{u}_{k(2\omega)} \right] \right\}. \quad (3.21)$$

We use Eq. (3.20) and Eq. (3.21) in Eq. (3.18) and use the eigenvalue equation for $\mathbf{u}_{k(2\omega)}$ [analogous to Eq. (2.38)] to cancel certain terms. The result can be written as

$$\begin{aligned} i \frac{dE_2}{dz} & \left[-2K_{2\omega} \mathbf{e}_z \times [\mathbf{e}_z \times \mathbf{u}_{k(2\omega)}] - i \mathbf{e}_z \times [\nabla \times \mathbf{u}_{k(2\omega)}] - i \nabla \times [\mathbf{e}_z \times \mathbf{u}_{k(2\omega)}] \right] \\ & = e^{iK(2\omega)z} e^{-i2\omega t} \left[-\frac{1}{c^2} \right] \frac{\partial^2}{\partial t^2} \mathbf{P}_{\text{NL}}(\mathbf{r}, t). \end{aligned} \quad (3.22)$$

Next, we form the inner product of both sides of Eq. (3.22) with $\mathbf{u}_{k(2\omega)}^*$ and integrate over t and \mathbf{r} as in Eq. (2.36). Using Eq. (2.40) at the second harmonic frequency, the left-hand side of Eq. (3.22), which we write as \mathcal{L} , becomes

$$\mathcal{L} = i \frac{dE_2}{dz} v_2 \left[\frac{4\omega}{c^2} - i \frac{2}{c^2} \int d^4r \epsilon(\mathbf{r}) [\mathbf{u}_{k(2\omega)}]^* \cdot \frac{\partial \mathbf{u}_{k(2\omega)}}{\partial t} \right]. \quad (3.23)$$

We simplify the right-hand side of Eq. (3.22) using Eq. (D.8) if we may assume an undepleted fundamental, or using Eq. (D.9) otherwise. The differences between the two cases are mostly notational and we'll consider the former first. With the following definitions,

$$\begin{aligned} \Delta k_n & \equiv k_1(\omega) + k_2(\omega) - k(2\omega) + n \frac{2\pi}{R}, \\ \mathbf{p}(\mathbf{r}, t) & \equiv \mathbf{u}_{k_1(\omega)}(\mathbf{r}, t - z/v_1) \mathbf{u}_{k_2(\omega)}(\mathbf{r}, t - z/v_1) \end{aligned} \quad (3.24)$$

forming the abovementioned inner product of the right-hand side of Eq. (3.22), which we write as \mathcal{R} , yields

$$\mathcal{R} = -\frac{1}{c^2} E_1^2 \int d^4r e^{-i\Delta k_n z} e^{in \frac{2\pi}{R} z} [\mathbf{u}_{k(2\omega)}(\mathbf{r}, t)]^* \cdot \tilde{d}(\mathbf{r}) \left[\frac{\partial^2 \mathbf{p}}{\partial t^2} + 2i(2\omega) \frac{\partial \mathbf{p}}{\partial t} + (i2\omega)^2 \mathbf{p} \right]. \quad (3.25)$$

From Eqs. (3.23) and (3.25), it's clear that E_2 will remain small unless there exists an integer n such that Δk_n is very small. Then, $\exp(-i\Delta k_n z)$ is essentially constant

over one unit cell and can be pulled out of the integral. Therefore,

$$\mathcal{R} = \frac{4\omega^2}{c^2} E_1^2 e^{-i\Delta k_n z} \left[D_n^{(0)} - i\frac{1}{\omega} D_n^{(1)} - \frac{1}{4\omega^2} D_n^{(2)} \right], \quad (3.26)$$

where

$$D_n^{(0)} \equiv \int d^4 r e^{in\frac{2\pi}{R}z} [\mathbf{u}_{k_2(2\omega)}(\mathbf{r}, t)]^* \cdot \tilde{d}(\mathbf{r}) \mathbf{u}_{k_1(\omega)}(\mathbf{r}, t - z/v_1) \mathbf{u}_{k_2(\omega)}(\mathbf{r}, t - z/v_1), \quad (3.27)$$

$$D_n^{(1)} \equiv \int d^4 r e^{in\frac{2\pi}{R}z} [\mathbf{u}_{k_2(2\omega)}(\mathbf{r}, t)]^* \cdot \tilde{d}(\mathbf{r}) \frac{\partial}{\partial t} [\mathbf{u}_{k_1(\omega)}(\mathbf{r}, t - z/v_1) \mathbf{u}_{k_2(\omega)}(\mathbf{r}, t - z/v_1)], \quad (3.28)$$

$$D_n^{(2)} \equiv \int d^4 r e^{in\frac{2\pi}{R}z} [\mathbf{u}_{k_2(2\omega)}(\mathbf{r}, t)]^* \cdot \tilde{d}(\mathbf{r}) \frac{\partial^2}{\partial t^2} [\mathbf{u}_{k_1(\omega)}(\mathbf{r}, t - z/v_1) \mathbf{u}_{k_2(\omega)}(\mathbf{r}, t - z/v_1)]. \quad (3.29)$$

As discussed in Appendix D, we can extend the above analysis to allow for variations in the envelope of the fundamental, $\mathbf{E}_1(\mathbf{r}, t)$. We drop the factor of E_1^2 in Eq. (3.26) and instead define

$$\mathbf{p}(\mathbf{r}, t) \equiv E_1(z)^2 \mathbf{u}_{k_1(\omega)}(\mathbf{r}, t - z/v_1) \mathbf{u}_{k_2(\omega)}(\mathbf{r}, t - z/v_1). \quad (3.30)$$

We write down the equation that describes the evolution of the envelope of the second harmonic mode at the frequency 2ω in its complete form for convenient reference in subsequent analyses,

$$\begin{aligned} \frac{dE_2}{dz} = & \left[i\frac{4\omega}{c^2} + \frac{2}{c^2} \int d^4 r \epsilon(\mathbf{r}) [\mathbf{u}_{k(2\omega)}(\mathbf{r}, t)]^* \cdot \frac{\partial}{\partial t} \mathbf{u}_{k(2\omega)}(\mathbf{r}, t) \right]^{-1} \frac{4\omega^2}{v_2 c^2} \\ & \times e^{-i[k_1(\omega) + k_2(\omega) - k(2\omega) + n\frac{2\pi}{R}]z} \left\{ \int d^4 r e^{in\frac{2\pi}{R}z} [\mathbf{u}_{k_2(2\omega)}(\mathbf{r}, t)]^* \cdot \tilde{d}(\mathbf{r}) \right. \\ & E_1(z)^2 \left[\mathbf{u}_{k_1(\omega)}(\mathbf{r}, t - z/v_1) \mathbf{u}_{k_2(\omega)}(\mathbf{r}, t - z/v_1) - \frac{i}{\omega} \int d^4 r e^{in\frac{2\pi}{R}z} [\mathbf{u}_{k_2(2\omega)}(\mathbf{r}, t)]^* \cdot \right. \\ & \tilde{d}(\mathbf{r}) \frac{\partial}{\partial t} [\mathbf{u}_{k_1(\omega)}(\mathbf{r}, t - z/v_1) \mathbf{u}_{k_2(\omega)}(\mathbf{r}, t - z/v_1)] - \frac{1}{4\omega^2} \int d^4 r e^{in\frac{2\pi}{R}z} \\ & \left. \left. [\mathbf{u}_{k_2(2\omega)}(\mathbf{r}, t)]^* \cdot \tilde{d}(\mathbf{r}) \frac{\partial^2}{\partial t^2} [\mathbf{u}_{k_1(\omega)}(\mathbf{r}, t - z/v_1) \mathbf{u}_{k_2(\omega)}(\mathbf{r}, t - z/v_1)] \right] \right\}. \end{aligned} \quad (3.31)$$

3.4 Solutions to the SHG equations

A closed form solution of Eq. (3.31) under general conditions is not known. In this section, we'll discuss certain simplifications which can lead to simple closed form solutions that highlight the physics behind their formulation. These solutions demonstrate a correspondence with known results in the theory of second-harmonic generation with CW waves [150].

As expected, dropping the time dependence and setting all time derivatives to zero in Eq. (3.31) yields the equation for second harmonic generation with CW fields. This is an ordinary differential equation for $E_2(z)$ and can be solved quite easily with the assumption of an undepleted constant envelope fundamental. Cumulative growth of the second harmonic field amplitude requires the phase matching condition,

$$k(2\omega) = k_1(\omega) + k_2(\omega) + n \frac{2\pi}{R} \quad (3.32)$$

$$n = 0, \pm 1, \pm 2, \dots$$

which explicitly involves the Bloch wave 'vector' $n 2\pi/R$.

Analytical time-dependent solutions may also be obtained under certain approximations. We'll continue to assume that E_1 is constant (undepleted constant fundamental) and introduce the parameter $p \equiv 1/(i 2\omega)$. Using Eqs. (3.27)–(3.29), we can write Eq. (3.31) as

$$v_2 \frac{dE_2}{dz} = - \frac{E_1^2}{2p v_2} \left[1 + p \int d^4r \epsilon(\mathbf{r}) [\mathbf{u}_{k(2\omega)}]^* \cdot \frac{\partial}{\partial t} \mathbf{u}_{k(2\omega)} \right]^{-1} \quad (3.33)$$

$$\times e^{-i\Delta k_n z} [D_n^{(0)} + 2p D_n^{(1)} + p^2 D_n^{(2)}].$$

For reasonably well-behaved picosecond pulses at the second harmonic [see Eq. (2.35)], we may assume

$$\left| p \int d^4r \epsilon(\mathbf{r}) [\mathbf{u}_{k(2\omega)}]^* \cdot \frac{\partial}{\partial t} \mathbf{u}_{k(2\omega)} \right| \ll 1. \quad (3.34)$$

To see this, we refer to Eq. (2.35) and consider a Gaussian pulse at a second harmonic frequency of 532 nm in a CROW, $\mathcal{E}_2(z=0, t) = \exp(-t^2/\tau^2)$, where the pulse width τ is 1 ps. Then, the left-hand side of Eq. (3.34) can be written as

$$\frac{1.8 \times 10^{-15} \text{ s}}{(1 \times 10^{-12})^2 \text{ s}^2} \int \frac{dt}{T} 2t \int d\mathbf{r} \epsilon(\mathbf{r}) [\mathbf{u}_{k(2\omega)}]^* \cdot \mathbf{u}_{k(2\omega)} \leq \frac{1.8 \times 10^{-15} \text{ s}}{(1 \times 10^{-12})^2 \text{ s}^2} 2T \quad (3.35)$$

since the range of t integration in Eq. (2.36) is over a time scale T . For picosecond pulses, T is on the order of picoseconds, and therefore, the above number is on the order of 10^{-2} or smaller.

The dominant contribution to second harmonic generation then follows the equation

$$\frac{dE_2^{(0)}}{dz} = -\frac{E_1^2}{2pv_2} e^{-i\Delta k_n z} \left[D_n^{(0)} + 2p D_n^{(1)} + p^2 D_n^{(2)} \right]. \quad (3.36)$$

Eq. (3.36) can be integrated to yield

$$E_2^{(0)}(z) \Big|_0^z = -i \frac{E_1^2 \omega}{2v_2} \left[D_n^{(0)} + 2p D_n^{(1)} + p^2 D_n^{(2)} \right] \left[\frac{1}{-i\Delta k_n/2} e^{-i\Delta k_n z} \right] \Big|_0^z. \quad (3.37)$$

If we assume the usual boundary condition $E_2^{(0)}(z=0) = 0$, the envelope of the second harmonic field distribution is

$$E_2^{(0)}(z) = -i \left[\frac{\sin[\Delta k_n z/2]}{\Delta k_n z/2} \right] e^{-i\Delta k_n z/2} z E_1^2 \frac{\omega}{v_2} \left[D_n^{(0)} - i \frac{1}{\omega} D_n^{(1)} - \frac{1}{4\omega^2} D_n^{(2)} \right]. \quad (3.38)$$

The phase-matching sinc function in Eq. (3.38) is exactly analogous to the results of CW second harmonic generation in bulk crystals, but with the definition of Δk_n following Eq. (3.32). The condition $\Delta k_n = 0$ (for some n) is known as quasi-phase matching [154, pp. 319–322] and reflects the important role of the waveguide geometry on the efficiency of nonlinear processes.

Eq. (3.38) also shows that at the phase-matched condition, the intensity of the second harmonic $|E_2|^2$ grows quadratically with distance z , the intensity of the fundamental $|E_1|^2$ and, in regions where it's a constant, the nonlinearity coefficient \tilde{d} ; these are features in common with the analysis of second harmonic generation in bulk media [126]. As expected for an undepleted fundamental and linear propagation, the boundary input propagates unchanged in shape, but delayed in time by z/v_2 where z is the length of the region under consideration and v_2 is the group velocity of a pulse at the second harmonic wavelength.

The linear growth of $E_2^{(0)}$ with z can't persist indefinitely; saturation may be accounted for by explicitly including the loss coefficient in the expression $\exp(-\Gamma_{2\omega} + i2\omega t)$ in place of $\exp(i2\omega t)$ in Eq. (3.16). It may be seen that Eq. (3.38) is valid in the regime $z \ll v_2/\Gamma_{2\omega}$ [150].

In this regime, we can compute the efficiency of second-harmonic generation by

comparing the intensity at the second harmonic obtained from Eq. (3.38) to the power flux of the fundamental. The electromagnetic energy density for the fundamental as written in Eq. (D.2) is $|E_1|^2 \epsilon(\mathbf{r}) \mathbf{u}_{k(\omega)}^* \cdot \mathbf{u}_{k(\omega)}$. The group velocity v_1 (the velocity of energy flow) is intuitively defined as the ratio of the average power flow P_ω to the time-averaged energy stored per unit length, so that

$$P_\omega = v_1 \int d^4r \epsilon[\mathbf{u}_{k(\omega)}]^* \cdot \mathbf{u}_{k(\omega)} = \frac{v_1}{R} |E_1|^2. \quad (3.39)$$

Using Eq. (3.38), and assuming that the process is phase-matched and $E_2(z=0, t)$ is negligible,

$$P_{2\omega}(z) = \frac{v_2}{R} \left| E_1^2 \frac{1}{v_1 v_2} \omega R P_\omega z \left[D_n^{(0)} - i \frac{1}{\omega} D_n^{(1)} - \frac{1}{4\omega^2} D_n^{(2)} \right] \right|^2. \quad (3.40)$$

From Eqs. (3.39) and (3.40), the second harmonic generation efficiency at $z = L$ is

$$\eta(L) = \frac{P_{2\omega}}{P_\omega} = \frac{1}{v_1^2 v_2} \omega^2 R P_\omega L^2 \left| D_n^{(0)} - i \frac{1}{\omega} D_n^{(1)} - \frac{1}{4\omega^2} D_n^{(2)} \right|^2. \quad (3.41)$$

The factors of $1/v_1^2$ and $1/v_2$ show that the efficiency of second harmonic generation is greatly increased by slowing down the propagation of pulses in the waveguide.

The equations describing sum-frequency generation in photonic crystal waveguides with time-independent envelopes have been formulated by Sakoda *et al.* and solved using a Green's function [119, 118]. There are similarities between their analysis and those in [150], and with the time-independent limit of this formulation. The expression derived by Sakoda *et al.* for an "effective nonlinear susceptibility" in Eq. (19) of [119] is similar to Eq. (3.27) and their final result Eq. (24) of [119] is similar to Eq. (3.38). In particular, the enhancement of the field intensity by a factor $1/v^2$ as in Eq. (3.41) and the conservation of crystal momentum $\Delta k_n(z) = 0$ are similar. We point out that in contrast with Appendix A of [119], plane waves are not eigenfunctions of a CROW and evaluation of the integrals in a Green's function approach to the problem may not be possible.

A numerical study of pulsed second harmonic generation in certain one-dimensional periodic structures (dielectric stacks) was presented by Scalora *et al.* [120]. The principle difference in their structure from a CROW lies in location of the dispersion

curve in the band diagram: in the structure of Scalora *et al.*, pulses are tuned to the band edge, whereas in the case of the CROW, the defect cavity modes lie within the bandgap, and pulse propagation results from the weak overlap of the spatial distributions of these eigenmodes [150].

Although the physics behind the observations is different, there are several common phenomena such as a large reduction in the group velocity of pulse propagation (when tuned to the appropriate part of the spectrum) and increased intensity inside the waveguide relative to free space. The plots of the ‘pump field eigenmode distribution’ as numerically obtained by Scalora *et al.* [120, Fig. 4] from numerical simulations also correspond closely to our theoretical formulation. This is a direct consequence of the similarities in the geometrical structure of deep-grating photonic bandgap structures [32] and a one-dimensional CROW.

Scalora *et al.* show that in the context of the slowly varying envelope approximation as used here, the assumption of an undepleted fundamental is valid (i.e., negligible absorption is observed) and in this regime, the efficiency of second harmonic is increased by orders of magnitude as predicted in Eq. (3.41). For certain aspects of the problem, numerical simulations offer insight not yet available from a theoretical investigation. As we have mentioned in Appendix C, the problem of coupling a pulse into or out of such a structure cannot be described as a Hermitian eigenvalue problem. Scalora *et al.* demonstrate via simulations the importance of the pulse width in coupling into such a structure—pulses with a spectral width larger than that of the transmission resonance at the band-edge experience little field intensity enhancement. It’s not clear at present if the bandwidth limitations that arise from the discrete geometry of a CROW [92] are related to this phenomena.

The propagation and generation of a pulse as a consequence of a nonlinear (second harmonic) polarization induced in a CROW is studied. We’ve derived an approximate but analytical expression for the efficiency of unsaturated second harmonic generation and have also shown how the characteristics of the second harmonic pulse envelope in a CROW has certain features in common with the well-known results in the generation of second harmonic via CW waves in bulk crystals.

Chapter 4

Holography and four-pulse mixing

*If one were running across the room in fast sixteenth notes
and wanted to reduce them to eighths or quarters,
something would have to happen between the first and second of the slower notes ...
or on the momentum generated by the fast notes, one would go flying through the wall ...*

—Ralph Kirkpatrick, *Interpreting Bach's Well-Tempered Clavier*, Yale (1984).

The interference pattern of two co-incident pulses in a nonlinear CROW creates an index grating that may cause power transfer from one waveform to another—this is known as two-beam coupling. Phenomena such as four-wave mixing and holography involve a third waveform which is Bragg-scattered from this grating, resulting in the generation of a fourth field that is related to the waveforms of the other fields. This relationship is governed by energy and wavevector conservation, and by the material properties of the medium.

The analysis of four-wave mixing is exactly analogous to that of holography, except for the time coordinates—we'll use the terminology interchangeably. We've obtained the spatial Fourier transform (in K -space) of $\mathcal{E}(z, t)$ in Eq. (2.30). We will use the symbols t' and t to denote the temporal coordinates at the time of writing the hologram and at the time of reconstruction, respectively. In general, $t = t' - T$ for some time interval T . (As before, we'll ignore the multiplicity of l values, assuming that only a single mode from each of the individual resonators contributes to the waveguide mode under consideration.) A typical geometry involves a grating written by two counterpropagating pulses. We assume that two pulses $\mathcal{E}_1(z = 0, t')$ and $\mathcal{E}_2(z = L, t')$ are input at the two opposite ends of a CROW. The pulses propagate in opposite directions with wavevectors k_1 and $-k_2$ and group velocities v_1 and v_2 , respectively. The total field $\mathcal{E}(z, t)$ is given by the sum of the fields due to these two

pulses, and in K -space, can be written as

$$\begin{aligned} \tilde{\mathcal{E}}(K, t') = & \\ & e^{i\omega_1 t'} \sum_n e^{-i(k_1+K)nR} \tilde{\psi}(K) E_1 \left(z = 0, t' - \frac{nR}{v_1} \right) \\ & + e^{i\omega_2 t'} \sum_m e^{-i(-k_2+K)mR} \tilde{\psi}(K) E_2 \left(z = L, t' - \frac{mR}{v_2} \right) \end{aligned} \quad (4.1)$$

analogous to the K -space representation of a single pulse.

The interference pattern of the spectral components of this field (for example, considering the component at K_1 from the forward-propagating pulse and the component at K_2 of the backward-propagating pulse) is weighted by a complex coupling coefficient $\delta n(K_1, K_2)$ which depends on the material properties, the orientation of the medium and the polarization of the waves [154, 123]. Therefore, we may write the grating as

$$\begin{aligned} \delta n(z, t') = & \frac{1}{F_0} e^{i(\omega_1 - \omega_2)t'} \sum_{n,m} \int \frac{dK_1}{2\pi} \frac{dK_2}{2\pi} e^{-i(K_1 - K_2)z} e^{-i(k_1 + K_1)nR} e^{-i(-k_2 + K_2)mR} \\ & \times \delta \hat{n}(K_1, K_2) E_1 \left(z = 0, t' - \frac{nR}{v_1} \right) E_2^* \left(z = L, t' - \frac{mR}{v_1} \right) \\ & \times \tilde{\psi}(K_1) \tilde{\psi}^*(K_2) + \text{c.c.}, \end{aligned} \quad (4.2)$$

where F_0 is the total optical power.

We assume that this grating persists for a certain amount of time, so that at a later time t , $\delta n(z, t) = \delta n(z, t')$ and we can relabel the temporal coordinate t' to t in Eq. (4.2) to describe the reconstruction process. We will only focus on the term in Eq. (4.2) written out in full, with the remark that analogous results hold for the complex conjugate term (written in Eq. (4.2) as c.c.)¹

We then use a backward-propagating reference pulse $\mathcal{E}_r(z, t)$ to illuminate the grating, and preserve its distinction from the reference pulse at the time of grating formation $\mathcal{E}_2(z, t)$ to maintain the generality of this discussion. At a later stage, we'll assume that these two pulses are in fact identical, and simplify the expressions

¹This term will ultimately give rise to a field propagating in the direction opposite to that of \mathcal{E}_1 , and is not of interest in this discussion.

appropriately. We can write $\mathcal{E}_r(z, t)$ in the Fourier domain using Eq. (2.30),

$$\tilde{\mathcal{E}}_r(K_r, t) = \int \frac{dK_r}{2\pi} e^{i\omega_r t} \sum_p e^{-i(-k_r + K_r)pR} \tilde{\psi}(K_r) E_r \left(z = L, t - \frac{pR}{v_r} \right). \quad (4.3)$$

Upon illumination by $\mathcal{E}_r(z, t)$, the polarization driving the propagation equation [154] for the reconstructed field $\mathcal{E}_c(z, t)$ is given in the instantaneous response approximation by

$$\mathcal{P}_c(z, t) = \delta n(z, t) \mathcal{E}_r(z, t). \quad (4.4)$$

The evolution of the reconstructed field $\mathcal{E}_c(z, t)$ will follow that of the original signal field $\mathcal{E}_1(z, t)$ if this polarization Eq. (4.4) can be shown to be proportional to $\mathcal{E}_1(z, t)$. The multiplicative constant in this relationship includes the third-order susceptibility $\chi^{(3)}$ rather than the linear susceptibility $\chi^{(1)}$ since the grating $\delta n(z, t)$ given by Eq. (4.2) is proportional to the product of two optical fields [154].

We can multiply both sides of Eq. (4.4) by $\exp(-iK_c z)$ and integrate over z to write Eq. (4.4) in Fourier-transformed K -space. In doing so, we use Eqs. (4.2) and (4.3) which describe the grating and the reference pulse, to obtain

$$\begin{aligned} \tilde{\mathcal{P}}_c(K_c, t) &= \frac{1}{F_0} e^{i(\omega_1 - \omega_2 + \omega_r)t} \sum_{n,m,p} \int \frac{dK_1}{2\pi} \frac{dK_2}{2\pi} \frac{dK_r}{2\pi} \delta \hat{n}(K_1, K_2) \left\{ \int dz e^{i(K_1 - K_2 + K_r - K_c)z} \right\} \\ &\times e^{-i(k_1 + K_1)nR} e^{-i(-k_r + K_r)pR} e^{i(-k_2 + K_2)mR} \tilde{\psi}(K_1) \tilde{\psi}(K_r) \tilde{\psi}^*(K_2) \\ &\times E_1 \left(z = 0, t - \frac{nR}{v_1} \right) E_r \left(z = L, t - \frac{pR}{v_r} \right) E_2^* \left(z = L, t - \frac{mR}{v_2} \right). \end{aligned} \quad (4.5)$$

The phase-matching integral over z can be approximated by $2\pi \delta(K_1 - K_c) \delta(K_2 - K_r)$ and we can carry out the integrals over K_2 and K_1 . We write $K_r \equiv K'$ and $K_c \equiv K$ to generalize the notation. In order to focus the discussion on holographic reconstruction of the signal pulse, we now assume that $E_r(z = L, t) = E_2(z = L, t')|_{t'=t}$, $k_r = k_2$, $\omega_r = \omega_2$ and $v_r = v_2$, i.e., we use a replica of the reference write-in pulse \mathcal{E}_2 (in the original temporal coordinate t') as the reference reconstruction pulse.

Then, Eq. (4.5) becomes

$$\begin{aligned} \tilde{\mathcal{P}}_c(K_c, t) = & e^{i\omega_1 t} \sum_n e^{-i(k_1+K_1)nR} \tilde{\psi}(K_1) E_1 \left(z = 0, t - \frac{nR}{v_1} \right) \left[\frac{1}{2\pi F_0} \int \frac{dK'}{2\pi} \right. \\ & \delta\hat{n}(K, K') \sum_{m,p} e^{-i(-k_2+K')pR} e^{i(-k_2+K')mR} \tilde{\psi}(K') \tilde{\psi}^*(K') \\ & \left. \times E_2 \left(z = L, t - \frac{pR}{v_2} \right) E_2^* \left(z = L, t - \frac{mR}{v_2} \right) \right]. \end{aligned} \quad (4.6)$$

The term in square brackets in Eq. (4.6) can be written as

$$[\dots] = \frac{1}{2\pi F_0} \int \frac{dK'}{2\pi} \delta\hat{n}(K, K') G(K', t) G^*(K', t), \quad (4.7)$$

where

$$G(K', t) = \sum_p e^{-i(-k_2+K')pR} \tilde{\psi}(K') E_2 \left(z = L, t - \frac{pR}{v_2} \right). \quad (4.8)$$

Clearly, we can multiply $G(K', t)$ by $\exp(i\omega_2 t)$ without changing Eq. (4.7).

Then, using the relationship established in Eq. (2.30),

$$\tilde{\mathcal{P}}_c(K, t) = \tilde{\mathcal{E}}_1(K, t) \times h(K, t), \quad (4.9)$$

where

$$h(K, t) = \frac{1}{2\pi F_0} \int \frac{dK'}{2\pi} \delta\hat{n}(K, K') |\tilde{\mathcal{E}}_2(K', t)|^2. \quad (4.10)$$

We assume that the photorefractive properties of the CROW characterized by $\delta\hat{n}$ are spectrally nonselective, i.e.,

$$\delta\hat{n}(K, K') \equiv \delta\hat{n} \delta(K - K') \quad \text{for all } K \text{ and } K'. \quad (4.11)$$

Further, we assume that the (backward-propagating) reference pulses are narrow, so that a fair mathematical approximation to the input free-space reference pulse $\mathcal{E}_2(z = L, t)$ is

$$\mathcal{E}_2(z = L, t) = e^{i\omega_2 t} E_0 \delta(t - t_0). \quad (4.12)$$

The corresponding field in the CROW is given by Eq. (2.30),

$$\tilde{\mathcal{E}}_2(K', t) = E_0 e^{i\omega_2 t} \sum_m e^{i(-k_2 + K')mR} \tilde{\psi}(K') \delta\left(t - t_0 - \frac{mR}{v_2}\right). \quad (4.13)$$

Next, if the individual resonator modes are highly localized, $\psi(z) = \hat{\psi} \delta(z - z_0)$, we can write

$$\begin{aligned} \tilde{\mathcal{E}}_2(K', t) \tilde{\mathcal{E}}_2^*(K', t) &= |E_0|^2 |\hat{\psi}|^2 \sum_{m, m'} e^{-i(-k_2 + K')(m - m')R} \\ &\times \left[\delta\left(t - t_0 - \frac{mR}{v_2}\right) \delta\left(t - t_0 - \frac{m'R}{v_2}\right) \right]. \end{aligned} \quad (4.14)$$

In order that power transfer over a significant time interval is cumulative, as given by integrating the above expression over a region of t comparable to or greater than R/v_2 , the term in square brackets in Eq. (4.14) can be replaced by the Kronecker delta $\delta_{mm'}$, and the result is

$$\tilde{\mathcal{E}}_2(K', t) \tilde{\mathcal{E}}_2^*(K', t) = |E_0|^2 |\hat{\psi}|^2 M, \quad (4.15)$$

where M is the number of resonators.

Using the normalization relationship $M \int dz |\psi(z)|^2 = 1$, we can simplify Eq. (4.10),

$$h(K, t) = \frac{1}{(2\pi)^2 F_0} \delta \hat{n} |E_0|^2, \quad (4.16)$$

which is a constant $\equiv \hat{h}$, and therefore,

$$\tilde{\mathcal{P}}_c(K, t) = \hat{h} \tilde{\mathcal{E}}_1(K, t). \quad (4.17)$$

This shows that the polarization term driving the evolution of the reconstructed pulse is indeed proportional to the input signal pulse, as it would be for the input signal pulse itself. Note that the scaling constant is dependent on the intensity of the reference pulse, but for weak signal pulses, the total field intensity is dominated by the reference and $F_0 \approx |E_0|^2$ so that the two factors cancel each other.

Photorefractive holography of single pulses has been difficult because of the low efficiency of the process, and usually, multiple write-in procedures of thousands of repeated pulses are necessary to obtain a sufficiently strong quasi-steady state grating. In a CROW, the highly concentrated optical field can also enhance this aspect of the

photorefractive effect. The propagating power flux P in a CROW is proportional to the group velocity of the CROW band [156],

$$P = \frac{1}{8\pi R} v_g E_0^2, \quad (4.18)$$

and therefore, we can obtain a higher optical field for a given power flux because of the reduction in group velocity. Consequently, the time constant which determines the photorefractive response time (and which varies linearly with the intensity [154]) is reduced by a factor $v_g \approx 10^{-3}$ compared to the group velocity in a medium with spatially uniform dielectric properties and refractive index n_2 . The quasi-steady state equilibrium is reached with orders of magnitude lower intensities in a photorefractive CROW as compared to a photorefractive bulk medium. As was pointed out by Yeh [158], the fundamental limit on the speed of the photorefractive effect depends on the intensity rather than phenomenological parameters induced by doping or heat treatment.

We have analyzed optical pulse propagation in a coupled-resonator optical waveguide (CROW), and propose a new method for the storage and reconstruction of optical pulses using photorefractive holography in a CROW. The advantages of this method include a substantial reduction in the group velocity leading to spatial compression of the signal pulse so that it may be contained in a relatively short waveguide compared to the spatial extent of the pulse in free space. The highly localized field distribution enhances the photorefractive effect, and we have examined in detail the process of the formation of the grating and the reconstruction of the signal pulse by holography. There are many possible applications of such room-temperature, compact, nondestructive and low-intensity pulse storage mechanisms; two important ones are buffers for optical switches and correlators for optical measurement devices.

4.1 Applications: Nonlinear Delay Lines

In a 2-D periodic medium, such as a 2-D photonic crystal ‘slab,’ there are two main types of waveguides: line defect waveguides, where a row of holes is filled in

to create a guiding channel [78, 61], and via the coupling of resonator eigenmodes of adjacent points defects which have been introduced in the desired geometry, e.g., the CROW. Although the physics behind waveguiding is quite different in these two cases, they share the same spectrum of linear and nonlinear optics applications, e.g., guide light around sharp bends, highly selective spectral filtering, slowing down the group velocity of light, efficient second harmonic generation, low-threshold lasing, etc. In addition to these applications, which attempt to improve on existing methods of carrying out the same functions in different geometries, these waveguides may realize the proposals for new types of optical devices, with new functionalities in optical communications. In particular, these structures offer the first practical possibility to realize the proposal of ‘nonlinear optical delay lines’ (NLDDL’s) [106], a class of all-optical information processing devices at the mesoscopic and microscopic scale.

NLDDL’s operate on the principle of the nonlinear interactions giving rise to power transfer between several temporally encoded optical fields within a nonlinear medium. Many of the important applications can be realized in two-wave or four-wave mixing coupling processes, which we have investigated in the earlier sections. Photorefractive index gratings are an effective way to realize such effects with moderate intensity levels, as would be necessary in practical applications. There are many applications of NLDDL’s in all-optical signal processing, including temporal multiplication, correlation, and convolution, envelope time reversal, and space-to-time coding [106].

We will focus on photorefractive effects [154], but other grating mechanisms at a variety of different timescales are also of potential interest, including free-carrier index gratings, acousto-optic standing waves, or arrays of nonlinear waveguides written by spatial solitons. Such effects have been predicted to be particularly prominent in coupled-defect waveguides, where the field intensity is highly localized to the individual resonators, and thereby locally enhancing the conversion to second-harmonic [150], or reducing the build-up time of photorefractive gratings [91]. The effect of the spatial localization of the field in such waveguides is related to the sampling theorems in communications, and doesn’t invalidate the use of these waveguides if they’re designed for the appropriate range of waveform parameters (temporal width of the envelope and its spectral bandwidth) [92].

The second important requirement for the practical realization of NLDDL’s is slow group velocity, so that the grating written by the pulse envelopes can be completely contained in the physical extent of the waveguide. In linear defect waveguides in

photonic crystals, this can be achieved near the band edge [34], but at the cost of distortion arising from higher-order dispersion terms in the rapidly varying dispersion relationship in this regime. In coupled-resonator waveguides (whether in photonic crystals or not), slow group velocity can always be achieved more simply as a natural consequence of the weak overlap between individual high-Q resonator modes [150].

While so far, either class of waveguides can be considered as candidates for realizing NLDL's, the fundamental physics of the grating dynamics preferentially indicates the choice of coupled-resonator waveguides. We investigate the nonlinear coupling processes between two pulses, rather than two cw beams, and the propagating envelopes in an infinitely long coupled-resonator waveguides have two length scales: an overall envelope and a faster variation of the field distribution due to the quasi-discrete nature of the physical structure. Temporal waveforms with two time scales incident on a thin sample offer a closely related picture, with the advantage of being able to monitor the dynamics of the grating on the shorter time scale using pump-probe techniques. The material must be able to respond to the variations of the envelope on the time-scale required for use in, e.g., a typical 10 Gbit/s communications system.

Considering at the physical aspects of such an experiment, the chosen material may have a defect state at the wavelengths of interest, which we may or may not want to use depending on the practical application. We have investigated a particular geometry and used a material that permits both approaches, but these results refer to a 'direct' two-photon process without an intermediate stage.

The theoretical formulation follows [26]. We consider the interaction of a two-level system with a pulse, $\mathbf{E}(\mathbf{r}, t) = \hat{\mathbf{e}} E(t) \cos \omega_0 t$, where $\hat{\mathbf{e}}$ describes the state of the polarization, ω_0 is the optical carrier frequency, and $E(t)$ is the envelope. A two-level atom (levels a and b) located at $\mathbf{r} = \mathbf{0}$ interacts with this pulse.

We establish two times, t_1 and t_2 , such that the envelope $E(t)$ of width T is contained in the interval (t_1, t_2) . We'll assume that the turn-on and turn-off time intervals for $E(t)$ are large compared to $1/\omega_0$. We'll also assume that T is large enough for the validity of the S -matrix approach, i.e., longer than the lifetime of level b .

The quantity we're interested in is the S -matrix element

$$S = \lim_{t_1 \rightarrow -\infty, t_2 \rightarrow +\infty} \langle b | e^{iH_0 t_2/\hbar} U(t_2, t_1) e^{-iH_0 t_1/\hbar} | a \rangle \quad (4.19)$$

where U is the evolution operator for the $a \rightarrow b$ transition, and H_0 describes the free evolution of the atom outside (t_1, t_2) and is the atomic Hamiltonian in the absence of an incident field.

Recall that the interaction Hamiltonian for a particle with charge q and mass m in the presence of an external field described by potentials $(\mathbf{A}(\mathbf{r}, t), U(\mathbf{r}, t))$ is [26, p. 267],

$$H^{(I)} = -\frac{q}{m}\mathbf{p} \cdot \mathbf{A}(\mathbf{r}, t) + \frac{q^2}{2m}\mathbf{A}^2(\mathbf{r}, t) + qU(\mathbf{r}, t). \quad (4.20)$$

The last term is absent in this case. We assume that the levels a and b can't be connected via a one-photon transition (we'll see shortly how this was realized experimentally). We keep terms to order q^2 in our calculation.

The second term of Eq. (4.20) doesn't contribute, since it gives a term proportional to $\langle b | a \rangle$. The expansion of the first term of Eq. (4.20) to order q^2 gives

$$S = \left(\frac{q}{\hbar m}\right)^2 \iint d\tau d\tau' \theta(\tau - \tau') e^{i\omega_b\tau} \sum_r \langle b | \mathbf{p} \cdot \mathbf{A}(\mathbf{0}, \tau) | r \rangle \times e^{-i\omega_r(\tau - \tau')} \langle r | \mathbf{p} \cdot \mathbf{A}(\mathbf{0}, \tau') | a \rangle e^{-i\omega_a\tau'}. \quad (4.21)$$

The sum over r labels all possible intermediate levels—in our case, we will focus on one particular value of r .

Dropping the nonresonant terms, and using the identity

$$e^{-i(\omega_{ra} - \omega)(\tau - \tau')} \theta(\tau - \tau') = -\frac{1}{2\pi i} \int_{-\infty}^{\infty} d\Omega \frac{e^{-i\Omega(\tau - \tau')}}{(\Omega - \omega_{ra} + \omega_0) + i\epsilon} \quad (4.22)$$

where $\epsilon \rightarrow 0_+$, we can write

$$S = \left(\frac{q}{\hbar m}\right)^2 \frac{p_{br}p_{ra}}{i} \int_{-\infty}^{\infty} \frac{\tilde{E}(\Omega)\tilde{E}(\omega_{ba} - 2\omega_0 - \Omega)}{4[(\Omega - \omega_{ra} + \omega_0) + i\epsilon]}, \quad (4.23)$$

where $\tilde{E}(\Omega) \equiv 1/\sqrt{2\pi} \int E(t) \exp(i\Omega t) dt$ is the Fourier transform of the envelope.

Since we've assumed that a one-photon transition is not resonant, and $|\omega_0 - \omega_{ra}| \gg$

$1/\theta$ where θ is the width of $\tilde{E}(\Omega)$, we can write

$$\begin{aligned} S &= \frac{1}{i\hbar} \left(\frac{q}{m}\right)^2 \frac{p_{br}p_{ra}}{\hbar(\omega_0 - \omega_{ra})} \int_{-\infty}^{\infty} d\Omega \frac{\tilde{E}(\Omega)\tilde{E}(\omega_{ba} - 2\omega_0 - \Omega)}{4} \\ &= \frac{1}{i\hbar} \left[\left(\frac{q}{m}\right)^2 \frac{p_{br}p_{ra}}{\hbar(\omega_0 - \omega_{ra})} \right] \int_{-\infty}^{\infty} d\tau \left[\frac{E(\tau)}{2} \right]^2 e^{i(\omega_{ba} - 2\omega_0)\tau}. \end{aligned} \quad (4.24)$$

The expression in square brackets outside the integral in Eq. (4.24) defines M , an effective matrix element, so that we can simplify the notation:

$$S = \frac{1}{i\hbar} M \int_{-\infty}^{\infty} d\tau \left[\frac{E(\tau)}{2} \right]^2 e^{i(\omega_{ba} - 2\omega_0)\tau}. \quad (4.25)$$

This is the same expression we would've obtained for a one-photon transition, with the change to $[E(\tau)/2]^2 \exp(-i2\omega_0 t)$ for the field.

The transition amplitude depends on the square of the envelope rather than the correlation at different times (or convolution for counterpropagating fields), since there is no intermediate level for a one-photon process to occur. A classical treatment of the formation of photorefractive gratings, with particular reference to coupled-resonator waveguides, leads to similar conclusions with regard to the temporal dependency [91].

4.2 Picosecond dynamics of photorefractive gratings in GaAs

But, while we can be certain that parasitic parameters do exist, their magnitude is usually not known, and even less do we know their ratios.

—A. A. Andronov, A. A. Witt, and S. E. Khaikin, *Theory of Oscillators*, Dover (1987).

We use 100 ps actively-mode-locked Gaussian pulses within a 270 ns Q-switched envelope from a Nd:YAG laser emitting at 1.06 microns, as shown in Fig. 4.1. As the photodiode had a bandwidth of a few gigahertz, an individual mode-locked pulse cannot be resolved directly, but standard interferometry techniques can be used. The setup is shown in Fig. 4.2. The pump and probe beam average powers were 1.5 W and 15 mW, respectively. In light of Eq. (4.25), instead of the usual sample cut with incident-face normal along $[\bar{1}10]$ in the four-wave mixing geometry, we use a sample with the surface-normal along $[100]$. The grating formed between the two co-polarized pump beams will not transfer energy in the direction of the incident probe.

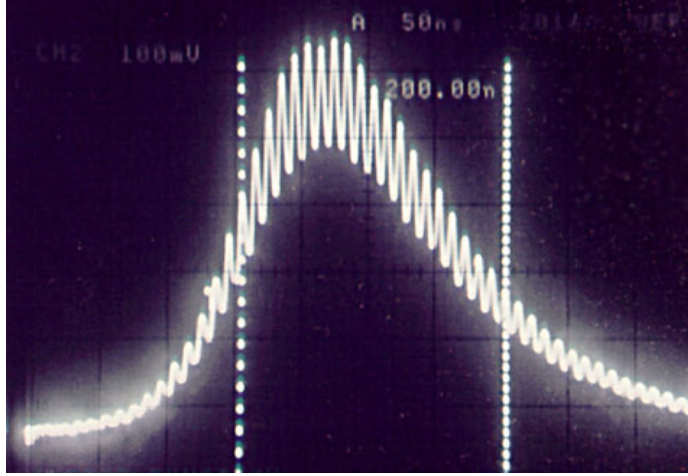


Figure 4.1: Photodiode output of the Q-switched envelope, with cursors (dotted lines) separated by 200 ns, corresponding to 20 mode-locked pulses.

The quantity $\Delta T/T_0$ is defined as the change in the probe transmission in the presence of the pump divided by the probe transmission without the pump, with positive values indicating gain. Experimental and fitted results as a function of the probe delay are shown in Fig. 4.3. We have optimized for the photorefractive effect by rotating the sample about the surface normal for maximum probe gain, and have doubled the yield (without broadening the two-photon response) by using two temporally coincident pump-probe interactions.

The probe gain shows, initially, the signature of a two-photon process, i.e., the peak is well fitted by the theory, Eq. (4.25) with a minimum-squared-deviation width of 98 ps. This agrees with both the nominal width of 100 ps, and the value determined from Michelson interferometry, 95 ± 5 ps. As the delay increases, the efficiency of the interaction between the probe and the pump in the sample is decreased, leading to a fall-off in the response.

At these time scales, we also see the effects of a single-pole response of the material, which results in an exponential tail (for positive time) to be appended to the two-photon process signature. The fitted decay time constant translates to a diffusion length of 5.8 microns, using the mobility of the electrons in semi-insulating GaAs [141].

This results in strong constraints on the waveguide geometry for single-mode waveguiding. These experiments were carried out in bulk semiconductor, so that

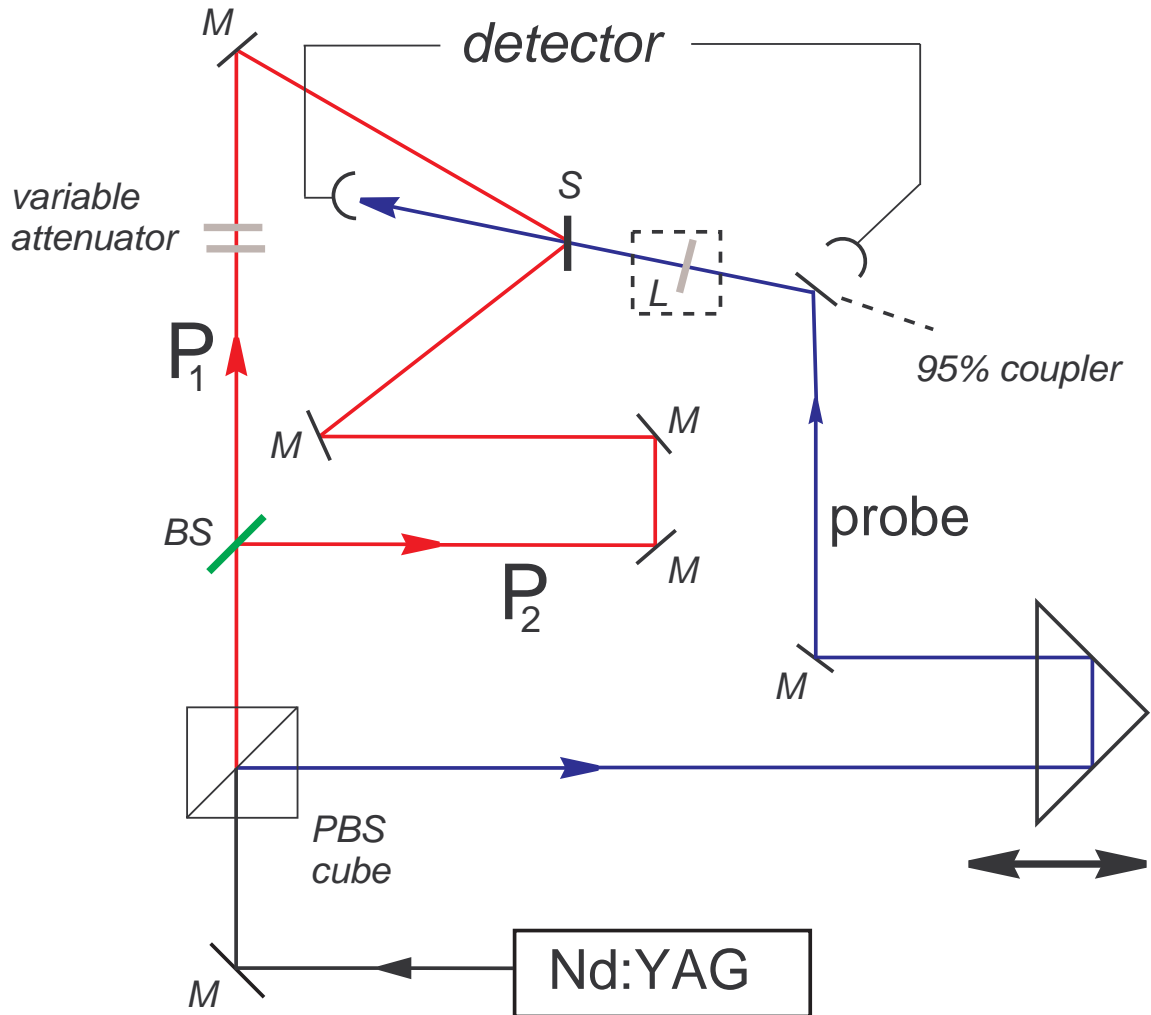


Figure 4.2: Schematic showing the interaction of pump P_1 and P_2 pulses with a probe pulse. The sample is oriented so that two mutually independent and temporally coincident pathways to probe gain are realized. M: mirror, L : $\lambda/2$ waveplate to rotate the state of polarization of the probe, BS: nonpolarizing beam-splitter, PBS: polarizing beam splitter, S: sample.

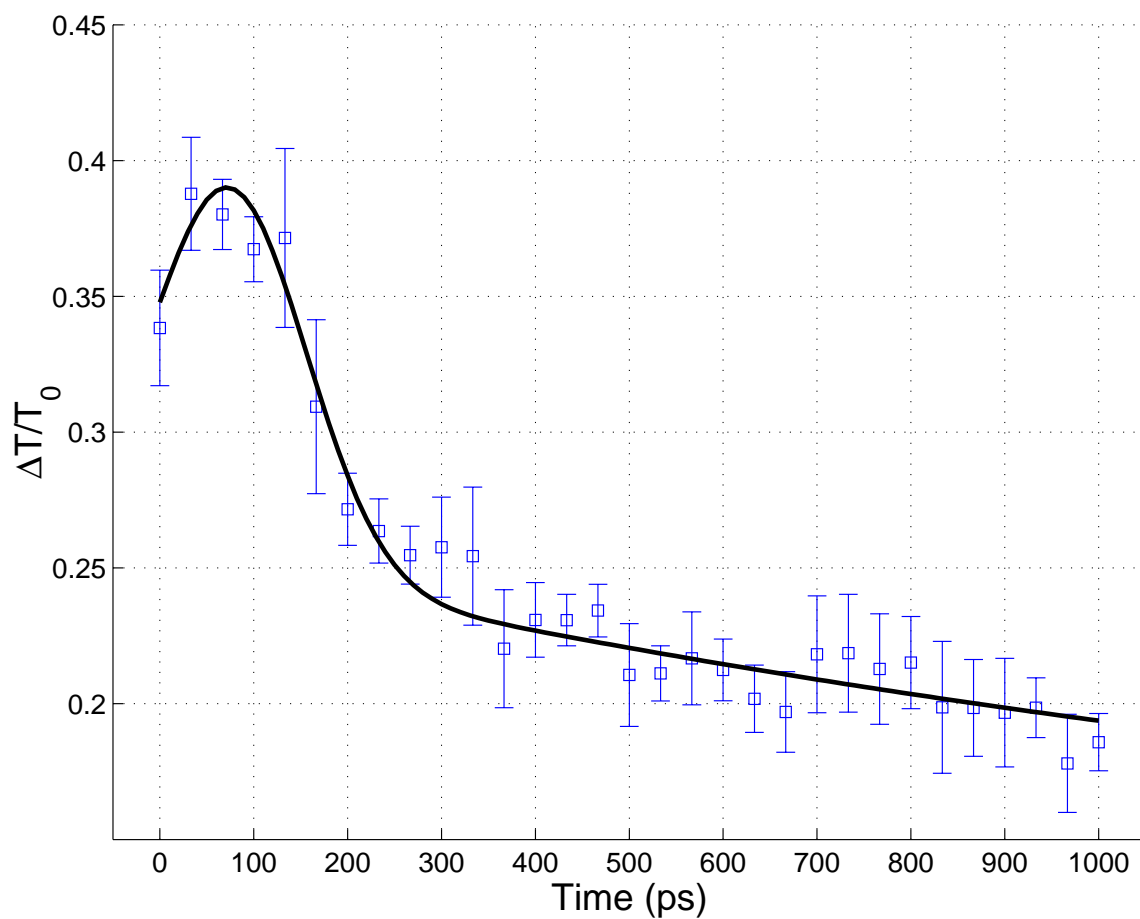


Figure 4.3: The normalized change in transmittance $\Delta T/T_0$ as a function of probe delay over a nanosecond window with an arbitrary origin. The experimental points are fitted by a functional form obtained from the idealized theory convolved with a single-pole response, yielding an exponentially decaying tail.

geometry-induced distortions to the write-read processes can be ignored². The finite width of a waveguide—be it a line-defect waveguide in a photonic crystal slab or a CROW—needs to be large compared to the diffusion length, otherwise the diffusing carriers will be affected by the edges and the hologram will not faithfully reflect the field envelope. A waveguide width of 6 μm is not single-moded at typical communications wavelengths ($\lambda = 1.55 \mu\text{m}$) for typical values of the dielectric constant in semiconductor materials (GaAs, InGaAsP, etc.).

For these applications, a more suitable semiconductor would have a smaller diffusion length, which would require a slower mobility for the electrons. At the same time, we require that the photorefractive grating be established on the time-scales of typical pulse envelopes as in this experiment. Of course, the material should be optically transparent, and photorefractive, at these wavelengths. We don't know of a better choice than the GaAs family at the present time, but their limitations are evident.

In light of these results, it's unlikely that photorefractive holography is a practical approach to realizing all-optical memory elements in CROWs at the bit rates of modern communication systems. The development of materials with faster responses and slower drift velocities may change this assessment. More promising is the approach we'll discuss in the next chapter: we can excite a localized envelope—a super-resonant mode—in the CROW, which decays only with the time constant of the individual resonators. This stationary field distribution, rather than the propagating pulse, can be used to form the hologram as discussed in this chapter: the advantage is that the time constraints on the material response are considerably relaxed.

²Such perturbations can be considered, as in the analysis of noisy communication channels, as distorting filters so that the overall input-to-output response is the convolution of the transfer functions of the undistorted holography and the nonidealities.

Chapter 5

The Kerr effect and super-resonant modes

*Our basic dynamic variables shall be the vielbein and the connection.
These superfields contain a large number of component fields.
Some will be eliminated through covariant constraint
conditions. Others will be gauged away with (14.2).
In this way we shall arrive at a theory with the minimum number of component fields.*
—J. Wess and J. Bagger, *Supersymmetry and Supergravity*, Princeton (1992).

As we've seen in Section 2.6, the dispersion relationship in CROWs is intrinsically non-polynomial, but the propagation of localized excitations, i.e., optical pulses can be characterized non-perturbatively to all orders of dispersion [95]. This is a somewhat surprising result, and it leads to a description of the distortion that results from the nonlinear dispersion relationship. Weighted sums of Bessel functions take the role of cosines in the Fourier-series decomposition of the propagating field [87].

In optical fibers and similar waveguides, the effects of (anomalous) group-velocity dispersion can be exactly balanced by the self-phase modulation induced by the Kerr effect, an intensity-dependent change in the refractive index of the material. This is the basis for the formation of the (fundamental) Schrödinger soliton in optical fibers, for instance. Here, we investigate the Kerr effect in coupled-resonator waveguides, with particular emphasis on determining whether self-phase modulation can compensate for the distortion consequent of the nonlinear dispersion relationship. Such solutions would lead to the existence of envelopes that can exist or propagate without distortion in CROWs as eigensolutions of a nonlinear propagation equation (solitary waves and solitons).

In considering the various choices of basis functions in which to expand the field, we choose the propagating Bloch wave solutions of the CROWs without optical nonlinearities, which were derived using the tight-binding method in Chapter 2. We take

the field to be a superposition of such waves with slowly (time-) varying coefficients. This expansion has the merit that in the absence of nonlinearities, each field in this expansion is an eigenmode.

5.1 Formulation of the nonlinear propagation problem

In our treatment of linear pulse propagation in CROWs, we wrote the field describing a pulse $\mathcal{E}(\mathbf{r}, t)$ as a superposition of waveguide modes $\phi_k(\mathbf{r})$ within the Brillouin zone, and using Eq. (2.8),

$$\begin{aligned}\mathcal{E}(\mathbf{r}, t) &\approx \int \frac{dk}{2\pi} e^{-i\omega_k t} c_k \phi_k(\mathbf{r}) \\ &= e^{-i\omega_0 t} \int_{-\pi/R}^{\pi/R} \frac{dK}{2\pi} e^{-i\Delta\omega t \cos[(k_0+K)R]} c_{k_0+K} \phi_{k_0+K}(\mathbf{r}).\end{aligned}\quad (5.1)$$

Since nonlinear phenomena such as the Kerr effect change the relative weights of the eigenmodes Eq. (2.3) as the waveform evolves with time, it's necessary to introduce a time-dependency in the superposition coefficients c_k appearing in Eq. (5.1). We write

$$\mathcal{E}(\mathbf{r}, t) = e^{-i\omega_0 t} \int_{-\pi/R}^{\pi/R} \frac{dK}{2\pi} \left[e^{-i\Delta\omega t \cos[(k_0+K)R]} c_{k_0+K}(t) \phi_{k_0+K}(\mathbf{r}) \right]. \quad (5.2)$$

We substitute Eq. (5.2) which describes the field in the waveguide in terms of the time-varying coefficients $c_{k_0+K}(t)$ into Maxwell's equations written with an explicit nonlinear polarization term describing the Kerr effect,

$$\nabla \times \nabla \times \mathcal{E}(\mathbf{r}, t) - \mu \epsilon_{\text{wg}}(\mathbf{r}) \frac{\partial^2}{\partial t^2} \mathcal{E}(\mathbf{r}, t) = \mu \frac{\partial^2}{\partial t^2} \mathbf{P}_{\text{NL}}(\mathbf{r}, t) \quad (5.3)$$

where

$$\mathbf{P}_{\text{NL}}(\mathbf{r}, t) = \frac{3}{4} \epsilon_0 \chi^{(3)} |\mathcal{E}(\mathbf{r}, t)|^2 \mathcal{E}(\mathbf{r}, t). \quad (5.4)$$

in the instantaneous response approximation.

In simplifying the terms, we use the normalization [91]

$$M \sum_m \int d\mathbf{r} \epsilon_{\text{wg}}(\mathbf{r}) |\mathbf{E}_{\text{res}}(\mathbf{r} - mR\mathbf{e}_z)|^2 = 1 \quad (5.5)$$

where the CROW waveguide comprises M resonators.

If we assume that $c_{k_0+K}(t)$ varies slowly over time intervals $\sim O(2\pi/\omega_0)$, as is usually the case, then we obtain

$$\begin{aligned} \frac{dc_{k_0+K}(t)}{dt} = i\gamma \int_{-\pi/R}^{\pi/R} \int_{-\pi/R}^{\pi/R} \frac{dK_1}{2\pi} \frac{dK_2}{2\pi} \exp \left[-i\kappa\Omega t \left\{ -\cos[(k_0 + K_1)R] + \cos[(k_0 + K_2)R] \right. \right. \\ \left. \left. + \cos[(k_0 + K_3)R] - \cos[(k_0 + K)R] \right\} \right] c_{k_0+K_1}(t)^* c_{k_0+K_2}(t) c_{k_0+K_3}(t) \end{aligned} \quad (5.6)$$

where $K_1 + K = K_2 + K_3$ and γ is the nonlinearity coefficient in the CROW geometry, defined as

$$\gamma = 2n_0 n_2 \epsilon_0 \omega_0 \int d\mathbf{r} \sum_m |\mathbf{E}_{\text{res}}(\mathbf{r} - mR\mathbf{e}_z)|^4, \quad (5.7)$$

using the relationship $3\chi^{(3)}/8 = n_0 n_2$ [4], and we have ignored the dispersion (variation in ω) of γ .

As an aside, Eq. (5.6) is equivalent to the differential equation

$$i \frac{da_n}{dt} + \frac{\Delta\alpha}{2} \Omega a_n - \frac{\kappa}{2} \Omega (a_{n+1} + a_{n-1}) + \gamma |a_n|^2 a_n = 0, \quad (5.8)$$

obtained by Christodoulides and Efremidis [24] for a related set of coefficients, $a_n(t)$, where

$$\begin{aligned} a_n(t) = \int_{-\pi/R}^{\pi/R} \frac{dK}{2\pi} c_{k_0+K}(t) \exp[in(k_0 + K)R] \\ \times \exp \left[i \left\{ \frac{\Delta\alpha}{2} \Omega - \kappa \Omega \cos[(k_0 + K)R] \right\} t \right]. \end{aligned} \quad (5.9)$$

The notational correspondence from our paper to theirs is $(\Delta\alpha/2)\Omega \mapsto \Delta\omega$ and $-(\kappa/2)\Omega \mapsto c$. The a_n 's are the coefficients that appear in the expansion of the field in terms of individual resonator modes, rather than the waveguide modes. It's easily verified that substituting the plane-wave ansatz, $a_n = \exp\{i[(\Omega - \omega_{k_0+K})t - (k_0 + K)nR]\}$ in Eq. (5.8) with $n_2 = 0$ leads to the dispersion relationship, Eq. (2.8).

Returning our attention to Eq. (5.6), it's useful to separate the amplitude and phase of $c_{k_0+K}(t)$,

$$c_{k_0+K}(t) = A_{k_0+K}(t) \exp[i\phi_{k_0+K}(t)]. \quad (5.10)$$

We'll look for solutions that retain their shape, i.e., $dA/dt = 0$. Substituting Eq. (5.10) into Eq. (5.6) and separating the real and imaginary parts, we obtain a pair of equations,

$$\frac{dA_{k_0+K}}{dt} = -\gamma \iint \frac{dK_1}{2\pi} \frac{dK_2}{2\pi} A_{k_0+K_1} A_{k_0+K_2} A_{k_0+K_3} \sin \Phi, \quad (5.11)$$

$$\frac{d\phi_{k_0+K}}{dt} = \frac{\gamma}{A_{k_0+K}} \iint \frac{dK_1}{2\pi} \frac{dK_2}{2\pi} A_{k_0+K_1} A_{k_0+K_2} A_{k_0+K_3} \cos \Phi, \quad (5.12)$$

where Φ is defined as

$$\begin{aligned} \Phi \equiv & -\{\phi_{k_0+K_1} - \kappa \Omega t \cos[(k_0 + K_1)R]\} + \{\phi_{k_0+K_2} - \kappa \Omega t \cos[(k_0 + K_2)R]\} \\ & + \{\phi_{k_0+K_3} - \kappa \Omega t \cos[(k_0 + K_3)R]\} - \{\phi_{k_0+K} - \kappa \Omega t \cos[(k_0 + K)R]\} \end{aligned} \quad (5.13)$$

Based on Eq. (5.11), the A 's will be independent of t if $\sin \Phi \equiv 0$ for all t . This implies that $\cos \Phi = 1$, and based on Eq. (5.12), we take ϕ_{k_0+K} to be a linear function of t ,

$$\phi_{k_0+K}(t) = a + bt + \kappa \Omega t \cos[(k_0 + K)R], \quad (5.14)$$

where a and b are constants independent of t and K . We drop the constant a which represents a fixed phase that can be absorbed into the initial conditions. Substituting this form for $\phi_{k_0+K}(t)$ into Eq. (5.12), we get

$$b + \kappa \Omega \cos[(k_0 + K)R] = \frac{\gamma}{A_{k_0+K}} \iint_{-\pi/R}^{\pi/R} \frac{dK_1}{2\pi} \frac{dK_2}{2\pi} A_{k_0+K_1} A_{k_0+K_2} A_{k_0+K_3}. \quad (5.15)$$

We'll now discuss a particular regime in which there exist stationary (i.e., non-propagating) solutions of Eq. (5.15). Such solutions utilize the optical Kerr effect to exist stably in a confined section of the waveguide, isolated from the edges of the structure.

5.2 The stationary super-resonant mode

In this section, we investigate in what regime the nonlinear CROW admits solutions of the Schrödinger soliton form, i.e., the hyperbolic secant. The basic physics reflects a balance between the phase modulation effects of the Kerr effect and (anoma-

lous) group-velocity dispersion (GVD). The GVD term in the nonlinear Schrödinger equation appears as the coefficient of a second derivative term, which in the Fourier domain with the Fourier (frequency) variable K , translates to multiplication by $(iK)^2$.

In Eq. (5.15), if we assume that k_0R is a multiple of 2π and $|KR| \ll 1$, then we may write $\cos[(k_0 + K)R] \approx 1 - (KR)^2/2$, which is the desired effective GVD term. Observe from the dispersion relationship, Eq. (2.8), that ω_{k_0+K} is a quadratic function of K only at the edges of the Brillouin zone, where $d\omega_{k_0+K}/dK$ vanishes, i.e., the group velocity is zero. We expect, therefore, that the solutions of Eq. (5.15) in this regime will be *stationary*, describing a localized state that is frozen in its initial ($t = 0$) spatial distribution and does not propagate along the waveguide.

Using this approximation, Eq. (5.15) becomes

$$b + \kappa\Omega = \kappa\Omega \frac{(KR)^2}{2} + \frac{\gamma}{A_{k_0+K}} \int_{-\pi/R}^{\pi/R} \frac{dK_1}{2\pi} \frac{dK_2}{2\pi} A_{k_0+K_1} A_{k_0+K_2} A_{k_0+K_3}. \quad (5.16)$$

We'll assume that the A 's are defined to be zero outside the regions of integration $-\pi/R$ and π/R so that the limits of integration can be taken as $-\infty$ to ∞ . Eq. (5.16) may then be solved [109],

$$A_{k_0+K} = A_{k_0+K}^{(0)} \operatorname{sech}(K/\bar{K}), \quad (5.17)$$

where \bar{K} is a spectral width parameter whose relevance will become clear in the following discussion. Substituting Eq. (5.17) into Eq. (5.16), we get

$$b + \kappa\Omega = \kappa\Omega \frac{(KR)^2}{2} + 2 \left[A_{k_0+K}^{(0)} \right]^2 \frac{\gamma}{(2\pi R)^2} \left[(KR)^2 + \left(\frac{\pi \bar{K} R}{2} \right)^2 \right]. \quad (5.18)$$

If b is to be independent of K , then we need

$$A_{k_0+K}^{(0)} = \sqrt{-(2\pi R)^2 \frac{\kappa\Omega}{4\gamma}}. \quad (5.19)$$

Since the left-hand side represents a real and positive number, we require that κ as defined in Eq. (2.9) be a negative number (as is physically expected from the meaning of ϵ_{wg} and ϵ_{res}). This is equivalent to anomalous dispersion in optical fibers and similar

waveguides.

Using Eq. (5.14) and Eq. (5.19) in Eq. (5.10), we write the final expression for $c_{k_0+K}(t)$,

$$c_{k_0+K}(t) = c_{k_0+K}(0) \exp \left\{ -i\kappa\Omega t \left[1 + \pi^2(\bar{K}R)^2/8 - \cos(KR) \right] \right\}, \quad (5.20)$$

where

$$c_{k_0+K}(0) \equiv 2\pi R \sqrt{-\frac{\kappa\Omega}{4\gamma}} \operatorname{sech}(K/\bar{K}), \quad |KR| \leq \pi. \quad (5.21)$$

The field described by these coefficients is

$$\mathcal{E}(\mathbf{r}, t) = e^{-i\omega_0 t} e^{-i\kappa\Omega t [1 + \pi^2(\bar{K}R)^2/8]} \int_{-\pi/R}^{\pi/R} \frac{dK}{2\pi} c_{k_0+K}(0) \phi_{k_0+K}(\mathbf{r}). \quad (5.22)$$

In light of Eq. (5.21), the integral on the second line of Eq. (5.22) is not expressible in a simpler form. However, if $\bar{K}R \lesssim 1$, the hyperbolic secant function decays rapidly, and the limits of integration may be changed to $(-\infty, \infty)$. The integral then can be evaluated easily—the Fourier transform of a hyperbolic secant is itself a hyperbolic secant function. We derive the approximation,

$$\mathcal{E}(\mathbf{r}, t) \approx e^{-i\omega_0 t} e^{-i\kappa\Omega t [1 + \pi^2(\bar{K}R)^2/8]} \sqrt{-\frac{\kappa\Omega}{4\gamma}} \pi \bar{K}R \sum_n \operatorname{sech}\left(\frac{\pi \bar{K}}{2} nR\right) \mathbf{E}_{\text{res}}(\mathbf{r} - nR\hat{z}). \quad (5.23)$$

The modulus of the amplitude $|\mathcal{E}(z, t = 0)|$ normalized to its maximum value (in this approximation) is plotted in Fig. 5.1. Values of the hyperbolic secant function in Eq. (5.23) at nR (which has the dimensions of length) are the weights of the individual resonator eigenmodes. In this approximation, the envelope of these weights is a hyperbolic secant function whose width is inversely proportional to \bar{K} .

As we had expected from physical arguments, the envelope of $\mathcal{E}(\mathbf{r}, t)$ is a stationary state that is independent of time: its spatial distribution at $t = 0$ is of finite extent and is maintained for all subsequent t . This is consistent with the observation that although the group velocity dispersion coefficient is nonzero, the group velocity itself is zero. We call the stationary state a super-resonant field since it is formed in a waveguide that itself comprises the coupling of individual (stationary) resonator modes. There are two requirements for such a solution: (1) the slowly varying as-

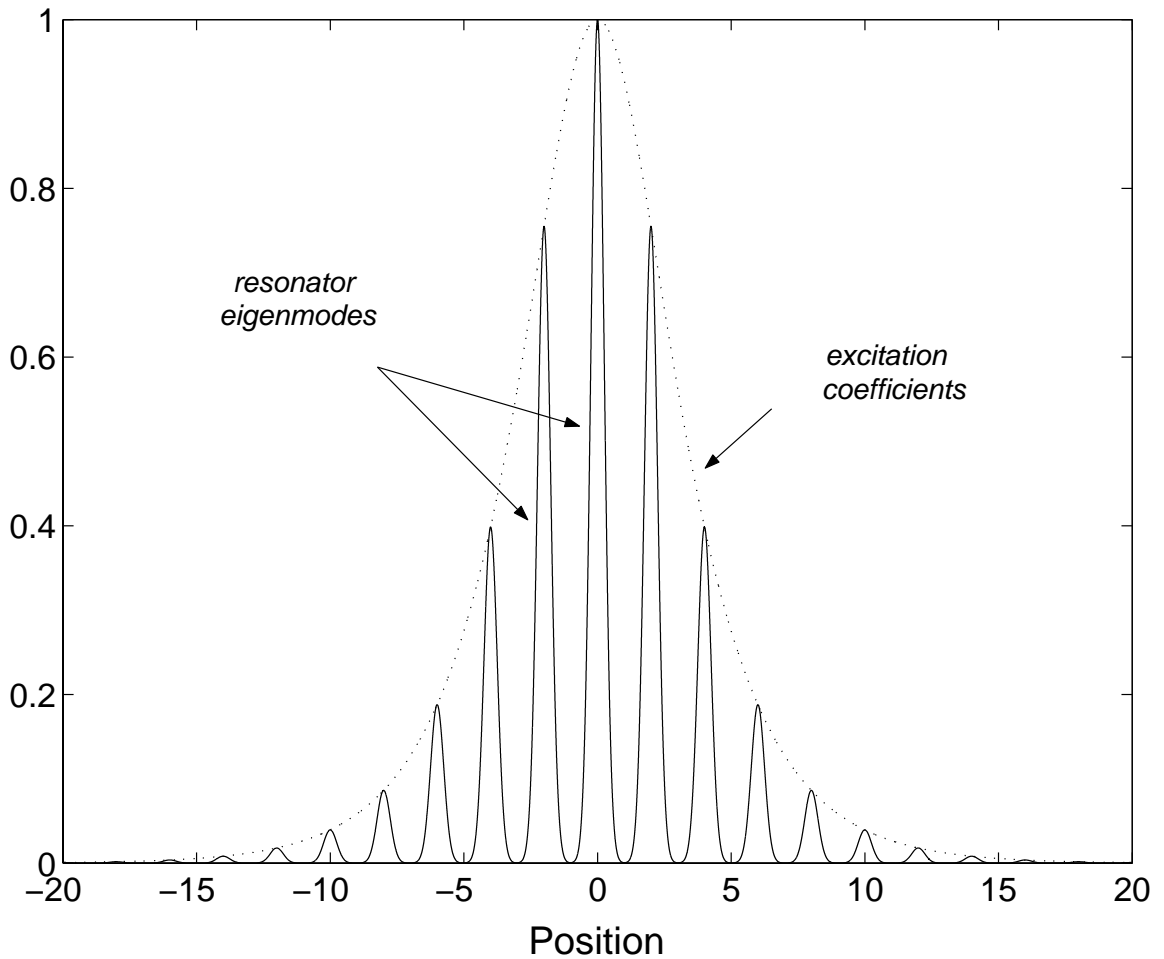


Figure 5.1: An approximate super-resonant field distribution, assuming that the individual resonator eigenmodes are Gaussians. ‘Position’ is normalized to R , the inter-resonator spacing and the ordinate represents $|\mathcal{E}(z, t = 0)|$ normalized to its maximum value. The dotted line is an envelope—a hyperbolic secant—connecting the excitation coefficients multiplying the individual resonator eigenmodes. We have used $\pi\bar{K}/2 = \pi/(4R)$.

sumption, which simplifies Eq. (5.22) to Eq. (5.23) and (2) the *necessary* condition that $k_0 R$ is an integer multiple of 2π .

Using Eq. (5.9), Eq. (5.23) may be rephrased as an expression for the individual-resonator coefficients $a_n(t)$,

$$a_n(z_n) = \left[\sqrt{-\frac{\kappa\Omega}{4\gamma}} \pi \bar{K} R \right] e^{-i\mu t} \operatorname{sech} \left(\frac{\pi \bar{K}}{2} z_n \right), \quad (5.24)$$

where $\mu \equiv \kappa\Omega [1 + \pi^2(\bar{K}R)^2/8]$ is a constant frequency detuning and $z_n \equiv nR$ is a discretization of the spatial axis.

Christodoulides and Efremidis [24] have analyzed this problem using the a_n coefficients, and have derived the expression (in our notation),

$$a_n(z_n, t) = \left[\sqrt{-\frac{\kappa\Omega}{4\gamma}} \pi \bar{K} R \sqrt{\cos q} \right] e^{-i\mu t \cos q} \operatorname{sech} \left[\frac{\pi \bar{K}}{2} (z_n - vt) \right], \quad (5.25)$$

which described an envelope that propagates with the group velocity $v \equiv -\kappa\Omega R \sin q$ defined in terms of an undetermined parameter q in their analysis. The solution Eq. (5.25) for nonzero v is derived from a nonlinear Schrödinger equation, which involves linear dispersion and quadratic terms only. There's no such point on the dispersion relationship, Eq. (2.8) and the validity of this approximation is questionable. In fact, the dispersion relationship is quadratic only at the edges of the Brillouin zone where the group velocity goes to zero. A quadratic dispersion relationship is what is needed to have exact hyperbolic-secant solutions of the nonlinear Schrödinger equation: the presence of higher-order dispersion doesn't lead to this form [4].

We've investigated the effects of the optical Kerr nonlinearity in coupled-resonator optical waveguides (CROWs) with regard to the propagation of optical pulses. In particular, there exists a stationary field distribution of the hyperbolic secant form which balances the effects of group velocity dispersion and the Kerr self-phase modulation. This field distribution remains frozen in space with zero group velocity.

The super-resonant mode in a CROW composed of high-Q resonators can have a long lifetime, since it decays with the time constant associated with the quality factor

of the isolated individual resonators [150] rather than the time constant associated with the coupling between high-Q resonators and external waveguides. In addition, an optical pulse (with nonzero group velocity) traveling down the waveguide can be made to interact with such a static distribution; their interaction can be enhanced using quasi-phase-matching (grating) techniques, [91]. This leads to the possibility of the application of these localized states as memory elements in optical switches, particularly in conjunction with the photorefractive holography processes discussed in Chapter 4.

The general phenomenon of the localization of light is not necessarily a consequence of defects in a uniform photonic crystal. In the presence of optical (electromagnetic) nonlinearities, intrinsic localized modes or discrete breathers can be formed [86]. This has been proven mathematically for using a class of time-periodic, spatially localized solutions to a Hamiltonian coupled-oscillator nonlinear lattice [80]. Discrete breathers have been predicted for 2-D and 3-D photonic crystals with Kerr (cubic) nonlinearity [59], at nonlinear interfaces with quadratic nonlinearity [132] and along dielectric waveguide structures with a nonlinear Kerr-type response [85].

A waveguide that, unlike a CROW, exhibits continuous translational symmetry in the longitudinal z direction, and in the transverse plane, consists of an array of thin quadratically nonlinear layers embedded in a linear slab waveguide, can inhibit light propagation along the transverse x axis under certain conditions [133]. “Two-color” spatially localized nonlinear modes can be formed as a consequence of parametric coupling of the fundamental and second-harmonic fields excited at the nonlinear interfaces. Such modes are related to spatial quadratic solitons that are localized in homogeneous media by two-wave parametric mixing of the fundamental and the second-harmonic waves [64].

A related structure is a one-dimensional grating consisting of $\chi^{(2)}$ material. Forward- and backward-propagating waves of the fundamental frequency and the second-harmonic interact via terms reminiscent of the cubic Kerr effect. This gives rise to localized slowly moving two-color envelopes, on picosecond timescales for fundamental beam intensities of approximately 10 GW/cm^2 in LiNbO_3 [27]. What is especially interesting is that the second-harmonic beam is *locally* generated in the backward direction, but its envelope is locked to the forward-propagating fundamental frequency component—it also travels forward.

The interface between two semi-infinite bulk optical media with inversion symmetry breaks the inversion symmetry, and consequently possesses a nonzero surface

quadratic response. Recent experiments on second-harmonic generation in periodic photonic bandgap structures with embedded nonlinear defect layers have observed enhanced parametric interaction in the vicinity of these defects [138]. This suggests that second-harmonic generation occurs in localized modes, but is suppressed for propagating modes [133].

Chapter 6

Dispersion-managed solitons and breathers

... the variational principle is generally useful in unifying a subject and consolidating a theory rather than in breaking ground for a new advance ... This is not to minimize the importance of finding the Lagrange density L , for ... the form of the variational equations often suggests fruitful analogies and generalizations.

—P. M. Morse and H. Feshbach, *Methods of Theoretical Physics*, McGraw-Hill, 1953.

Nonlinear pulses, such as solitons [44, 51], are intuitively the pulse envelopes of choice in high bit-rate optical communications, since they are solutions to the envelope propagation equation accounting for both the dispersion and the nonlinearity of optical fibers. Some of the principal objections (conceptual and practical) to the proposals of repeaterless long-haul soliton communication systems have been addressed by the introduction and development of dispersion-managed (DM) solitons [128, 134], and it is expected that such systems will be used as the primary means of optical transport beyond 40 Gbit/s per wavelength-division multiplexing (WDM) channel (recent review papers on the theory and experiments of solitons and DM solitons include [43] and [103]).

The slowly varying normalized envelope $u(z, t)$ of an optical pulse in a lossless single-mode fiber with dispersion management in the group-velocity dispersion parameter and third-order dispersion follows the nonlinear Schrödinger equation derived in Eq. (1.27),

$$i \frac{\partial u}{\partial z} + \frac{\sigma(z)}{2} \frac{\partial^2 u}{\partial t^2} + |u|^2 u - i\gamma \frac{\partial^3 u}{\partial t^3} = 0, \quad (6.1)$$

where t is the temporal coordinate in the moving reference frame, and is defined with respect to the laboratory space and time coordinates z and T by the equation $t = T - z/v_g$, where v_g is the group velocity of the pulse. As discussed in Section 1.4, the

parameters σ and γ are functions of the propagation distance z ; in a later section, we will focus on pulse propagation characteristics in a piecewise constant (step-function) dispersion map $\sigma(z) = \sigma_{\pm}$, with $\sigma_+ > 0 > \sigma_-$, and periodicity $\sigma(z) = \sigma(z + z_T)$.

Recent studies on the use of solitons in dispersion-managed optical communications systems have shown that the effect of third-order dispersion, which arises from $d^3\beta/d\omega^3$ where $\beta(\omega)$ is the mode propagation constant at optical frequency ω , may be significant since the average group-velocity dispersion can be much lower than the local group-velocity dispersion.

We derive explicit analytical expressions for the dynamic behavior of soliton-like pulses (breathers) in such a system. Nonperturbative Lagrangian and Hamiltonian formulations have been useful in understanding the physical behavior of propagation in systems characterized by second-order dispersion alone [68]. This work forms a counterpart to the perturbative analysis of Lakoba and Agrawal [72] based on a Hermite-Gaussian expansion of the pulse shape. The analysis presented here should also help understand the physical origins of certain features found in numerical simulations of the effects of third-order dispersion [38]. Since the nonlinear (nonintegrable [71]) partial differential (wave) equation is now of a higher order, it may be useful to show the applicability of a mathematical technique that is easily understood and widely used in a different problem.

We limit our attention to the steady-state (asymptotic) behavior of such pulses, and therefore neglect the effect of continuum radiation on the dispersion-managed breather [72]. A soliton losing energy to linear dispersive waves in the normal dispersion regime “recoils” further into the anomalous regime of the spectrum [6]. This lowers the radiation amplitude, which arises as a consequence of the tail of the soliton spectrum in the normal dispersion regime. It can then be expected that a quasi-stationary state is reached where the radiation rate is so small that the soliton recoil is negligible, and we can ignore further radiation losses. Further, a practical communication system using dispersion management is likely to use optical filters and band-limited amplifiers, which can suppress out-of-band dispersive radiation and frequency shifts due to spectral recoil [140].

Consequently, we are justified in assuming a symmetrical pulse shape. Given that we do not predict the generation of any new harmonics in this approximation, we would not expect any associated frequency shift; indeed this will be shown to be a conserved quantity (as a generalized momentum canonically conjugate to a

cyclic coordinate). It is interesting to note that the perturbative approach used by Lakoba and Agrawal [72] also does not predict any frequency shift for the lossless case considered here.

We quantify our results in terms of a representative hyperbolic secant pulse shape, but the method can be generalized to a number of different (localized) pulse shapes, e.g., Gaussian, triangular, etc. An appropriate Lagrangian is constructed for the nonlinear Schrödinger equation, and the condition of its extremality with respect to our pulse Ansatz forms variational equations of motion for the pulse parameters [7]. Identifying generalized coordinates and their conjugate momenta leads to the Hamiltonian and a phase-plane analysis in terms of the acyclic coordinates. We highlight the modifications brought about by third-order dispersion to the well-known results of second-order dispersion-managed propagation.

6.1 Lagrangian and Hamiltonian formulation

The partial differential equation (6.1) and its conjugate can be reduced to a system of ordinary differential equations using the averaged variational method, first introduced in the context of the evolution of solitons by Anderson [7]. The motivation for this approach is well known and we shall only point out that in the presence of third-order dispersion, the final term in (6.1) modifies the Euler-Lagrange equation,

$$\frac{\delta \mathcal{L}}{\delta u} \equiv \frac{\partial \mathcal{L}}{\partial u} - \frac{\partial}{\partial t} \frac{\partial \mathcal{L}}{\partial(\partial u / \partial t)} - \frac{\partial}{\partial z} \frac{\partial \mathcal{L}}{\partial(\partial u / \partial z)} + \frac{\partial^2}{\partial t^2} \frac{\partial \mathcal{L}}{\partial(\partial^2 u / \partial t^2)} = 0 \quad (6.2)$$

and similarly for u^* in place of u .

It may be easily verified, e.g., by direct substitution, that the following Lagrangian density (assumed to be at least C^1 in u and its derivatives, except possibly on a set of measure zero) satisfies this condition,

$$\mathcal{L}(u, u^*) = i \left(u \frac{\partial u^*}{\partial z} - u^* \frac{\partial u}{\partial z} \right) + \sigma(z) \left| \frac{\partial u}{\partial t} \right|^2 - |u|^4 - i\gamma \left(\frac{\partial^2 u}{\partial t^2} \frac{\partial u^*}{\partial t} - \frac{\partial^2 u^*}{\partial t^2} \frac{\partial u}{\partial t} \right), \quad (6.3)$$

where a piecewise continuous $\sigma(z)$ satisfies the condition in parentheses.

The pulse shape we choose to base our analysis on should be capable of predicting pulse evolution, and therefore, in view of the term in (6.3) that contributes to third-

order dispersion, we have to choose a pulse shape (envelope) somewhat more involved than for second-order dispersion alone [68]. We take

$$u(z, t) = A\sqrt{\eta} \operatorname{sech}[\eta(t - c)] \exp \left[i \left(\Omega(t - c) + \beta(t - c)^2 + \frac{\phi}{2} \right) \right], \quad (6.4)$$

where η , β , Ω , c and ϕ are free parameters that depend on z and represent the amplitude (and width), quadratic chirp, frequency shift from the carrier frequency (or velocity), pulse center in the moving reference frame (or group-velocity variation in laboratory coordinates) and phase, respectively. In the interests of legibility, we will not write out this dependence explicitly. The pulse energy is then evaluated to

$$\int_{-\infty}^{\infty} dt u(z, t)^* \cdot u(z, t) = 2A^2. \quad (6.5)$$

Similar forms of the envelope Ansatz have been used elsewhere [56] for analyzing pulse interactions in second-order dispersion-managed systems, and reflect the fact that the equations under consideration need more degrees of freedom than offered by simpler assumptions.

We now write down the Lagrangian using (6.3) and (6.4). A fair amount of algebra leads to the following expressions for the four terms on the right-hand side of (6.3), where we use the shorthand $\beta' \equiv d\beta/dz$, etc.

$$\begin{aligned} i \left(u \frac{\partial u^*}{\partial z} - u^* \frac{\partial u}{\partial z} \right) &\rightarrow 2 \left[(t - c)^2 \beta' + (t - c)(\Omega' - 2\beta c') + (\phi' - \Omega c') \right] u^* u, \\ \sigma \left| \frac{\partial u}{\partial t} \right|^2 &\rightarrow \sigma \left[4(t - c)^2 \beta^2 + \eta^2 \tanh^2[\eta(t - c)] \right. \\ &\quad \left. + 4(t - c)\beta\Omega + \Omega^2 \right] u^* u, \\ -|u|^4 &\rightarrow -A^2 \eta \operatorname{sech}^2[\eta(t - c)] u^* u, \\ -i\gamma \left(\frac{\partial^2 u}{\partial t^2} \frac{\partial u^*}{\partial t} - \frac{\partial^2 u^*}{\partial t^2} \frac{\partial u}{\partial t} \right) &\rightarrow \gamma \left[16(t - c)^3 \beta^3 + 24(t - c)^2 \beta^2 \Omega + 2\Omega(\eta^2 + \Omega^2) \right. \\ &\quad \left. - 2\beta \left[\eta \tanh[\eta(t - c)] - (t - c)(\eta^2 + 3\Omega^2) \right] \right] u^* u. \end{aligned} \quad (6.6)$$

In each of the above expressions, we can drop those terms that are odd in t as such terms do not contribute when multiplied by $u^* u$ and integrated over t . These

include terms that are proportional to odd powers of $(t - c)$ and those that vary as $\tanh(t - c)$. After some simplification, we can write the Lagrangian as

$$L = A^2 \left\{ \frac{\pi^2}{3\eta^2} \frac{d\beta}{dz} + 4 \left(\frac{d\phi}{dz} - \Omega \frac{dc}{dz} \right) - 4A^2 \frac{\eta}{3} + 2\sigma \left[\Omega^2 + \frac{1}{3} \left(\frac{\pi^2 \beta^2}{\eta^2} + \eta^2 \right) \right] + 4\gamma\Omega \left[\frac{\pi^2 \beta^2}{\eta^2} + \Omega^2 + \eta^2 \right] \right\}. \quad (6.7)$$

with a clearly nontrivial role for γ . The Lagrangian function (6.7) has no explicit z dependence, and so the Hamiltonian is a constant of the motion. This will be the starting point of our discussion in the following section.

We note in passing that it is possible to construct a Lagrangian for pulse shapes other than the hyperbolic secant reminiscent of the Schrödinger soliton, generalizing to any localized Ansatz for which the amplitude and pulse width are related in the same way as above.

We apply the Legendre transformation [121] to the Lagrangian (6.7) to generate the Hamiltonian. We take our canonical coordinates as β and c with conjugate momenta

$$\begin{aligned} p_\beta &= \frac{\partial}{\partial \beta'} L = \frac{\pi^2 A^2}{3\eta^2}, \\ p_c &= \frac{\partial}{\partial c'} L = -4A^2 \Omega \end{aligned} \quad (6.8)$$

and express the Lagrangian in terms of these variables, substituting p_β for η and p_c for Ω ,

$$L = A^2 \left\{ \gamma p_c \left(\frac{p_c^2}{16A^6} + \frac{\pi^2}{3p_\beta} + \frac{3p_\beta \beta^2}{A^4} \right) + \sigma \left(\frac{2\pi^2 A^2}{9p_\beta} + \frac{p_c^2}{8A^4} + \frac{2p_\beta \beta^2}{A^2} \right) - \frac{4\pi A^3}{3\sqrt{3p_\beta}} + 4 \frac{d\phi}{dz} \right\} + p_\beta \beta' + p_c c'. \quad (6.9)$$

(It can be verified after extensive algebra (symbolic manipulation tools such as *Mathematica* are useful) that $\det(\partial^2 L / \partial p_i \partial p_j) \neq 0$.)

The Hamiltonian is

$$\begin{aligned}
H(\beta, c; \eta, \Omega; z) &= p_\beta \beta' + p_c c' - L \\
&= 2A^2 \left\{ - (2\gamma\Omega + \frac{\sigma}{3}) \left(\frac{\pi^2 \beta^2}{\eta^2} + \eta^2 + \Omega^2 \right) \right. \\
&\quad \left. + \frac{2}{3} [A^2 \eta - \Omega^2 \sigma] - 2 \frac{d\phi}{dz} \right\}, \tag{6.10}
\end{aligned}$$

where we need not explicitly consider the phase dependence $\phi(z)$ and its canonical momentum in the equations of motion as these terms drop out (indicating that the phase depends on the other parameters and plays no role in the dynamics [54]). For a conserved Hamiltonian, $dH/dz = 0$ or $H = \text{constant}$, so that we can construct level sets of H . We shall return to this in the next section. Although such an analysis (similar to that carried out elsewhere for second-order dispersion [68]) can lead to a closed-form expression for $\eta(z)$, the results are extremely unwieldy and unlikely to be of much practical use.

Instead, we obtain the equations of motion from (6.10),

$$\begin{aligned}
\frac{d\beta}{dz} &= -\frac{2}{\pi^2} A^2 \eta^3 - 2[\sigma + 6\gamma\Omega] \left[\beta^2 - \frac{\eta^4}{\pi^2} \right], \\
\frac{d\eta}{dz} &= -2\beta\eta[\sigma + 6\gamma\Omega], \tag{6.11}
\end{aligned}$$

$$\begin{aligned}
\frac{dc}{dz} &= \sigma\Omega + \gamma \left(\frac{\pi^2 \beta^2}{\eta^2} + \eta^2 + 3\Omega^2 \right), \\
\frac{d\Omega}{dz} &= 0, \tag{6.12}
\end{aligned}$$

where we have used the fact that $\sigma(z)$ is piecewise-constant with derivative zero on the entire domain of z except for a set of measure zero. The last equation of the above set follows from the observation that L does not contain the cyclic coordinate c explicitly—its associated momentum is then a constant of the motion.

The modification brought about by the third-order nonlinearity in the first two of the above set of equations is to alter the strength of the dispersion map. The third equation describes the drift in the center of the pulse (in the moving reference frame). Clearly there are terms in these equations that are explicitly dependent on the third-order dispersion coefficient γ , and describe effects predicted only when third-order

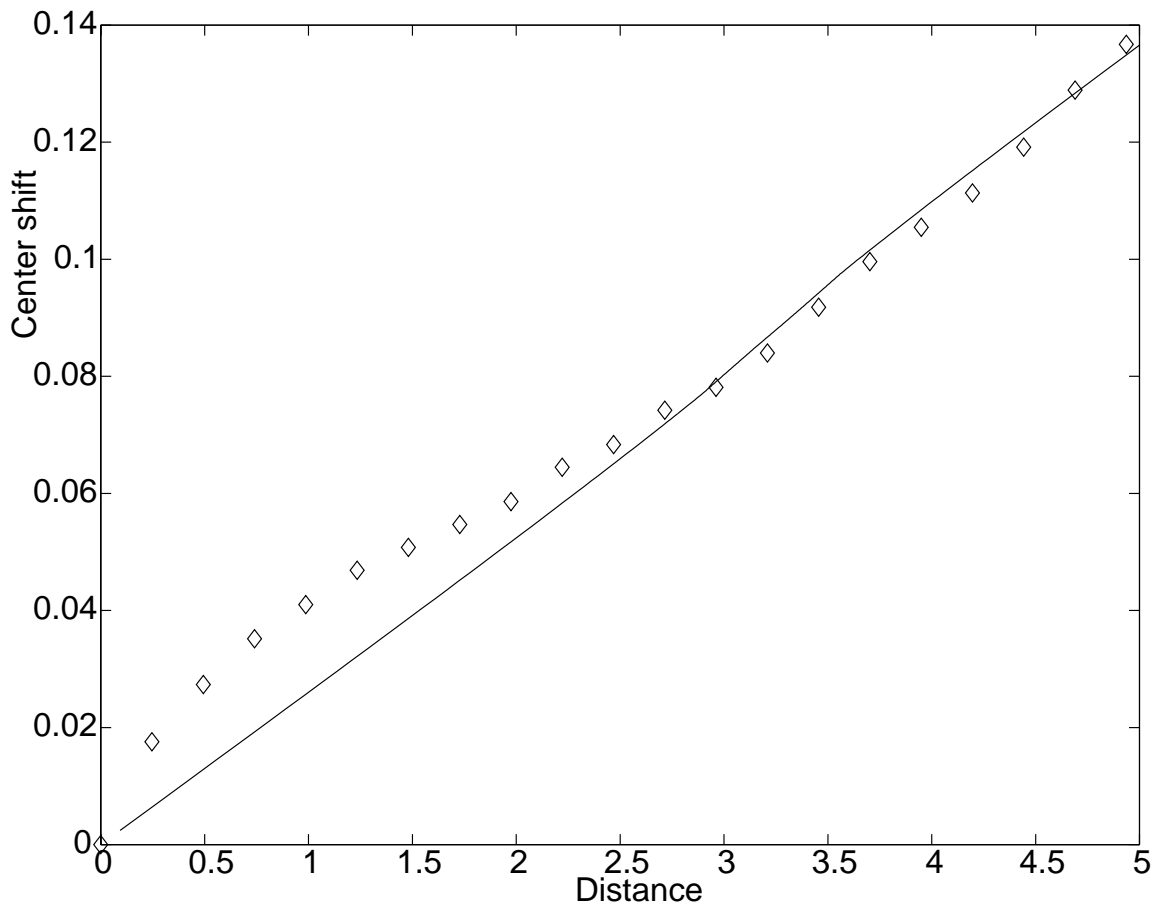


Figure 6.1: Position of pulse center $c(t)$, normalized to the input pulse-width, versus propagation distance z , normalized to the single-soliton period. The data points are from a split-step Fourier simulation, and the solid line is from numerical integration of equation (6.12.1), which was derived from theoretical considerations.

dispersion is taken into account. In Fig. 6.1 we show a comparison between our theory (Eq. (6.12a)) and direct numerical simulation of the drift in pulse center brought about by third-order dispersion. The close agreement for the higher ranges of z (recall that our analysis is an asymptotic one) shows the robustness of the Hamiltonian approach, withstanding the presence of dispersive waves in the numerical simulation that we have to neglect in a Hamiltonian approach. We note that the peak amplitude does indeed move more or less linearly towards the positive time axis, associated with a change in the group velocity of the pulse as was predicted from a purely numerical simulation in Ghafouri-Shiraz et al. [38].

6.1.1 Existence of breathing solutions for third-order dispersion

It may be useful to show mathematically that breathing solutions can exist even with third-order dispersion. We carry out a linearized stability analysis, and begin by determining the fixed points of the system by setting the left-hand sides of (6.11) to zero. There are two solutions:

$$\begin{aligned} \text{(I.) } \quad & \beta = 0, \quad \eta = 0, \\ \text{(II.) } \quad & \beta = 0, \quad \eta = \frac{A^2}{\sigma + 6\gamma\Omega} \equiv \eta_0. \end{aligned} \tag{6.13}$$

The first fixed point is (triple) degenerate, and cannot be used in linear stability theory. We can say, however, that the origin cannot be a center in the phase plane: orbits approaching a center point tend to oscillate around it, and negative amplitudes are not physically meaningful. The solutions that involve this fixed point are homoclinic orbits, i.e., they approach one and the same fixed point as $z \rightarrow \pm\infty$.

With regard to the second fixed point, we take small perturbations $(\Delta\eta, \Delta\beta)$ around the fixed point, and linearizing the equations, after some algebra,

$$\begin{aligned} \Delta\eta' &= -2A^2\Delta\beta, \\ \Delta\beta' &= \frac{2}{\pi^2}A^2\eta_0^2\Delta\eta, \end{aligned} \tag{6.14}$$

which leads to the eigenvalues

$$\lambda_{\pm} = \pm i \frac{2}{\pi} \eta_0^2 [\sigma + 6\gamma\Omega] = \pm i \frac{2}{\pi} \frac{A^4}{\sigma + 6\gamma\Omega}, \tag{6.15}$$

and eigenvectors

$$\mathbf{v}_{\pm} = \left(\pm i \frac{\pi}{\eta + 0}, 1 \right). \tag{6.16}$$

Since both the eigenvalues are purely imaginary, the point $(\eta_0, 0)$ is a center in the phase plane [142], which is physically satisfying for a model without dissipation. Furthermore, for constant $\sigma(z) = \sigma_{\pm}$, since from (6.11)

$$\nabla \cdot (d\eta/dz, d\beta/dz) = -6\beta(\sigma_{\pm} + 6\gamma\Omega) \tag{6.17}$$

changes in sign in the range of β that we consider, we expect that the above (au-

tonomous) system of equations can have periodic solutions according to the Bendixson criterion [142]. Moreover, for the case of anomalous dispersion, these periodic solutions can be physically interpreted as breathers similar to the case of the model without third order dispersion [68].

6.2 Phase-plane analysis

We use a phase-plane analysis similar to Kutz et al. [68] to further understand the behavior of the system. Since c is a cyclic coordinate, its conjugate momentum is a conserved quantity and we plot the level sets of the Hamiltonian from (6.10) in the (η, β) plane. Since (6.1) is autonomous (the independent variables do not appear explicitly), trajectories in phase space do not intersect. We take $\sigma(z)$ to be constant $= \sigma$ when we plot the analytical results, and consider normal ($\sigma < 0$) and anomalous ($\sigma > 0$) dispersion separately. This corresponds to propagation in fibers of uniform second-order dispersion and dispersion maps can be constructed by adding together such sections of appropriate length. We will return to this important point later. As in the case of the model without third-order dispersion, the dynamics are markedly different in the two cases.

The phase-plane plots for normal and anomalous dispersion are shown in Figs. 6.2 and 6.3. The mirror symmetry of both plots about the axes $\beta = 0$ implies invariance of the solutions to (6.11.1) and (6.11.2) under the transformations $t \rightarrow -t$ and $(\eta \rightarrow \eta, \beta \rightarrow -\beta)$. For normal dispersion ($\sigma < 0$), the phase flow is clockwise, and all orbits limit at the origin as $z \rightarrow \pm\infty$. In contrast, for anomalous dispersion ($\sigma > 0$), the counterclockwise phase flow indicates not only homoclinic orbits to the origin, as in the previous case, but also periodic solutions inside the separatrix.

The separatrix defines the boundary between solutions that are periodic and those that flow into the origin. Its equation for dispersion-managed systems with third-order dispersion can be obtained from (6.10) by setting $\beta = 0$ and solving for the Hamiltonian value H_0 such that the origin is part of the solution. The result is

$$\beta = \pm \frac{\eta}{\pi} \left(\frac{2}{3} \frac{A^2 \eta}{\sigma/3 + 2\gamma\Omega} - \eta^2 \right)^{1/2}. \quad (6.18)$$

Further, we note that for the case of anomalous dispersion, the width (in β) of the

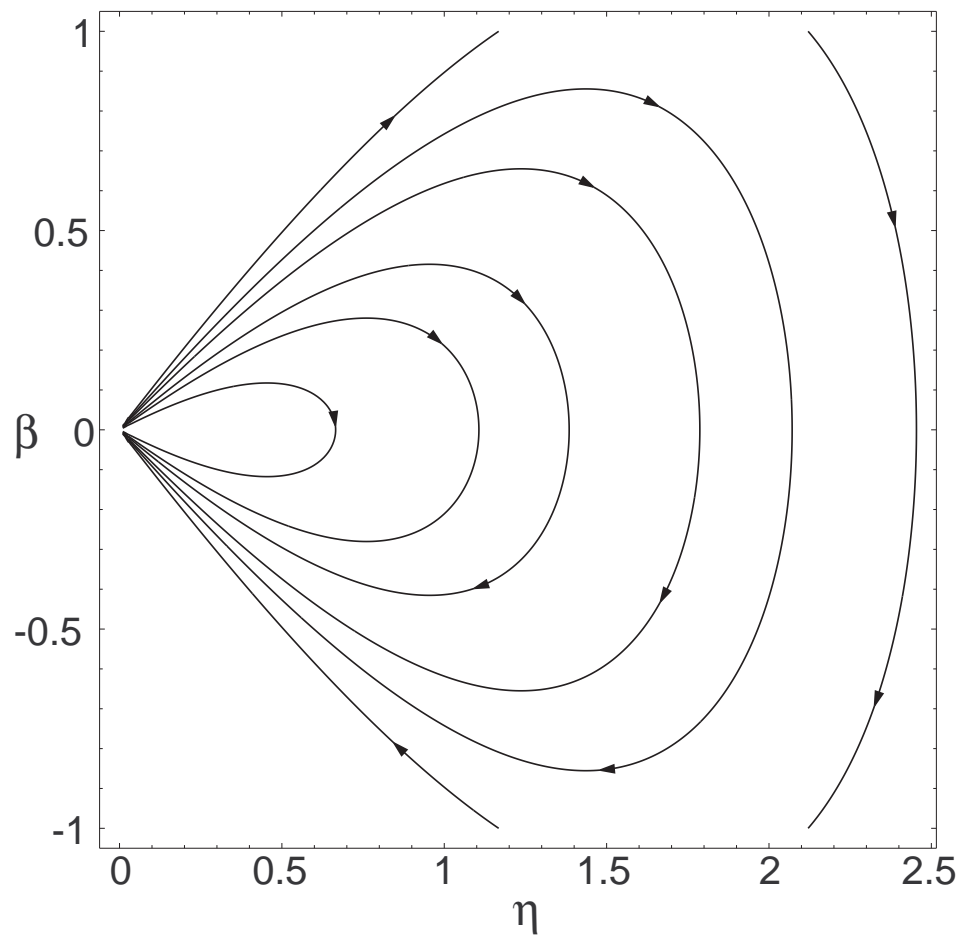


Figure 6.2: Phase portraits for normal dispersion: level sets of the Hamiltonian in the (η, β) plane with $\sigma = -1$. Note that all trajectories start and end at the origin.

separatrix at its widest in the (η, β) space is given by

$$\delta\beta = \frac{2\pi}{\sqrt{3}} \left(\frac{A^2}{2\pi(\sigma/3 + 2\gamma\Omega)} \right)^2, \quad (6.19)$$

which shows that third-order dispersion quadratically lowers the phase-space domain over which periodic solutions exist. The corresponding maximum swing in the quadratic chirp is, of course, smaller. This analytical result is of importance in designing communication systems and protocols that must have available estimates for the effects of third-order dispersion in the evolution of the pulse width/chirp with propagation distance. We can, in principle, compensate for the increase of the denominator for $\gamma \neq 0$ by increasing A . Viewed from a different perspective, breathers with third-order dispersion that maintain the same width in phase space as defined by (6.19) have greater energy leading to lower error rates in typical communications systems.

We can use Figs. 6.2 and 6.3 to construct a dispersion map, similar to the procedure carried out in Kutz et al. [68]. Fig. 6.4 shows a superposition of phase-space orbits from propagation along uniform normal dispersion (ND) and anomalous dispersion (AD) fibers, with two of the many possible dispersion-mapped orbits identified, each starting, for example, with an unchirped pulse at the $\beta = 0$ line. First we encounter (clockwise) propagation along a certain length $z_1/2$ of ND fiber followed by (counterclockwise) propagation along a length z_2 of AD fiber. Finally, to symmetrize the map, we require propagation along length $z_1/2$ of the same normal dispersive fiber as before. The breather traverses this map in the direction of the arrows. The transitions between ND and AD fiber are marked with circles: we clearly are free to pick contours, e.g., so that the pulse amplitude (width) satisfies certain limits imposed by a systems design criterion. More complicated dispersion maps can be very easily constructed simply by tracing out the trajectory of the breather, and ensuring that we return to the initial point after some distance that then defines the period. As mentioned earlier, orbits in phase space do not intersect one another, so the evolution of a breather along a trajectory we construct is necessarily deterministic and unique.

Propagation along such a symmetric map comprised of two types of fiber with lengths L_1 and L_2 and group-velocity dispersion coefficients β_1'' and β_2'' , respectively,

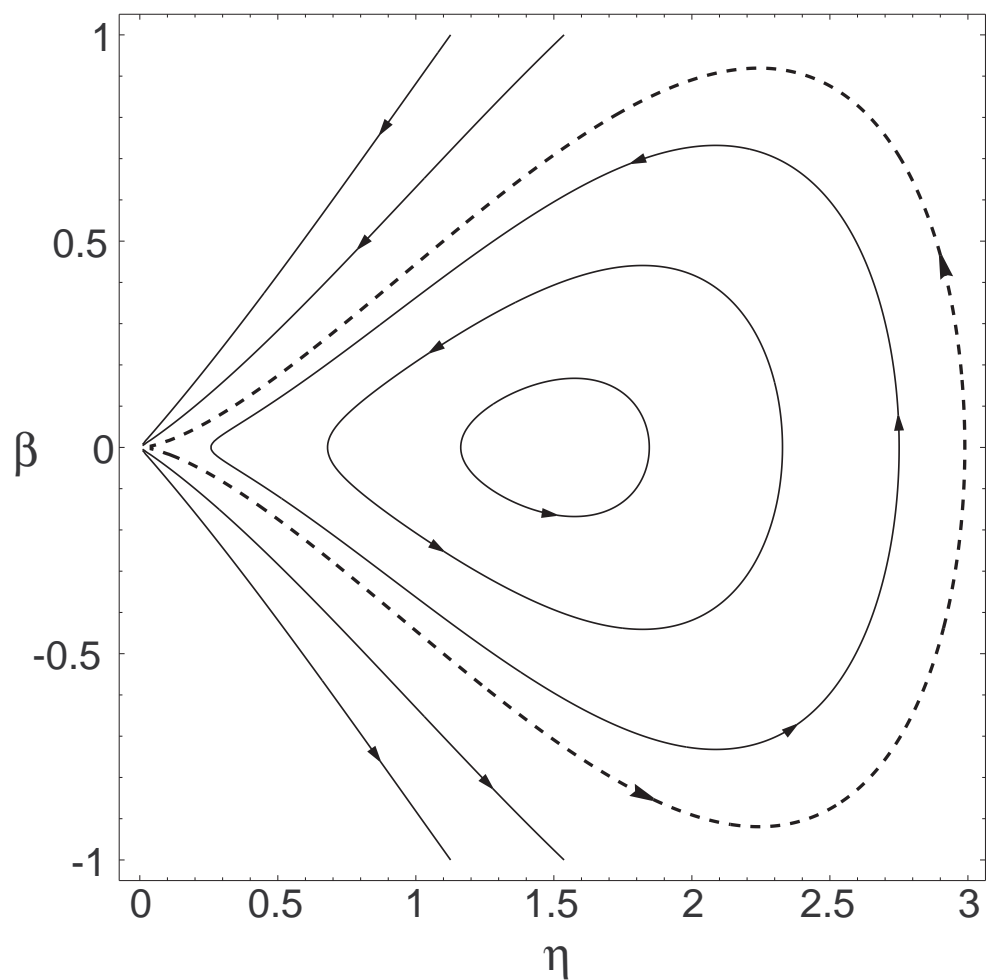


Figure 6.3: Phase portraits for anomalous dispersion: level sets of the Hamiltonian in the (η, β) plane with $\sigma = 1$. Trajectories within the separatrix, shown by the dotted line, are periodic.

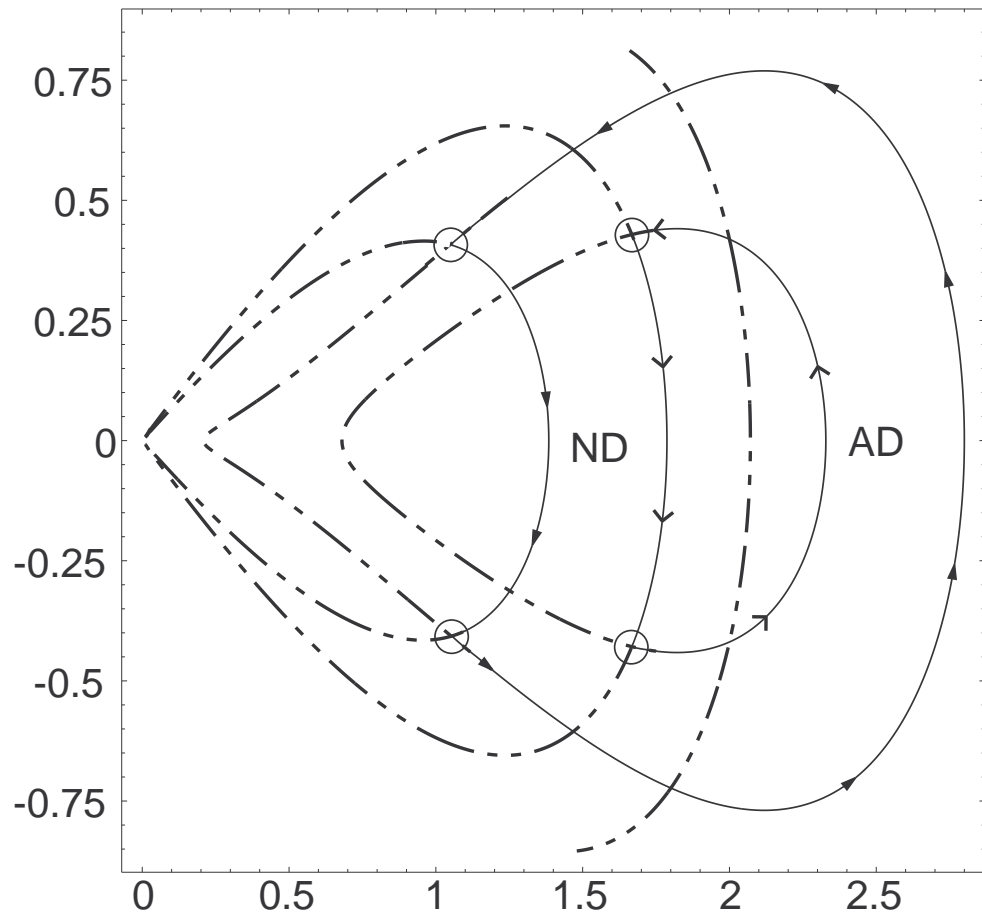


Figure 6.4: Construction of dispersion maps based on Figs. 6.2 and 6.3. Transitions between the two types of fiber are indicated with circles. Two possible trajectories traversed by a breather are indicated by arrows.

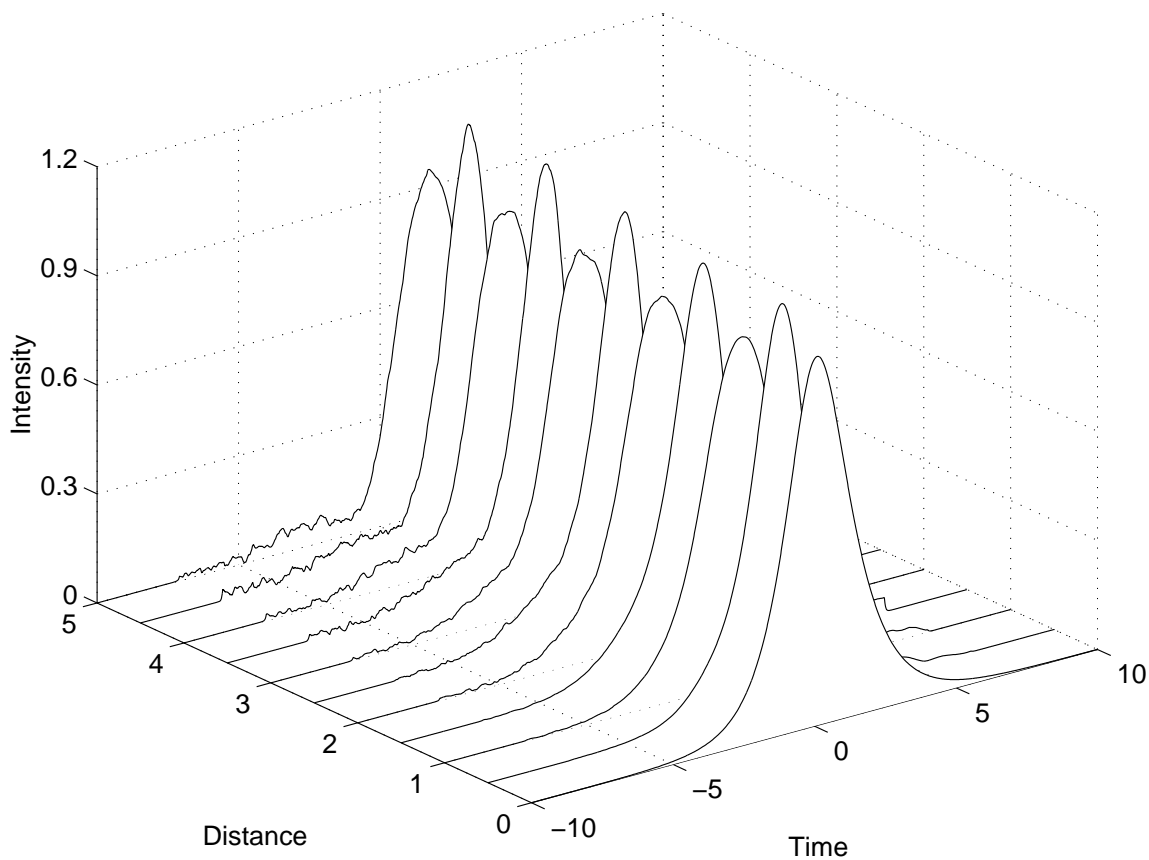


Figure 6.5: Numerical simulation of pulse propagation over several periods along a dispersion map constructed using Fig 6.4.

is shown in Fig. 6.5. The map is defined by the following normalized relationships,

$$\frac{\beta_2''(z)}{\beta_1''(z)} = \frac{-5.5}{+1}, \quad \frac{L_2}{L_1 + L_2} = \frac{0.2}{0.8 + 0.2}. \quad (6.20)$$

The slight asymmetry and dispersive tails are ignored in the above Hamiltonian analysis and could conceivably be compensated for to a certain extent by optical filtering [67]. Nevertheless, the breathing nature of the pulse is clearly visible.

We have analyzed the nonlinear Schrödinger equation accounting for third-order dispersion using a nonperturbative variational approach. A Lagrangian was constructed from the modified Euler-Lagrange equation, and identification of appropriate generalized coordinates and their conjugate momenta leads to a Hamiltonian formulation of the pulse dynamics. Using a hyperbolic secant Ansatz and allowing for quadratic chirp as well as shifts in the group velocity, we have formed equations of motion of the principal pulse parameters, and have shown via a phase-plane analysis that breathers can be formed in the anomalous dispersion regime. The presence of third-order dispersion reduces the relevant (η, β) parameter space over which such periodic solutions exist; conversely, breathers with third-order dispersion have enhanced energy which can be of benefit in optical communications. We have shown how to compute dispersion maps for systems that include third-order dispersion, and have indicated their agreement with numerical simulations. The results are particularly useful in the design of dispersion-managed communication systems, with low average second-order dispersion.

6.3 Dispersion maps including third-order dispersion

We extend the analysis of the previous sections to now discuss dispersion maps constructed in the third-order dispersion coefficient. This is analyzed by coconsidering piecewise constant $\gamma(z)$ rather than constant γ and we will analyze the construction and properties of dispersion maps by highlighting in particular the differences from pure second-order dispersion management, as signified by a nonzero γ in the phase-plane separatrix.

These differences are shown clearly in a plot of η versus β as functions of z in the “phase-plane” as shown in Fig. 6.6 for certain values of H corresponding to particular initial conditions for the launch of the soliton and for both normal and anomalous dispersion fiber. (Since c is a cyclic coordinate, its conjugate momentum is a conserved quantity; trajectories in phase space corresponding to a particular type of fiber do not intersect since Eq. (6.1) is autonomous.) We see that just as for second-order dispersion alone, breathing solutions are possible for anomalous dispersion fiber, but

the contours are scaled nonlinearly in the phase plane. In this regime, the separatrix defines the boundary between solutions that are periodic and those that flow into the origin.

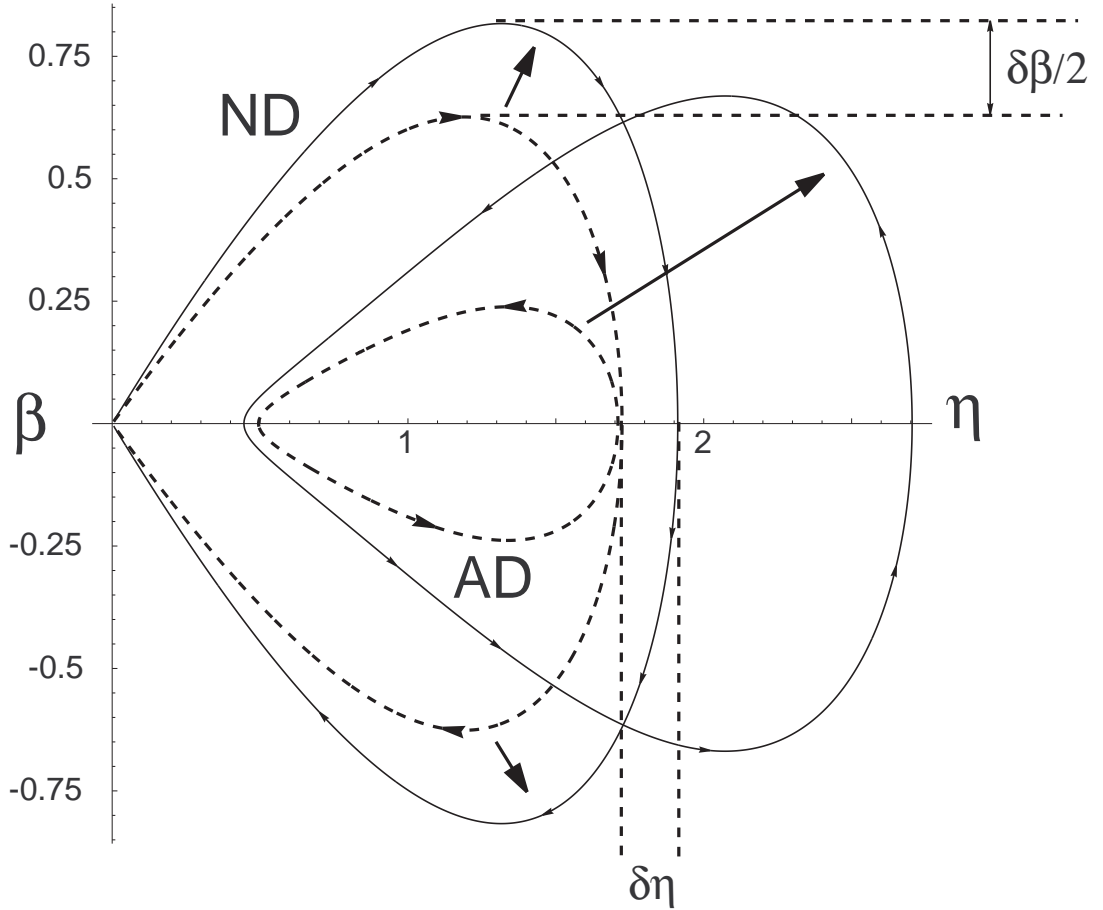


Figure 6.6: Change in the trajectory of a breather from second-order dispersion alone (dotted line) to combined second- and third-order dispersion (solid line). Normal dispersion (ND) fibers are traversed clockwise and anomalous dispersion (AD) fibers anticlockwise. The $\delta\beta$ and $\delta\eta$ in this figure do not refer to the separatrix but to a generic trajectory as shown.

From the separatrix Eq. (6.18), we can derive certain phase-space widths of interest. At its widest along the β coordinate, the separatrix width is obtained by solving

$d\beta/d\eta = 0$ for $\eta = \hat{\eta}$ and then finding $\delta\beta = 2\beta(\hat{\eta})$, which yields

$$\delta\beta = \frac{2\pi}{\sqrt{3}} \left(\frac{A^2}{2\pi(\sigma/3 + 2\gamma\Omega)} \right)^2, \quad (6.21)$$

where $\hat{\eta} = A^2/[2(\sigma/3 + 2\gamma\Omega)]$. Similarly, stipulating that $d\beta/d\eta$ becomes infinite for finite η leads to the maximum value of η , since $(\eta, \beta) = (0, 0)$ is trivially part of the separatrix Eq. (6.18),

$$\delta\eta = \frac{2\pi}{\sqrt{3}} \frac{A^2}{\sigma/3 + 2\gamma\Omega}. \quad (6.22)$$

We see that the effects of nonzero γ are different along the two coordinates. Consider the case where σ and γ have the same sign: whereas the separatrix contracts linearly along the η -axis, it contracts quadratically along the β axis. The role of TOD is therefore nontrivial and cannot be simply “cancelled” by choosing an appropriately scaled-up contour relative to the separatrix for second-order dispersion alone. While this conclusion is intuitive, the precise argument is most meaningful and precise when approached from the Hamiltonian formalism described here.

Since we know a Hamiltonian describing the evolution of a breather along sections of normal or anomalous dispersive fiber, we can ask if the effect of TOD in shrinking the contours can be compensated for by varying the TOD coefficient γ in sign between the two sections of fiber that comprise a dispersion map in the second-order dispersion coefficient σ . We note that TOD also results in a translation of the contours, i.e., of the linearized center in the phase plane [90] but that is of less importance in this context, since a dispersion map may always be constructed in theory by selecting sufficiently outlying contours.

Contours in phase space aside from the separatrix are parametrized by a particular value H^* of the Hamiltonian (6.10). For any given H^* , we can find the greatest extent of the contour along the η axis (with $\beta = 0$). Since the equation of motion (6.11) for β is symmetric in $\beta \rightarrow -\beta$, this point can be found by determining that $\eta \equiv \zeta$ for which $d\beta/d\eta$ goes to infinity at finite η . Alternatively, we can set $\beta(\eta) = 0$ and solve for the greatest η . The results are identical and we obtain after some algebra that

the maximum value of η is

$$\zeta = \frac{A^2}{\sigma + 6\gamma\Omega} \left[1 \mp \sqrt{1 - \left(\frac{\sigma + 6\gamma\Omega}{A^2}\right)^2 \left[\frac{3H^*}{2A^2(\sigma + 6\gamma\Omega)} + \Omega^2 \left(1 + 2\frac{\sigma}{\sigma + 6\gamma\Omega}\right) \right]} \right], \quad (6.23)$$

where the minus sign corresponds to a section of fiber with normal dispersion ($\sigma < 0$) and the plus sign for anomalous dispersion ($\sigma > 0$).

The simplest dispersion maps involve two sections of fiber with σ taking on opposite signs, i.e., $\sigma(z) = \mp\sigma$ for normal and anomalous dispersion fiber, respectively. We now ask if it is possible to design a dispersion map with TOD to maintain the same separation between the two contours in phase space along the η axis. We use a subscript N or A on ζ to indicate normal or anomalous dispersion fiber, and a superscript $\zeta^{(0)}$ for second-order dispersion alone and $\zeta^{(1)}$ for a dispersion map that includes TOD. Stated mathematically, we seek the conditions under which

$$\Delta\zeta_N \equiv \zeta_N^{(0)} - \zeta_N^{(1)} = \zeta_A^{(0)} - \zeta_A^{(1)} \equiv \Delta\zeta_A, \quad (6.24)$$

where the normal dispersion contour is selected by a Hamiltonian value H_N^* and the anomalous dispersion contour by H_A^* .

From (6.23), we have

$$\begin{aligned} \zeta_N^{(0)} &= \frac{A^2}{-\sigma} \left[1 - \sqrt{1 - \left(\frac{\sigma}{A^2}\right)^2 \left[\frac{3H_N^*}{2A^2(-\sigma)} + 3\Omega^2 \right]} \right], \\ \zeta_N^{(1)} &= \frac{A^2}{-\sigma + 6\gamma_N\Omega} \left[1 - \sqrt{1 - \left(\frac{-\sigma + 6\gamma_N\Omega}{A^2}\right)^2 \left[\frac{3H_N^*}{2A^2(-\sigma + 6\gamma_N\Omega)} + \Omega^2 \left(1 + 2\frac{-\sigma}{-\sigma + 6\gamma_N\Omega}\right) \right]} \right], \end{aligned} \quad (6.25)$$

and similarly for $\zeta_A^{(0)}$ and $\zeta_A^{(1)}$ with the replacements $\gamma_N \rightarrow \gamma_A$, $-\sigma \rightarrow \sigma$ and the appropriate sign from (6.23).

Therefore,

$$\Delta\zeta_N = \left[\frac{A^2}{-\sigma} - \frac{A^2}{-\sigma + 6\gamma_N\Omega} \right] + \left\{ \frac{A^2}{\sigma} \sqrt{1 - \left(\frac{\sigma}{A^2}\right)^2 \left[\frac{-3H_N^*}{2A^2\sigma} + 3\Omega^2 \right]} \right. \\ \left. - \frac{A^2}{\sigma - 6\gamma_N\Omega} \sqrt{1 - \left(\frac{\sigma - 6\gamma_N\Omega}{A^2}\right)^2 \left[\frac{-3H_N^*}{2A^2(\sigma - 6\gamma_N\Omega)} + \Omega^2 \left(1 + \frac{2\sigma}{\sigma - 6\gamma_N\Omega}\right) \right]} \right\} \quad (6.26)$$

$$\Delta\zeta_A = \left[\frac{A^2}{\sigma} - \frac{A^2}{\sigma + 6\gamma_A\Omega} \right] + \left\{ \frac{A^2}{\sigma} \sqrt{1 - \left(\frac{\sigma}{A^2}\right)^2 \left[\frac{3H_A^*}{2A^2\sigma} + 3\Omega^2 \right]} \right. \\ \left. - \frac{A^2}{\sigma + 6\gamma_A\Omega} \sqrt{1 - \left(\frac{\sigma + 6\gamma_A\Omega}{A^2}\right)^2 \left[\frac{3H_A^*}{2A^2(\sigma + 6\gamma_A\Omega)} + \Omega^2 \left(1 + \frac{2\sigma}{\sigma + 6\gamma_A\Omega}\right) \right]} \right\}. \quad (6.27)$$

Substituting the above expressions into (6.24) yields a complicated equation, which can be simplified by noting that if for four rationals $x + \sqrt{y} = a + \sqrt{b}$, then $x = a$ and $y = b$ unless y and b are the squares of rationals. Inspection of (6.26) and (6.27) shows that the general condition holds, except possibly for one particular set of values of H^* , which is unlikely to be the exact H^* that constructs a satisfactory dispersion map. In any case, it is not practical to impose the Hamiltonian energy to exactly equal a particular irrational number. Consequently, we can split the condition $\Delta\zeta_N = \Delta\zeta_A$ into a pair of simultaneous equations, one for the rational part free from radicals (in this case, the square root) and the other involving (only) radicals (also known as a “surd”). The first equation of this pair [see (6.26) and (6.27)] then leads to the requirement

$$\frac{1}{-\sigma} - \frac{1}{-\sigma + 6\gamma_N\Omega} = \frac{1}{\sigma} - \frac{1}{\sigma + 6\gamma_A\Omega}, \quad (6.28)$$

which after a little algebra simplifies to

$$\frac{1}{6\Omega} \left(\frac{1}{\gamma_N} - \frac{1}{\gamma_A} \right) = \frac{2}{\sigma}. \quad (6.29)$$

Next, the second terms of (6.26) and (6.27) (involving the radical) can be seen to be identical for both $\Delta\zeta_N$ and $\Delta\zeta_A$ if

$$\gamma_N = -\gamma_A \quad (6.30)$$

and we choose contours (i.e., H^*) appropriately. Combining (6.29) and (6.30) yields the simple condition

$$\sigma = 6\gamma\Omega, \quad (6.31)$$

where $\gamma_N = -\gamma_A \equiv \gamma$ just as $\sigma_A = -\sigma_N \equiv \sigma$. But $\sigma_N + 6\gamma_N\Omega = 0$, which sets the denominator of (6.23) to zero—therefore, the result (6.31) is not a physically meaningful one. This shows that third-order dispersion fundamentally modifies even the swing in pulse amplitude and since this is a typical design criterion in dispersion-managed systems, it is important to design dispersion maps explicitly taking the effects of γ into account. An example of such a map was discussed elsewhere [90].

This analysis of dispersion-mapped TOD solitons can considerably help the search for effective ways to compensate for dispersion-slope [3] mismatch in dispersion-mapped systems [148]. In systems that use nonlinear breathing pulse shapes (envelopes), we can explicitly use the dispersion-slope mismatch between different sections of nonlinear fiber to pick appropriate contours in the phase space. The periodic dispersion map thereby constructed has breathing solutions that inherently utilize the different third-order dispersion coefficients encountered along the propagation channel and the residual mismatch is then of fourth order in chromatic dispersion and consequently much weaker. The emphasis is now on utilizing third-order dispersion constructively rather than trying to completely get rid of the effect. Of course, the Hamiltonian analysis is valid only within certain regimes, and TOD dispersion maps can be used to utilize the residual dispersion-slope mismatch after reasonably simple dispersion-slope mismatch compensation schemes have been applied—this will ease the burden on the latter functionality.

We have shown that the presence of third-order dispersion (TOD) scales the representative periodic orbit in phase-space—the separatrix—differently along the two coordinates η and β . For both normal dispersion and anomalous dispersion fiber, we have quantified the changes in the variations of the amplitude (or pulse width) and the quadratic chirp of the pulse envelope. It is clear that TOD modifies the orbits in phase-space nontrivially; we have also shown that it is necessary to explicitly consider TOD even with simpler design constraints, such as the maximum periodic change in pulse amplitude.

Chapter 7

Multilevel communications in nonlinear fibers

Oh.

We have reached the crux of the matter.

The argument that the location of the pole in the quark propagator is an observable quantity rests upon the assumption that there is no confinement.

Those who look for confinement in the singularities of the quark propagator are like the man who settled in Casablanca for the waters.

They have been misinformed.

—S. Coleman, *Aspects of Symmetry*, Cambridge, 1985.

As we have seen in Chapter 6, a physically intuitive framework for understanding and predicting the nonlinear evolution of optical pulses (applicable to non-integrable systems) is the variational characterization of breather dynamics [100, 7] based on a Lagrangian functional and an appropriate *Ansatz* for the pulse envelope. The resulting equations of motion of the pulse parameters, Eqs. (6.11) and (6.12), can be represented in the phase-plane, simplifying the construction of appropriate dispersion maps of the group-velocity dispersion (GVD) coefficient [68].

We have proposed a multilevel optical communications scheme using nonlinear pulses that can substantially increase the bitrate of current signalling formats, since the advantages are essentially independent of wavelength- and time-division multiplexing. This scheme is simply not possible with conventional linear transmission formats that ignore the Kerr effect in optical fibers, and it relies extensively on understanding the implications of the equations of motion of the pulse parameters. The context of this proposal is introduced in Section 7.1, and an overview is presented in Section 7.3. The remainder of this chapter is mainly concerned with the technical details of implementing a practical system in the presence of amplifier noise. Quantitative estimates of the benefit of this scheme using realistic estimates of the various

system parameters are also presented.

7.1 Formulation

As we have seen in Eq. (6.1), the slowly-varying normalized envelope $Q(Z, T)$ of an optical pulse in a single-mode fiber with dispersion-management in the group-velocity dispersion (GVD) parameter σ follows the nonlinear Schrödinger equation,

$$i\frac{\partial Q}{\partial Z} + \frac{\sigma}{2}\frac{\partial^2 Q}{\partial T^2} + a^2|Q|^2Q = \epsilon R, \quad (7.1)$$

using the terminology of Table 7.1 (in which numerical values are quoted in physical units, rather than normalized quantities), where Q is the electric field envelope normalized by the peak field power and further divided by $a(Z)$, Z is the physical distance normalized by the dispersion length [4], and T is related to the physical time t , distance z , and the group velocity v_g according to the relationship $T = t - z/v_g$, and is further normalized by the $1/e$ width of the pulse envelope.

Dispersion maps are constructed using sections of fiber with piecewise-constant dispersion coefficients [83, 125]: the particular dispersion map we consider here is composed of SMF-28 and SMF-LS (non-zero dispersion-shifted) fiber. $R(Z, T)$ is a complex-valued white noise process characterizing the amplified spontaneous emission (ASE) noise added by the amplifiers along the transmission channel, and is further discussed later.

In Eq. (6.1), $a(Z)$ represents the effects of the background loss in the fiber and the gain provided by optical amplifiers. We consider two particular cases: (1) the gain is provided by distributed amplification (e.g., Raman amplifiers) and is only a weak perturbation to the pulse dynamics, and (2) the gain is provided by lumped amplifiers (e.g., EDFA's) so that the gain-loss variations in the amplitude are $O(1)$ or larger. In the former case, we can simply take $a(Z) = 1$, and, if necessary, treat the effect of the gain-loss variations as an additional term in the definition of R . In the latter case, the exponential path-integrated gain-loss variation, $a(Z)$, is defined as

$$a(Z) = a(0) \exp \left\{ \int_0^Z dZ' \left[G \sum_{n=1}^N \delta(Z' - nZ_a) - \alpha \right] \right\}, \quad (7.2)$$

where G is the gain due to one of the N amplifiers spaced uniformly by Z_a (physical distance normalized by the dispersion length) along the total source-receiver length, L , and α is the background loss per unit distance multiplied by the dispersion length [44, pp. 111-112]. In Eq. (7.2), $a(Z)$ is usually defined with an average value of unity [44, pp. 114–116]. While the analysis for the lumped-gain case is more complicated, the results are qualitatively similar to those for the distributed-gain case, and we will mostly work in the distributed-gain approximation.

λ	carrier wavelength	1.55 μm
γ	nonlinearity coefficient	2 $\text{km}^{-1}\text{W}^{-1}$
D_+	GVD for anomalous dispersion fiber	17.45 $\text{ps}/\text{km}\text{-nm}$
D_-	GVD for normal dispersion fiber	-2.1 $\text{ps}/\text{km}\text{-nm}$
Z_+	length of anomalous dispersion fiber	6 km
Z_-	length of normal dispersion fiber	22.5 km
L	source-receiver length	4080 km
Z_a	inter-amplifier spacing	51 km
N	number of amplifiers	80 ($= L/Z_a$)
T_0	pulse width (1/e-intensity point)	9.0 ps
α	fiber loss	0.2 dB/km
N_{sp}	spontaneous emission factor	2
G	amplifier gain	10.2 dB

Table 7.1: Definitions of symbols and numerical values of parameters (in physical units)

7.2 Analytical framework

The nonlinear breathing of dispersion-managed solitons is clearly visible in the direct numerical simulations of Eq. (7.1) using the split-step Fourier method [4]. Such data is shown, for a train of breathing pulses in Fig. 7.1. A clear and simple framework for analyzing and predicting this behavior is the Lagrangian formalism, which represents the field amplitude using a finite number of parameters, each with a direct physical meaning, e.g., width of the envelope, or chirp [7, 20, 21]. In exchange for limiting our attention to a finite number of degrees of freedom, the resultant equations of motion for the parameters become ordinary differential equations [39, 121].

In the presence of noise perturbations, the solution to the stochastic PDE, Eq. (6.1),

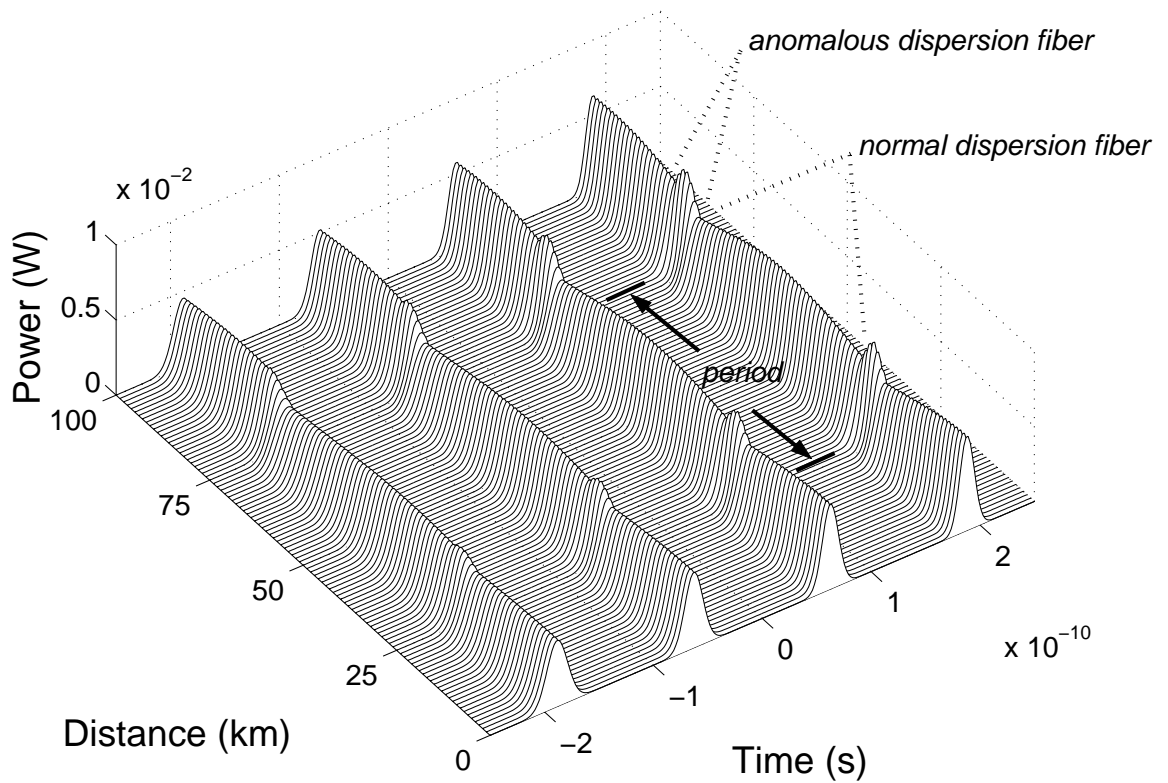


Figure 7.1: Propagation of a pulsetrain of breathing dispersion-managed solitons, numerically calculated directly from the nonlinear Schrödinger equation with $\epsilon = 0$, over two dispersion map periods, with the map specified as in Table 7.1. Four time-slots are shown with different initial pulseshapes and, therefore, different breathing patterns. Eq. (7.3) is used to specify the pulseshapes that are transmitted.

is written as $Q(Z, T) = Q_0(Z, T) + \epsilon Q_1(Z, T) + \dots$. For the zeroth-order term, we use a Gaussian ansatz [68]

$$Q_0(Z, T) = Ab\sqrt{\eta} \exp \left\{ -[\kappa\eta(T - C)]^2 + i\Omega(T - C) + i \left[\beta\kappa^2(T - C)^2 + \frac{\phi}{2} \right] \right\}, \quad (7.3)$$

where η , β , Ω , C and ϕ depend solely on Z and represent the amplitude (and width), quadratic chirp, frequency shift from the carrier frequency (or velocity), pulse center position in the moving reference frame (or group-velocity variation in laboratory coordinates) and phase respectively. κ is a pulsewidth scaling constant, taken as equal to 1.18/1.76 so that Eq. (7.3) has the same FWHM as the first-order hyperbolic secant soliton, b is an energy scaling constant determined by $b^2 = 2\kappa\sqrt{2/\pi}$ so that the energy of the Gaussian pulse is the same as that of the hyperbolic secant soliton.

The dispersion map is symmetric and comprises a section of anomalous dispersion (AD) fiber, of dispersion coefficient D_+ and length Z_+ , between two sections of normal dispersion fiber (ND) of dispersion coefficient D_- and length $Z_-/2$ (for each of the two sections). The amplitude enhancement factor A is then defined as

$$A = \left[1 + \xi \left\{ \frac{\lambda_0^2}{2\pi c T_0^2} [(D_+ - \bar{D})Z_+ - (D_- - \bar{D})Z_-] \right\} \right]^{1/2} \quad (7.4)$$

in terms of the path-averaged dispersion coefficient \bar{D} , and a ‘free’ parameter ξ which will play an important role in the following discussion.

The variational principle is characterized by

$$\frac{\delta \mathcal{L}_0}{\delta Q^*} = i\epsilon 2R, \quad (7.5)$$

where \mathcal{L}_0 is the Lagrange density functional for the unperturbed problem,

$$\mathcal{L}_0(Q, Q^*) = i \left[Q \frac{\partial Q^*}{\partial Z} - Q^* \frac{\partial Q}{\partial Z} \right] + \sigma(Z) \left| \frac{\partial Q}{\partial T} \right|^2 - a^2 |Q|^4. \quad (7.6)$$

In terms of the solution Q_0 to the unperturbed problem, Eq. (7.5) can be re-written as

$$\frac{\delta \mathcal{L}_0}{\delta Q_0^*} = i\epsilon 2R - \epsilon \mathcal{L}_1(Q_0, Q_0^*; Q_1, Q_1^*), \quad (7.7)$$

where \mathcal{L}_1 is given by [44, pp. 80–82]

$$\mathcal{L}_1(Q_0, Q_0^*; Q_1, Q_1^*) = \lim_{\epsilon \rightarrow 0} \frac{1}{\epsilon} \left\{ \frac{\delta \mathcal{L}_0}{\delta Q^*} [Q_0 + \epsilon Q_1, Q_0^* + \epsilon Q_1^*] - \frac{\delta \mathcal{L}_0}{\delta Q^*} [Q_0, Q_0^*] \right\}. \quad (7.8)$$

The derivatives $\partial Q_0/\partial \zeta$ and $\partial Q_0^*/\partial \zeta$, where $\zeta = \{\eta, \beta, \dots\}$ stands for any of the canonical coordinates, give a solution of the linearized equation. This is given by setting $\mathcal{L}_1(Q_0, Q_0^*, \partial Q_0/\partial \zeta, \partial Q_0^*/\partial \zeta) = 0$.

Also, from the chain rule, the partial derivatives of the Lagrangian functional in terms of a canonical coordinate $\zeta = \{\eta, \beta, \dots\}$ can be expressed in terms of the variations of the Lagrangian density with respect to the pulse ansatz,

$$\frac{\partial L_0}{\partial \zeta} = \int dT \left(\frac{\delta \mathcal{L}_0}{\delta Q_0} \frac{\partial Q_0}{\partial \zeta} + \frac{\delta \mathcal{L}_0}{\delta Q_0^*} \frac{\partial Q_0^*}{\partial \zeta} \right). \quad (7.9)$$

Thus, in the presence of the perturbation R , the equations of motion for the envelope parameters η and β (which is the conjugate momentum to the canonical coordinate η) are

$$\frac{d\eta}{dZ} = -2\kappa^2 \sigma \beta \eta + \epsilon \kappa^2 \frac{\eta^3}{A^2} \int dT (T - C)^2 2 \operatorname{Im}[RQ_0^*], \quad (7.10)$$

$$\begin{aligned} \frac{d\beta}{dZ} = & -\frac{2\kappa}{\sqrt{\pi}} a^2 A^2 \eta^3 + 2\kappa^2 \sigma (\eta^4 - \beta^2) \\ & - \epsilon \frac{\eta^3}{A^2} \int dT \left[\frac{1}{2\eta} - 2\kappa^2 (T - C)^2 \eta \right] 2 \operatorname{Re}[RQ_0^*]. \end{aligned} \quad (7.11)$$

The solutions to Eqs. (7.10) and (7.11) with $\epsilon = 0$, representing the noiseless dynamics of pulse evolution, may be plotted against each other as contours (orbits), as shown in Fig. 7.2 for different initial conditions. The curved trajectories are characteristic of the evolution of many nonlinear dynamical systems in the phase plane [121]. In fibers of constant GVD (constant σ), contours are parametrized by the value of the Hamiltonian and they do not intersect one another [54]. In anomalous dispersion fiber, there exist closed non-degenerate orbits [evolution along which does not end up at the origin, $(\eta, \beta) = (0, 0)$] that represent breathing evolution of pulse shapes, i.e., the pulse width and chirp are periodic functions of Z .

Dispersion maps can be constructed from sections of fiber of opposite GVD signs.

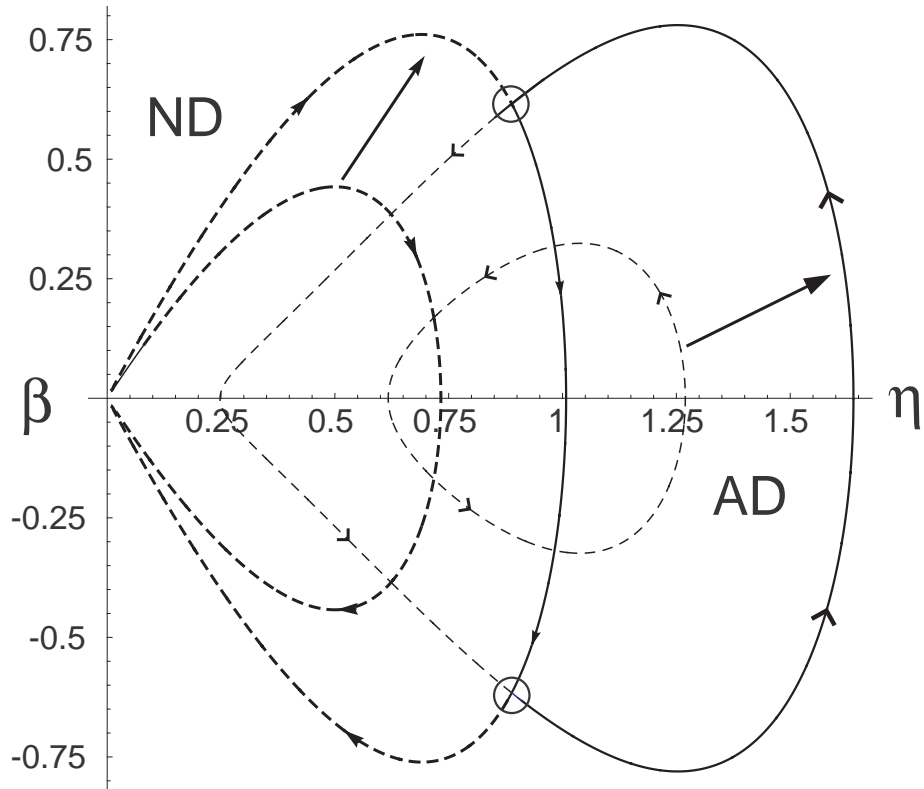


Figure 7.2: Trajectories in phase space (η -width, β -chirp) for the evolution of breathers in the direction shown along normal (ND) and anomalous (AD) dispersion fiber. The latter is capable of supporting closed orbits that do not evolve into the origin. Changing the value of the Hamiltonian leads to a nonlinear scaling of the orbits as indicated by the arrows. The solid line shows the evolution of η and β over one dispersion map period.

With reference to Fig. 7.2, the pulse traverses a section of a particular contour for ND fiber (clockwise), and a complementary section of a particular AD fiber (anticlockwise). The two lengths of fibers are chosen so that, taken together, they form a closed (connected and piecewise smooth) orbit in the η - β plane. The transition from ND to AD fiber (and vice-versa) at the splice locations is indicated by small circles in Fig. 7.2.

Here, we highlight an interesting and important feature of solitary wave propagation in dispersion maps, which we will discuss in the context of the data shown in Fig. 7.1. Assume that a pulse is launched into a dispersion map, whose periodicity (length) is Z_{map} , with parameters η_{initial} and β_{initial} . As shown in Fig. 7.3, we can plot the (η, β) parameters in the phase plane for propagation through integer multiples of the distance Z_{map} . For N concatenated dispersion maps spanning the distance L between the source and the receiver, so that $N = L/Z_{\text{map}}$, there are N such points in the phase plane. This trajectory defines the Poincaré section of the phase plane diagram [54]. For special choices of η_{initial} and β_{initial} , all of these points may exactly coincide, but in general they do not. It is the latter cases which we will focus on, when the Poincaré sections for different launch conditions form distinct trajectories in the phase plane.

7.3 Multiple orbits and multiplexing

From the data shown in Fig. 7.1, the η and β parameters for the second and fourth ‘1’ bits *at the end of each dispersion map period* are plotted against each other in Fig. 7.4. (Successive points are connected by lines for clarity.) In this example, the ξ parameters for these pulses are 1.2 and 1.7, respectively, and we have taken $(\eta_{\text{initial}}, \beta_{\text{initial}})$ as $(0.4, 0)$ and $(0.9, 0)$. Note that between successive points in Fig. 7.4, the pulses trace out a trajectory on their respective phase planes. In Fig. 7.4, the η and β parameters are obtained from a fitting algorithm between the numerically computed pulse envelope and the ansatz, Eq. (7.3) which minimizes the sum of squared residuals. Further, we have verified that over the propagation distance considered here, the pulses do not drift significantly from their initial position. In WDM applications, the gain deviation among different channels and the spectral characterization of ASE [33] are further perturbative effects that need to be accounted for separately, e.g., by using equalization filters [144].

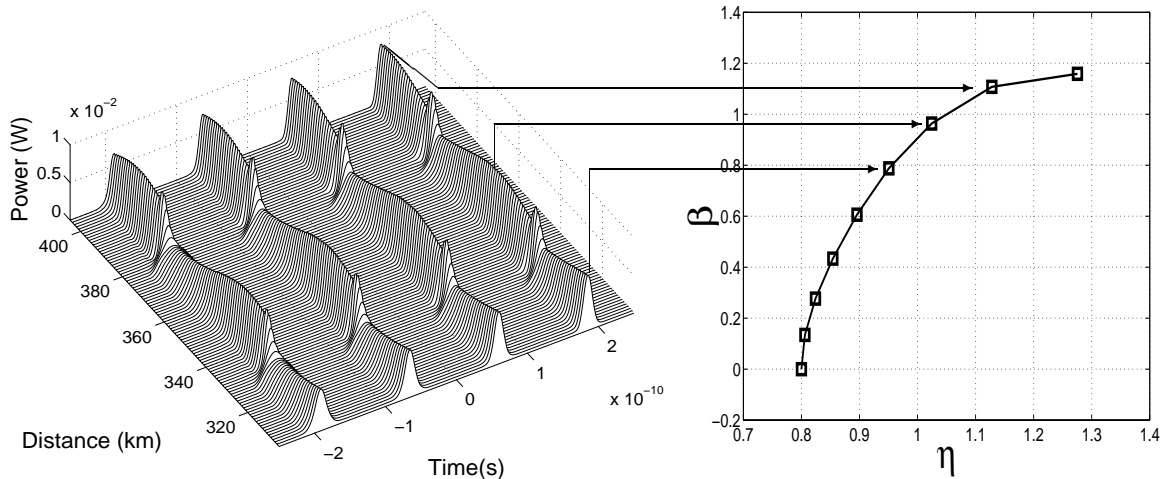


Figure 7.3: The correspondence between the numerically calculated temporal profile and the fitted parameters in the phase-plane, emphasizing that points in the phase plane are plotted at the end of each dispersion map period. Three such points are highlighted in this representation. Each of the points shown in Fig. 7.4 is obtained in this manner.

As Fig. 7.4 shows, there can exist more than one closed orbit in the phase-plane (for clarity, we have shown only two). The multiplexing scheme works as follows: the source (laser+modulator) launches a pulse with a particular combination of amplitude (width), η , and chirp, β to place a particular pulse onto a selected trajectory, i.e., by choosing an initial value for $\eta = \eta_{\text{initial}}$ and for $\beta = \beta_{\text{initial}}$, we select the unique contour that the pulse follows as it propagates. Small unpredicted variations in the initial parameters will select an adjacent contour, but this is not of much concern if the separation between the contours assigned to different codes is chosen to be large enough.

Different contours are assigned to the various alphabets of a multi-level code. The cardinality of the alphabet depends on the complexity of the receivers. For current receiver technology, it is practical to require an unchirped pulse be received at the detector. In this case, there are two allowed pairs, $(\eta_{\text{final}}, 0)$, for each orbit, and the two orbits shown in Fig. 7.4 implement a four-symbol multiplexing scheme. The single channel bit rate ($1/\text{inter-pulse separation}$) is multiplied by four.

Components of the technology needed to implement such a multiplexing scheme have already been demonstrated. For the transmitter, a simple and practical way of

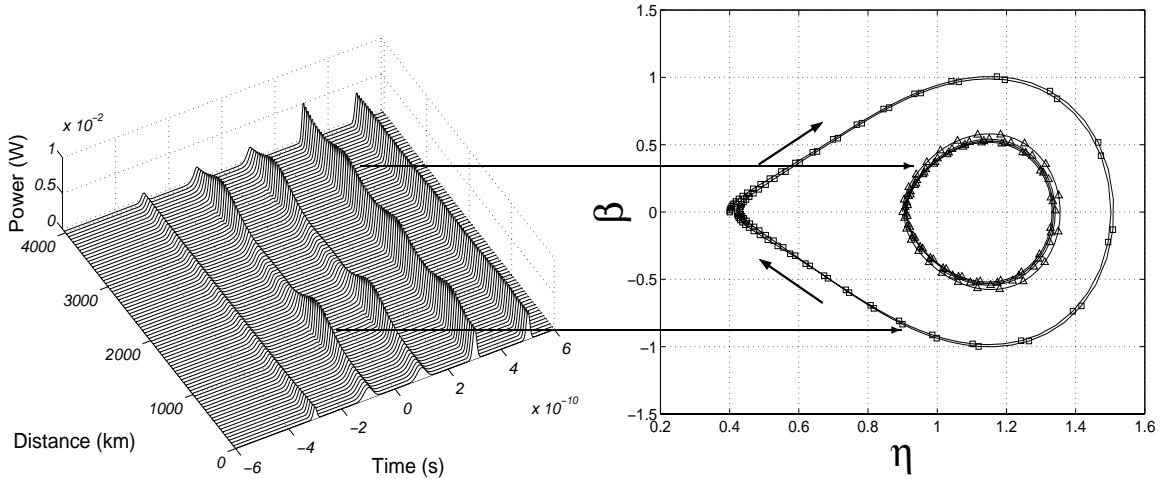


Figure 7.4: Numerically calculated from the nonlinear Schrödinger equation over 4000 km and using a minimum squared residuals fitting algorithm, the η and β parameters for the second and fourth non-zero bits (from the left) are plotted against each other, and form closed orbits in the phase plane. The dispersion map is specified in Table 7.1.

generating solitons of specific widths in the picosecond regime has been demonstrated recently by utilizing adiabatic compression in Raman amplifiers [114, 31, 101]. At the receiver, simple techniques to distinguish between different envelope widths have been demonstrated [46], using the soliton self-frequency shift [40]. [This approach has the advantage of being highly sensitive to the pulsewidth, as the frequency shift is (inversely) proportional to the fourth power of the pulsewidth.]

A communication scheme that uses multiple orbits operates on the basis of a table of $(\eta_{\text{initial}}, \beta_{\text{initial}})$ and ξ values for each orbit, calculated using the (fixed) distance, L , between source and receiver and the period of each orbit, Z_{map} . In the noise-free case, the number of such orbits is essentially infinite, since contours in phase-plane need not intersect. But noise broadens the contours [69] and may cause near-lying orbits to overlap. The dominant noise source is amplified spontaneous emission (ASE) noise from optical amplifiers.

For example, Fig. 7.5 shows the breathing evolution of pulses for a different set of parameters: dispersion map constructed of fiber with a stronger nonlinearity coefficient, $\gamma = 20 \text{ km}^{-1}\text{W}^{-1}$, and with fiber lengths $Z_+ = 6.5 \text{ km}$, $Z_- = 24.5 \text{ km}$, pulse width ($1/e$ -intensity point) $T_0 = 7.5 \text{ ps}$. The ξ parameters for these pulses (two dif-

ferent kinds are considered in this example) are 0.3 and 0.5, respectively, and we have taken $(\eta_{\text{initial}}, \beta_{\text{initial}})$ as $(0.35, 0)$ and $(0.65, 0)$. In this case, the orbits in the phase plane are quite close to each other as shown in Fig. 7.6, and the broadening effect of noise perturbations will cause the orbits to overlap. The goal is to select orbits that are sufficiently apart in phase space that they do not overlap when broadened by noise. Hence, the design of Fig. 7.4 is better than that of Fig. 7.6.

Next, we will include the effects of ASE noise in the direct numerical simulations and show the constraints thereby imposed. Then, we will evaluate an important figure-of-merit—the effective noise radius thickness in the phase plane—which allows for a fairly accurate closed-form estimate of these observations and comment on optimization of the various parameters.

In the presence of ASE (or other) noise perturbations, the contours shown in Fig. 7.4 broaden, which may cause adjacent contours to overlap, thereby leading to errors in converting the sequence of optical pulses to a digital bitstream. The physical basis for this broadening is clear: each of the points in Fig. 7.4 represents η and β at the end of a dispersion map, at which point a noise-source (ASE noise from a spatially-localized amplifier) is encountered. These two parameters experience a noise ‘kick’—a perturbation in two dimensions—with zero mean and finite variance, resulting in the contour being smeared out when viewed over many iterations. Using an adiabatic variational approach [15, 69], we can define an effective root-mean-square distance (radius) r_{eff} for each orbit that represents how ‘thick’ the contours become, on the average, when η and β are perturbed by the stochastic noise kicks at the optical amplifiers.

We select orbits that are sufficiently far apart in the phase plane so that they do not overlap to the required probability of error, i.e., pick contours in the phase plane so that their r_{eff} -broadened orbits do not intersect, as shown in Fig. 7.7. Assuming for practical purposes that we require unchirped envelopes at the receiver ($\beta_{\text{final}} = 0$), there are four multiplexing levels allowed as indicated by the circles of radius r_{eff} around the points on the phase plane that define the four levels of the code. The greater density of points at one unchirped extremum of the orbits compared to the other is not a problem, since a short section of fiber (of length less than a dispersion map period) can be inserted in front of the receiver to ensure that (on the average) an unchirped envelope is received.

In analyzing Eqs. (7.10) and (7.11), we substitute $\eta(Z) = \eta_0(Z) + \epsilon \Delta\eta(Z)$ and

$\beta(Z) = \beta_0(Z) + \epsilon \Delta\beta(Z)$ and β_0 are the solutions to the unperturbed equations of motion. The explicit forms of η_0 and β_0 are not important in this analysis. Matching terms of like powers in ϵ yields equations in $d\Delta\eta/dZ$ and $d\Delta\beta/dZ$.

The noise perturbation is assumed to be of the form,

$$R(Z, T) = \sum_m S(T) \delta(Z - mZ_a), \quad m = 1, 2, \dots, \quad (7.12)$$

i.e., a spatially-localized noise “kick” that is encountered once per period. If the random process $S(T)$ is wide-sense stationary, we may define its spectral representation (the Fourier transform)

$$\tilde{S}(\Omega) = \int dT e^{i\Omega T} S(T), \quad (7.13)$$

which, in general, defines a nonstationary white noise process in the frequency domain where the frequency components of the process corresponding to distinct frequencies are uncorrelated [30]. We will assume that the ASE noise of the optical amplifiers can be characterized using such a model for $S(T)$, with the following expectation values [82],

$$\begin{aligned} E[\tilde{S}(\Omega), \tilde{S}(\Omega')] &= 0, \\ E[\tilde{S}(\Omega), \tilde{S}(\Omega')^*] &= \frac{\mathcal{N}}{2\pi} \delta(\Omega - \Omega'). \end{aligned} \quad (7.14)$$

where \mathcal{N} is the power spectral density (PSD) of ASE noise normalized by $a(0)$ as defined by Eq. (7.2). Note that since we account for gain-loss fluctuations in a way that defines the path-averaged $a(Z)$ to be unity, the value of a at the amplifiers (noise sources) is greater than unity [44, Fig. 7.1], leading to a reduction in the effective PSD of the noise.

The terms that govern the evolution of $\Delta\eta(Z)$ and $\Delta\beta(Z)$ involve integrals over T or equivalently, over $\tau \equiv T - C$. Now, $Q_0(Z, T)$ in Eq. (7.3) can be written as $Q_0 = q \exp(i\Omega\tau)$. Therefore we can write,

$$\frac{d\Delta\eta}{dZ} = -\frac{\kappa^2 \eta^3}{A^2} 2 \text{Im} I_1(\Omega) \quad (7.15)$$

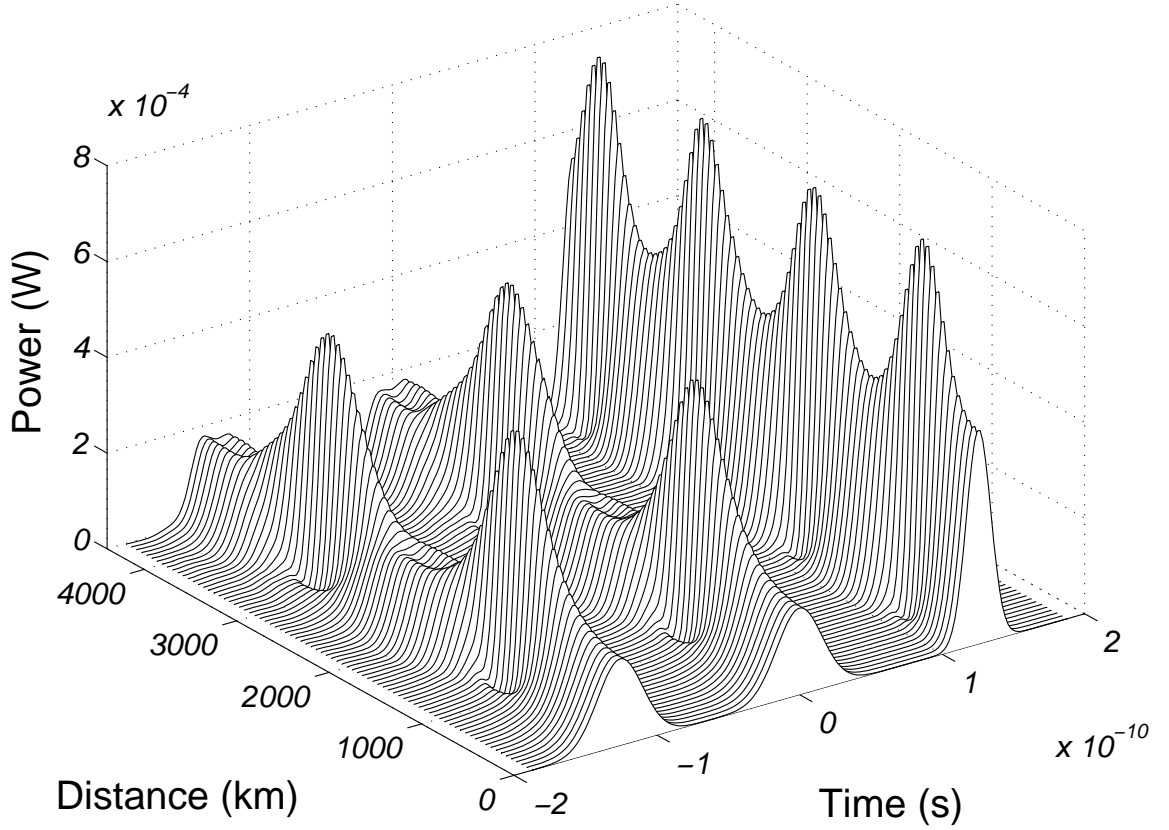


Figure 7.5: Propagation of a pulsetrain of breathing dispersion-managed solitons, numerically calculated directly from the nonlinear Schrödinger equation with $\epsilon = 0$ as for Fig. 7.1, using a different dispersion map and a set of parameters as described in the text.

where $I_1(\Omega)$ is the Fourier transform of $R\tau^2q^*$,

$$I_1(\Omega) \equiv \int d\tau e^{-i\Omega\tau} R\tau^2q^*. \quad (7.16)$$

Similarly, we obtain,

$$\frac{d\Delta\beta}{dZ} = -\frac{\eta^3}{A^2} 2 \operatorname{Im} I_2(\Omega) \quad (7.17)$$

where

$$I_2(\Omega) \equiv \int d\tau e^{-i\Omega\tau} R \left[\frac{1}{2\eta} - 2\kappa^2\eta\tau^2 \right] q^*. \quad (7.18)$$

We will represent the spectral representation of various functions (i.e., Fourier-transformed with respect to τ) by a tilde over the original symbol, e.g., $\tilde{R}(Z, \Omega)$ is obtained from $R(Z, T)$ as follows

$$\tilde{R}(Z, \Omega) = \int d\tau e^{-i\Omega\tau} R(Z, \tau) \quad (7.19)$$

and similarly for other functions.

We define

$$\psi(Z, \tau) \equiv \begin{cases} \tau^2 q(Z, \tau), & \kappa = \eta, \\ \left[\frac{1}{2\eta_0} - 2\kappa^2 \eta_0 \tau^2 \right] q(Z, \tau), & \kappa = \beta. \end{cases} \quad (7.20)$$

Then, Eqs. (7.15) and (7.17) have similar forms,

$$\Delta\kappa \sim \int d\tau e^{i\Omega\tau} [S(T)\psi(Z, T)^* \pm S(T)^*\psi(Z, T)], \quad (7.21)$$

We can therefore obtain the expectations for the spectral density of the variances,

$$E [\Delta\eta(Z, \Omega) \Delta\eta(Z, \Omega)^*] = \left[\frac{3}{8} \sqrt{\frac{\pi}{2}} \frac{b^2}{A^2 \kappa} \right] \mathcal{N} \eta_0^2, \quad (7.22)$$

$$E [\Delta\beta(Z, \Omega) \Delta\beta(Z, \Omega)^*] = \left[\frac{1}{2} \sqrt{\frac{\pi}{2}} \frac{b^2}{A^2 \kappa} \right] \mathcal{N} \eta_0^4. \quad (7.23)$$

7.3.1 RMS radius of the random walk in the phase plane

We assume that the noise terms $\Delta\eta$ and $\Delta\beta$ added by successive amplifiers are independent. If the orbit is traversed a large number of times, each of the points in Fig. 7.4 undergoes a random walk around its unperturbed value. More concisely, the stochastic Poincaré section is characterized by 2D Brownian motion, the variance of which is given by Eqs. (7.22) and (7.23). Connecting the Poincaré section between the k -th and $(k+1)$ -th periods,

$$\begin{aligned} \eta_{k+1} &= \eta_k(1 - r_1), \\ \beta_{k+1} &= \beta_k - \eta_k^2 r_2, \end{aligned} \quad (7.24)$$

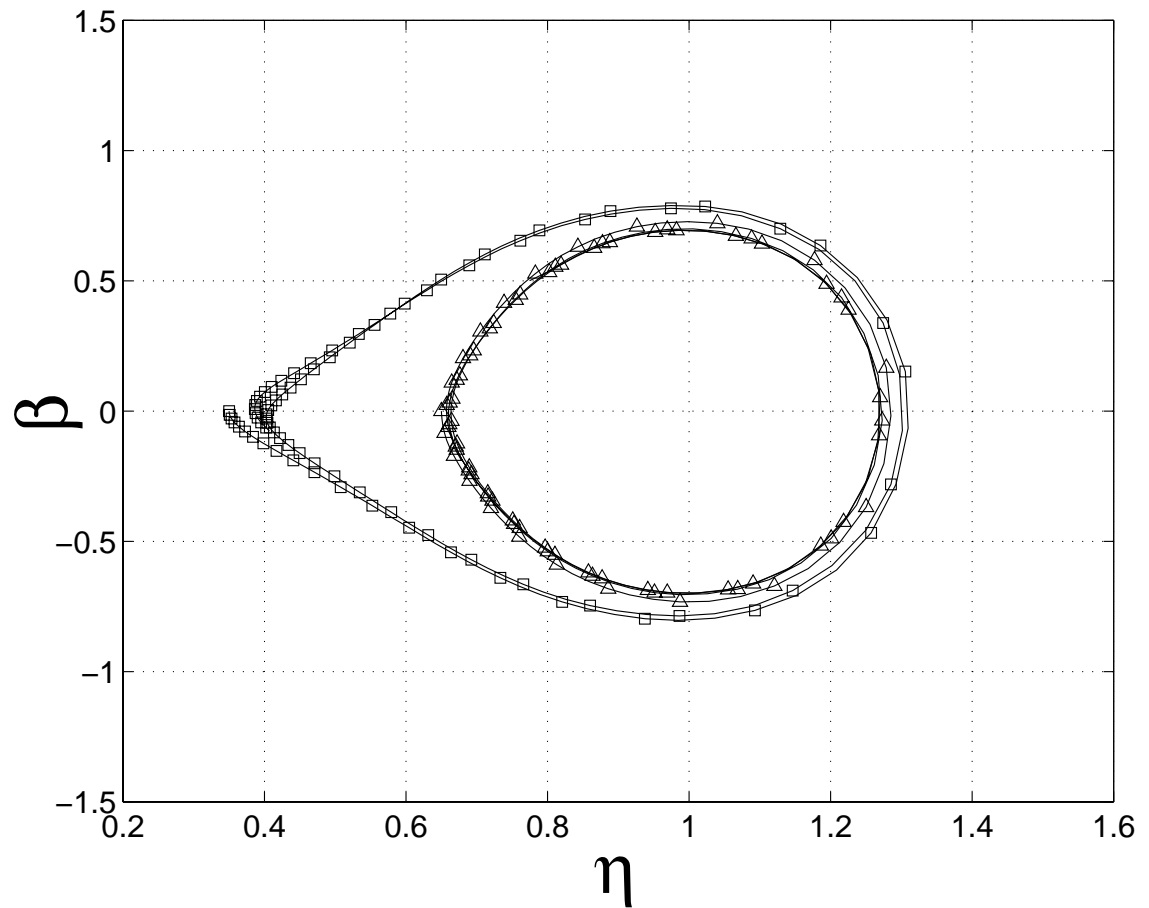


Figure 7.6: The η and β parameters for the second and third bits (from the left) in Fig. 7.5 are plotted against each other, and form closed orbits in the phase plane as before, but the orbits are closer to each other, and are likely to overlap when the effects of ASE noise are accounted for.

where r_1 and r_2 are Gaussian random variables with mean zero and variances σ_η^2 and σ_β^2 defined as the right-hand sides of Eqs. (7.22) and (7.23), respectively. A similar picture in the Argand diagram (amplitude-phase representation) is useful to understand the effect of spontaneous emission on the field of a laser above threshold [79, Fig. (7.10)].

The mean-square radius of this random walk is defined as

$$E[R_k^2] \equiv E [(\eta_k - \eta_0)^2 + (\beta_k - \beta_0)^2] \quad (7.25)$$

in terms of the unperturbed location in the phase plane (η_0, β_0) . This can be calculated explicitly,

$$\begin{aligned} \sqrt{E[R_k^2]} &= \eta_0^2 \left[(1 + \sigma_\eta^2)^k - 1 \right] + \eta_0^4 \frac{\sigma_\beta^2}{3\sigma_\eta^2} \\ &\times \frac{1 + 6\sigma_\eta^2 + 3\sigma_\eta^4}{2 + \sigma_\eta^2} \left[(1 + 6\sigma_\eta^2 + 3\sigma_\eta^4)^k - 1 \right] \end{aligned} \quad (7.26)$$

and since $\mathcal{N} \ll 1$,

$$\sqrt{E[R_k^2]} \approx \eta_0 \sqrt{k} \sqrt{\sigma_\eta^2 + \eta_0^2 \sigma_\beta^2}. \quad (7.27)$$

We may approximate the “effective” RMS radius of an orbit as the average of the RMS radii for each of the η values between the minimum and maximum η values of that particular orbit,

$$r_{\text{eff}} \equiv \Upsilon \int_{\eta \in (\eta_{\min}, \eta_{\max})} E \left[\sqrt{E[R_k^2]} \right]. \quad (7.28)$$

The multiplicative factor of Υ may need some explanation: assuming that the receiver effectively uses the maximum-likelihood (ML) criterion for distinguishing between received pulse widths, the probability of error in distinguishing between η_1 and η_2 is given by the probability of the following event,

$$\eta_1 + \Upsilon \sigma_1 \geq \eta_2 - \Upsilon \sigma_2, \quad (7.29)$$

where σ_i is the standard deviation of η_i , for $i = 1, 2$ (which is given by Eq. (7.28) without the factor of Υ). For example, since each of the two events in Eq. (7.29) is independent of the other, to achieve an error probability of $[\text{erfc}(1/\sqrt{2})]^2 \approx 10\%$, we may set $\Upsilon = 1$, but this is usually too high an error rate for communications. We

choose Υ so that the probability of the above event, Eq. (7.29), is less than 10^{-9} , i.e., $\Upsilon = 4.161$. Each point on the orbit is then assumed to be “broadened” by the effective RMS radii r_{eff} as defined in Eq. (7.28).

Using Table 7.1 for definitions and numerical values of the elementary physical parameters, we find that $2r_{\text{eff}}$ is approximately 0.17 for the orbits shown in Fig. 7.4, as shown in Fig. 7.7. With the parameters we have chosen, propagation over substantially longer distances would be unacceptable as the the circles would overlap.

7.4 Gordon-Haus timing jitter

A phenomenon that does not play a role in the η - β dynamics, but is nevertheless important in the design of the communication scheme is the noise-induced frequency shift, and its conversion into a jitter in the center position of the pulse through the dispersion. The analysis in this section parallels the discussion of the Gordon-Haus effect [42, 82] in dispersion-managed soliton transmission [66, 104].

The differential equation for the evolution of Ω is obtained, in the absence of noise [$\epsilon = 0$ in Eq. (6.1)], from the following equation

$$\frac{\delta L_0}{\delta C} = \frac{\partial L_0}{\partial C} - \frac{d}{dZ} \frac{\partial L_0}{\partial \left(\frac{dC}{dZ} \right)} = 0, \quad (7.30)$$

which shows that

$$-4A^2 \frac{d\Omega}{dZ} = 0, \quad (7.31)$$

i.e., Ω is a conserved quantity when $\epsilon = 0$. However, in the presence of ASE noise, we obtain the equation

$$\begin{aligned} \frac{d\Omega}{dZ} = & -\epsilon \frac{1}{A^2} \int d\tau \kappa^2 \eta^2 \tau 2 \operatorname{Re}[RQ_0^*] \\ & + \epsilon \frac{1}{4A^2} \int d\tau (\Omega + 2\beta\kappa^2\tau) 2 \operatorname{Im}[RQ_0^*]. \end{aligned} \quad (7.32)$$

The same procedure as outlined earlier is followed: we substitute $\Omega(Z) = \Omega_0(Z) + \epsilon \Delta\Omega(Z)$ where Ω_0 is a solution to the unperturbed equation of motion, Eq. (7.31). In the right-hand side of Eq. (7.32), we replace η , β , and Ω with η_0 , β_0 , and Ω_0

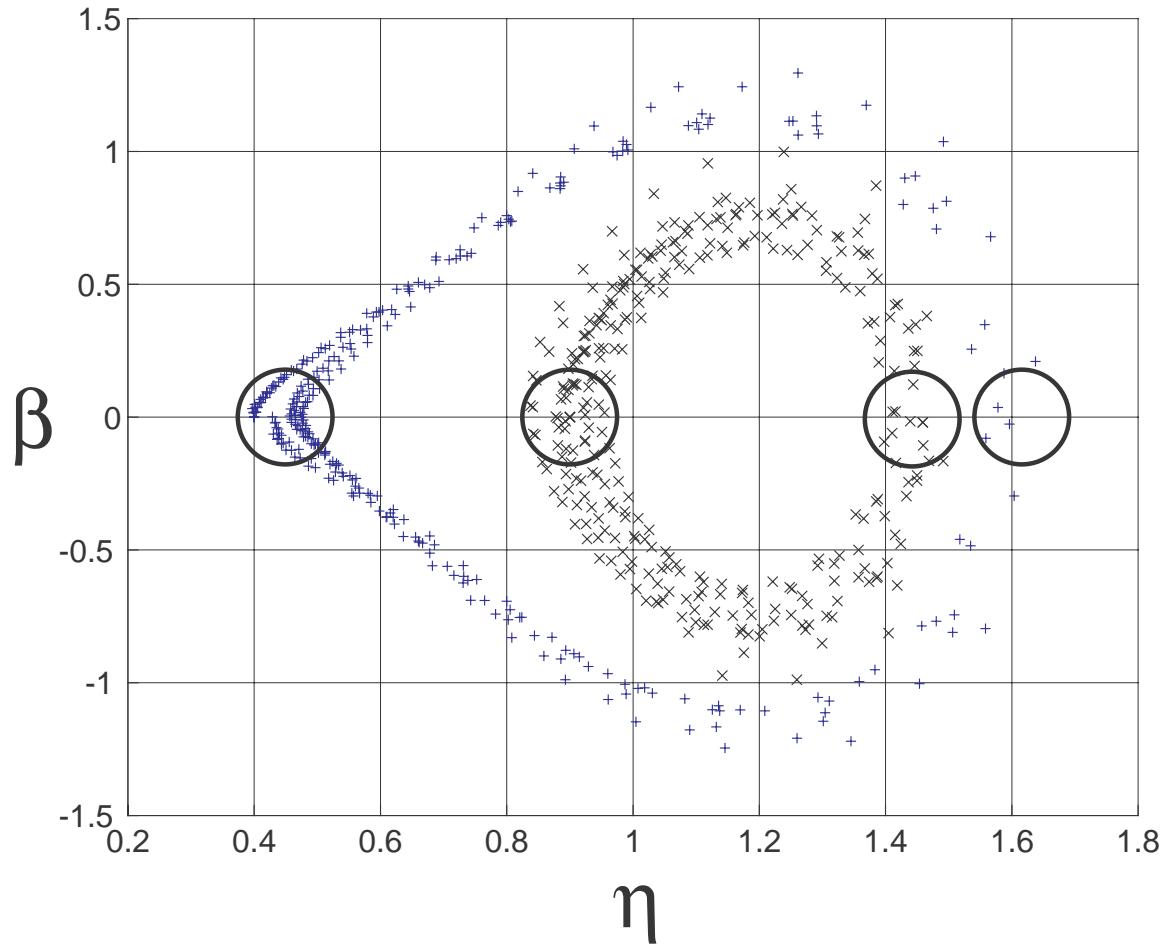


Figure 7.7: Noise-induced broadening of the two contours in the phase-plane shown in Fig. 7.1. The circles drawn around the points representing the received envelope η and β values indicate the effective noise radius for a 10^{-9} probability of error of overlap. The non-uniform density of the points is not of concern, as it indicates only the velocity of the pulse in traversing different parts of the phase plane.

which are the leading-order terms in the respective variables. Eq. (7.12) specifies the perturbation $R(Z, T)$, and the spectral properties of S are given by Eq. (7.14).

In a similar fashion to the earlier analysis, we obtain the expectation for spectral density of the variance of $\Delta\Omega$,

$$E[\Delta\Omega \Delta\Omega^*] = \frac{\kappa^2}{A^2} \left(\eta_0^2 + \frac{1}{4} \frac{\beta_0^2}{\eta_0^2} + \frac{1}{4} \frac{\Omega_0^2}{\kappa^2} \right) \mathcal{N}. \quad (7.33)$$

Similar to Eqs. (7.22) and (7.23), Eq. (7.33) characterizes the effect of a single noise source. As evident from Fig. 7.7, the (η, β) locations of the amplifiers are positioned randomly along the orbit. To obtain approximate analytical expressions, we assume that the coordinates for the n -th amplifier (noise source) η_n and β_n are uniformly distributed and mutually independent random variables,

$$\begin{aligned} \eta_n &\sim U[\eta_{\min}, \eta_{\max}], \\ \beta_n &\sim U[-\beta_{\max}, \beta_{\max}] \end{aligned} \quad n = 1, 2, \dots, N. \quad (7.34)$$

where η_{\min} , η_{\max} , and β_{\max} can be obtained from the results of simulations as shown in Fig. 7.4.

The variance in the frequency Ω leads to a jitter in the temporal position of the pulse: since the group delay is directly proportional to $\beta' \equiv d\beta/d\omega$ [4], a change in the group delay will be caused by a nonzero $\beta'' \Delta\omega$ [42, 82], or $\sigma(z)\Delta\Omega$ in our notation. If we assume that the noise contributions of successive amplifiers are independent, the overall jitter is given by [66]

$$E[\Delta T^2] = \sum_n E[\Delta\Omega_n \Delta\Omega_n^*] \left[\int_{nZ_a}^{N Z_a} dZ \sigma(Z) \right]^2, \quad (7.35)$$

where Z_a is the spacing between amplifiers, and N such amplifiers span the distance between the source and the receiver (see Table 7.1).

Based on the discussion in the previous paragraph, we treat η_n^2 etc. in the argument of the summation in the above equation as functions of uniformly distributed random variables, and replace them with their expected values. We assume $\Omega_0 = 0$ corresponding to the ansatz used in Fig. 7.1. Since in this paper we only consider fibers of uniform GVD, $\sigma(Z) \equiv \bar{D}$, and assume equal spacing between amplifiers, the

expression can be evaluated in closed-form,

$$E [\Delta T^2] = \bar{D}^2 \mathcal{N} \frac{\kappa^2}{A^2} \left\{ \frac{\eta_{\min}^2 + \eta_{\min} \eta_{\max} + \eta_{\max}^2}{3} + \frac{\beta_{\max}^2}{12 \eta_{\min} \eta_{\max}} \right\} \frac{N(N+1)(2N+1)}{6} Z_a^2. \quad (7.36)$$

For large N , the last term in Eq. (7.36) is approximately $(NZ_a)^3/3Z_a$, which identifies with the well-known cubic dependence of the Gordon-Haus jitter on the total transmission length [42, Eq. (16)].

Kumar and Lederer [66] have commented that in dispersion-managed soliton systems that use several amplifiers within a period (i.e., noise sources are encountered at different locations in the phase plane as in this analysis), a path-averaged interpretation of the Gordon-Haus jitter is a good approximation to the actual dynamics. This would be especially true here, since the period of the orbit is not the same as the distance between two successive amplifiers.

To account for the normalizations implicit in Eq. (7.36), we multiply the expression for $E [\Delta T^2]$ by the factor $[1.665\lambda^2/(2\pi c T_{\text{FWHM}})]^2$ [104]; the dimensions of this factor are nm^2 which account for the nm^{-2} from \bar{D}^2 in Eq. (7.36). Using numerical values from Table 7.1, we evaluate the RMS timing jitter for the pulses described in Fig. 7.4:

$$\begin{aligned} \kappa &= 1.18/1.76, \quad A = 1.827, \quad P_0 = 1.57 \text{ mW}, \\ L_D &= \frac{2\pi c}{\lambda^2 \bar{D}} \left(\frac{T_{\text{FWHM}}}{1.665} \right)^2 = 318 \text{ km}, \\ a(0) &= \left[\frac{2\alpha Z_a}{1 - \exp(-2\alpha Z_a)} \right]^{1/2} = 2.177 \\ \eta_{\min} &= 0.80, \quad \eta_{\max} = 1.50 \end{aligned} \quad (7.37)$$

which leads to the RMS timing jitter,

$$\Delta T_{\text{RMS}} \equiv \sqrt{E [\Delta T^2]} \approx 1.63 \text{ ps}. \quad (7.38)$$

For comparison, we have carried out 256 numerical simulations of pulse propagation similar to Fig. 7.7, and using a minimum squared residuals fitting algorithm, we evaluate that $E [\Delta T] = 0.066 \text{ ps} \approx 0$, i.e., zero mean, and $\Delta T_{\text{RMS}} \approx 2.38 \text{ ps}$. The

difference (0.75 ps) between the numerically evaluated RMS timing jitter and the theoretical prediction is less than 0.5% of the inter-pulse time interval and less than 5% of the pulse width, which is very good agreement in light of the approximations made in this analysis (Gaussian statistics, etc.)

A rule of thumb [82] is to allow a detection window of approximately six times the RMS timing jitter for a bit-error-rate of 10^{-9} . In the present case, this fits well within the inter-pulse delay shown in Fig. 7.4, and additional filtering is not needed. The Gordon-Haus jitter is not the dominant limitation with these parameters, but may become more important if we use shorter pulses, or propagate over longer distances.

7.5 Comments

Our analysis so far has focused on the dynamics of pulse propagation in the distributed amplifier approximation. In the case of lumped amplifiers, the pulse amplitude experiences significant variations on a short length scale, and therefore, it is convenient to factor out these variations using $a(Z)$ as described in Section 7.1, and in particular, by using Eq. (7.2). Since $a(Z)$ also appears in Eq. (7.11), the phase-plane dynamics are altered. Fig. 7.8 shows the change in the contour corresponding to one of the orbits that was shown in Fig. 7.4. It is evident that the geometrical structure of the phase plane is not altered and therefore the main conclusions of this paper are equally valid, although the quantitative estimates must of course be recalculated. Further aspects of the differences will be discussed in a separate paper.

The goal of constellation design is simply to pick contours in the phase plane so that their r_{eff} -widened orbits do not intersect, as shown by non-overlapping circles in Fig. 7.7. In the language of nonlinear dynamic systems, we divide the space of orbits $S \in \mathbb{R}^2$ into subsets S_i each of which is invariant (stochastically, with 10^{-9} probability of error) with respect to the flow of the initial value problem (IVP) vector field, i.e., for $\mathbf{x} = (\eta, \beta)^T$,

$$\begin{aligned} \text{If } \mathbf{x}(Z = 0) \equiv \mathbf{x}_0 \in S_k \text{ for a particular } k \\ \text{then } \Pr\{\mathbf{x}(Z) \notin S_k\} \leq 10^{-9} \text{ for all } Z. \end{aligned} \quad (7.39)$$

In the example that we have used for illustrative purposes in this paper, there are

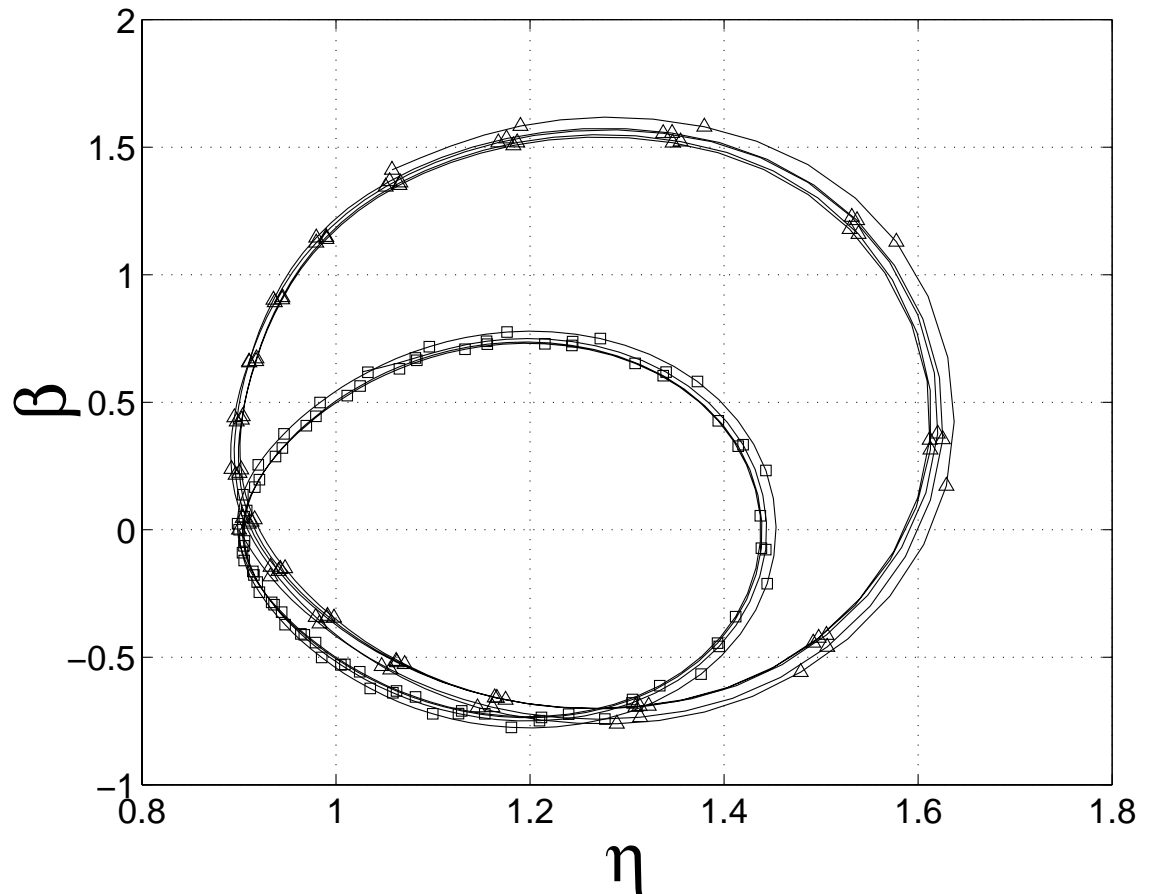


Figure 7.8: As a consequence of strong gain-loss variations ($O(1)$ changes in $a(Z)$ over a period), the contours may change quantitatively, although their geometrical structure is unchanged (isomorphism). Data plotted with squares was shown earlier in Fig. 7.4, and is transformed to the data plotted with triangles as a consequence the strong gain-loss variations.

four multiplexing levels defined by the four circles in Fig. 7.7. These additional levels of multiplexing arise from the nonlinear evolution of the pulse in the phase-plane; critical to their existence is the fact that the Kerr nonlinearity acts in a deterministic manner, and is not merely one of the noise terms as in conventional wavelength-division multiplexing (WDM) transmission formats.

Such a multiplexing scheme is best utilized if receivers can reliably detect the quadratic chirp of the received pulse in real time and with milliwatt pulse powers [137]. Then more than four multiplexing levels can be allowed by selecting non-overlapping neighborhoods for the parameters at the output of the channel. These neighborhoods are isomorphic to circles in \mathbb{R}^2 or n -balls in \mathbb{R}^n . The ultimate limits of such multiplexing are directly related to sphere (or ellipsoid) packing problems in n -dimensions, where n is the number of statistically significant parameters. For shorter distances, more levels may be defined since the noise radii are smaller.

7.5.1 Optimum amplifier gain for fixed total distance

For a fixed distance L between source and receiver, the number of amplifier stages is L/Z_a which can be re-written in terms of the amplifier gain G as $\alpha L/\log G$, where α is the attenuation per unit length of the fiber. Clearly, the number of noise sources encountered by the pulse is inversely proportional to the gain of the amplifiers, G . On the other hand, the noise radius increases with G , since higher gain amplifiers add more ASE noise to the signal [154].

From Eq. (7.27), we can write, as a function of G ,

$$r_{\text{eff}}(G) \sim \left[\frac{G-1}{\log G} \right]^{1/2} \hat{r}_{\text{eff}}, \quad G \geq 1. \quad (7.40)$$

where \hat{r}_{eff} is independent of G . Note that the noise radius increases, and therefore fewer levels of multiplexing are allowed, if high gain amplifiers are used. Further,

$$\lim_{G \rightarrow 1} r_{\text{eff}}(G) = \hat{r}_{\text{eff}}, \quad (7.41)$$

which is the minimum noise radius that can be achieved, i.e., in the limit of a lossless channel. It is interesting that the figure-of-merit for a prototypical *linear* optical transmission shows a similar behavior [153].

In contrast with the proposal by Hasegawa and Nyu [45] for a different nonlinear multiplexing scheme using (non dispersion-managed) solitons, this scheme does not require that the information-carrying parameters (η and β) are unchanged during the course of transmission, but merely that a receiver can clearly distinguish, at its specific location, between their values corresponding to different codes. In addition, this scheme explicitly accounts for dispersion-managed fiber links; this is significant in light of the considerable spans of normal-dispersion fiber already installed in commercial networks.

Higher-dimensional generalizations are richer analytically, but with greater complications in the dynamical evolution. The behavior in the vicinity of non-hyperbolic critical points (such as the center in the phase plane for the AD fibers) requires a more sophisticated analysis of the behavior on the central manifold, using normal form theory, and may result in chaotic behaviour in certain circumstances. If the section of the phase plane in which we define the channel contains several compound separatrix cycles (graphics), with the separatrices homoclinic to the origin (e.g., the topology of the n -bouquet), this would allow zones of multiplexing, with a reduced probability of crossing zones. The physical (design) implications of such topologies are a current research topic.

Each particular implementation has particular features that deserve special attention. In optical transmission, for example, interactions between nonlinearly-multiplexed pulses have been suppressed, since we have taken the nonlinear multiplexing to be super-imposed on top of a WDM and TDM specification. This scheme precludes strong interactions between two pulses with the same carrier frequency and in the same time slot. But multiaccess channels do not typically maximize capacity by orthogonal multiplexing techniques. Optimizing the design of systems in the presence of multiaccess interference *in nonlinear channels* is an open problem. Optical filtering will probably be implemented in the transmission channel to suppress out-of-band radiation and the accumulation of dispersive waves, and to guide the evolution of the nonlinear pulseshapes along desired trajectories.

We have introduced a new format for multiplexed signal transmission dispersion-managed optical fiber communication systems which constructively utilizes the group-velocity dispersion and Kerr nonlinearity present in commonly-used optical fibers. This scheme, called PulseWidth and Chirp Division Multiplexing (PWCDM), is based on the evolution of the chirp and amplitude (width) parameters describing the pulse envelope in the phase plane, most conveniently characterized using a variational approach. Amplified spontaneous emission (ASE) noise from optical amplifiers results in amplitude and chirp jitter, and determines the selection of appropriate multiplexing levels and the design of the signalling constellation. In addition, ASE also results in the Gordon-Haus timing jitter, and if this effect is not compensated, an additional constraint may be imposed on the interpulse temporal separation.

Chapter 8

Space-time analogies in pulse propagation

With the successes of the Glashow-Weinberg-Salam theory of electroweak interactions, the renormalizability proof of gauge theories by t'Hooft, and the developments of QCD, it is now universally accepted that all interactions are based on the gauge principle. I had coined the phrase Symmetry Dictates Interactions to describe this view about the role that symmetry plays in the conceptual structure of nature's fundamental forces, a view that is a dominant theme of contemporary physics.
—C. N. Yang, *Gauge Fields I*, Proc. 20th Int. School Subnuclear Phys. (Ettore Majorana), Erice (1982).

This chapter is an *ab initio* study of pulse propagation phenomena analogous to spatial CW diffraction behavior. We address both linear dispersive evolution as well as the self-phase modulation effects of the nonlinear index of refraction [29]. The latter is responsible for much of the current interest in nonlinear optical communications, since pulse shapes such as solitons and dispersion-managed solitons display much more attractive transmission properties than linear transmission formats (e.g., NRZ) [22].

Such nonlinear pulses are usually self-consistent eigensolutions of a wave equation, which is the primary reason for their robustness to uncompensated spectral broadening and resultant dissipation into the continuum. The conventional hyperbolic secant soliton is an exact solution of the nonlinear Schrödinger equation [4], and propagates indefinitely in a lossless medium without losing its shape. Lossless media can be realized in practice quite effectively by using lumped amplification stages, and erbium-doped fiber amplifiers offer excellent characteristics in this regard.

Breathers, sometimes called dispersion-managed solitons [135, 128], are also self-consistent eigensolutions of the wave equation that propagate with periodic pulse width, chirp, etc., but do not require that the governing system of equations is integrable. While not strictly unchanging in shape, breathers are self-trapped—evolve

back to their initial configuration, essentially traversing a closed, nondegenerate orbit in phase space [68]. Unlike pulse shapes designed for linear transmission channels, these pulses do not require periodic dispersion compensation along the transmission channel, and so offer an attractive alternative to the strong control requirements of the nonlinear Schrödinger soliton.

Characterizing the solutions of the nonlinear wave equation is often simplest via direct numerical simulation, and this has been particularly true for dispersion mapped solitons [81]. In order to understand, capture, and then predict and utilize the essential physics that guides this behavior, a more conceptually accessible framework is sometimes preferable, such as the variational approach with a pulse shape Ansatz [7]. The pulse shape is described as a dynamical system; we write the Hamiltonian based on the action principle and seek solutions to the Euler-Lagrange equations of motion [100, 39]. This approach is not always applicable, however, especially when the Ansatz is incapable of capturing some essential physical behavior. Also, it is somewhat more of an analytical tool for probing the dynamics of systems that we already know something about, or can predict at least partially, and it may be convenient to have other approaches that can offer quick insight into constructive aspects of nonlinear propagation, so that different geometries can be analyzed and compared quickly and easily.

The parallels between dispersive pulse propagation in optical fibers and paraxial CW Gaussian beam diffraction in free space have been identified for some time [5, 157, 14]. More recently, the analogies have been extended to include temporal lenses as a way to translate the imaging properties of spatial lenses into the temporal domain [65]. In this way, pulse correlation and convolution devices may also be constructed [77]. Still more recently, it was shown that temporal lenses can characterize nonlinear effects in the wave equation, leading for example, to the formation of a class of steady-state repeating pulses [155]. This is perhaps the most potentially useful of the space-time analogies, and in this chapter, we will discuss a further extension of this formalism to describe still more powerful applications such as Gaussian pulse propagation in dispersion-managed optical fiber systems, including the effects of the nonlinear index of refraction.

8.1 Gaussian beam diffraction and pulse propagation

Consider the diffraction of an electromagnetic field $E(x, z, t)$ of carrier frequency ω and scalar complex amplitude $u(x, z)$, which obeys the Helmholtz equation

$$\nabla^2 u + k^2 u = 0, \quad k^2 = \omega^2 \mu \epsilon = \left(\frac{2\pi n}{\lambda} \right)^2. \quad (8.1)$$

In the paraxial approximation, we consider only those optical beams whose plane wave components propagate at small angles to the z axis [154],

$$u(z, t) = \sqrt{\frac{ik}{2\pi z}} \int u_0(x') \exp \left[-\frac{ik}{2z} (x - x')^2 \right] dx', \quad (8.2)$$

where $u_0(x)$ is the envelope of the field at $z = 0$.

The propagation of CW Gaussian beams in free space and rotationally symmetric quadratic graded-index media is conveniently described by assuming that the envelope has the form [154]

$$u = \exp \left\{ -i \left[P(z) + \frac{k}{2q(z)} r^2 \right] \right\} \quad (8.3)$$

where we find by substitution into the wave equation (8.1) that $dP/dz = -i/q(z)$ for such media. The q -parameter describes the Gaussian beam completely,

$$\frac{1}{q(z)} = \frac{1}{R(z)} - i \frac{\lambda}{\pi n w^2(z)}. \quad (8.4)$$

In the above definition, $R(z)$ describes the radius of curvature of the beam and $w(z)$ describes the beam spot size.

The usefulness of the q parameter lies in the bilinear transformation ($ABCD$ law) that characterizes how this parameter evolves with propagation. For an optical system described by a real (or complex) 2×2 $ABCD$ matrix, the output q parameter q_o is given by

$$q_o = \frac{Aq_i + B}{Cq_i + D}, \quad (8.5)$$

in terms of the input q parameter q_i . The real and imaginary parts of q_o describe the radius of curvature and spot size of the Gaussian beam at the output of the optical system. Many practically important optical systems and their corresponding

Spatial frequency (Fourier variable)	k_x	Ω	frequency (Fourier variable)
Transverse distance	x	$t - \frac{z}{v_g}$	time (moving ref. frame)
Propagation distance	z	z	propagation distance
Wave vector (inverse)	k^{-1}	$-\beta''$	GVD coefficient (negative)

Table 8.1: Space-time translation rules.

phenomena can be described by simple $ABCD$ matrices, such as propagation in a uniform medium, focusing via a thin lens, beam transformation at a dielectric interface, propagation through a curved dielectric interface and thick lens, propagation in a medium with a quadratic index variation, etc. [154, Table 2-1].

In the temporal case, a single mode in an optical fiber (usually the lowest-order fundamental mode) can be written in terms of the wavenumber β_0 ,

$$E(z, t) = u(z, t) \exp[i(\omega_0 t - \beta_0 z)], \quad (8.6)$$

assuming that the optical field is quasi-monochromatic centered at ω_0 . The differential equation satisfied by u is, to second order of derivatives with respect to the optical frequency ω of the mode propagation constant $\beta(\omega)$ [4],

$$\frac{\partial u}{\partial z} + \beta' \frac{\partial u}{\partial t} + \frac{1}{2} \beta'' \frac{\partial^2 u}{\partial t^2} = 0. \quad (8.7)$$

The solution to the above equation is [156]

$$u(z, t) = \sqrt{\frac{1}{i2\pi\beta''z}} \int u_0(t') \exp\left[\frac{i}{2\beta''z}(T - t')^2\right] dt', \quad (8.8)$$

where $T = t - \beta' z = t - z/v_g$ is the time coordinate in the frame of reference comoving with the pulse envelope at the group velocity $v_g = 1/\beta'$, and $u_0(t)$ is the envelope at $z = 0$. Group-velocity dispersion (GVD) is represented by the parameter β'' .

The formal similarity between Eqs. (8.2) and (8.8) is the principal motivation for this analysis. We can write down a set of space-time translation rules (see Table 8.1) to apply results from spatial diffraction to temporal dispersion and vice versa. One family of results that can be derived from this space-time analogy corresponds to spatial imaging, e.g., the $2-f$ and $4-f$ optical systems. These can be applied to pulse compression or expansion experiments, etc. [65].

But we will see in later sections that many linear and nonlinear pulse propagation systems can be described by cascading simple *ABCD* matrices, and this can result in substantially simpler calculations and more direct physical understanding of the physical processes involved in nonlinear pulse propagation. We will first need to develop some additional facility in characterizing optical systems associated with the pulse propagation equations.

The spatial q -parameter has a temporal equivalent q_t in accordance with the space-time translation rules of Table 8.1 defined by

$$\frac{1}{q_t(z)} = \frac{1}{R_t(z)} + i \frac{2\beta''}{\tau^2(z)}, \quad (8.9)$$

where $\tau(z)$ represents the pulse width (scaled in the T frame by $\sqrt{2}$) and $R_t(z)$ is its chirp. A Gaussian pulse in linearly dispersive fibers is then represented by the envelope [156]

$$u(z, t) = u_0 \frac{\tau_0}{\tau(z)} \exp \left[i \tan^{-1} \frac{z}{\zeta_0} + i \frac{t^2}{2\beta'' R_t(z)} + \frac{\beta''}{|\beta''|} \frac{t^2}{\tau^2(z)} \right], \quad (8.10)$$

where the pulse width and chirp satisfy evolution equations in linear dispersive fibers exactly analogous to their spatial counterparts, beam spot size and radius of curvature, in free space [155]

$$\begin{aligned} \tau^2(z) &= \tau_0^2 \left(1 + \frac{z^2}{\zeta_0^2} \right), \\ R_t(z) &= z \left(1 + \frac{\zeta_0^2}{z^2} \right), \end{aligned} \quad (8.11)$$

with $\zeta_0 = \tau_0^2/2|\beta''|$ defining the dispersion length [4].

8.2 The *ABCD* formalism for Gaussian pulses

As a simple example of the application of the above translation rules, we consider the propagation of a Gaussian input pulse with envelope

$$U(0, T) = \exp \left(-\frac{T^2}{2T_0^2} \right). \quad (8.12)$$

The transmission medium comprises two concatenated sections of fiber with lengths z_1 and z_2 and with GVD coefficients β_1'' and β_2'' respectively. We ignore any nonlinear effects in this simple problem and assume that the medium is lossless. We will determine the pulse characteristics at the output of the second medium, i.e., the pulse width at $z = z_1 + z_2$.

One way of solving this problem is by recourse to the wave equation solution Eq. (8.8) by the Fourier transform technique. We have

$$\begin{aligned}\tilde{U}(z_2, \Omega) &= \tilde{U}(z_1, \Omega) \exp\left(\frac{i}{2}\beta_2'' z_1 \Omega^2\right) \\ &= \tilde{U}(z_0, \Omega) \exp\left[\frac{i}{2}(\beta_1'' z_1 + \beta_2'' z_2) \Omega^2\right].\end{aligned}\quad (8.13)$$

Taking the inverse Fourier transform,

$$\begin{aligned}U(z_1 + z_2, T) &= \frac{1}{2\pi} \int_{-\infty}^{\infty} \tilde{U}(0, \Omega) \exp\left[\frac{i}{2}(\beta_1'' z_1 + \beta_2'' z_2) \Omega^2 - i\Omega T\right] d\Omega \\ &= \left[\frac{T_0^2}{T_0^2 - i(\beta_1'' z_1 + \beta_2'' z_2)}\right]^{1/2} \exp\left[-\frac{T^2}{2(T_0^2 - i(\beta_1'' z_1 + \beta_2'' z_2))}\right],\end{aligned}\quad (8.14)$$

from which we see that the ratio of the output to input pulse width is

$$\frac{T_1}{T_0} = \left[1 + \left(\frac{\beta_1'' z_1 + \beta_2'' z_2}{T_0^2}\right)^2\right]^{1/2}.\quad (8.15)$$

We will now verify Eq. (8.15) using the *ABCD* matrix approach. The system is described very simply by the product of three matrices,

$$\begin{aligned}M &= \begin{pmatrix} 1 & z_2 \\ 0 & 1 \end{pmatrix} \begin{pmatrix} 1 & 0 \\ 0 & \frac{\beta_2''}{\beta_1''} \end{pmatrix} \begin{pmatrix} 1 & z_1 \\ 0 & 1 \end{pmatrix} \\ &= \begin{pmatrix} 1 & z_1 + \frac{\beta_2''}{\beta_1''} z_2 \\ 0 & \frac{\beta_2''}{\beta_1''} \end{pmatrix}\end{aligned}\quad (8.16)$$

so that

$$q_2 = \frac{Aq_1 + B}{Cq_1 + D} = \frac{\beta_1''}{\beta_2''} q_1 + \frac{\beta_1''}{\beta_2''} z_1 + z_2.\quad (8.17)$$

Using the shorthand notation

$$\begin{aligned} R_2 &\equiv R(z_1 + z_2), & R_1 &\equiv R(0), \\ \tau_2 &\equiv \tau(z_1 + z_2), & \tau_1 &\equiv \tau(0), \end{aligned} \quad (8.18)$$

we have

$$\frac{\frac{1}{R_2} - i\frac{2\beta_2''}{\tau_2^2}}{\left(\frac{1}{R_2}\right)^2 + \left(\frac{2\beta_2''}{\tau_2^2}\right)^2} = \frac{\beta_1''}{\beta_2''} \frac{\frac{1}{R_1} - i\frac{2\beta_1''}{\tau_1^2}}{\left(\frac{1}{R_1}\right)^2 + \left(\frac{2\beta_1''}{\tau_1^2}\right)^2} + \frac{\beta_1''}{\beta_2''} z_1 + z_2. \quad (8.19)$$

The real and imaginary parts of both sides of the above equation have to be equal, leading to a pair of simultaneous equations. For an unchirped input pulse, $R_1 = 0$ so that equality of the imaginary parts leads to

$$\left(\frac{1}{R_2}\right)^2 + \left(\frac{2\beta_2''}{\tau_2^2}\right)^2 = \left(\frac{2\beta_2''}{\tau_2\tau_1}\right)^2.$$

Substituting this expression into the equation of equality of the real parts of Eq. (8.19) and some algebraic manipulation leads to

$$\frac{\tau(z_1 + z_2)}{\tau(0)} = \frac{\tau_2}{\tau_1} = \left[1 + \left(\frac{\beta_1'' z_1 + \beta_2'' z_2}{\tau_1^2/2}\right)^2\right]^{1/2}, \quad (8.20)$$

which is the same as Eq. (8.15), since $\tau = \sqrt{2} \Delta T$.

In the above calculation, we have carried out some algebraic simplifications by hand in order to show that the result obtained by the *ABCD* matrix approach is the same as that obtained by the Fourier transform approach. Nevertheless, the former is computationally much simpler, and separating the real and imaginary parts of Eq. (8.19) as part of a numerical algorithm can be carried out without the notational complexity of, for example, rationalizing the denominator.

Our *ABCD* formalism would be of limited interest if the only phenomena it could capture were that of dispersive propagation. The time-lens formalism lets us describe nonlinear mechanisms as well. By analogy to spatial lenses that are characterized by a lens factor $\exp(ikr^2/2f)$ which multiplies an incoming optical beam, we define a temporal lens as a device that multiplies the pulse envelope by a factor [155, 65]

$$\text{Lens Factor} = \exp\left[-i\frac{t^2}{2\beta'' f_t}\right] \equiv \exp[-ibt^2]. \quad (8.21)$$

The $ABCD$ matrix representing a temporal lens has the same form as that of a spatial lens,

$$M = \begin{pmatrix} 1 & 0 \\ -\frac{1}{f_t} & 0 \end{pmatrix}, \quad (8.22)$$

where f_t represents the temporal ‘‘focal length.’’

A comparison of spatial and temporal lensing is shown in Fig. 8.1. In the spatial case, the lens compensates for the spreading of the beam waist and ‘‘flips’’ the phase fronts to convert a diverging beam into a converging one. Similarly, a temporal lens reverses the sign of the chirp, so that further propagation in a $\beta'' < 0$ dispersive fiber will compensate for the chirp (phase modulation) caused this far. This is also an interesting and physically illuminating approach to discussing the physics of the formation of solitons [154, Chap. 19].

One possible implementation, as proposed in [155], is to achieve temporal lensing by self-phase modulation during the passage of the pulse through a section of nonlinear fiber ($\beta'' \approx 0$, $n_2 > 0$). For short distances, $z \ll \pi\tau_0^2/|\beta''|$ and when $\beta''/\tau_0^2 \ll (2\pi n_2/\lambda)I_p$ for peak intensity I_p , a pulse with input electric field envelope $u(0, T)$ emerges from a length z of nonlinear fiber with phase modulation

$$u(z, T) = u(0, T) \exp \left[-i \frac{\omega_0 n_2 z}{2c\eta} |u(0, T)|^2 \right] \quad (8.23)$$

where $\eta = \sqrt{\mu/\epsilon}$ defines the impedance of free space. We write the pulse intensity as

$$I = \frac{|u|^2}{2\eta} = I_p \exp \left[-2 \left(\frac{T}{\tau_0} \right)^2 \right], \quad (8.24)$$

and keep the first two terms in the Taylor expansion of the exponential in Eq. (8.23),

$$u(z, T) = u(0, T) \exp \left[i \frac{2\omega_0 n_2 I_p z}{c\tau_0^2} T^2 \right], \quad (8.25)$$

modulo a phase term linear in z that is independent of T . The effect of propagation through length L of nonlinear fiber is to impart a quadratic chirp to the pulse, which we represent by the multiplicative term $\exp(-ibt^2)$ so that

$$b = \frac{1}{2\beta'' f_t} = -\frac{2\omega_0 n_2 I_p L}{c\tau_0^2}. \quad (8.26)$$

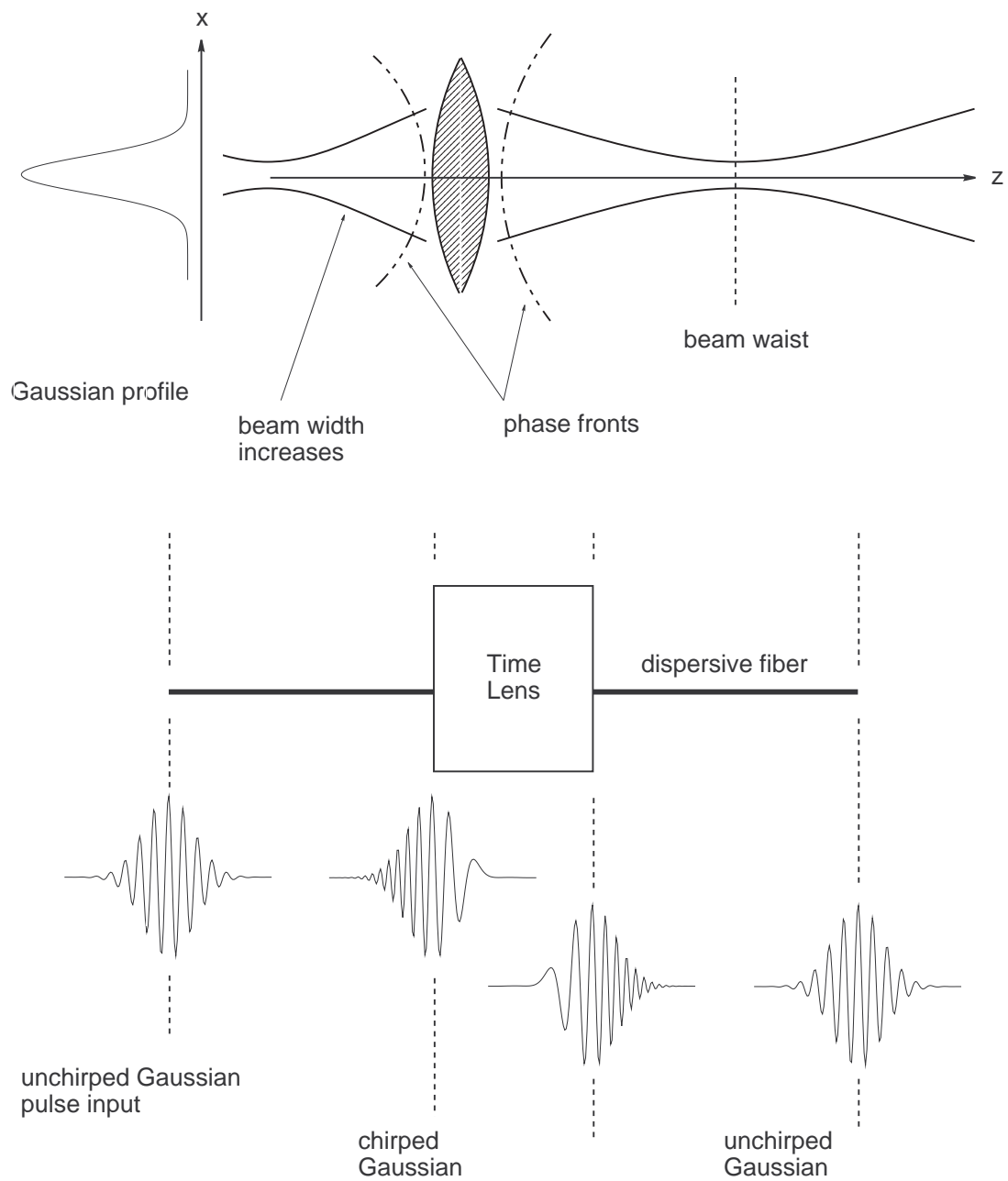


Figure 8.1: (a) Spatial lens and (b) temporal lens showing the parallels between diffraction and dispersion, and techniques for their compensation.

Another method of obtaining time lensing is based on the principle of electro-optic modulation [65]. An electro-optic phase modulator driven by a sinusoidal bias voltage of angular frequency ω_m results in a phase modulation that is approximately quadratic under either extremum of the sinusoid. The phase shift can be written as

$$\exp[i\phi(t)] = \exp \left[-iK \left(1 - \frac{\omega_m^2 t^2}{2} \right) \right], \quad (8.27)$$

where K is the modulation index [154, Sec. 9.4]. In this case,

$$b = \frac{2}{K\omega_m^2}. \quad (8.28)$$

We have described our temporal lens by a section of nonlinear fiber of $\beta'' \approx 0$, analogous to a spatial thin lens, which is assumed to have no thickness. Just as practical lenses do have some thickness, practical fibers have nonzero β'' . For those situations in which this cannot be ignored, or may even be utilized constructively, we derive the corresponding equivalent of a spatial “thick lens.”

Our first step is to characterize the temporal equivalent of a curved dielectric interface: a spatial lens consists of two such interfaces separated by a length of material of enhanced refractive index. At a planar dielectric interface between two media of refractive indices n_1 and n_2 , a Gaussian beam undergoes a change in the radius of curvature, but is unchanged in beam width, [16]

$$R_2 = \frac{n_2}{n_1} R_1, \quad w_1 = w_2. \quad (8.29)$$

By analogy, a chirped Gaussian pulse at the interface between two fibers of GVD coefficients β_1'' and β_2'' transforms to a different chirp, but with unchanged pulse width,

$$\frac{1}{\beta_2'' R_2} = \frac{1}{\beta_1'' R_1}, \quad \tau_1 = \tau_2. \quad (8.30)$$

Of course, the pulse width evolves differently in the two sections of the fiber,

$$\tau_i^2(z) = \tau_{0i}^2 \left(1 + \frac{z^2}{\zeta_{0i}^2} \right), \quad i = 1, 2, \quad (8.31)$$

where ζ_{0i} is the dispersion length in fiber i .

The *ABCD* matrices for a (spatial) spherical dielectric interface and its temporal translation are

$$M : \begin{pmatrix} 1 & 0 \\ \frac{n_2-n_1}{n_2 R} & \frac{n_1}{n_2} \end{pmatrix} \mapsto \begin{pmatrix} 1 & 0 \\ \frac{1-\beta_2''/\beta_1''}{R_l} & \frac{\beta_2''}{\beta_1''} \end{pmatrix}. \quad (8.32)$$

To see what this matrix represents, we use the *ABCD* bilinear transformation,

$$q_2 = q_1 \left/ \left[\frac{1}{R_l} \left(1 - \frac{\beta_2''}{\beta_1''} \right) q_1 + \frac{\beta_2''}{\beta_1''} \right] \right., \quad (8.33)$$

which implies that

$$\begin{aligned} \frac{1}{q_2} &= \left(\frac{1}{R_2} + i \frac{2\beta_2''}{\tau_2^2} \right) \\ &= \frac{1}{R_l} \left(1 - \frac{\beta_2''}{\beta_1''} \right) + \left(\frac{1}{R_1} + i \frac{2\beta_1''}{\tau_1^2} \right) \frac{\beta_2''}{\beta_1''}. \end{aligned} \quad (8.34)$$

After some algebraic manipulation, we can write the above as

$$\beta_1'' \left(\frac{1}{R_l} - \frac{1}{R_2} \right) = \beta_2'' \left(\frac{1}{R_l} - \frac{1}{R_1} \right), \quad (8.35)$$

showing explicitly how the chirp transforms at this interface.

The *ABCD* matrix for a temporal lens of “thickness” d is written as the product of three *ABCD* matrices representing, when read from right to left, a transition from the input fiber to the fiber that defines the thin temporal lens, propagation in the second fiber, and a transition back to the input fiber,

$$M = \begin{pmatrix} 1 & 0 \\ \frac{1-\beta_1''/\beta_2''}{R_2} & \frac{\beta_1''}{\beta_2''} \end{pmatrix} \begin{pmatrix} 1 & d \\ 0 & 1 \end{pmatrix} \begin{pmatrix} 1 & 0 \\ \frac{1-\beta_2''/\beta_1''}{R_1} & \frac{\beta_2''}{\beta_1''} \end{pmatrix}.$$

Multiplying the matrices together, we get a single *ABCD* matrix that defines the output q_t parameter via the usual bilinear transformation $(Aq_t + B)/(Cq_t + D)$,

$$M = \begin{pmatrix} 1 + \frac{d}{R_1} \left(1 - \frac{\beta_2''}{\beta_1''} \right) & d \frac{\beta_2''}{\beta_1''} \\ \frac{d}{R_1(-R_2)} \left(\frac{\beta_2''}{\beta_1''} - 1 \right) \left(1 - \frac{\beta_1''}{\beta_2''} \right) - \left(\frac{1}{R_1} + \frac{1}{-R_2} \right) \left(1 - \frac{\beta_1''}{\beta_2''} \right) & 1 + \frac{d}{-R_2} \left(1 - \frac{\beta_2''}{\beta_1''} \right) \end{pmatrix}. \quad (8.36)$$

The temporal focal length \hat{f}_t is analogous to the spatial focal length and is given by $-A/C$,

$$\hat{f}_t = \left[1 + \frac{d}{R_1} \left(1 - \frac{\beta_2''}{\beta_1''} \right) \right] / \left[\left(\frac{1}{R_1} + \frac{1}{-R_2} \right) \left(1 - \frac{\beta_1''}{\beta_2''} \right) - \frac{d}{R_1(-R_2)} \left(\frac{\beta_2''}{\beta_1''} - 1 \right) \left(1 - \frac{\beta_1''}{\beta_2''} \right) \right]. \quad (8.37)$$

The temporal focal length defines the time from the output plane at which an initially unchirped pulse becomes unchirped again.

We can write the above in slightly simpler notation, for the specific case $R_1 = -R_2 = R$, and let $\kappa = d/R$, $\Delta\beta'' = \beta_2'' - \beta_1''$,

$$\hat{f}_t = \left[\frac{1 - \kappa \frac{\Delta\beta''}{\beta_1''} \frac{\beta_2''}{\Delta\beta''}}{1 - \frac{\kappa \Delta\beta''}{2 \beta_1''} \frac{\Delta\beta''}{\Delta\beta''}} \right] \frac{R}{2}, \quad (8.38)$$

where the term in parentheses represents an enhancement factor over the “thin lens” formula.

For $\kappa \ll 1$, we can simplify the above expression keeping terms of $O(\kappa)$,

$$\begin{aligned} \frac{1}{\hat{f}_t} &\approx \left(1 - \frac{\kappa \Delta\beta''}{2 \beta_1''} \right) \left(1 + \kappa \frac{\Delta\beta''}{\beta_1''} \right) \frac{2\Delta\beta''}{R \beta_2''} \\ &\approx \left(1 + \frac{\kappa \Delta\beta''}{2 \beta_1''} \right) \frac{2\Delta\beta''}{R \beta_2''}. \end{aligned} \quad (8.39)$$

The above relation confirms our physical intuition that if $\beta_2'' - \beta_1'' = \Delta\beta'' < 0$, then we have reduced f_t , the distance to the point of zero chirp from the output plane, for an initially unchirped input pulse.

We now have the tools we need to analyze a reasonably complicated practical problem: designing the length of a dispersion map so as to get self-consistent eigenpulses with periodic pulse width and chirp.

8.3 DM soliton transmission experiment

It has been recently found that a stable, self-consistent pulse solution exists in a dispersion-managed fiber transmission system [128]. While these are not solitons in the strict mathematical sense, they have been called dispersion-managed solitons or perhaps more appropriately, breathers. They demonstrate periodic behavior: the pulse width and chirp of Gaussian breathers, for instance, are periodic functions of the propagation distance. Breathers share a property in common with solitons, in that they can propagate indefinitely without losing shape; even though the pulse shape undergoes changes within a dispersion map period, the pulse does not disperse away to infinity or tend to self-focus to a point, either of which invalidate the applicability of the nonlinear Schrödinger equation after a certain distance.

A dispersion-managed (DM) soliton is closer to a Gaussian shape than the hyperbolic secant of the nonlinear Schrödinger equation [73], and it is interesting to ask whether our analysis is capable of capturing the essential aspects of its evolution along a dispersion-managed transmission channel.

We consider, as our example, the paper by Mu et al. [97] who have simulated DM soliton dynamics in a recirculating fiber loop. Their dispersion map consists of 100 km of dispersion shifted fiber (SMF-LS) with normal dispersion D_1 equal to -1.10 ps/nm-km at 1551 nm, followed by an “approximately 7 km span” of standard single-mode fiber (SMF-28) with an anomalous dispersion D_2 equal to 16.6 ps/nm-km at 1551 nm. The results of the paper indicate that Gaussian shaped pulses of pulse duration 5.67 ps and peak power 9 dBm were used. We will derive the result that, for these parameters and given the length of SMF-LS fiber, the length of SMF-28 fiber that needs to be used is indeed “approximately 7 km.” In other words, we will show that this given dispersion map can support lowest-order chirped Gaussian self-consistent solutions, i.e., breathers.

The dispersion map, shown schematically in Fig. 8.2, consists of three fiber segments: a length $z_1/2$ equal to 50 km of SMF-LS fiber, followed by a length z_2 of SMF-28 fiber whose numerical value is to be determined, and then the remainder $z_1/2$ of SMF-LS fiber. Each segment of fiber has nonlinear characteristics, which we model via a time lens situated for simplicity at the individual midpoints of the respective segments. Consequently, each segment is described by the cascaded product of three $ABCD$ matrices, with two additional matrices representing the transitions

between fibers of different β'' . For simplicity, we will assume that the nonlinear properties of the fibers are identical.

The overall $ABCD$ matrix for the system can be written as the product of the following eleven matrices,

$$\begin{aligned}
 M = & \begin{pmatrix} 1 & z_1/4 \\ 0 & 1 \end{pmatrix} \begin{pmatrix} 1 & 0 \\ -1/f_t & 1 \end{pmatrix} \begin{pmatrix} 1 & z_1/4 \\ 0 & 1 \end{pmatrix} \begin{pmatrix} 1 & 0 \\ 0 & \beta_1''/\beta_2'' \end{pmatrix} \\
 & \begin{pmatrix} 1 & z_2/2 \\ 0 & 1 \end{pmatrix} \begin{pmatrix} 1 & 0 \\ -1/f_t & 1 \end{pmatrix} \begin{pmatrix} 1 & z_2/2 \\ 0 & 1 \end{pmatrix} \begin{pmatrix} 1 & 0 \\ 0 & \beta_2''/\beta_1'' \end{pmatrix} \\
 & \begin{pmatrix} 1 & z_1/4 \\ 0 & 1 \end{pmatrix} \begin{pmatrix} 1 & 0 \\ -1/f_t & 1 \end{pmatrix} \begin{pmatrix} 1 & z_1/4 \\ 0 & 1 \end{pmatrix}, \tag{8.40}
 \end{aligned}$$

which after some algebra can be written as a single 2×2 $ABCD$ matrix with the following elements,

$$\begin{aligned}
 A = & \left[\left(1 - \frac{z_1}{4f}\right) \left(1 - \frac{z_2}{2f}\right) - \frac{z_1 \beta_1''}{4f \beta_2''} \left(2 - \frac{z_1}{4f}\right) \right] \left(1 - \frac{z_1}{4f}\right) \\
 & - \left[\frac{\beta_2''}{\beta_1''} \left(1 - \frac{z_1}{4f}\right) \left(2 - \frac{z_2}{2f}\right) \frac{z_2}{2f} + \left(2 - \frac{z_1}{4f}\right) \left(1 - \frac{z_2}{2f}\right) \frac{z_1}{4f} \right], \tag{8.41}
 \end{aligned}$$

$$\begin{aligned}
 B = & \left[\left(1 - \frac{z_1}{4f}\right) \left(1 - \frac{z_2}{2f}\right) - \frac{z_1 \beta_1''}{4f \beta_2''} \left(2 - \frac{z_1}{4f}\right) \right] \frac{z_1}{4} \left(2 - \frac{z_1}{4f}\right) \\
 & + \left[\frac{\beta_2''}{\beta_1''} \left(1 - \frac{z_1}{4f}\right) \left(2 - \frac{z_2}{2f}\right) \frac{z_2}{2} + \left(2 - \frac{z_1}{4f}\right) \left(1 - \frac{z_2}{2f}\right) \frac{z_1}{4} \right] \left(1 - \frac{z_1}{4f}\right), \tag{8.42}
 \end{aligned}$$

$$\begin{aligned}
 C = & -\frac{1}{f} \left[\left(1 - \frac{z_2}{2f}\right) + \frac{\beta_1''}{\beta_2''} \left(1 - \frac{z_1}{4f}\right) \right] \left(1 - \frac{z_1}{4f}\right) \\
 & - \frac{1}{f} \left[-\frac{\beta_2''}{\beta_1''} \frac{z_2}{2f} \left(2 - \frac{z_2}{2f}\right) + \left(1 - \frac{z_2}{2f}\right) \left(1 - \frac{z_1}{4f}\right) \right]. \tag{8.43}
 \end{aligned}$$

$$\begin{aligned}
 D = & -\frac{z_1}{4f} \left[\left(1 - \frac{z_2}{2f}\right) + \frac{\beta_1''}{\beta_2''} \left(1 - \frac{z_1}{4f}\right) \right] \left(2 - \frac{z_1}{4f}\right) \\
 & - \left[\frac{\beta_2''}{\beta_1''} \frac{z_2}{2f} \left(2 - \frac{z_2}{2f}\right) - \left(1 - \frac{z_2}{2f}\right) \left(1 - \frac{z_1}{4f}\right) \right] \left(1 - \frac{z_1}{4f}\right), \tag{8.44}
 \end{aligned}$$

The algebraic complexity of writing out the expressions explicitly should not mask the simplicity of multiplying 2×2 matrices, usually numerically. Note that the expression Eq. (8.44) for D is algebraically identical to that for A , Eq. (8.41), and it may be verified that $AD - BC = 1$.

The q parameter (we have dropped the t subscript in this section for notational elegance) evolves according to the bilinear transformation law and we require that the pulse repeat itself after propagation through one such $ABCD$ matrix,

$$\frac{1}{q} = \frac{A + B/q}{C + D/q}, \quad (8.45)$$

which has the solution

$$\frac{1}{q} = \frac{D - A}{2B} \pm i \frac{\sqrt{1 - \left(\frac{D + A}{2}\right)^2}}{B}. \quad (8.46)$$

Since $D = A$ in our above analysis, we already see that q is purely imaginary at $z = 0$, i.e., the pulse has zero chirp at the midplanes as we would expect a breather to have.

At this stage, we can substitute numerical values for the various parameters (except z_2 , which is what we seek) into the expressions for the A , B , C , and D elements Eqs. (8.41–8.44) and solve Eq. (8.46) numerically for z_2 . While this is not difficult and already yields a quick solution to the problem at hand, we can get further insight via a well-justified simplification as follows.

The q parameter at the midplanes, where it is purely imaginary, is given by

$$\frac{1}{q_0} = \frac{2|\beta_1''|}{\tau_0^2}, \quad (8.47)$$

where $\beta_1'' = 1.40 \times 10^{-27} \text{ s}^2/\text{m}$ and input pulse width $\tau_0 = 5.67 \times 10^{-12} \text{ s}$. Consequently, for such pulses $1/q \approx 0$ and since $A = D$ this implies that $A = 1$ in Eq. (8.46).

With the notational substitutions

$$x = \frac{z_2}{2f}, \quad y = \frac{z_1}{4f}, \quad \beta_r'' = \frac{\beta_1''}{\beta_2''} \quad (8.48)$$

we get the necessary condition

$$\begin{aligned} & [(1 - y)^2 - (2 - y)y] (1 - x) - \beta_r'' y (2 - y) (1 - y) \\ & - \frac{1}{\beta_r''} (1 - y) (2 - x) x = 1. \end{aligned} \quad (8.49)$$

The solution of this equation is given by

$$x = \beta_r'' \frac{y(2-y)}{1-y}, \quad (8.50)$$

or, in terms of the initial variables,

$$z_2 = \left| \frac{\beta_1''}{\beta_2''} \right| \frac{\frac{z_1}{2} \left(2 - \frac{z_1}{4f} \right)}{\left(1 - \frac{z_1}{4f} \right)}, \quad (8.51)$$

which is the necessary condition in order to have a stable self-consistent Gaussian eigenpulse (breather) solution to the dispersion-map problem.

All that remains is for us to interpret the variables in terms of the original problem and numerically evaluate this expression to get the desired length z_2 of SMF-28 fiber in this dispersion map. The various numerical values are as follows:

$$\begin{aligned} \beta_1'' &= 1.40 \times 10^{-27} \text{ s}^2/\text{m}, \\ \beta_2'' &= -2.12 \times 10^{-26} \text{ s}^2/\text{m}, \\ \tau_0 &= 5.67 \times 10^{-12} \text{ s}, \\ z_1 &= 10^5 \text{ m}. \end{aligned}$$

Given the nature of the problem, we realize our time lens with the nonlinear fiber as described earlier (Eq. 8.26), so that

$$\frac{1}{f} = -4\beta_{NL}'' \left(\frac{2\pi}{\lambda} \right) \frac{n_2 I_p L_{NL}}{\tau^2} \quad (8.52)$$

and take $\beta_{NL}'' = \beta_2''$, $I_p = 3.62 \times 10^6 \text{ W/m}^2$ so that with fiber core area $A_{\text{eff}} = 47 \text{ } \mu\text{m}^2$, we get $P = 8 \text{ mW} = 9 \text{ dBm}$. Also, we take $L_{NL} = z_2$ consistent with our choice of β_{NL}'' .

The numerical solution (of the quadratic equation) for z_2 is equal to 7.00 km, which is indeed the value ‘‘approximately 7 km’’ stated in the paper [97]. In spite of apparent exact agreement, we should be careful to appreciate that this analysis is a characterization of only the most important processes in this experiment. Possible sources for approximation include the fact that a DM soliton is only approximately

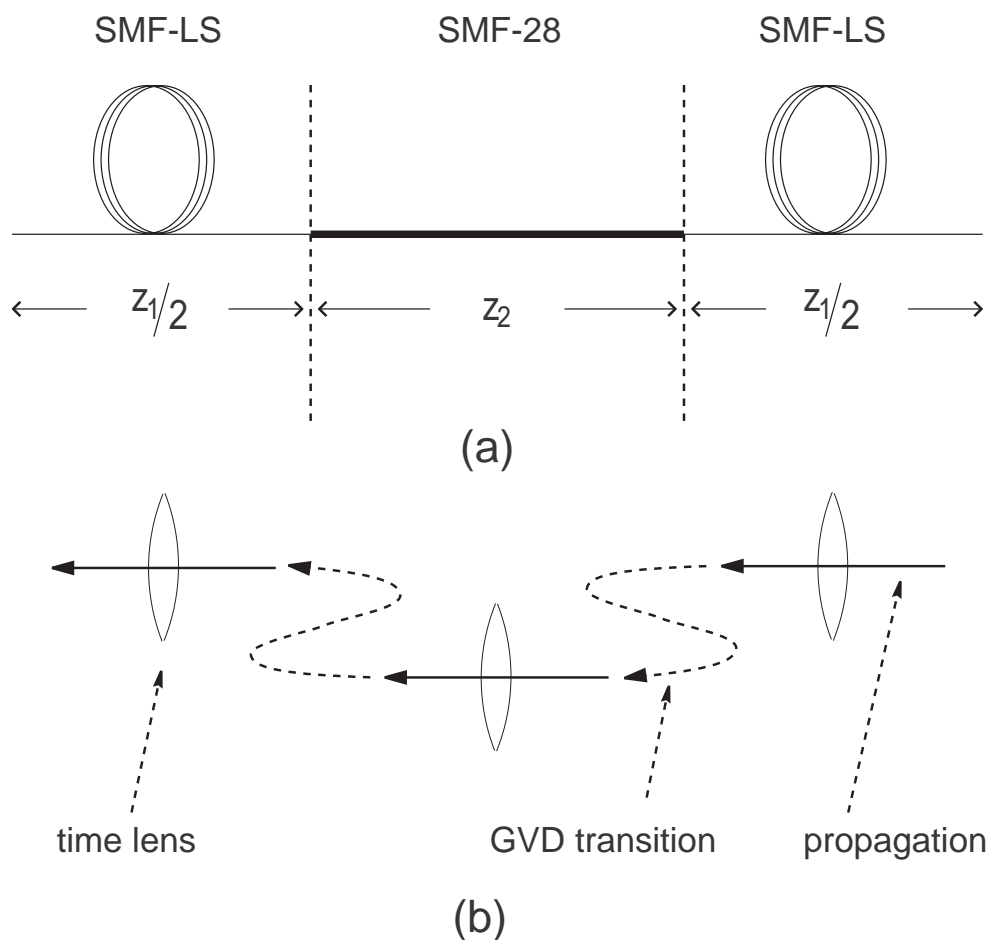


Figure 8.2: (a) Analytical schematic of dispersion map from [97] and (b) its representation to express in terms of $ABCD$ matrix elements.

Gaussian, and that we have represented the combined dispersive and nonlinear properties of the fiber segments by a single temporal lens. A better approximation may be to include several temporal lenses for each segment of the fiber; this would make the algebraic expressions in this paper quite cumbersome to write down explicitly, but the numerical computation would not be much more difficult since the matrices are only 2×2 in size and comprise of purely real elements. The experimental configuration of [97] also includes several other elements that can affect the pulse shape such as filters, fiber amplifiers, and polarization controllers.

8.4 Hermite-Gaussian basis

Our $ABCD$ matrix formalism for pulse propagation applies to chirped Gaussian pulses. To analyze more complicated shapes, we can expand the given pulse shape in a basis of chirped Hermite-Gaussian functions, which form a complete orthonormal basis [50, 73]. The Hermite-Gaussian function (we consider only unchirped Gaussians here for simplicity) of order n is defined as the product of the Hermite polynomial of order n with a Gaussian function,

$$\psi_n(t) \equiv H_n(t) \exp(-t^2/2), \quad (8.53)$$

where, for example,

$$H_0(t) = 1, \quad H_1(t) = 2t, \quad H_2(t) = 4t^2 - 2. \quad (8.54)$$

We can expand an arbitrary input amplitude $u_0(t)$ in this basis, analogous to expanding a field in terms of plane wave components, as in solution techniques of the standard parabolic diffraction equation by means of the Fourier transform,

$$u_0(t) = \sum_{n=0} c_n H_n(t) \exp(-t^2/2), \quad (8.55)$$

where because of orthogonality of the Hermite-Gaussian functions, the expansion coefficients are given by

$$c_n = \frac{1}{\sqrt{\pi} 2^n n!} \int_{-\infty}^{\infty} u_0(t) H_n(t) \exp(-t^2/2). \quad (8.56)$$

The propagation equation (8.8) defines the output pulse shape as the convolution of the input shape with a Gaussian kernel. Hermite-Gaussian functions, when convolved with a Gaussian, yield the product of a Hermite polynomial and a Gaussian [50],

$$\int_{-\infty}^{\infty} dt_0 \psi_n(t_0) \exp\left[-\frac{a}{2}(t-t_0)^2\right] = \sqrt{\frac{2\pi}{a+1}} \left(\frac{a-1}{a+1}\right)^{n/2} \exp\left[\frac{a t^2}{2(a^2-1)}\right] \psi_n\left[\frac{a}{\sqrt{a^2-1}}t\right]. \quad (8.57)$$

Taking as input the n th Hermite-Gaussian mode $u_0 = \psi_n(t)$ (which has width

$\tau_0 = \sqrt{2}$), the amplitude of this mode after propagation through distance z is

$$u_n(z, T) = \sqrt{\frac{1}{1 + i\beta''z}} \left[\frac{1 + \frac{i}{\beta''z}}{1 - \frac{i}{\beta''z}} \right]^{n/2} \times \exp \left[\frac{i}{2\beta''z} \frac{T^2}{1 + \frac{1}{(\beta''z)^2}} \right] \psi_n \left[\frac{T}{\sqrt{1 + (\beta''z)^2}} \right], \quad (8.58)$$

which can be seen to agree with (8.11).

A Hermite-Gaussian function therefore maintains its shape during propagation, but adds a chirp (which is the same for all modes) and a scaling of the width according to Eq. (8.11). Power conservation implies that the amplitude correspondingly scales down. The only term that is dependent on the order of the Hermite-Gaussian function is a phase term; higher-order modes have greater phase advances, since their spectral content is higher. The important observation is that the orthogonality of the Hermite-Gaussian expansion is preserved, and so this expansion may be used to predict the pulse shape obtained by propagating an input pulse. Our formalism remains valid as long as the differential equation describing the propagation of a particular order Hermite-Gaussian function is of the form Eq. (8.7), i.e., the slowly varying envelope approximation is valid. Therefore, we can expect that the lower-order expansions are usually valid; the results of applying our analysis to higher-order expansion terms generate the residual field corrections to the lower-order results [136].

We have developed a 2×2 *ABCD* matrix formalism for pulse propagation in media described by Maxwell's equations, accounting for dispersion, nonlinear, and gain/loss mechanisms. The method is analogous to techniques used in CW beam diffraction analysis, and correspondingly similar phenomena can be predicted, such as chirp transformation, focusing, periodic pulse width expansion and narrowing, etc. The spatial q parameter has a temporal equivalent q_t in accordance with the given space-time translation rules. The real and imaginary parts of q_t^{-1} represent the chirp and the width of the pulse as a function of propagation distance z .

The propagation of various input pulse shapes can be described by expanding the given pulse in a basis of Hermite-Gaussian functions; the $ABCD$ formalism applies to each Gaussian wave function separately. Propagation through a complicated system of optical elements is simple to calculate in terms of $ABCD$ matrices: the resultant matrix is the cascaded product of the $ABCD$ matrices of each of the individual elements with the appropriate ordering. The overall q_t parameter is given by a bilinear transformation in terms of the $ABCD$ elements of the overall product matrix, exactly analogous to the spatial case.

8.5 Geometric analogies

As we have seen in the previous sections, analogies between spatial Gaussian beam diffraction and temporal Gaussian pulse dispersion have been well established [5] and extended more recently to introduce the concept of a time lens as a quadratic phase modulator, applied in temporal imaging configurations, for temporal filtering and transforms [65, 77] and in nonlinear dispersive optical communications [155, 89]. Now, we investigate Gaussian optical pulse propagation with periodically varying pulse width and chirp (“breathers”) in a nonlinear dispersive fiber in the context of such space-time analogies, but from a topological perspective rather than the algebraic correspondence of variables. This method, illustrated in this section for the simplest of cases, can lead to a deeper understanding of pulse propagation based on the geometrical structure of the topological space of solutions and their classifications in terms of homotopy groups [88].

The problem of pulse propagation in a dispersive nonlinear medium has some basic features which are strongly suggestive of steady-state optical beam propagation in a medium with a quadratic radial index dependence. This can be seen for instance in Fig. 8.3 which shows the results of numerical simulations of (a) Gaussian pulse evolution in a hypothetical optical fiber described such that the propagation equations are exactly analogous to those describing Gaussian beam evolution in a rotationally symmetric quadratic graded-index medium and (b) Gaussian pulse evolution in an optical fiber with the Kerr effect. Since, as will be discussed, closed-form spatially periodic solutions to the earlier problem (a) are known, it is intriguing to inquire if the same form of the solution can be applied to the second problem (b) which is of practical interest, and if not, where the analogy fails in spite of the easily visible

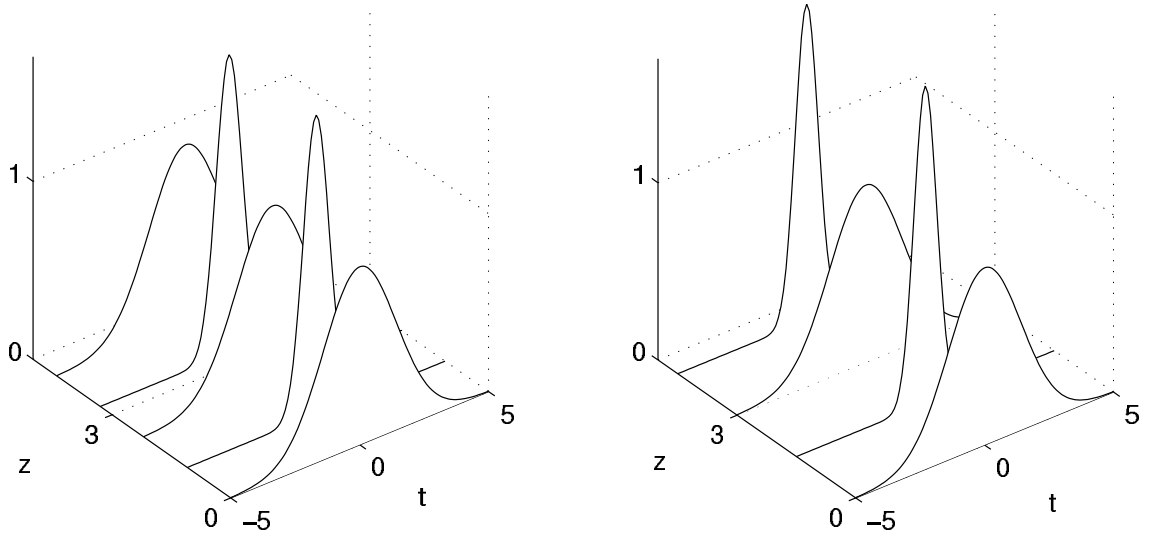


Figure 8.3: Temporal evolution of a Gaussian breather pulse: (a) in a hypothetical medium described by Eq. (8.65), and exactly analogous to Gaussian beam propagation in a RSQ-GRIN fiber and (b) in a realistic fiber with the Kerr effect, and described by Eq. (8.68).

affinity shown in Fig. 8.3.

We study this problem in the context of space-time dualities by first looking at the spatial beam diffraction problem. For plane waves with a Gaussian envelope $A(r, z)$ propagating with a complex propagation constant $k(r)$ in a rotationally-symmetric quadratic graded-index (RSQ-GRIN) media characterized by a quadratic constant k_2 [154], Maxwell's equations and the slowly varying envelope approximation lead to a parabolic partial differential equation for $A(r, z)$,

$$\nabla_{\perp}^2 A - 2ik \frac{\partial A}{\partial z} - kk_2 r^2 A = 0 \quad (8.59)$$

where ∇_{\perp}^2 is the transverse Laplacian operator and r is the distance from the cylindrical axis of symmetry. We typically use the following form for the envelope [154]

$$A(r, z) = \exp \left[i \left(P(z) + \frac{k}{2q(z)} r^2 \right) \right], \quad (8.60)$$

with the q -parameter

$$\frac{1}{q(z)} \equiv \frac{1}{R(z)} - i \frac{2\lambda}{kw^2(z)} \quad (8.61)$$

defined in terms of the the beam spot size $w(z)$ and the radius of curvature of the beam $R(z)$. The solution $q(z)$ for a given unchirped ($R(0) = 0$) input characterized by $q(0) = q_0$ is expressed in closed form by an $ABCD$ bilinear transformation [154],

$$q(z) = \frac{A(z)q_0 + B(z)}{C(z)q_0 + D(z)}, \quad (8.62)$$

where

$$\begin{aligned} A(z) &= \cos\left(\sqrt{\frac{k_2}{k}}z\right), & B(z) &= \sqrt{\frac{k}{k_2}} \sin\left(\sqrt{\frac{k_2}{k}}z\right), \\ C(z) &= -\sqrt{\frac{k_2}{k}} \sin\left(\sqrt{\frac{k_2}{k}}z\right), & D(z) &= \cos\left(\sqrt{\frac{k_2}{k}}z\right). \end{aligned} \quad (8.63)$$

This form of the solution clearly shows the breathing nature of the wave envelope, i.e., periodic in width and in radius of curvature.

Next, in discussing temporal Gaussian pulse propagation, we know that group-velocity dispersion (GVD) leads to broadening or narrowing of the temporal envelope depending on the signs of the GVD parameter β'' and chirp, although the shape remains Gaussian. We may counteract this effect by utilizing self-phase modulation (SPM) caused by a nonzero nonlinear-index coefficient n_2 . Breathers can be formed when spectral broadening from a positive n_2 balances anomalous dispersion ($\beta'' < 0$) in fibers. Similarly, negative n_2 as found in AlGaAs waveguides [70] can compensate the effect of normal dispersion, and breathers can be created in this case as well. Self-consistent Gaussian breathers differ from conventional solitons [154] in that the pulse parameters vary periodically in such a way that the pulse envelope can, by assumption, always be described by a Gaussian function.

If SPM were to result in a (temporal) term analogous to the kk_2r^2 term in (8.59), the solution would be temporally breathing Gaussian pulses similar to the spatial case of breathing Gaussian beams, and this would satisfactorily explain the similarities of Fig. 8.3: the solution would be given in closed form by the temporal equivalent of

Eq. (8.62), using the space-time translation rules tabulated in Table 8.1,

$$z \mapsto z, \quad r \mapsto T, \quad \nabla_{\perp}^2 \mapsto \nabla_T^2, \quad k \mapsto -1/\beta'', \quad k_2 \mapsto 4\gamma, \quad (8.64)$$

where $T = t - z/v_g$ is the temporal coordinate in the reference frame co-moving with the pulse at the group velocity and $\gamma = n_2\omega_0/(cA_{\text{eff}})$ is the nonlinearity coefficient defined in terms of the optical frequency ω_0 and effective core area A_{eff} .

It is easily seen, however, that this is not the case. Applying the translation rules (8.64) to Eq. (8.59) yields

$$-i\frac{\partial A}{\partial z} + \frac{\beta''}{2}\frac{\partial^2 A}{\partial T^2} + \frac{b_2}{2}T^2A = 0, \quad (8.65)$$

which we will refer to in this paper as the temporal RSQ-GRIN problem, whose solution is obtainable in closed form using the *ABCD* form. But the wave equation governing the propagation of the envelope of a Gaussian pulse in a nonlinear dispersive fiber is [154]

$$-i\frac{\partial A}{\partial z} + \frac{\beta''}{2}\frac{\partial^2 A}{\partial T^2} - \gamma\frac{\Delta n}{n_2}A = 0, \quad (8.66)$$

where n_2 is the (constant) nonlinear index of refraction and $\Delta n(z, T)$ is the Kerr effect field-induced change in the refractive index. For a Gaussian pulse envelope of width $\tau(z)$, Δn can be approximated as

$$\Delta n(z, T) = n_2 \exp\left[-2\frac{T^2}{\tau^2(z)}\right] \approx n_2 \left[1 - \frac{2T^2}{\tau^2(z)}\right], \quad (8.67)$$

where we assume that the nonlinearity responds instantaneously. Eq. (8.66) becomes

$$-i\frac{\partial A}{\partial z} + \frac{\beta''}{2}\frac{\partial^2 A}{\partial T^2} - \gamma\left[1 - \frac{2T^2}{\tau^2(z)}\right]A = 0. \quad (8.68)$$

and clearly, Eqs. (8.68) and (8.65) are not identical. Therefore, the *ABCD* form of the solution cannot apply to Eq. (8.68).

In order to explain the similarity shown in Fig. 8.3, we seek a different approach. To identify analogies with the analysis of the spatial RSQ-GRIN problem Eq. (8.60),

we write the temporal pulse Ansatz as

$$A(z, T) = \exp \left[i \left(P(z) + \frac{T^2}{2\beta'' q(z)} \right) \right], \quad (8.69)$$

with a temporal q parameter,

$$\begin{aligned} \frac{1}{q(z)} &\equiv \frac{1}{R(z)} + i \frac{2\beta''}{\tau^2(z)} \\ &\equiv r(z) [\cos \theta(z) + i \sin \theta(z)], \end{aligned} \quad (8.70)$$

where $R(z)$ describes the chirp of the pulse and $\tau(z)$ its width. (We will use the polar representation in our analysis later.) The chirped Gaussian envelope that this formalism describes may, for instance, be one member of a complete orthonormal basis of Hermite-Gaussian functions.

We can simplify each of the partial differential equations Eqs. (8.65) and (8.68) into a pair of ordinary differential equations for $P(z)$ and $q(z)$ by substituting in for the Ansatz given by Eq. (8.69) and then equating the coefficients of different powers of T . We know from Gaussian beam diffraction analysis [154] that the equation with terms quadratic in T involves only the initial-value problem for $q(z)$. As $q(z)$ is complex, it is simplest to carry out a phase-plane analysis in each of the two systems in polar (r, θ) co-ordinates using the definition presented in Eq. (8.70). In polar coordinates, we can graph and compare the evolution of the solutions in the $r - \theta$ “phase” plane, with z as the implicit variable driving the evolution of the instantaneous solution along one of the contours in the phase plane.

The temporal RSQ-GRIN problem Eq. (8.65) in polar coordinates can be written as

$$\begin{aligned} dr/dz &= r^2 \cos \theta + 2\gamma \cos \theta, \\ d\theta/dz &= \frac{1}{r} [r^2 \sin \theta - 2\gamma \sin \theta], \\ r(0) &\equiv r_0, \quad \theta(0) \equiv \theta_0 = \pi/2, \end{aligned} \quad (8.71)$$

and for the equations describing pulse propagation in a nonlinear dispersive fiber Eq. (8.68),

$$\begin{aligned} dr/dz &= r^2 \cos \theta + 2\gamma \cos \theta (r \sin \theta), \\ d\theta/dz &= \frac{1}{r} [r^2 \sin \theta - 2\gamma \sin \theta (r \sin \theta)], \\ r(0) &\equiv r_0, \quad \theta(0) \equiv \theta_0 = \pi/2. \end{aligned} \quad (8.72)$$

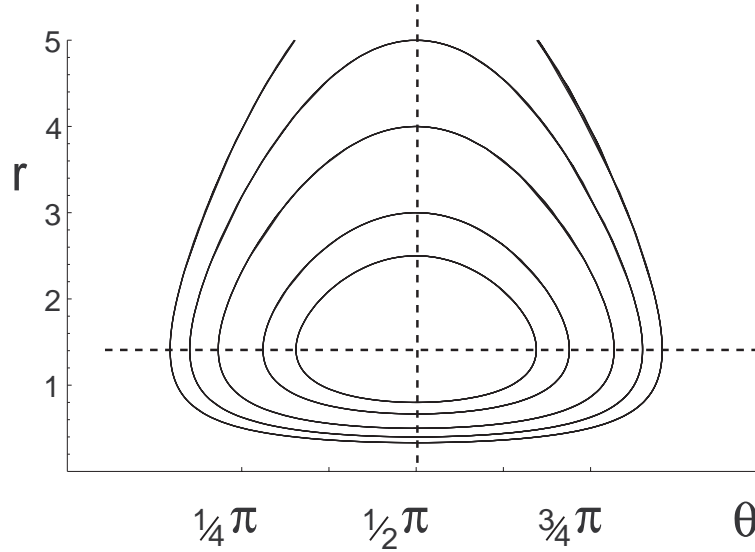


Figure 8.4: Temporal evolution of a Gaussian breather in the (hypothetical) temporal RSQ-GRIN medium: phase-plane analysis of Eq. (8.71).

The phase-plane analysis, shown in Fig. 8.4 and Fig. 8.5 for a particular set of orbits with the same initial conditions, shows the essential difference between Eq. (8.71) and Eq. (8.72): note that in the regime of interest, the multiplicative term $r \sin \theta$, which appears in Eq. (8.72) but not in Eq. (8.71), is always positive. The evolution of the temporal RSQ-GRIN solution to Eq. (8.71) (for which we have a closed form $ABCD$ expression) is symmetric in the phase plane about $\theta = \pi/2$. So, the term that changes in dr/dz for Eq. (8.72) results in scaling the contours outwards from the nonlinear center in the phase plane without affecting the symmetry about $\theta = \pi/2$. Consequently, closed orbits which are the solutions of one remain closed for the other, although the fixed points for the two problems are different.

Along similar lines, the difference in the $d\theta/dz$ equations maintains the same sign for that term in both equations. If $r \sin \theta < 1$, the rate of change of θ is decreased, and the period of the breathing solutions increases, which has been verified by numerically solving Eqs. (8.71) and (8.72).

The orbits in phase space are scaled nonlinearly around the fixed point in such a way as to preserve the *structure* of the solution space. Consider the sets of solutions of Eq. (8.71), $X_1 = \{S_1(r_0, \theta_0)\}$ and of Eq. (8.72), $X_2 = \{S_2(r_0, \theta_0)\}$. We take $\theta_0 \equiv \pi/2$

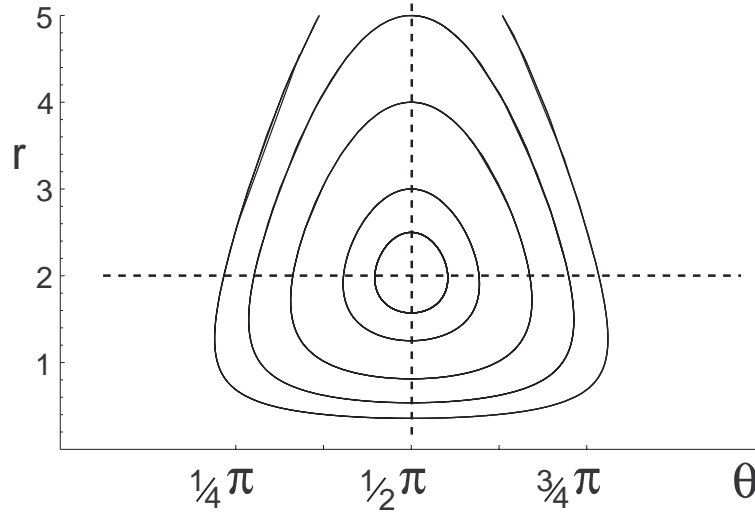


Figure 8.5: Temporal evolution of a Gaussian breather in the presence of the Kerr effect: phase-plane analysis of Eq. (8.72).

for simplicity. The collection of subsets of X_1 and X_2 defined as

$$\tau_i = \{S_i(r_0) \mid a < r_0 < b\}, \quad \forall a, b \geq 0 \quad (8.73)$$

define a topology on X_1 and X_2 . The orbits of the sets of solutions X_1 and X_2 are homotopic, which is an equivalence relation on the set of topological spaces [102]. In fact, the fundamental groups (first homotopy groups) are isomorphic to \mathbb{Z} , the fundamental group of the circle,

$$\pi_1(X_1) \cong \pi_1(X_2) \cong \pi_1(S^1) \cong \mathbb{Z}. \quad (8.74)$$

This isomorphism between the first homotopy groups explains the very close similarity of breathing Gaussian pulses in the case of the Kerr effect and Gaussian beams in a graded-index medium, even though the equations for one are *not* a direct translation of the other.

We mention that if there was a closed-form solution to the problem of Gaussian beam propagation in a rotationally-symmetric graded index medium described by a more general relationship than was assumed in Eq. (8.59)—for example, involving

higher powers of r^2 —then we could retain further terms in the Taylor series expansion in Eq. (8.67) and apply the same topological arguments to justify the similarities of the two families of solutions. The practical usefulness of such arguments depends, however, on the existence of closed-form solutions in at least one of the two cases—spatial or temporal—so that the solutions in the other case can be demonstrated to be topologically equivalent or related. We expect that more such examples will be identified in the future, leading to a deeper understanding of space-time analogies in optical propagation.

Epilogue

*śreyān dravyamayād yajñāj jñānayajñāḥ param̐tapa
sarvaṁ karmā 'khilam̐ pārtha jñāne parisamāpyate*

*tad viddhi praṇipatena paripraśnena sevayā
upadekṣyanti te jñānam̐ jñāninas tattvadarśinaḥ*

—The Bhagavadgītā IV (33–34), S. Radhakrishnan ed., Blackie (1976).



The indispensable first-base coach.

Appendix A

Superstructure gratings

A grating in a semiconductor or an optical fiber is characterized by a periodic variation in the refractive index of the medium, typically in one dimension, e.g., $n(z) = n_0 + \Delta n(z) \cos(2\pi z/d)$ where n_0 is the average (“background”) refractive index, d is the period of the grating and $\Delta n(z)$ is the amplitude of the index variation. The simplest gratings are those for which $\Delta n(z)$ is a constant, e.g., $\Delta n(z) = \Delta n_0$ for all z . Superstructure gratings, (SSGs, or superstructure Bragg gratings, SBGs) are gratings whose parameters in the description of $\Delta n(z)$ vary periodically along the length of the grating [17, 35, 32], e.g., $\Delta n(z) = \Delta n_0 \cos(2\pi z/\Lambda)$. Typically, the SSG period Λ is much longer than d , the period of the underlying uniform grating, which is on the scale of the wavelength of light. The reflection spectrum of weak gratings consists of a peak at the Bragg frequency $f = c/(2n_0d)$ where n_0 is the average refractive index in the grating, surrounded by a comb of peaks at $f_k = c/2n_0(1/d + k/\Lambda)$, $k = \pm 1, \pm 2, \dots$ which are called Rowland ghosts. SSGs in semiconductor have been used in tunable DFB lasers, and in optical fibers for dispersion compensation of WDM systems [17].

Using a coupled-mode theory with slowly varying envelopes, Broderick and de Sterke have formulated equations describing propagation through a nonlinear SSG [17]. The ansatz for the field envelope is

$$E(z, t) = a(z, t) \Psi_{nk}(z) e^{-iv\Delta_{nk}t}, \quad (\text{A.1})$$

where Ψ_{nk} is a Bloch function of the superstructure and Δ_{nk} is the detuning from its

corresponding eigenfrequency. The envelope¹ $a(z, t)$ is assumed to be slowly varying² and if we consider only one band (i.e., only one Bloch function and its corresponding envelope), it satisfies a nonlinear Schrödinger equation which has soliton solutions.

When two Bloch functions (and two envelopes) are considered in Eq. (A.1), the single equation for $a(z, t)$ becomes a pair of coupled mode equations for $a_1(z, t)$ and $a_2(z, t)$ or equivalently, for $a_{\pm}(z, t) \equiv a_1(z, t) \pm a_2(z, t)$, which are called “supercoupled mode equations” (SCMEs) by Broderick and de Sterke [17]³. For frequencies sufficiently close to a Rowland ghost gap, these equations reduce to those describing a shallow uniform nonlinear grating and therefore have soliton solutions (gap solitons for a uniform grating, Rowland ghost solitons for an SSG in this regime) which have been verified by numerical simulations [18] and experiments in optical fiber [35]. In addition to these bright soliton solutions, dark solitons and bright solitons on a pedestal are also known [17].

A deep SSG is more appropriately described by the tight-binding method, as was pointed out by de Sterke [32]. Such a grating can be thought of as a periodic array of regions with evanescent and propagating wave behavior, which is also seen in the solutions to the simple quantum-mechanical problem of a periodic (square well) potential [25]. In the weakly coupled regime, the eigenfield (waveguide mode) for an SSG is written as a superposition of the eigenmodes of the individual wells, exactly as in the description of a CROW [156]. It follows that our description of pulse propagation in Chapter 2 and of second-harmonic generation in Chapter 3 can be carried over to a deep SSG. It may easily be seen that the formulation of linear pulse propagation in [92, MPEG movie] has many features in similar with the numerical simulation of Rowland ghost solitons in a nonlinear SSG in [18, Fig. 4].

¹Broderick and de Sterke refer to this as the “superenvelope” but since there is no other “envelope” in this formalism, we may simply refer to $a(z, t)$ as the envelope (of the waveguide eigenmode).

²In space with respect to Γ , and in time with respect to $(v\kappa_0)^{-1}$ where κ_0 is the lowest order Fourier component of $\kappa(z) = \pi\Delta n(z)/\lambda$.

³Again, there is nothing particularly “super” about this coupling, as physically the equations simply describe the coupling of (eigen-) modes defined in a specific way; the particular form of the equations is dictated by the choice of the Ansatz.

Appendix B

Watson's criterion and Gaussian envelopes

As discussed by Watson [145, pp. 533–535], there are three criteria that need to be satisfied by an odd function $f(x)$ in order for the expansion Eq. (2.50) to be valid. In our case, $f(x)$ is related (by a linear transformation) to the envelope of the pulse at the $z = 0$ cross-section of the CROW, and it is entirely reasonable to assume that

1. $\int_0^\infty f(x)dx$ exists and is absolutely convergent.

In our analysis, the most important class of functions that represent pulse envelopes are Gaussians (of real arguments) and we may assume that

2. $f(x')$ has a continuous differential coefficient for all positive values of $x' < x$, where x refers to the particular value of x chosen in the left hand side of Eq. (2.50).

Watson's third criterion is in the form of an integral equation,

3. For all $t < x$,

$$2f'(t) = \int_0^\infty \frac{dv}{v} J_1(v) [f(v+t) + f(v-t)]. \quad (\text{B.1})$$

We do not need to rigorously analyze this condition, and will appeal instead to physical arguments. We assume that the envelopes we consider [such as taking the form of Eq. (2.52)] are sufficiently well behaved so that, using the definition of a derivative,

$$f'(t) = \frac{1}{2} \lim_{v \rightarrow 0} \left[\frac{f(t+v) - f(t)}{v} + \frac{f(t) - f(t-v)}{v} \right], \quad (\text{B.2})$$

and since $f(t)$ is odd,

$$2f'(t) = \lim_{v \rightarrow 0} \frac{f(v+t) + f(v-t)}{v}. \quad (\text{B.3})$$

It is now evident that one simple way of approximately satisfying Eq. (B.1) is to stipulate $f(t+v) \approx f(t-v)$, and in the limit of equality of the last relationship, the former is satisfied exactly (and trivially). In the context of Eq. (2.52), broader Gaussian envelopes, with larger T , are "better" represented by the Webb-Kapteyn-Neumann series. This is easily verified numerically.

More detailed investigations of Eq. (B.1) in the context of Eq. (2.52) are unlikely, we believe, to reveal much more useful information. A criterion established by Bateman [10] for the validity of Eq. (2.50) is

$$\int_0^\infty dt f(t) J_0(tx) = \begin{cases} \psi(x), & \text{if } x < 1, \\ 0, & \text{otherwise,} \end{cases} \quad (\text{B.4})$$

where $\psi(x)$ is a function that takes nonzero values only on the interval $0 < x < 1$. Using Eq. (2.52) for $f(t)$,

$$\begin{aligned} \int_0^\infty dt e^{-\frac{t^2}{T^2}} J_0(tx) &= \frac{\sqrt{\pi} T}{2} e^{-T^2 x^2/8} I_0\left(\frac{T^2 x^2}{8}\right) \\ &\sim \frac{1}{x} \quad \text{as } x \rightarrow \infty, \end{aligned} \quad (\text{B.5})$$

and Eq. (B.4) is clearly not satisfied for any value of T . Nevertheless, Gaussian envelopes [and others with a property similar to Eq. (B.5)] are of considerable interest practically. In this context, the approach we have taken in the previous paragraph circumvents the assumptions underlying Eq. (B.4) and Bateman's subsequent conclusions.

Appendix C

Outline of the proof of the Hermiticity of H

Using the two vector identities,

$$\begin{aligned}\nabla \cdot (\mathbf{a} \times \mathbf{b}) &= \mathbf{b} \cdot (\nabla \times \mathbf{a}) - \mathbf{a} \cdot (\nabla \times \mathbf{b}), \\ \mathbf{a} \cdot (\mathbf{b} \times \mathbf{c}) &= -(\mathbf{b} \times \mathbf{a}) \cdot \mathbf{c},\end{aligned}\tag{C.1}$$

it is easy to show that the operator H defined in Eq. (2.38) is Hermitian, provided that the boundary conditions are of the appropriate form [96]. To show this explicitly for each of the 6 component terms of H as written in Eq. (2.38) is needlessly tedious, as all the necessary operations can be demonstrated by considering terms 3 and 4 of H . We will therefore show that the operator H' , which is defined by

$$H' \mathbf{u}_{k(\omega)} \equiv -ik [\nabla \times [\mathbf{e}_z \times \mathbf{u}_{k(\omega)}] + \mathbf{e}_z \times [\nabla \times \mathbf{u}_{k(\omega)}]],\tag{C.2}$$

is Hermitian, i.e., satisfies the following equality among inner products,

$$(\mathbf{u}_{k(\omega)}, H' \mathbf{u}_{k(\omega)}) = (H' \mathbf{u}_{k(\omega)}, \mathbf{u}_{k(\omega)}),\tag{C.3}$$

with the inner product definition following Eq. (2.36). The full operator H can be checked in a similar way.

If the following boundary condition holds,

$$\int \frac{dt}{T} \int d\mathbf{r} \epsilon(\mathbf{r}) \nabla \cdot [(\nabla \times \mathbf{u}_{k(\omega)}) \times \mathbf{u}_{k(\omega)}^*] = 0,\tag{C.4}$$

where the region of \mathbf{r} integration is over a unit cell and the region of t integration is

over the temporal extent of the envelope, then using Eq. (C.1),

$$\begin{aligned}
(\mathbf{u}_{k(\omega)}, H' \mathbf{u}_{k(\omega)}) &= \int \frac{dt}{T} \int d\mathbf{r} [-ik \epsilon(\mathbf{r})] \left[(\nabla \cdot \mathbf{u}_{k(\omega)})^* \cdot [\mathbf{e}_z \times \mathbf{u}_{k(\omega)}] \right. \\
&\quad \left. - (\mathbf{e}_z \times \mathbf{u}_{k(\omega)})^* \cdot (\nabla \times \mathbf{u}_{k(\omega)}) \right] \\
&= \int \frac{dt}{T} \int d\mathbf{r} [-ik \epsilon(\mathbf{r})] \left[- (\mathbf{e}_z \times [\nabla \times \mathbf{u}_{k(\omega)}])^* \cdot \mathbf{u}_{k(\omega)} \right. \\
&\quad \left. - (\nabla \times [\mathbf{e}_z \times \mathbf{u}_{k(\omega)}])^* \cdot \mathbf{u}_{k(\omega)} \right] \\
&= (H' \mathbf{u}_{k(\omega)}, \mathbf{u}_{k(\omega)}). \tag{C.5}
\end{aligned}$$

For terms 5 and 6 of H as given by Eq. (2.38), the following boundary condition is needed:

$$\int d\mathbf{r} \epsilon(\mathbf{r}) \left[[\mathbf{u}_{k(\omega)}]^* \cdot \left(\frac{\epsilon(\mathbf{r})}{c^2} \frac{\partial \mathbf{u}_{k(\omega)}}{\partial t} \right) \right]_{t_-}^{t_+} = 0. \tag{C.6}$$

Eqs. (C.4) and (C.6) are satisfied physically since the CROW is a spatially periodic structure and the pulse envelope goes to zero at both ends of the t integration.

Such boundary conditions are a mathematical statement of the assumption that the problem of interest is physically completely contained in the CROW. Problems of coupling a pulse into or out of a CROW of finite length cannot be described by Hermitian eigenvalue equations as the bilinear concomitant between the original differential equation and its Hermitian adjoint is no longer periodic [96]. In such circumstances, one can resort to direct numerical methods of analysis [149].

The imposition of closed boundary conditions in the temporal domain is for simplicity. A more correct approach would allow the positive temporal boundary to go to infinity and impose appropriate Cauchy boundary conditions (value and slope specified) on the wave equation. Whereas Cauchy boundary conditions overspecify a closed boundary hyperbolic differential equation, they provide for a unique and stable solution to the open boundary problem [96].

Appendix D

Nonlinear polarization for SHG

Based on the discussion of the waveguide modes of a CROW in Chapters 2 and 3, we assume the following forms for two eigenfields at the fundamental frequency ω with amplitudes E_1 ,

$$\mathbf{E}_a(\mathbf{r}, t) = E_1 e^{i\omega t} e^{-ik_1(\omega)z} \mathbf{u}_{k_1(\omega)}(\mathbf{r}, t), \quad (\text{D.1})$$

$$\mathbf{E}_b(\mathbf{r}, t) = E_1 e^{i\omega t} e^{-ik_2(\omega)z} \mathbf{u}_{k_2(\omega)}(\mathbf{r}, t). \quad (\text{D.2})$$

For each field, the frequency-domain (temporal Fourier transformed) field can be written as

$$\begin{aligned} \tilde{\mathbf{E}}(\mathbf{r}, \Omega) &\equiv E_1 \int dt e^{-i\Omega t} \mathbf{E}(\mathbf{r}, t) \\ &= E_1 e^{-ik_1(\omega)z} \tilde{\mathbf{u}}_{k_1}(\mathbf{r}, \Omega), \end{aligned} \quad (\text{D.3})$$

where we use the tilde to represent Fourier transformed fields.

The frequency-domain nonlinear polarization for second harmonic generation at ω_2 is given by [154, 126]

$$\tilde{\mathbf{P}}_{\text{NL}}(\mathbf{r}, \omega_2) = \tilde{d}(\mathbf{r}) \int_{-\infty}^{\infty} d\Omega \tilde{\mathbf{E}}_a(\mathbf{r}, \omega_2 - \Omega) \tilde{\mathbf{E}}_b(\mathbf{r}, \Omega), \quad (\text{D.4})$$

where \tilde{d} is the effective second-order nonlinearity coefficient of the medium. Using

Eq. (D.3), Eq. (D.4) can be written as

$$\begin{aligned} \tilde{\mathbf{P}}_{\text{NL}}(\mathbf{r}, \omega_2) &= \tilde{d}(\mathbf{r}) E_1^2 \int_{-\infty}^{\infty} d\Omega e^{-i[k_1(\omega_2 - \Omega) + k_2(\Omega)]z} \\ &\times \tilde{\mathbf{u}}_{k_1}(\mathbf{r}, \omega_2 - \Omega - \omega) \tilde{\mathbf{u}}_{k_2}(\mathbf{r}, \Omega - \omega). \end{aligned} \quad (\text{D.5})$$

The dispersion relationship between k and ω implies that we can expand $k(\omega)$ in a Taylor series about the central frequency of each pulse [154]. We retain terms upto the linear in ω to write

$$\begin{aligned} k_1(\omega_2 - \Omega) &= k_1 + \left. \frac{dk}{d\omega} \right|_{\omega} (\omega_2 - \Omega - \omega), \\ k_2(\Omega) &= k_2 + \left. \frac{dk}{d\omega} \right|_{\omega} (\Omega - \omega). \end{aligned} \quad (\text{D.6})$$

The group velocity at ω_1 is defined by the relation $1/v_1 = (dk/d\omega)|_{\omega_1}$. The assumption of a linear dispersion relationship in a CROW is not as restrictive as one might expect based on ω - K curves for conventional waveguides. From the tight-binding analysis, the dispersion relationship for a weakly coupled CROW can be written as

$$\omega(k) = \Omega \left[1 - \frac{\Delta\alpha}{2} + \kappa \cos(kR) \right] \quad (\text{D.7})$$

where Ω is the mode frequency of the individual resonators, $\Delta\alpha$ is an overlap integral and κ is a coupling coefficient. The group velocity $d\omega/dk$ goes to zero at the edges of the Brillouin zone $k = 0, \pm\pi/R$, but is approximately constant in the central portion of the zone, where the dispersion relationship is linear.

We can use Eq. (D.6) in Eq. (D.5) and take the inverse Fourier transform to write the nonlinear polarization in the time domain,

$$\mathbf{P}_{\text{NL}}(\mathbf{r}, t) = \int \frac{d\omega_2}{2\pi} e^{i\omega_2 t} \tilde{\mathbf{P}}_{\text{NL}}(\mathbf{r}, \omega_2)$$

¹Consequently, there are no linear propagating eigenmodes at these points, and referring to the various waveguide modes as “states,” we can say that the density of states is zero. In the solid-state physics of electron levels, these points are known as van Hove singularities [9].

or when written out completely,

$$\begin{aligned}
\mathbf{P}_{\text{NL}}(\mathbf{r}, t) &= \tilde{d}(\mathbf{r}) E_1^2 e^{-i(k_1 - \omega/v_1)z} e^{-i(k_2 - \omega/v_1)z} \\
&\times \int \frac{d\omega_2}{2\pi} e^{i\omega_2(t-z/v_1)} \int_{-\infty}^{\infty} d\Omega \left[\tilde{\mathbf{u}}_{k_1}(\mathbf{r}, \omega_2 - \Omega - \omega) \tilde{\mathbf{u}}_{k_2}(\mathbf{r}, \Omega - \omega) \right] \\
&= \tilde{d}(\mathbf{r}) E_1^2 \left[e^{i(\omega t - k_1 z)} \mathbf{u}_{k_1(\omega)}(\mathbf{r}, t - z/v_1) \right] \left[e^{i(\omega t - k_2 z)} \mathbf{u}_{k_2(\omega)}(\mathbf{r}, t - z/v_1) \right].
\end{aligned} \tag{D.8}$$

This can be easily generalized to include a spatial and temporal dependency in the envelope E_1 . We can simply include the non-constant part of E_1 with the spatial and temporally varying function $\mathbf{u}_{k(\omega)}(\mathbf{r}, t)$ as the physical interpretation of $\mathbf{u}_{k(\omega)}$ as a Bloch wavefunction is irrelevant here. The result is

$$\begin{aligned}
\mathbf{P}_{\text{NL}}(\mathbf{r}, t) &= \tilde{d}(\mathbf{r}) \left[E_a(z) e^{i(\omega t - k_1 z)} \mathbf{u}_{k_1(\omega)}(\mathbf{r}, t - z/v_1) \right] \\
&\left[E_b(z) e^{i(\omega t - k_2 z)} \mathbf{u}_{k_2(\omega)}(\mathbf{r}, t - z/v_1) \right].
\end{aligned} \tag{D.9}$$

For simplicity, we will usually assume that the envelopes E_a and E_b are constant $= E_1$, signifying an undepleted eigenmode at the fundamental carrier frequency ω .

Appendix E

Period of orbits in the phase plane

Rather than work with the direct form of the Hamiltonian, Eq. (6.10), we introduce the following change of variables: $\beta = \bar{\beta}/\pi$, $Z = \bar{Z}(\pi/2)$, and then drop the bars for notational simplicity. Writing $H' = -2/3 H$ and assuming that $a(Z) \equiv 1$ we obtain

$$H' = (\sigma + 6\gamma\Omega) \left[\frac{\beta^2}{\eta^2} + \eta^2 + \Omega^2 \right] - 2(\eta - \Omega^2\sigma) \quad (\text{E.1})$$

and Eq. (6.12) becomes

$$\frac{d\eta}{dz} = -(\sigma + 6\gamma\Omega)\beta\eta, \quad (\text{E.2})$$

$$\frac{d\beta}{dz} = (\sigma + 6\gamma\Omega)(\eta^4 - \beta^2) - \eta^3. \quad (\text{E.3})$$

For a given level set of this redefined Hamiltonian, parametrized by H' , Eq. (E.1) is of quadratic order in β , so that

$$\beta = \pm\eta\sqrt{\frac{H' + 2(\eta - \Omega^2\sigma)}{\sigma + 6\gamma\Omega} - (\eta^2 + \Omega^2)}. \quad (\text{E.4})$$

Since $d\Omega/dz = 0$, and both σ and γ are assumed to be piecewise constant, we can use Eq. (E.2) to find the distance $Z_2 - Z_1$ between the points $\eta = \eta_2$ and η_1 on the H' contour,

$$\int_{\eta_1}^{\eta_2} d\eta \left\{ \pm\eta^2 \sqrt{\frac{H' + 2(\eta - \Omega^2\sigma)}{\sigma + 6\gamma\Omega} - (\eta^2 + \Omega^2)} \right\}^{-1} = -(Z_2 - Z_1)(\sigma + 6\gamma\Omega). \quad (\text{E.5})$$

Identifying $a = (H' - 2\Omega^2\sigma)/(\sigma + 6\gamma\Omega) - \Omega^2$, $b = 2/(\sigma + 6\gamma\Omega)$, and $c = -1$, we can use the following identity to evaluate the integral,

$$\int \frac{dx}{x^2\sqrt{a+bx+cx^2}} = -\frac{\sqrt{a+bx+cx^2}}{ax} + \frac{b}{2a^{3/2}} \log \left[-\frac{2}{bx} \left(2a^{3/2} + \sqrt{a}bx + 2a\sqrt{a+bx+cx^2} \right) \right]. \quad (\text{E.6})$$

We now take η_1 and η_2 to correspond to the minimum and maximum extents of the orbit along the η axis (see Fig. 1). These two points are given by the solutions of the following algebraic equation,

$$\eta^2 - \frac{2}{\sigma + 6\gamma\Omega} + \left(\Omega^2 - \frac{H' - 2\Omega^2\sigma}{\sigma + 6\gamma\Omega} \right) = 0. \quad (\text{E.7})$$

The round-trip period of the H' orbit is given by the value of $2(Z_2 - Z_1)$, obtained from Eq. (E.5).

Based on Eq. (E.4), we can solve $d\beta/d\eta = 0$ to find the η value corresponding that point on the orbit where β is maximum,

$$\eta|_{\beta_{\max}} = \frac{3}{4(\sigma + 6\gamma\Omega)} + \frac{1}{2} \sqrt{\frac{9}{4(\sigma + 6\gamma\Omega)^2} + \frac{2(E - 3\sigma\Omega^2 - 6\gamma\Omega^3)}{\sigma + 6\gamma\Omega}}. \quad (\text{E.8})$$

Using this value for η in Eq. (E.4) leads to a value for β_{\max} .

References

- [1] M. A. Abramowitz and I. A. Stegun. *Handbook of Mathematical Functions*. Dover, 1972.
- [2] A. Adibi, Y. Xu, R. K. Lee, A. Yariv, and A. Scherer. Properties of the slab modes in photonic crystal optical waveguides. *Journal of Lightwave Technology*, 18(11):1554–1564, 2000.
- [3] G. P. Agrawal. *Fiber-Optic Communication Systems*. John Wiley & Sons, second edition, 1997.
- [4] G.P. Agrawal. *Nonlinear Fiber Optics*. Academic Press, 1989.
- [5] S. A. Akhmanov, A. S. Chirkin, K. N. Drabovich, A. I. Kovrigin, R. V. Khokhlov, and A.P. Sukhorukov. Nonstationary nonlinear optical effects and ultrashort light pulse pulse formation. *IEEE Journal of Quantum Electronics*, QE-4(10):598, 1968.
- [6] N. Akhmediev and M. Karlsson. Cherenkov radiation emitted by solitons in optical fibers. *Physical Review A*, 51(3):2602–2607, 1995.
- [7] D. Anderson. Variational approach to nonlinear pulse propagation in optical fibers. *Phys. Rev. A*, 27:3135–3145, 1983.
- [8] T. M. Apostol. *Mathematical Analysis*. Addison-Wesley, 1957.
- [9] N. W. Ashcroft and N. D. Mermin. *Solid State Physics*. Harcourt, Fort Worth, 1976.
- [10] H. Bateman. On an expansion of an arbitrary function in a series of Bessel functions. *The Messenger of Mathematics*, XXXVI:31–37, 1907.
- [11] M. Bayer, I. Gutbrod, A. Forchel, T. Reinecke, P. Knipp, R. Werner, and J. Reithmaier. Optical demonstration of a crystal band structure formation. *Physical Review Letters*, 83:5374, 1999.
- [12] M. Bayer, I. Gutbrod, J. P. Reithmaier, A. Forchel, T. L. Reinecke, P. A. Knipp, A. A. Dremin, and Kulakovskii V. D. Optical modes in photonic molecules. *Physical Review Letters*, 81(12):2582–2585, 1998.
- [13] M. Bayindir, B. Temelkuran, and E. Ozbay. Tight-binding description of the coupled defect modes in three-dimensional photonic crystals. *Physical Review Letters*, 84(10):2140–2143, 2000.

-
- [14] P. A. Bélanger and P. Mathieu. On an extremum property of Gaussian beams and Gaussian pulses. *Optics Communications*, 67(6):396–398, 1988.
- [15] A. Bondeson, M. Lisak, and D. Anderson. Soliton perturbations: a variational principle for the soliton parameters. *Physica Scripta*, 20:479–485, 1979.
- [16] M Born and E. Wolf. *Principles of Optics*. Cambridge University Press, seventh edition, 1999.
- [17] N. G. R. Broderick and C. M. de Sterke. Theory of grating superstructures. *Physical Review E*, 55(3):3634–3647, 1997.
- [18] N. G. R. Broderick, C. M. de Sterke, and B. J. Eggleton. Soliton solutions in Rowland ghost gaps. *Physical Review E*, 52(6):R5788–R5791, 1995.
- [19] K. Busch and S. John. Liquid-crystal photonic band-gap materials: The tunable electromagnetic vacuum. *Physical Review Letters*, 83(5):967–970, 1999.
- [20] E. Caglioti, B. Crosignani, and P. Di Porto. Hamiltonian description of nonlinear propagation in optical fibers. *Physical Review A*, 38(8):4036–4042, 1988.
- [21] E. Caglioti, S. Trillo, S. Wabnitz, B. Crosignani, and P. Di Porto. Finite-dimensional description of nonlinear pulse propagation in optical-fiber couplers with applications to soliton switching. *Journal of the Optical Society of America B*, 7(3):374–385, 1990.
- [22] G. M. Carter, R.-M. Mu, V. S. Grigoryan, C. R. Menyuk, P. Sinha, F. Carruthers, M. L. Dennis, and I. N. Duling III. Transmission of dispersion-managed solitons at 20 Gbits/s over 20 000 km. *Electronics Letters*, 35:133–134, 1999.
- [23] E. Chow, S. Y. Lin, S. G. Johnson, P. R. Villeneuve, J. D. Joannopoulos, J. R. Wendt, G. A. Vawter, W. Zubrzycki, H. Hou, and A. Alleman. Three-dimensional control of light in a two-dimensional photonic crystal slab. *Nature*, 407:983–986, 2000.
- [24] D. N. Christodoulides and N. K. Efremidis. Discrete temporal solitons along a chain of nonlinear coupled microcavities embedded in photonic crystals. *Optics Letters*, 27(8):568–570, 2002.
- [25] C. Cohen-Tannoudji, B. Diu, and F. Laloë. *Quantum Mechanics*. Hermann and John Wiley & Sons, 1977.
- [26] C. Cohen-Tannoudji, J. Dupont-Roc, and G. Grynberg. *Photons and Atoms*. John Wiley & Sons, New York, 1989.
- [27] C. Conti, S. Trillo, and G. Assanto. Energy localization in photonic crystals of a purely nonlinear origin. *Physical Review Letters*, 85:2502–2505, 2000.
- [28] B. Crosignani. Nonlinear effects in optical fibers. *Fiber and Integrated Optics*, 11:235–252, 1992.
- [29] B. Crosignani, P. Di Porto, and E. Caglioti. The optical Kerr effect in fibers. In A.R. Boardman, M. Bertolotti, and T. Twardowski, editors, *Nonlinear Waves in Solid State Physics*, NATO ASI Series B. Vol. 247. Plenum Press, 1990.

- [30] W. B. Davenport and W. L. Root. *An Introduction to the Theory of Random Signals and Noise*. McGraw-Hill, New York, 1958.
- [31] C. J. S. de Matos, D. A. Chestnut, and J. R. Taylor. Wavelength- and duration-tunable soliton source based on a 20-GHz Mach-Zehnder modulator and adiabatic Raman compression. *Applied Physics Letters*, 81:2932–2934, 2002.
- [32] C. M. de Sterke. Superstructure gratings in the tight-binding approximation. *Physical Review E*, 57(3):3502–3509, 1998.
- [33] E. Desurvire, M. Zirngibl, H. M. Presby, and D. DiGiovanni. Characterization and modeling of amplified spontaneous emission in unsaturated erbium-doped fiber amplifiers. *IEEE Photonics Technology Letters*, 3:127–129, 1991.
- [34] J. P. Dowling, M. Scalora, M. J. Bloemer, and C. M. Bowden. The photonic band edge laser: a new approach to gain enhancement. *Journal of Applied Physics*, 75:1896–1899, 1994.
- [35] B. J. Eggleton, C. M. de Sterke, and R. E. Slusher. Nonlinear propagation in superstructure Bragg gratings. *Optics Letters*, 21(16):1223–1225, 1996.
- [36] A. Erdélyi, editor. *Higher Transcendental Functions*, volume II. McGraw-Hill, 1953.
- [37] R. P. Feynman. Forces in molecules. *Physical Review*, 56:340–343, 1939.
- [38] H. Ghafouri-Shiraz, P. Shum, and M. Nagata. A novel method for analysis of soliton propagation in optical fibers. *IEEE Journal of Quantum Electronics*, 31(1):190–200, 1995.
- [39] H. Goldstein. *Classical Mechanics*. Addison-Wesley, 1950.
- [40] J.P. Gordon. Theory of the soliton self-frequency shift. *Optics Letters*, 11(10):662–664, 1986.
- [41] J.P. Gordon. Dispersive perturbations of solitons of the nonlinear schrödinger equation. *Journal of the Optical Society of America B*, 9:91–97, 1992.
- [42] J.P. Gordon and H.A. Haus. Random walk of coherently amplified solitons in optical fiber transmission. *Optics Letters*, 11(10):665–667, 1986.
- [43] A. Hasegawa. Soliton-based optical communications: an overview. *IEEE Journal of Selected Topics in Quantum Electronics*, 6(6):1161–1172, 2000.
- [44] A. Hasegawa and Y. Kodama. *Solitons in Optical Communications*. Oxford, 1995.
- [45] A. Hasegawa and T. Nyu. Eigenvalue communication. *Journal of Lightwave Technology*, 11(3):395–399, 1993.
- [46] H. Hatami-Hanza, J. Hong, A. Atieh, P. Mylinski, and J. Chrotowski. Demonstration of all-optical demultiplexing of a multilevel soliton signal employing soliton decomposition and self-frequency shift. *IEEE Photonics Technology Letters*, 9(6):833–835, 1997.
- [47] H. A. Haus. Optical fiber solitons, their properties and uses. *Proceedings of the IEEE*, 81(7):970–983, 1993.

- [48] H. A. Haus and M. N. Islam. Theory of the soliton laser. *IEEE Journal of Quantum Electronics*, QE-21(8):1172–1188, 1985.
- [49] H. A. Haus, K. Tamura, L. Nelson, and E. P. Ippen. Stretched-pulse additive pulse mode-locking in fiber ring lasers: Theory and experiment. *IEEE Journal of Quantum Electronics*, 31(2):591–598, 1995.
- [50] H.A. Haus. *Waves and Fields in Optoelectronics*. Prentice-Hall, 1984.
- [51] H.A. Haus and W.S. Wong. Solitons in optical communications. *Reviews of Modern Physics*, 68(2):423–444, 1996.
- [52] H. Hellman. *Einführung in die Quantenchemie*. Deuticke, 1937.
- [53] R. Hirota. Exact envelope-soliton solutions of a nonlinear wave equation. *Journal of Mathematical Physics*, 14(7):805–809, 1973.
- [54] P. Holmes and J.N. Kutz. Dynamics and bifurcations of a planar map modeling dispersion managed breathers. *SIAM J. Appl. Math*, 59(4):1288–1302, 1999.
- [55] E. Infeld and G. Rowlands. *Nonlinear Waves, Solitons and Chaos*. Cambridge University Press, second edition, 2000.
- [56] T. Inoue, H. Suguhara, A. Maruta, and Y. Kodama. Interactions between dispersion-managed solitons in optical time-division-multiplexed system. *IEEE Photonics Technology Letters*, 12(3):299–301, 2000.
- [57] J. D. Jackson. *Classical Electrodynamics*. John Wiley & Sons, third edition, 1999.
- [58] J. D. Joannopoulos, R. D. Meade, and J. N. Winn. *Photonic Crystals*. Princeton University Press, 1995.
- [59] S. John and N. Akozbek. Nonlinear optical solitary waves in a photonic band-gap. *Physical Review Letters*, 71(8):1168–1171, 1993.
- [60] S. G. Johnson and J. D. Joannopoulos. Block-iterative frequency-domain methods for maxwell’s equations in a planewave basis. *Optics Express*, 8:173–190, 2001.
- [61] S. G. Johnson, P. R. Villeneuve, S. Fan, and J. D. Joannopoulos. Linear waveguides in photonic-crystal slabs. *Physical Review B*, 62(12):8212–8222, 2000.
- [62] H. Jones. *The Theory of Brillouin Zones and Electronic States in Crystals*. North-Holland, 1960.
- [63] V. I. Karpman. Soliton evolution in the presence of perturbations. *Physica Scripta*, 20:462–478, 1979.
- [64] Y. S. Kivshar and D. E. Pelinovsky. Self-focusing and transverse instabilities of solitary waves. *Physics Reports*, 331:117–195, 2000.
- [65] B. H. Kolner and M. Nazarathy. Temporal imaging with a time lens. *Optics Letters*, 14(12):630, 1989.

- [66] S. Kumar and F. Lederer. Gordon-Haus effect in dispersion-managed soliton systems. *Optics Letters*, 22(24):1870–1872, 1997.
- [67] J. Kumasako, M. Matsumoto, and S. Waiyapot. Linear stability analysis of dispersion-managed solitons controlled by filters. *Journal of Lightwave Technology*, 18(8):1064–1068, 2000.
- [68] J.N. Kutz, P. Holmes, S.G. Evangelides, and J.P. Gordon. Hamiltonian dynamics of dispersion managed breathers. *J. Opt. Soc. Am. B*, 15(1):87–96, 1998.
- [69] J.N. Kutz and P.K.A. Wai. Noise-induced amplitude and chirp jitter in dispersion-managed soliton communications. *Optics Letters*, 23(13):1022–1024, 1998.
- [70] M. J. LaGasse, K. K. Anderson, C. A. Wang, H. A. Haus, and J. G. Fujimoto. Femtosecond measurements of the nonresonant nonlinear index in AlGaAs. *Applied Physics Letters*, 56(5):417–419, 1990.
- [71] T. I. Lakoba. Non-integrability of equations governing pulse propagation in dispersion-managed optical fibers. *Physics Letters A*, 260:68–77, 1999.
- [72] T. I. Lakoba and G. P. Agrawal. Effects of third-order dispersion on dispersion-managed solitons. *Journal of the Optical Society of America B*, 16(9):1332–1343, 1999.
- [73] T. I. Lakoba and D. J. Kaup. Hermite-gaussian expansion for pulse propagation in strongly dispersion managed fibers. *Physical Review E*, 58(5):6728–6741, November 1998.
- [74] R. J. Lang and A. Yariv. Analysis of the dynamic response of multielement semiconductor lasers. *IEEE Journal of Quantum Electronics*, QE-21(10):1683–1688, 1985.
- [75] R. J. Lang and A. Yariv. Local-field rate equations for coupled optical resonators. *Physical Review A*, 34(3):2038–2043, 1986.
- [76] G. Lehmann and P. Ziesche. *Electronic Properties of Metals*, volume 64 of *Materials Science Monographs*. Elsevier, 1990.
- [77] A. W. Lohmann and D. Mendlovic. Temporal filtering with time lenses. *Applied Optics*, 31(9):6212, 1992.
- [78] M. Lončar, D. Nedeljković, T. Doll, J. Vučković, A. Scherer, and T.P. Pearsall. Waveguiding in planar photonic crystals. *Applied Physics Letters*, 77(13):1937–1939, 2000.
- [79] R. Loudon. *The Quantum Theory of Light*. Oxford, second edition, 1997.
- [80] R. S. Mackay and S. Aubry. Proof of existence of breathers for time-reversible or Hamiltonian networks of weakly coupled oscillators. *Nonlinearity*, 7(6):1623–1643, 1994.
- [81] D. Marcure and C. R. Menyuk. Simulation of single-channel optical systems at 100 Gb/s. *Journal of Lightwave Technology*, 17(4):564–569, 1999.
- [82] D. Marcuse. An alternative derivation of the Gordon-Haus effect. *Journal of Lightwave Technology*, 10(2):273–278, 1992.

- [83] M. Matsumoto and H. A. Haus. Stretched-pulse optical fiber communications. *Optics Letters*, 22(6):785–787, 1997.
- [84] S. L. McCall, P. M. Platzman, R. Dalichaouch, D. Smith, and S. Schultz. Microwave propagation in two-dimensional dielectric lattices. *Physical Review Letters*, 67:2017, 1991.
- [85] A. R. McGurn. Intrinsic localized modes in nonlinear photonic crystal waveguides. *Physics Letters A*, 251(5):322–335, 1999.
- [86] S. F. Mingaleev, Y. S. Kivshar, and R. A. Sammut. Long-range interaction and nonlinear localized modes in photonic crystal waveguides. *Physical Review E*, 62(4):5777–5782, 2000.
- [87] S. Mookherjea, D. S. Cohen, and A. Yariv. Nonlinear dispersion in a coupled-resonator optical waveguide. *Optics Letters*, 27:933–935, 2002.
- [88] S. Mookherjea and A. Yariv. Algebraic and geometric space-time analogies in nonlinear optical pulse propagation. *Optics Letters*, 26(17):issue 1–3, 2001.
- [89] S. Mookherjea and A. Yariv. Analysis of optical pulse propagation with two-by-two (ABCD) matrices. *Physical Review E*, 64:016611, July 2001.
- [90] S. Mookherjea and A. Yariv. Hamiltonian dynamics of breathers with third-order dispersion. *Journal of the Optical Society of America B*, 18(8):1150–1155, October 2001.
- [91] S. Mookherjea and A. Yariv. Optical pulse propagation and holographic storage in a coupled-resonator optical waveguide. *Physical Review E*, 64:066602, 2001.
- [92] S. Mookherjea and A. Yariv. Optical pulse propagation in the tight-binding approximation. *Optics Express*, 9(2):91–96, 2001.
- [93] S. Mookherjea and A. Yariv. Second harmonic generation with pulses in a coupled-resonator optical waveguide. *Physical Review E*, 65:026607, 2001.
- [94] S. Mookherjea and A. Yariv. Coupled resonator optical waveguides. *IEEE Journal of Selected Topics in Quantum Electronics*, 8(3):448–456, 2002.
- [95] S. Mookherjea and A. Yariv. Pulse propagation in a coupled resonator optical waveguide to all orders of dispersion. *Physical Review E*, 65:056601, 2002.
- [96] P.M. Morse and H. Feshbach. *Methods of Theoretical Physics*. McGraw-Hill, 1953.
- [97] R.-M. Mu, V. S. Grigoryan, C. R. Menyuk, G. M. Carter, and J. M. Jacob. Comparison of theory and experiment for dispersion-managed solitons in a recirculating fiber loop. *IEEE Journal of Selected Topics in Quantum Electronics*, 6(2):248, 2000.
- [98] T. Mukaiyama, K. Takeda, H. Miyazaki, Y. Jimba, and Kuwata-Gonokami M. Tight-binding photonic molecule modes of resonant bispheres. *Physical Review Letters*, 82(23):4623–4626, 1999.

-
- [99] M. Murakami, T. Matsuda, H. Maeda, and T. Imai. Long-haul WDM transmission using higher-order fiber dispersion management. *Journal of Lightwave Technology*, 18(9):1197–1204, 2000.
- [100] D.J. Muraki and W.L. Kath. Hamiltonian dynamics of solitons in optical fibers. *Physica D*, 48:53–64, 1991.
- [101] T. E. Murphy. 10-GHz 1.3-ps pulse generation using chirped soliton compression in a Raman gain medium. *IEEE Photonics Technology Letters*, 14:1424–1426, 2002.
- [102] M. Nakahara. *Geometry, Topology and Physics*. Institute of Physics, 1990.
- [103] M. Nakazawa. Solitons for breaking barriers to terabit/second WDM and OTDM transmission in the next millennium. *IEEE Journal on Selected Topics in Quantum Electronics*, 6(6):1332–1343, 2000.
- [104] T. Okamawari, A. Maruta, and Y. Kodama. Analysis of Gordon-Haus jitter in a dispersion-compensated optical transmission system. *Optics Letters*, 23(9):694–696, 1998.
- [105] S. Olivier, C. Smith, M. Rattier, H. Benisty, C. Weisbuch, T. Krauss, R. Houdré, and U. Oesterlé. Miniband transmission in a photonic crystal coupled-resonator optical waveguide. *Optics Letters*, 26(13):1019–1021, 2001.
- [106] T. R. O’Meara and A. Yariv. Time-domain signal processing via four-wave mixing in nonlinear delay lines. *Optical Engineering*, 21:237–242, 1982.
- [107] A. V. Oppenheim, A. S. Willksy, and I. T. Young. *Signals and Systems*. Prentice-Hall, 1995.
- [108] O. J. Painter, J. Vučković, and A. Scherer. Defect modes of a two-dimensional photonic crystal in an optically thin dielectric slab. *Journal of the Optical Society of America B*, 16(2):275–285, 1999.
- [109] C. Pask and A. Vatarescu. Spectral approach to pulse propagation in a dispersive nonlinear medium. *Journal of the Optical Society of America B*, 3(7):1018–1024, 1986.
- [110] M. E. Peskin and D. V. Schroeder. *An Introduction to Quantum Field Theory*. Perseus, 1995.
- [111] M. Plihal and A. A. Marududin. Photonic band structure of two-dimensional systems: The triangular lattice. *Physical Review B*, 44(16):8565–8571, 1991.
- [112] S. Raimes. *The Wave Mechanics of Electrons in Metals*. North-Holland, 1961.
- [113] S. Ramo, J. R. Whinnery, and T. Van Duzer. *Fields and Waves in Communication Electronics*. John Wiley & Sons, third edition, 1994.
- [114] P. C. Reeves-Hall, S. A. E. Lewis, S. V. Chernikov, and J. R. Taylor. Picosecond soliton pulse-duration-selectable source based on adiabatic compression in Raman amplifier. *Electron. Lett.*, 36:622, 2000.
- [115] K. Sakoda. Optical transmittance of a two-dimensional triangular photonic lattice. *Physical Review B*, 51:4672–4675, 1995.

- [116] K. Sakoda. Enhanced light amplification due to group-velocity anomaly peculiar to two- and three-dimensional photonic crystals. *Optics Express*, 4(5):167–176, March 1999.
- [117] K. Sakoda. *Optical Properties of Photonic Crystals*. Springer, New York, 2001.
- [118] K. Sakoda and K. Ohtaka. Optical response of three-dimensional photonic lattices: Solutions of inhomogeneous maxwell’s equations and their applications. *Physical Review B*, 54(8):5732–5741, 1996.
- [119] K. Sakoda and K. Ohtaka. Sum-frequency generation in a two-dimensional photonic lattice. *Physical Review B*, 54(8):5742–5749, 1996.
- [120] M. Scalora, M. J. Bloemer, A. S. Manka, J. P. Dowling, C. M. Bowden, R. Viswanathan, and J. W. Haus. Pulsed second-harmonic generation in nonlinear, one-dimensional, periodic structures. *Physical Review A*, 56:3166–3174, 1997.
- [121] F.A. Scheck. *Mechanics: From Newton’s Laws to Deterministic Chaos*. Springer, third edition, 1999.
- [122] M. Segev. Optical spatial solitons. *Optical and Quantum Electronics*, 30:503–533, 1998.
- [123] M. Segev and A. Yariv. Phase conjugation involving incoherent counterpropagating beams in photorefractive media. *Optics Letters*, 16(24):1938–1940, 1991.
- [124] E. G. Shapiro and S. K. Turitsyn. Theory of guiding-center breathing soliton propagation in optical communication systems with strong dispersion management. *Optics Letters*, 22(20):1544–1546, 1997.
- [125] E. G. Shapiro and S. K. Turitsyn. Theory of guiding-center breathing soliton propagation in optical communication systems with strong dispersion management. *Optics Letters*, 22:1544–1546, 1997.
- [126] Y. R. Shen. *The Principles of Nonlinear Optics*. John Wiley & Sons, 1984.
- [127] S. Shoji and S. Kawata. Photofabrication of three-dimensional photonic crystals by multibeam laser interference into a photopolymerizable resin. *Applied Physics Letters*, 76(19):2668–2670, 2000.
- [128] N.J. Smith, F.M. Knox, N.J. Doran, K.J. Blow, and I. Bennion. Enhanced power solitons in optical fibers with periodic dispersion management. *Electronics Letters*, 32:54–55, 1996.
- [129] R. A. Smith. *Wave Mechanics of Crystalline Solids*. Chapman and Hall, 1969.
- [130] A. W. Snyder, S. J. Hewlett, and D. J. Mitchell. Periodic solitons in optics. *Physical Review E*, 51(6):6297–6300, 1995.
- [131] N. Stefanou and A. Modinos. Impurity bands in photonic insulators. *Physical Review B*, 57(19):12127–12133, 1998.
- [132] A. A. Sukhorukov, Y. S. Kivshar, and O. Bang. Two-color nonlinear localized photonic modes. *Physical Review E*, 60(1):R41–R44, 1999.

- [133] A. A. Sukhorukov, Y. S. Kivshar, O. Bang, and C. M. Soukoulis. Parametric localized modes in quadratic nonlinear photonic structures. *Physical Review E*, 63:016615, 2000.
- [134] K. Suzuki, H. Kubota, A. Sahara, and M. Nakazawa. 640Gbit/s (40Gbit/s \times 16 channel) dispersion-managed DWDM soliton transmission over 1000km with spectral efficiency of 0.4bit/Hz. *Electronics Letters*, 36(5):443–445, 2000.
- [135] M. Suzuki, I. Morita, S. Yamamoto, N. Edagawa, H. Taga, and S. Akiba. Reduction of Gordon-Haus timing jitter by periodic dispersion compensation in soliton transmission. *Electronics Letters*, 31:2027–2028, 1995.
- [136] P. Tchofo Dinda, K. Nakkeeran, and A. B. Moubissi. Optimized Hermite-Gaussian ansatz functions for dispersion-managed solitons. *Optics Communications*, 187:427, 2001.
- [137] R. Trebino, P. O’Shea, M. Kimmel, and X. Gu. Measuring ultrashort laser pulses. *Optics and Photonics News*, 12:22–25, 2001.
- [138] J. Trull, R. Vilaseca, J. Martorell, and R. Corbolán. Second-harmonic generation in local modes of a truncated periodic structure. *Optics Letters*, 20(17):1746–1748, 1995.
- [139] S. K. Turitsyn and V. K. Mezentsev. Chirped solitons with strong confinement in transmission links with in-line fiber Bragg gratings. *Optics Letters*, 23(8):600–602, 1998.
- [140] I.M. Uzunov, M. Göllés, and F. Lederer. Soliton interaction near the zero-dispersion wavelength. *Physical Review E*, 52:1059–1071, 1995.
- [141] G. C. Valley and A. L. Smirl. Theory of transient energy transfer in Gallium Arsenide. *IEEE J. Quantum Electron.*, 24:304–310, 1988.
- [142] F. Verhulst. *Nonlinear Differential Equations and Dynamical Systems*. Springer, 2000.
- [143] P. R. Villeneuve, S. Fan, and J. D. Joannopoulos. Microcavities in photonic crystals: Mode symmetry, tunability, and coupling efficiency. *Physical Review B*, 54(11):7837–7842, 1996.
- [144] P. K. A. Wai, C. R. Menyuk, and B. Raghavan. Wavelength division multiplexing in an unfiltered soliton communication system. *Journal of Lightwave Technology*, 14(6):1449–1454, 1996.
- [145] G. N. Watson. *A Treatise on the Theory of Bessel Functions*. Cambridge, 1944.
- [146] D. M. Whittaker and I. S. Culshaw. Scattering-matrix treatment of patterned multilayer photonic structures. *Physical Review B*, 60(4):2610–2618, 1999.
- [147] J. M. Wozencraft and I. M. Jacobs. *Principles of Communication Engineering*. John Wiley & Sons, 1967.
- [148] Y. Xie, S. Lee, Z. Pan, J.-X. Cai, A. E. Willner, V. Grubsky, D. S. Starodubov, E. Sallik, and J. Feinberg. Tunable compensation of the dispersion slope mismatch in dispersion-managed systems using a sampled nonlinearly chirped FBG. *IEEE Photonics Technology Letters*, 12(10):1417–1419, 2000.

-
- [149] Y. Xu, R.K. Lee, and A. Yariv. Adiabatic coupling between conventional dielectric waveguides and waveguides with discrete translational symmetry. *Optics Letters*, 25(10):755–757, 2000.
- [150] Y. Xu, R.K. Lee, and A. Yariv. Propagation and second-harmonic generation of electromagnetic waves in a coupled-resonator optical waveguide. *Journal of the Optical Society of America B*, 17(3):387–400, 2000.
- [151] T. Yamamoto and M. Nakazawa. Third- and fourth-order active dispersion-compensation with a phase modulator in a terabit-per-second optical time-division multiplexed transmission. *Optics Letters*, 26(9):647–649, 2001.
- [152] A. Yariv. *Quantum Electronics*. John Wiley & Sons, third edition, 1989.
- [153] A. Yariv. Signal-to-noise considerations in fiber links with periodic or distributed optical amplification. *Optics Letters*, 15:1064–1066, 1990.
- [154] A. Yariv. *Optical Electronics in Modern Communications*. Oxford University Press, fifth edition, 1997.
- [155] A. Yariv. Steady state repeating optical pulses in a periodic nonlinear fiber. *Journal of Nonlinear Optical Physics & Materials*, 8(1):165–170, 1999.
- [156] A. Yariv, Y. Xu, R. K. Lee, and A. Scherer. Coupled-resonator optical waveguide: a proposal and analysis. *Optics Letters*, 24(11):711–713, 1999.
- [157] A. Yariv and P. Yeh. The application of Gaussian beam formalism to optical propagation in nonlinear media. *Optics Communications*, 27(2):295, 1978.
- [158] P. Yeh. Fundamental limit on the speed of photorefractive effect and its impact on device applications and material research. *Applied Optics*, 26(4):602–604, 1987.
- [159] P. Yeh and A. Yariv. Bragg reflection waveguides. *Optics Communications*, 19:427–430, 1976.
- [160] V. E. Zakharov and A. B. Shabat. Exact theory of two-dimensional self-focusing and one-dimensional self-modulation of waves in nonlinear media. *Soviet Physics JETP*, 34(1):62–69, 1972.
- [161] J. M. Ziman. *Principles of the Theory of Solids*. Cambridge University Press, second edition, 1998.